

Hybrid Lattice Boltzmann and Finite Volume Method for Fluid Flow and Heat Transfer Simulations

A Dissertation

Presented to

the Faculty of the Graduate School

University of Missouri-Columbia

In Partial Fulfillment

of the Requirement for the Degree

Doctor of Philosophy

By

Zheng Li

Dissertation Supervisor: Dr. Yuwen Zhang

December 2015

The undersigned, appointed by the dean of Graduate School have examined the dissertation entitled

**Hybrid Lattice Boltzmann and Finite Volume Method for
Fluid Flow and Heat transfer Simulations**

Presented by Zheng Li, a candidate for degree of doctor of philosophy, and hereby certify that, in their opinion, it is worthy of acceptance.

Professor Yuwen Zhang

Professor Gary Solbrekken

Professor Hongbin "Bill" Ma

Professor Qingsong Yu

Professor Stephen Montgomery-Smith

Acknowledgement

I am highly grateful to my supervisor Dr. Yuwen Zhang, Chairman of Department of Mechanical and Aerospace Engineering, for his encouragement, support, patience and guidance throughout this research work also in daily life. This dissertation would not have been possible without guidance and help of him. I would like to thank the members of my thesis evaluation committee, Dr. Hongbin Ma, Dr. Gary Solbrekken, Dr. Qingsong Yu and Dr. Stephen Montgomery-Smith for giving the time to provide valuable comments. I would like to express my gratitude to my parents, Runchao Li and Yanling Bao. Last but not least, I want to thank my wife Qing Yang for her support and understanding.

Support for this work by the U.S. National Science Foundation under grant number CBET- 1066917 is gratefully acknowledged.

Contents

Acknowledgement	ii
List of Figures	vi
List of Tables	xiii
NOMENCLATURE	xiv
Abstract	xx
Chapter 1. Introduction	1
1.1 Backgrounds	1
1.2 Literature Review.....	2
1.3 Dissertation Objective.....	9
Chapter 2. Lattice Boltzmann Method.....	15
2.1 Boltzmann equation	15
2.2 Lattice Bhatnagar-Gross-Krook model.....	16
2.3 Chapman-Enskog Expansion	18
2.4 Thermal LBM model	20
Chapter 3 Two Schemes for Hybrid Lattice Boltzmann and Finite Volume Methods	22
3.1 Introduction.....	22
3.2 Algorithm.....	23
3.3 Hybrid LBM and FVM method	24
3.4. Results and discussions.....	36
3.5. Conclusions.....	42
Chapter 4 A Coupled Lattice Boltzmann and Finite Volume Method for Natural Convection Simulation.....	43
4.1 Introduction.....	43
4.2 Coupled LBM-FVM method	43
4.3 Results and discussions.....	50
4.4 Conclusions.....	58
Chapter 5 A Hybrid Lattice Boltzmann and Finite Volume Method for Natural Convection...	59
5.1 Introduction.....	59
5.2 Hybrid LBM-FVM approach.....	59
5.3 Results and discussions	62
5.4 Conclusions.....	67
Chapter 6 A Combined Lattice Boltzmann and Monte Carlo Method for Natural Convection Simulation.....	69

6.1 Introduction.....	69
6.2 Combined LBM-MCM method	69
6.3 Results and discussions	73
6.4 Conclusions.....	78
Chapter 7 Double MRT Thermal Lattice Boltzmann Method for Simulating Natural Convection of Low Prandtl Number Fluids.....	79
7.1 Introduction.....	79
7.2 Double MRT thermal lattice Boltzmann model.....	80
7.3 Results and discussions	84
7.4 Conclusions.....	96
Chapter 8 Numerical Simulation of Melting Problems Using Lattice Boltzmann Method with Interfacial Tracking Method	97
8.1 Introduction.....	97
8.2 Problem Statement	97
8.3 LBM with Interfacial Tracking Method.....	101
8.4 Results and discussions	104
8.5 Conclusions.....	116
Chapter 9 Numerical Solution of Melting in a Discretely Heated Enclosure using an Interfacial Tracking Method.....	117
9.1 Introduction.....	117
9.2 Problem statement.....	117
9.3 Numerical method.....	121
9.4 Results and discussions	123
9.5 Conclusions.....	134
Chapter 10 A Hybrid Lattice Boltzmann and Finite Volume Method for Melting with Convection	135
10.1 Introduction.....	135
10.2 Problem statement.....	135
10.3 Hybrid LBM and FVM method for melting problem	136
10.4 Results and discussions	138
10.5 Conclusions.....	145
Chapter 11 Lattice Boltzmann Method Simulation of 3-D Natural Convection with Double MRT Model	146
11.1 Introduction.....	146
11.2 Natural convection in cubic cavity.....	146

11.3 Lattice Boltzmann method for 3-D problems	149
11.4 Results and discussions.....	156
11.5 Conclusions.....	176
Chapter 12 Numerical Investigation for 3-D Melting Problems Using Lattice Boltzmann method	177
12.1 Introduction.....	177
12.2 Problem Statement	177
12.3 Results and Discussion	181
12.4 Conclusions.....	186
Chapter 13 Conclusions	187
Publication list	190
Peer Reviewed	190
Not Peer reviewed.....	191
Reference	192
VITA.....	208

List of Figures

Figure 2-1 Particle behavior.....	15
Figure 2-2 Nine directions in D2Q9 model.....	17
Figure 2-3 Five directions in D2Q5 model.....	20
Figure 3-1 Control volume in 2-D FVM.....	23
Figure 3-2 Lid-driven flow.....	24
Figure 3-3 Computational domain for LBM and SIMPLE.....	29
Figure 3-4 Variable locations in SIMPLE.....	30
Figure 3-5 Computational nodes in LBM.....	30
Figure 3-6 Details on one control volume in the message passing zone.....	31
Figure 3-7 Boundary condition in LBM at the interface.....	32
Figure 3-8 Streamlines at $Re = 100$	36
Figure 3-9 Streamlines at $Re = 400$	37
Figure 3-10 Streamlines at $Re = 1000$	38
Figure 3-11 Horizontal velocity profiles.....	39
Figure 3-12 Vertical velocity profiles.....	40
Figure 4-1 Physical model of the natural convection problem.....	44

Figure 4-2 Computational domains for LBM and FVM.....	47
Figure 4-3 Variables locations.....	49
Figure 4-4 Temperature fields at $Ra=10^4$	51
Figure 4-5 Nusselt numbers at $Ra=10^4$	52
Figure 4-6 Nusselt numbers at $Ra=10^4$	52
Figure 4-7 Temperature fields at $Ra=10^5$	53
Figure 4-8 Streamlines at $Ra=10^5$	54
Figure 4-9 Nusselt numbers at $Ra=10^5$	54
Figure 4-10 Temperature fields at $Ra=10^6$	56
Figure 4-11 Streamlines at $Ra=10^6$	57
Figure 4-12 Nusselt numbers at $Ra=10^6$	57
Figure 5-1 Control volume in FVM.....	60
Figure 5-2 Grid setting 1.....	60
Figure 5-3 Grid setting 2.....	61
Figure 5-4 Streamlines comparison at $Ra=10^4$	63
Figure 5-5 Temperature field comparison at $Ra=10^4$	63
Figure 5-6 Streamlines comparison at $Ra=10^5$	64
Figure 5-7 Temperature field comparison at $Ra=10^5$	64

Figure 5-8 Streamlines comparison at $Ra=10^6$	65
Figure 5-9 Temperature field comparison at $Ra=10^6$	65
Figure 5-10 Comparison of Nusselt numbers.....	66
Figure 6-1 Computing grid.....	70
Figure 6-2 Flowchart.....	72
Figure 6-3 Two-dimensional steady state heat conduction.....	74
Figure 6-4 Conduction temperature field comparison.....	75
Figure 6-5 Streamlines in case 1.....	76
Figure 6-6 Temperature field in case 1.....	76
Figure 6-7 Streamlines in case 2.....	77
Figure 6-8 Temperature field in case2.....	77
Figure 7-1 Case 1: average Nusselt number.....	84
Figure 7-2 Case 1: streamlines.....	85
Figure 7-3 Case 1: temperature field.....	85
Figure 7-4 Case 1: Nusselt number.....	86
Figure 7-5 Case 2: average Nusselt number.....	86
Figure 7-6 Case 2: streamlines.....	87
Figure 7-7 Case 2: temperature field.....	88

Figure 7-8 Case 2: Nusselt number.....	89
Figure 7-9 Case 3: average Nusselt number.....	90
Figure 7-10 Case 3: streamlines.....	91
Figure 7-11 Case 3: temperature field.....	92
Figure 7-12 Case 4: average Nusselt number.....	93
Figure 7-13 Case 4: streamlines.....	94
Figure 7-14 Case 4: temperature field.....	95
Figure 8-1 Phase change model.....	98
Figure 8-2 Melting front.....	102
Figure 8-3 Liquid fraction comparison in conduction melting.....	106
Figure 8-4 Temperature comparison in conduction melting.....	107
Figure 8-5 Case 1: temperature field ($ Fo = 4 $).....	108
Figure 8-6 Case 1: melting front comparison ($ Fo = 4 $).....	109
Figure 8-7 Case 1: temperature field ($ Fo = 10 $).....	109
Figure 8-8 Case 1: melting front comparison ($ Fo = 10 $).....	110
Figure 8-9 Case 1: Nusselt number and liquid fractions.....	110
Figure 8-10 Case 2: streamlines ($ Fo = 4 $).....	112
Figure 8-11 Case 2: temperature field ($ Fo = 4 $).....	112

Figure 8-12 Case 2: melting front comparison ($ Fo = 4 $)	113
Figure 8-13 Case 2: streamlines ($ Fo = 10 $)	113
Figure 8-14 Case 2 temperature field ($ Fo = 10 $)	114
Figure 8-15 Case 2: melting front comparison ($ Fo = 10 $)	114
Figure 8-16 Case 2: Nusselt number and liquid fractions	115
Figure 9-1 Physic model	118
Figure 9-2 Location of the liquid-solid interface	122
Figure 9-3 Temperature field $ Ste=2.36 $	125
Figure 9-4 Melting front comparison $ Ste=2.36 $	126
Figure 9-5 Comparison of melting volume fraction $ Ste=2.36 $	126
Figure 9-6 Temperature on the heat blocks changing with time $ Ste=2.36 $	127
Figure 9-7 Temperature field $ t=92 $ min, $ Ste=1.96 $	128
Figure 9-8 Melting volume fraction comparison $ t=92 $ min, $ Ste=1.96 $	128
Figure 9-9 Melting front comparison $ t=92 $ min, $ Ste=1.96 $	129
Figure 9-10 Temperature on the heat blocks changing with time $ t=92 $ min, $ Ste=1.96 $	129
Figure 9-11 Melting volume fraction comparison with different $ Ste $	130
Figure 9-12 Melting front comparison with different $ Ste $	130
Figure 9-13 Temperature on the heat blocks changing with time	131

Figure 9-14 Different locations of the heaters.....	132
Figure 10-1 Phase change model.....	136
Figure 10-2 Porous media assumption.....	137
Figure 10-3 Temperature field $Ste=0.0451$, $\tau=52700$	139
Figure 10-4 Melting front comparison $Ste=0.0451$, $\tau=52700$	140
Figure 10-5 Temperature field $Ste=0.0959$, $\tau=37250$	141
Figure 10-6 Melting front comparison $Ste=0.0959$, $\tau=37250$	141
Figure 10-7 Nusselt number comparison.....	143
Figure 10-8 Comparison of liquid fractions.....	143
Figure 10-9 Comparison of melting fronts.....	144
Figure 11-1 Cubic natural convection.....	147
Figure 11-2 D3Q19 model.....	150
Figure 11-3 D3Q7 model.....	154
Figure 11-4 Type 1, temperature results, $Ra = 1 \times 10^4$	161
Figure 11-5 Type 1, Streamtrace results, $Ra = 1 \times 10^4$	162
Figure 11-6 Type 1, temperature results, $Ra = 1 \times 10^5$	164
Figure 11-7 Type 1, Streamtrace results, $Ra = 1 \times 10^5$	165
Figure 11-8 Type 2, temperature results, $Ra = 1 \times 10^4$	167

Figure 11-9 Type 2, Streamtrace results, $Ra = 1 \times 10^4$	168
Figure 11-10 Type 2, temperature results, $Ra = 1 \times 10^5$	169
Figure 11-11 Type 2, Streamtrace results, $Ra = 1 \times 10^5$	170
Figure 11-12 Type 3, temperature results, $Ra = 1 \times 10^4$	172
Figure 11-13 Type 3, Streamtrace results, $Ra = 1 \times 10^4$	173
Figure 11-14 Type 3, temperature results, $Ra = 1 \times 10^5$	174
Figure 11-15 Type 3, Streamtrace results, $Ra = 1 \times 10^5$	175
Figure 12-1 Cubic cavity melting model.....	177
Figure 12-2 Liquid fraction comparison.....	182
Figure 12-3 Temperature distribution comparison.....	182
Figure 12-4 Case 1 results $Fo = 1.00$	184
Figure 12-5 Case 2 results $Fo = 1.57$	185

List of Tables

Table 5-1 Comparison of the maximum Nusselt numbers.....	65
Table 5-2 Comparison of the locations of maximum Nusselt numbers.....	67
Table 6-1 Comparison of Nusselt number.....	78
Table 9-1 Thermophysical properties	123
Table 9-2 temperatures on the heat blocks.....	133
Table 11-1 Type 1, \overline{Nu}_{3D} comparison.....	158
Table 11-2 Type 1, Nu_{\max} comparison.....	159
Table 11-3 Type 1, \overline{Nu}_{2D} comparison.....	159
Table 11-4 Type 1, Velocity comparison, $Ra = 1 \times 10^4$	160
Table 11-5 Type 1, Velocity comparison, $Ra = 1 \times 10^5$	163
Table 11-6 Type 2, \overline{Nu}_{3D} comparison.....	168
Table 11-7 Type 2 benchmark solutions.....	171
Table 11-8 Type 3 benchmark solutions.....	175
Table 12-1 Two convection melting cases.....	183

NOMENCLATURE

a constant in multiple relaxation time model

A non-dimensional parameter

A_0 aspect ratio of the enclosure, W/H

A_1 aspect ratio of the left wall, L/H

c lattice speed

c_s lattice sound speed

e_i velocity in all directions

f density distribution

F non-dimensional time

F_i body force

Fo Fourier number

f_p liquid fraction

g energy distribution

g gravity acceleration (m / s^2)

G effective gravity acceleration (m / s^2)

H height of the enclosure (m)

h_{sl} latent heat (J/kg)

\mathbf{I} identity tensor

k thermal conductivity (W/m k)

K coefficient in Chapman-Enskog expansion

\bar{k} modified thermal conductivity (W/m k)

L thickness of the left wall (m)

m dimension of the problem

M transform matrix for density distribution

m_i moment function for density distribution

Ma Mach number

N transform matrix for density distribution

Nu Nusselt number

n_i moment function for energy distribution

p pressure (N/m²)

P non-dimensional pressure

Pr Prandtl number

Q heat generation by the heaters (W/m)

\mathbf{Q} collision matrix for energy distribution

Q'' non-dimensional internal heat generation

q''' internal heat generation (W/m^3)

\mathbf{r} lattice location vector

R_g Gas constant

Ra Rayleigh number

Re Reynolds number

RN Random number

s location of melting front (m)

S non-dimensional location of melting front

\mathbf{S} collision matrix for density distribution

Sc subcooling

Ste Stefan number

t time (s)

T temperature (K)

T_m melting temperature (K)

u horizontal velocity (m/s)

u_0 lid velocity (m/s)

u_{sound} sound speed(m/s)

U non-dimensional horizontal velocity

v vertical velocity (m/s)

V non-dimensional vertical velocity

\mathbf{V} velocity

W width of the enclosure (m)

Greek Symbols

\mathbf{a} lattice acceleration

α thermal diffusivity (m^2 / s)

β volume expansion coefficient of the fluid (K^{-1})

Γ coefficient in SIMPLE

δ Kronecker's delta

Δ^{PCM} porous media effect term

Δt time step

$\boldsymbol{\varepsilon}$ lattice particle velocity

θ nondimensional temperature

$\mathbf{\Pi}$ moment of order 2

ν kinematic viscosity (m^2/s)

μ dynamic viscosity (N·s/m²)

ρ Density (kg/m³)

τ non-dimensional time

τ_v relaxation time for velocity

τ_T relaxation time for energy

Φ general variable

ω_i value factor for velocity

ω_i^T value factor for energy

Ω collision operator

Superscript

eq equilibrium

e east face of the control volume

i initial condition

l liquid

p control volume melting front located

s solid

w west face of the control volume

Subscript

- i direction of the discretized velocity
- L LBM
- S SIMPLE
- 1, 2 order for Chapman-Enskog expansion

Abstract

The fluid flow and heat transfer problems encountered in industry applications span into different scales and there are different numerical methods for different scales problems. Multiscale methods are needed to solve problems involving multiple scales. In this dissertation, multiscale methods are developed by combining various single scale numerical methods, including lattice Boltzmann method (LBM), finite volume method (FVM) and Monte Carlo method. Two strategies exist in combining these numerical methods. For the first one, the whole domain is divided into multiple subdomains and different domains use various numerical methods. Message passing among subdomains decides the accuracy of this type of multiscale numerical method. For the second one, various parameters are solved with different numerical methods. These two types of multiscale methods are both discussed in this dissertation.

In Chapters 3 and 4, the whole domain is divided into two subdomains and they are solved with LBM and FVM respectively. This LBM-FVM hybrid method is verified with lid driven flows and natural convections. In Chapter 5, a LBM-FVM hybrid method is proposed to take both advantages of LBM and FVM: velocity field and temperature field are solved with LBM and FVM respectively. MCM has advantages in solving radiative heat transfer, and LBM-MCM hybrid method is proposed in Chapter 6.

Numerical investigation for melting problems are carried on in this dissertation. The key point in solving the melting problem is how to obtain the interface location. To overcome the disadvantages in the now existing numerical methods, an interfacial tracking method is advanced to calculate the interface location. In Chapter 7, low Prandtl fluid

natural convections are solved with LBM to discuss the oscillation results. Based on these results, low Prandtl number melting problems are solved using LBM with interfacial tracking method in Chapter 8. High Prandtl number melting problems in a discrete heated enclosure are solved using FVM with interfacial tracking method in Chapter 9. To take both advantages of LBM and FVM, melting problems are solved with LBM-FVM hybrid method in chapter 10, while interfacial tracking method is advanced by porous media assumptions in fluid flow field simulation process.

Problems in Chapters 3-10 are all in two-dimensional and three-dimensional problems are more general than them in the realistic applications. Double LBM-MRT model for three-dimensional fluid flow and heat transfer is proposed and three types of natural convections in a cubic cavity are discussed in Chapter 11. For the first two types of cubic natural convections, the present results agreed very well with the benchmark solutions or experimental results in the literature. The results from the third type exhibited more general three-dimensional characters. Three-dimensional melting problems are solved with the proposed double LBM-MRT model with interfacial tracking method in Chapter 12. Numerical results in three conduction melting problems agree with the analytical results well. Taking Chapter 11 results in consideration, the double LBM-MRT model with interfacial tracking method is valid to solve three-dimensional conduction or convection controlled melting problems. Two convection melting problems in a cubic cavity are also solved. With a lower Rayleigh number, the convection effects are weaker; side wall effects are smaller; melting process carries on slower.

Chapter 1. Introduction

1.1 Backgrounds

The fluid flow and heat transfer problems encountered in industry applications span into different scales and there are different numerical methods for different scales problems. Molecular dynamics can be applied to solve nano- and microscale problems while lattice Boltzmann method (LBM) and Monte Carlo method are typical mesoscopic scale methods. Finite volume method (FVM) and finite difference method, on the other hand, are suitable for solving the macroscale problems.

Realistic problems may involve more than one scale and they are so-called multiscale problems. Multiscale transport phenomena exists in many industry areas, such as: fuel cell, laser material interaction and electronics cooling. Single scale numerical methods are not suitable for multiscale problem regarding applicability and calculation time. It's necessary to build multiscale method to solve these multiscale problems.

In this dissertation, multiscale methods are developed by combining various single scale numerical methods, including LBM, FVM and MCM and two strategies exist in combining these numerical methods. For the first one, the whole domain is divided into multiple subdomains and different domains use various numerical method. Message passing among subdomains decides the accuracy of this type of multiscale numerical method. For the second one, various parameters are solved with different numerical methods. These two types of multiscale methods both will be discussed in this dissertation.

On the other hand, phase change problems appear in different areas, such as thermal energy storage, electronics cooling, and food processing. These problems always involve nonlinearities, strong couplings and a moving boundary. The key point in solving the phase change problem is how to obtain the interface location. Various melting problems are investigated numerically in this dissertation. Both two-dimensional and three-dimensional cases are in consideration.

1.2 Literature Review

Lattice Boltzmann method [1-4] has been developed into a promising numerical method in the last two decades. The LBM developed from lattice gas automata (LGA) [5] is growing to be versatile in many fields [6] because of its three important features [3]: (1) the nonlinear convection term in Navier-Stokes (NS) equations is linear in the phase space, (2) the incompressible NS equations can be regained by Chapman-Enskog expansion [7], and (3) a minimal set of velocities in phase space is needed in LBM. It can be used to solve different fluid flow problems, such as incompressible fluid flow [8], compressible fluid flow [9] and multiphase fluid flow [10].

The lattice Boltzmann method was originally just used to solve the mass and momentum conservations [2] but the thermal LBM was also developed to solve the energy equation. LBM can be applied to simulate heat transfer problems with conduction [11], convection [12] and radiation [13]. There are several models for the fluid flow and heat transfer problems in LBM. He et al. proposed the internal energy function by relating internal energy with the kinetic energy of particle for the incompressible fluid flow and heat transfer [14]. Then its simplified thermal LBM model was advanced by Peng et al. [15] while Guo et al. introduced a coupled lattice BGK model based on Boussinesq

assumption [16]. The D2Q9 and D2Q5 models were respectively used to solve the velocity and temperature fields [17]. Choi [18] proposed LBM model for turbulent natural convection simulation. Novozhilov and Byrne [19] investigated thermal explosion in natural convection using LBM. Kefayati [20] simulated ferrofluid heat dissipation effect on natural convection at an inclined cavity filled with kerosene/cobalt utilizing LBM.

In general, when solving the heat transfer problems, the thermal LBM falls into two categories: the multispeed (MS) approach and the multi-distribution function (MDF) approach [21]. The MS approach uses the density distribution by introducing more discrete velocities to obtain the temperature [22], while MDF introduces an additional independent distribution to get the energy equation [14]. But both methods have some limitations: MS approach has numerical instability and narrow range of temperature variation, while MDF must be assumed that the Mach number of the flow is small and the density varies slowly in order to obtain the correct macroscopic equations [16].

Finite volume method [23] are well-accepted methods in Computational Fluid Dynamics (CFD). FVM is successful because its discrete methods always satisfy conservation laws, and can be adopted easily due to its clear physical meaning [24]. Semi-Implicit Method for Pressure Linked Equation (SIMPLE) [23] is a widely used algorithm in FVM to solve fluid flow and heat transfer problems. Combination of the LBM and FVM will allow us to take advantages of both of them.

Meanwhile, development of CFD involves very wide variation of scales [25] ranging from, nano-/micro-, meso- and macroscales. Molecular dynamics (MD) [26] is applicable to nano- and microscale problems and LBM is a typical mesoscopic scale method [27]; Finite difference method (FDM) [28] and FVM [29] on the other hand, falls into the

category of macroscale approach [24]. It is impossible to solve a multiscale problem using any single-scale method. For example, MD simulation cannot be used in the entire simulation domain, and FVM is not suitable for the microscopic region; LBM costs several times more computational time than the FVM to obtain the same accuracy in the macroscopic problem [30]. So there is a demand to develop multiscale methods to fully utilize all three methods. Two ways exist to fulfill the multiscale methods: for the first one, the whole domain is divided into several subdomains and these subdomains are solved with various numerical methods respectively; for the second one, various parameters are solved with different numerical methods.

For the first type of multiscale methods, there are some existing results reported in the literature: MD-FVM [31-33] hybrid methods were developed to combine microscale and macroscale numerical methods; In Ref. [34-36], LBM-MD was proposed to combine mesoscale and microscale numerical methods. This dissertation focuses on multiscale methods combining mesoscale and macroscale numerical methods. LBM-FDM [37-40] were advanced to solve various multiscale problems. However, the FDM itself has the limitation when solving problems with complex computational domains [24]. This shortfall restricts the development of LBM-FDM because one of the most attractive advantages of LBM is its suitability to solve the problems in complex computational domains. LBM-FVM [41-43] were developed to solve conduction-radiation heat transfer and compressible fluid flow problems. Luan et al. [44] solved natural convection using the LBM-FVM with the general reconstruction operator [45] reaching persuasive results. Chen et al. [46] used this method to fulfill LBM-FVM with various grid settings. However, general

reconstruction operator is newly proposed to fulfill the combine method which means more validations are needed for the general reconstruction operator itself.

In this dissertation, LBM-FVM hybrid methods for natural convection are in consideration. Mohamad and Kuzmin [47] evaluated the force term in LBM for the natural convection problem while Choi and Kim [48] compared the thermal models in the LBM simulation of natural convection in a square cavity. On the other hand, Christon et al. [49] discussed the computational predictability of time-dependent natural flow in enclosure using FVM. Zhang et al. [50] proposed a compact finite difference scheme based on projection method for FVM in natural convection simulation. Regarding these results in Refs. [47-50], LBM and FVM both can solve natural convection. Therefore, it's possible to build LBM-FVM hybrid method to solve natural convection.

Second type of multiscale method is a new choice for LBM to solve heat transfer problems. Several researchers [51, 52] obtained some good results using the LBM-FDM hybrid method. However, the FDM itself has the limitation when solving problems with complex computational domain [24]. This shortfall restricts the development of LBM-FDM because the one of the most attractive advantages of LBM is its suitability to solve the problems in complex computational domain. There are limited efforts on the hybrid lattice Boltzmann with finite volume method (LBM-FVM) [53, 54] for conduction-radiation problems. However, there is no report on application of LBM-FVM to natural convection problems that the velocity is coupled with temperature field.

Monte Carlo method (MCM) is a widely used numerical method for heat transfer problem [55]. It can solve conduction [56], convection [57] and radiation [58] heat transfer problems. In addition, both MCM and LBM belong to mesoscopic scale method. It is

possible to combine these two methods to solve convection heat transfer problems. However, there is no report on combining these two methods for a convection heat transfer problem.

Besides the multiscale method research, various melting problems are solved with LBM, FVM and LBM-FVM hybrid method, respectively. Melting problems appear in different areas such as thermal energy storage, electronics cooling, and food processing. These problems always involve nonlinearities, strong couplings and a moving boundary [59]. Analytical, experimental and numerical methods can be used to solve melting problems.

Some 1-D conduction controlled melting problems can be solved analytically. Under limited conditions, the exact solutions of one-region and two-region problems can be obtained analytically [60], but the melting problems that can be solved by exact solutions are very limited. The integral approximate method is another valid way to solve some melting problems analytically [61, 62]. Jany and Bejan [63] performed scale analysis to analyze melting problem with natural convection. Zhang and Bejan [64] studied the natural convection melting with conduction in the solid theoretically. Zhang and Chen [65] studied the effects of wall conduction and the size of the heat source on the melting process using the boundary layer theory. Melting problems can be solved analytically are limited.

Numerous experimental studies the melting problem has been reported in the literature. Okada [66] reported experimental results for melting in an enclosure with constant temperature on the side wall. Zhang and Bejan [67] investigated the melting problem in an enclosure with constant heating rate. The discrete heater can be either flush-mounted [68] or protruding [69] to the side wall. Benard et al. [70] studied the melting in rectangular

enclosure experimentally and numerically. Dong et al. [71] and Wang et al. [72] investigated the melting with natural convection in the rectangular enclosure experimentally.

Bertrand et al. compared the results from different numerical methods [73]. The numerical methods to solve solid-liquid phase change problem can be divided into two groups [74]: deforming grid and fixed grid approaches [75]. Deforming grid approach uses coordinate transformation technique to transfer the solid and liquid phase geometries into the fixed regions. The high computational cost and complexity of the governing equations and boundary conditions are the main shortcomings of this method. On the other hand, the fixed grid method uses the same set of governing equations for both phases throughout the simulation. Rather than explicitly tracking the interface in the deforming grid approach, the interface is obtained from the temperature distribution in the fixed grid approach. It was reported that the fixed grid approach can reach the same accuracy as the deforming grid approach with much less computational time [76]. The enthalpy method [77, 78] and equivalent heat capacity method [79, 80] are the two major methods in the fixed grid approaches. The equivalent heat capacity method can only solve the melting problem occurring in a range of temperature; when this range is small, it is difficult to reach the converged result using this method.

Sasaguchi et al. [81] simulated a similar melting process using enthalpy method for the case that the Rayleigh number was lower than that reported in Ref. [68]. Binet and Lacroix [82] reported numerical solution under the condition similar to that in Ref. [68], but the result was not satisfactory when time was equals 120 minutes. Ganaoui and Semma [83] reported the results of phase change problem obtained by hybrid method based on entropy

model. Cao and Faghri [84] proposed a temperature transforming model that can take advantages of both the enthalpy method and equivalent heat capacity method.

Melting problems have been solved using LBM in several literatures: Huber et al. [17] solved natural convection governed melting problems; Gao and Chen [85] solved the melting in a rectangular cavity filled with porous media with LBM. Semma et al. [86] suggested that the phase change zone can be considered as a porous medium and solved the phase change problem with pure LBM. Jourabian et al. [87] solved melting of NEPCM within a cylindrical tube. Miller et al. [88] proposed LBM model for anisotropic liquid-solid phase transition. Eshraghi and Felicelli [89] advanced an implicit lattice Boltzmann model for heat conduction with phase change. The above references are all based on enthalpy method. Although the enthalpy method can solve the melting problem taking place at a fixed temperature or in a range of temperature, it has difficulty in temperature oscillation.

To overcome the disadvantages in equivalent heat capacity method and enthalpy method, Zhang and Chen [90] proposed an interfacial tracking method for the melting under ultrafast laser heating. It has advantages in good computational stability, high computational efficiency and applicability in melting taking place at a fixed temperature or in a range of temperature. Chen et al. [91] applied this method to solve natural convection controlled melting in a rectangular enclosure under the constant wall temperature. All of the above applications of the interfacial tracking method are based on the finite volume method (FVM) [24]. Further research are carried for interfacial tracking method in this dissertation.

Melting problem can involve various phase change materials (PCM). Their Prandtl numbers vary from 10^{-3} (liquid metal) to 10^5 (functional oil) [92]. Low Prandtl number fluid flow and heat transfer problem may reach oscillation results. Kosec and Sarler [92] reported the solution of a low Prandtl number natural convection benchmark problem Hannoun et al. [59] discussed the fluid field bifurcation melting with convection. Hannoun et al. [93] included oscillation results in low Prandtl number fluid melting problem. Both low and high Prandtl number fluid melting problems are discussed in this dissertation.

The results in literatures above are all based on two-dimensional problems. In this dissertation, two-dimensional and three-dimensional problems are solved in this dissertation.

1.3 Dissertation Objective

Various multiscale methods are introduced in the literatures above, including MD-LBM, MD-FVM, MD-FDM, LBM-FVM and LBM-FVM. Two ways exist to fulfill the multiscale methods: for the first one, the whole domain is divided into several subdomains and these subdomain are solved with various numerical methods respectively; for the second one, various parameters are solved with different numerical methods. Now existing ways to fulfill the first type of LBM-FVM method request large amounts of additional computational time and need further validation; Second type of FVM-LBM method for convection simulation are vacant. These two types of hybrid LBM-FVM methods are proposed in this dissertation. And they are employed to solve natural convection and melting problems.

Melting problems have been solved analytically, experimentally and numerically by many researchers. Melting problems that can be solved analytically are limited and it's not possible to solve all the melting problems experimentally regarding high cost. Numerical investigation for melting problems are discussed in this dissertation. Now existing numerical methods to solve solid-liquid phase change problem can be divided into two groups: deforming grid and fixed grid approaches. The high computational cost and complexity of the governing equations and boundary conditions are the main shortcomings of deforming grid approach. On the other hand, the fixed grid method uses the same set of governing equations for both phases throughout the simulation. The enthalpy method and equivalent heat capacity method are the two major methods in the fixed grid approaches. The equivalent heat capacity method can only solve the melting problem occurring in a range of temperature; when this range is small, it is difficult to reach the converged result using this method. To avoid these short comings, this dissertation uses LBM, FVM and LBM-FVM with interfacial tracking method to solve various melting problems. Both two-dimensional and three-dimensional cases are in consideration.

The following works are carried on:

Two hybrid methods that combine LBM and FVM are proposed in Chapter 3. The D2Q9 model is used in LBM, while SIMPLE algorithm with QUICK scheme is chosen for FVM. The hybrid method is fulfilled by dividing the computational domain into the LBM and FVM zones, with a public message passing zone in between. Only macroscopic velocities are needed to be passed between the two separated zones and nonequilibrium extrapolation scheme and finite-difference velocity gradient method are used to pass information between the SIMPLE and LBM zones. The proposed methods are used to solve

of the lid-driven flow and the results obtained using pure LBM, pure SIMPLE, and the hybrid methods with different combine schemes agreed with each other very well in different range of Reynolds number.

A coupled lattice Boltzmann and finite volume method is proposed to solve natural convection in a differentially heated squared enclosure in Chapter 4. The computational domain is divided into two subdomains and a message passing zone is between them. The velocity and temperature fields are respectively solved using D2Q9 and D2Q5 models in LBM while SIMPLE algorithm is applied to the FVM. The velocity and temperature information transfers are fulfilled by a nonequilibrium extrapolation scheme. Pure FVM, pure LBM, and the coupled method with two different geometric settings are applied to solve the natural convection with different Rayleigh numbers. The results obtained from the coupled method agreed with those from pure FVM and LBM very well.

In Chapter 5, a hybrid lattice Boltzmann and finite volume method is proposed for fluid flow and heat transfer simulation. LBM is applied to obtain velocity field while FVM is used to obtain the temperature field. The D2Q9 model and nonequilibrium extrapolation scheme boundary condition are used in LBM and the SIMPLE algorithm with QUICK scheme is employed in the FVM. Natural convection with different Rayleigh numbers are solved by the hybrid method and the results agreed very well with that obtained from pure FVM and pure thermal LBM. This is the first time that the hybrid LBM-FVM is applied to solve natural convection problem.

In Chapter 6, a combined lattice Boltzmann and Monte Carlo method is proposed to solve the natural convection problem. Lattice Boltzmann method solves the velocity field while the temperature field is obtained by the Monte Carlo method. The two-dimensional

nine discrete velocities (D2Q9) model is used in lattice Boltzmann method, and random walker is employed in Monte Carlo method. Natural convection in differentially heated rectangular enclosure under different Rayleigh numbers are solved for validation and the results agree with the benchmark well. It indicates the proposed combined is valid for the natural convection simulation.

In Chapter 7 double multiple-relaxation-time thermal lattice Boltzmann method is employed to solve two-dimensional natural convection of for low Prandtl number (0.001 – 0.01) fluids. The velocity and temperature fields are solved using D2Q9 and D2Q5 models, respectively. With different Rayleigh number, the tested natural convection can either achieve to steady state or oscillatory; the results agree with those in the literature very well. Therefore, numerical method in use is valid for the low Prandtl number natural convection simulation. Rayleigh number and Prandtl number effects are also investigated when the natural convection results oscillate.

In Chapter 8, a lattice Boltzmann method with an interfacial tracking method is used to solve melting problem in an enclosure. Both conduction and convection controlled melting problems are solved to validate the proposed method. For the conduction controlled melting problem, the results agreed with those from analytical solution very well. The results for the convection controlled melting problem also agreed with those in the literature. The proposed approach is valid for numerical simulation of the melting problem.

In Chapter 9, melting in a discretely heated rectangular enclosure is solved using an interfacial tracking method. The interfacial tracking method combines advantages of both deforming and fixed grid approaches. The location of melting front was obtained by calculating the energy balance at the solid-liquid interface. Through validating the

numerical method with experimental results, it was demonstrated that the interfacial tracking method can be used to solve melting in a discretely heated enclosure at high Rayleigh numbers. Effect of Stefan number and geometry of the heaters on the melting process are also investigated.

In Chapter 10, a hybrid lattice Boltzmann and finite volume model is proposed to solve the natural convection controlled melting problem. Lattice Boltzmann method (LBM) is applied to solve the velocity field while the temperature field is obtained by the finite volume method (FVM). The D2Q9 model and finite-difference velocity gradient boundary condition are used in LBM and the SIMPLE algorithm with QUICK scheme is employed in FVM. An interfacial tracking model based on energy balance at the interface is applied to obtain the location of the solid-liquid interface. The results from the present hybrid method are validated with the experimental results and the good agreements were obtained.

In Chapter 11, three-dimensional double MRT model is proposed for the first time for fluid flow and heat transfer simulation. Three types of cubic natural convection problems are solved with proposed method at various Rayleigh numbers. Two opposite vertical walls on the left and right are kept at different temperatures for all three types, while the remained four walls are either adiabatic or have linear temperature variations. For the first two types of cubic natural convections that four walls are either adiabatic or vary linearly, the present results agreed very well with the benchmark solutions or experimental results in the literature. For the third type of cubic natural convection, the front and back surfaces has linearly variable temperature while the bottom and top surface are adiabatic. The results from the third type exhibited more general three-dimensional characters.

In Chapter 12, 3-D melting problems are solved with double MRT model proposed. Various 3-D conduction controlled melting problems are solved first to verify the numerical method. Liquid fraction tendency and temperature distribution obtained from numerical methods agree with the analytical results well. The proposed double MRT model with interfacial tracking method is valid to solve 3-D melting problems. Different convection controlled melting problems in a cubic cavity are then solved with the proposed numerical method. Melting fronts move faster and liquid PCM temperature are greater with height growing in the cavity. Melting front moving velocities are different with the same height of the cavity. Liquid velocities close to the side walls are limited due to the non-slip condition. Correspondently, the natural convection effect is weakened. Therefore melting front at the center moves fastest at the same height of the cavity. Rayleigh effects to the 3-D melting process are also discussed.

Chapter 2. Lattice Boltzmann Method

Lattice Boltzmann method is a promising mesoscale method for fluid flow and heat transfer simulation. Instead of solving mass, velocity and energy conservation equations as traditional CFD methods, LBM reaches macroscale parameter using statistical behaviors of particles, which represent large amounts of fluid molecules.

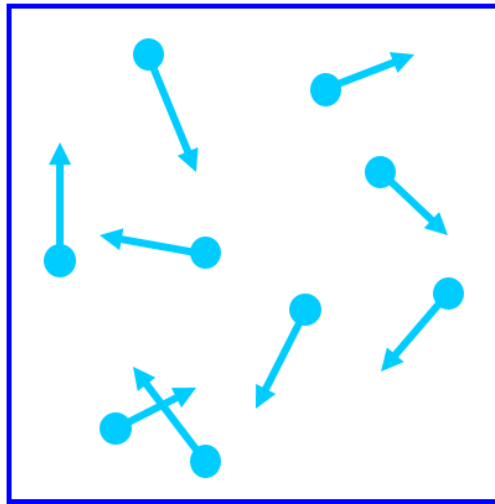


Fig. 2-1 Particle behavior

These particles can stream and collision to each other in the computational domain.

2.1 Boltzmann equation

Statistical behaviors of particles that are not in thermodynamic equilibrium can be described by the Boltzmann equation:

$$\frac{\partial f}{\partial t} + \boldsymbol{\varepsilon} \cdot \frac{\partial f}{\partial \mathbf{r}} + \mathbf{a} \cdot \frac{\partial f}{\partial \boldsymbol{\varepsilon}} = \Omega(f)_{\text{collision}} \quad (2.1)$$

where f is the density distribution, and Ω is the collision operator that is dictated by the collision rules. $\boldsymbol{\varepsilon}$, \mathbf{r} and \mathbf{a} are the particle's velocity, location and acceleration, respectively. To solve this Boltzmann equation, we need to simplify the collision term first. In this chapter, we introduce the widely used Bhatnagar-Gross-Krook model to fulfill this process.

2.2 Lattice Bhatnagar-Gross-Krook model

The Bhatnagar-Gross-Krook model (BGK) that uses the Maxwell equilibrium distribution, f^{eq} , will be used in this chapter:

$$f^{eq} = n \frac{1}{(2\pi R_g T)^{m/2}} \exp\left[-\frac{(\boldsymbol{\varepsilon} - \mathbf{u})^2}{2R_g T}\right] \quad (2.2)$$

where m is the dimension of the problem. Equation (2.2) describes the situation that the system has reached to the final equilibrium. The BGK model assumes that the collision term is the time relaxation from density distribution to the Maxwell equilibrium distribution. Assuming the relaxation time is τ_v , the Boltzmann equation under the BGK model can be expressed as:

$$\frac{\partial f}{\partial t} + \boldsymbol{\varepsilon} \cdot \frac{\partial f}{\partial \mathbf{r}} + \mathbf{a} \cdot \frac{\partial f}{\partial \boldsymbol{\varepsilon}} = -\frac{1}{\tau_v} (f - f^{eq}) \quad (2.3)$$

The LBM used in this thesis is a special scheme of LBGK. Only limited numbers of directional derivatives are applied to Eq. (2.3) and there must be enough information to obtain the macroscopic governing equation.

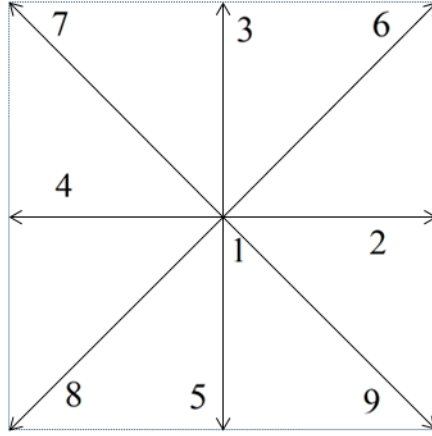


Figure 2-2 Nine directions in D2Q9 model

The D2Q9 model is used and nine directions are selected in the 2-D problem shown in the Fig. 2-2. The velocity in every direction is:

$$e_i = \begin{cases} (0,0) & i = 1 \\ c(-\cos \frac{a\pi}{2}, -\sin \frac{a\pi}{2}) & i = 2, 3, 4, 5 \\ \sqrt{2}c(-\cos \frac{(2a+1)\pi}{4}, -\sin \frac{(2a+1)\pi}{4}) & i = 6, 7, 8, 9 \end{cases} \quad (2.4)$$

where c is a constant in the lattice unit. The density distribution f_i in the fixed direction can be obtained by integrating Eq. (2.3):

$$f_i(\mathbf{r} + e_i \Delta t, t + \Delta t) - f_i(\mathbf{r}, t) = -\frac{1}{\tau_v} (f_i^{eq}(\mathbf{r}, t) - f_i(\mathbf{r}, t)) + \Delta t F_i(\mathbf{r}, t) \quad (2.5)$$

where Δt is the magnitude of the time step while F_i is the body force in the fixed direction.

When the velocity is low, f_i^{eq} can be simplified as:

$$f_i^{eq} = \rho \omega_i \left[1 + \frac{\mathbf{e}_i \cdot \mathbf{u}}{R_g T} + \frac{(\mathbf{e}_i \cdot \mathbf{u})^2}{2R_g^2 T^2} - \frac{u^2}{R_g T} \right] \quad (2.6)$$

$$\omega_i = (2\pi R_g T)^{-\frac{m}{2}} \exp\left(-\frac{e_i^2}{2R_g T}\right) \quad (2.7)$$

where f_i^{eq} can be further simplified with regarding c_s that is the speed of sound in the lattice unit:

$$f_i^{eq} = \rho \omega_i \left[1 + \frac{\mathbf{e}_i \cdot \mathbf{u}}{c_s^2} + \frac{(\mathbf{e}_i \cdot \mathbf{u})^2}{2c_s^4} - \frac{u^2}{2c_s^2} \right] \quad (2.8)$$

where

$$\omega_i = \begin{cases} \frac{4}{9} & i = 1 \\ \frac{1}{9} & i = 2, 3, 4, 5 \\ \frac{1}{36} & i = 6, 7, 8, 9 \end{cases} \quad (2.9)$$

2.3 Chapman-Enskog Expansion

Applying the following Chapman-Enskog expansion equations

$$\frac{\partial}{\partial \mathbf{r}} = K \frac{\partial}{\partial \mathbf{r}_1} \quad (2.10)$$

$$\frac{\partial}{\partial t} = K \frac{\partial}{\partial t_1} + K^2 \frac{\partial}{\partial t_2} \quad (2.11)$$

$$f_a = f_a^0 + K f_a^1 + K^2 f_a^2 \quad (2.12)$$

to Eq. (2.5), the macroscopic governing equations can be obtained from LBM:

$$\frac{\partial \rho}{\partial t} + \nabla \cdot (\rho \mathbf{V}) = 0 \quad (2.13)$$

$$\frac{\partial (\rho \mathbf{V})}{\partial t} + \nabla \cdot (\rho \mathbf{V} \mathbf{V}) = -\nabla p + \nabla \cdot \left[\rho \nu \left(\nabla \mathbf{V} + (\nabla \mathbf{V})^T - \frac{\nu}{c_s^2} \nabla \cdot (\rho \mathbf{V} \mathbf{V} \mathbf{V}) \right) \right] \quad (2.14)$$

$$\nu = c_s^2 \left(\tau_v - \frac{1}{2} \right) \Delta t \quad (2.15)$$

Equation (2.14) differs from the macroscopic momentum conservation from due to presence of the term $\nabla \cdot \left[\rho \nu \left(-\frac{\nu}{c_s^2} \nabla \cdot (\rho \mathbf{V} \mathbf{V} \mathbf{V}) \right) \right]$. Fortunately, it can be neglected when Mach number is low which is the case in consideration. Thus, the LBM satisfies the same macroscopic governing equations as the macroscopic method, which meets the requirement to combine LBM with FVM.

To obtain the macroscopic parameter, the following two additional equations are needed.

$$\rho = \sum_{i=1}^9 f_i \quad (2.16)$$

$$\rho \mathbf{V} = \sum_{i=1}^9 e_i f_i \quad (2.17)$$

where e_i is the vector representing the velocity in every discrete direction and \mathbf{V} is the vector of the macroscopic velocity.

Boundary condition plays an important role in LBM and Ref. [94] compared different LBM boundary conditions in incompressible fluid flow simulations.

2.4 Thermal LBM model

Two distribution functions are selected for the fluid flow and heat transfer in LBM. The density and energy distributions are represented by f_i and g_i , which are related by the buoyancy force. D2Q9 model for f_i has been included in Section 2.1.

The buoyancy force can be obtained as:

$$F_i = \Delta t \mathbf{G} \cdot \frac{(\mathbf{e}_i - \mathbf{V})}{p} f_i^{eq} \quad (2.18)$$

where the pressure, p , equals ρc_s^2 .

The D2Q5 model [17] is used for the temperature field. There are five discrete velocity at each computing node shown is Fig. 2-3.

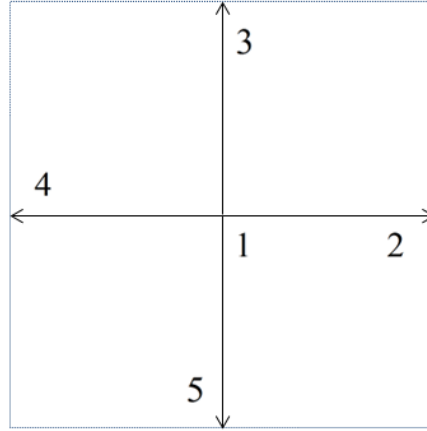


Figure 2-3 Five directions in D2Q5 model

Similar to the density distribution, the energy distribution can be obtained by

$$g_i(\mathbf{r} + \mathbf{e}_i \Delta t, t + \Delta t) - g_i(\mathbf{r}, t) = \frac{1}{\tau_T} (g_i^{eq}(\mathbf{r}, t) - g_i(\mathbf{r}, t)), \quad i = 1, 2, \dots, 5 \quad (2.19)$$

The macroscopic energy equation can be obtained from by Eq. (2.19) using Chapman-Enskog expansion.

Then the relaxation time τ_T is related to the thermal diffusivity α as

$$\alpha = c_s^2 \left(\tau_T - \frac{1}{2} \right) \Delta t \quad (2.20)$$

The equilibrium energy distribution in Eq. (2.19) is

$$g_i^{eq} = T \omega_i^T \left(1 + \frac{\mathbf{e}_i \cdot \mathbf{V}}{c_s^2} \right) \quad (2.21)$$

where:

$$\omega_i^T = \begin{cases} \frac{1}{3} & i = 1 \\ \frac{1}{6} & i = 2, 3, 4, 5 \end{cases} \quad (2.22)$$

The temperature at each computing node can be obtained as:

$$T = \sum_{i=1}^5 g_i \quad (2.23)$$

Chapter 3 Two Schemes for Hybrid Lattice Boltzmann and Finite Volume Methods

3.1 Introduction

The fluid flow and heat transfer problems encountered in engineering applications span into different scales and there are different numerical methods for different scales. Molecular dynamics can be applied to solve nano- and microscale problems while LBM is a typical mesoscopic scale method. Finite volume method, on the other hand, is suitable for solving the macroscale problems. The growing multiscale problems must be solved with multiscale method since there is no method is suitable for all the scales. Two ways exist to fulfill the multiscale methods: for the first one, the whole domain is divided into several subdomains and these subdomain are solved with various numerical methods respectively and it will discussed in Chapters 3 and 4; for the second one, various parameters are solved with different numerical methods and it will discussed in Chapters 5 and 6.

Two schemes for LBM-FVM hybrid method are proposed in this thesis. The key point of the hybrid method is to pass the information on the interface between LBM and FVM. It is difficult to transfer velocity obtained from FVM into node population that is needed in LBM. Density distribution function reconstruction was used to solve the interface problem in the hybrid method. Nonequilibrium extrapolation scheme and finite-difference velocity gradient method will be used in this thesis to pass information between the FVM and LBM zones. The lid-driven flow problem is solved to test the proposed methods.

3.2 Algorithm

Lattice Boltzmann method for 2-D fluid flow has been included in Chapter 2. LBGK model is employed in this chapter. Meanwhile, SIMPLE is a very popular FVM algorithm [23] that solves the general equations in macroscopic scale based on the control volume shown in Fig. 3-1.

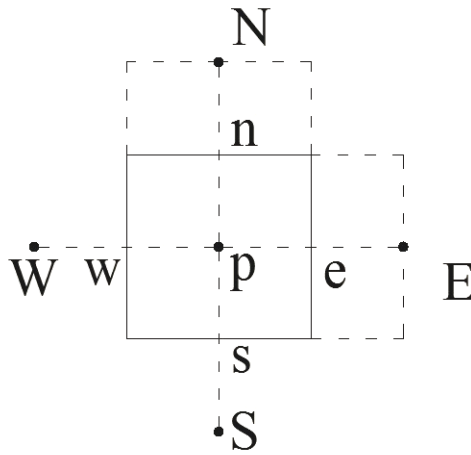


Figure 3-1 Control volume in 2-D FVM

For a 2-D problem in Cartesian coordinate system, the general equations can be expressed as:

$$\frac{\partial \Phi}{\partial t} + \frac{\partial(\rho u \Phi)}{\partial x} + \frac{\partial(\rho v \Phi)}{\partial y} = \frac{\partial}{\partial x} \left(\Gamma \frac{\partial \Phi}{\partial x} \right) + \frac{\partial}{\partial y} \left(\Gamma \frac{\partial \Phi}{\partial y} \right) + S \quad (3.1)$$

The SIMPLE algorithm is employed to solve Eq. (3.1) in this thesis. QUICK scheme [24] is selected to have an accuracy good enough.

3.3 Hybrid LBM and FVM method

3.3.1 Problem Statement

Lid driven flow is used to test the method to combine LBM and FVM. No-slip boundary conditions are applied to this 2-D problem, and the flow is driven by a constant lid velocity u_0 on the top of the square cavity while the velocities on all other boundaries are zero shown in Fig. 3-2.

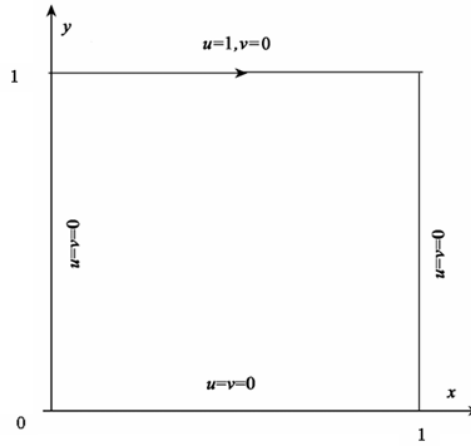


Figure 3-2 Lid-driven flow

This problem can be described by the following governing equations:

$$\frac{\partial \rho}{\partial t} + \frac{\partial(\rho u)}{\partial x} + \frac{\partial(\rho v)}{\partial y} = 0 \quad (3.2)$$

$$\frac{\partial(\rho u)}{\partial t} + \frac{\partial(\rho uu)}{\partial x} + \frac{\partial(\rho vu)}{\partial y} = -\frac{\partial p}{\partial x} + \mu \left(\frac{\partial^2 u}{\partial x^2} + \frac{\partial^2 u}{\partial y^2} \right) \quad (3.3)$$

$$\frac{\partial(\rho v)}{\partial t} + \frac{\partial(\rho uv)}{\partial x} + \frac{\partial(\rho vv)}{\partial y} = -\frac{\partial p}{\partial y} + \mu \left(\frac{\partial^2 v}{\partial x^2} + \frac{\partial^2 v}{\partial y^2} \right) \quad (3.4)$$

which are subject to the following boundary conditions:

$$x = 0 \quad u = 0 \quad v = 0 \quad (3.5)$$

$$x = H \quad u = 0 \quad v = 0 \quad (3.6)$$

$$y = 0 \quad u = 0 \quad v = 0 \quad (3.7)$$

$$y = H \quad u = u_0 \quad v = 0 \quad (3.8)$$

In addition, the Reynolds number is defined with the constant velocity on the top.

$$\text{Re} = \frac{u_0 h}{\nu} \quad (3.9)$$

3.3.2 Description of the combing method

3.3.2.1 Selection of units

Lattice unit is applied to LBM while SIMPLE algorithm uses non-dimensional procedure. As discussed above, e_i has different values in different directions in the lattice unit. In order to combine these two methods with different units together, they must be used to describe the same situation in the actual unit.

In the LBM unit conversion process, which changes all the properties into lattice unit, the speed of sound c_s and time step Δt are fixed so that the density distributions are all on the computational nodes.

$$c_s = 1/\sqrt{3}, \quad \Delta t = 1 \quad (3.10)$$

Assuming that the real speed of sound is u_{sound} and the number of nodes in the y -direction is $n + 1$, the dimensionless velocities in LBM are:

$$U_L = \frac{u}{\sqrt{3}u_{sound}} \quad (3.11)$$

$$V_L = \frac{v}{\sqrt{3}u_{sound}} \quad (3.12)$$

and the time step is

$$\Delta t = \frac{H_L}{\sqrt{3}c_s} = 1 \quad (3.13)$$

Thus the coordinates in lattice unit become

$$X_L = \frac{nx}{H} \quad (3.14)$$

$$Y_L = \frac{ny}{H} \quad (3.15)$$

In order to allow the boundary velocity in lattice unit in LBM to be same as the dimensionless velocity in SIMPLE, it is assuming that the lid velocity and the speed of sound have the following relationship:

$$10u_0 = \sqrt{3}u_{sound} \quad (3.16)$$

which requires that $10u_0$ to be used in the non-dimension process. The dimensionless lid velocity in the LBM becomes

$$U_0 = 0.1 \quad (3.17)$$

At this point, the only unknown parameter in lattice unit is the kinematic viscosity ν_L and it can be obtained from the Reynolds number:

$$\nu_L = \frac{U_0 H_L}{\text{Re}_L} \quad (3.18)$$

To satisfy Eq. (2.15), the relaxation time τ_v can be obtained to fulfill LBM

$$\tau_0 = 3\nu_L + 0.5 \quad (3.19)$$

As discussed above, to obtain the same boundary dimensionless velocity as that in lattice unit, the following non-dimensional variables are defined:

$$\left. \begin{aligned} U_s &= \frac{u}{10u_0}, V_s = \frac{v}{10u_0}, X_s = \frac{x}{H}, Y_s = \frac{y}{H} \\ F &= \frac{t}{H/(10u_0)}, P = \frac{p}{\rho(10u_0)^2}, \text{Re}_s = \frac{u_0 H}{\nu} \end{aligned} \right\} \quad (3.20)$$

The governing equations (3.1) to (3.7) can be nondimensionalized as:

$$\frac{\partial U_s}{\partial X_s} + \frac{\partial V_s}{\partial Y_s} = 0 \quad (3.21)$$

$$\frac{\partial U_s}{\partial F} + \frac{\partial(U_s U_s)}{\partial X_s} + \frac{\partial(V_s U_s)}{\partial Y_s} = -\frac{\partial P}{\partial X_s} + \frac{1}{10\text{Re}_s} \left(\frac{\partial^2 U_s}{\partial X_s^2} + \frac{\partial^2 U_s}{\partial Y_s^2} \right) \quad (3.22)$$

$$\frac{\partial V_s}{\partial F} + \frac{\partial(U_s V_s)}{\partial X_s} + \frac{\partial(V_s V_s)}{\partial Y_s} = -\frac{\partial P}{\partial Y_s} + \frac{1}{10\text{Re}_s} \left(\frac{\partial^2 V_s}{\partial X_s^2} + \frac{\partial^2 V_s}{\partial Y_s^2} \right) \quad (3.23)$$

$$X_s = 0 \quad U_s = 0 \quad V_s = 0 \quad (3.24)$$

$$X_s = 1 \quad U_s = 0 \quad V_s = 0 \quad (3.25)$$

$$Y_s = 0 \quad U_s = 0 \quad V_s = 0 \quad (3.26)$$

$$Y_s = 1 \quad U_s = 0.1 \quad V_s = 0 \quad (3.27)$$

In order to meet the requirement for describing the same situation in the actual unit in LBM and SIMPLE, the following two additional equations are needed.

$$\text{Re}_s = \text{Re}_L \quad (3.28)$$

$$\Delta F = \frac{\Delta t}{n} \quad (3.29)$$

where $n+1$ is the number of nodes in the y -direction. By following the above nondimensionalization procedures for LBM and SIMPLE, the non-dimensional lid velocity in both methods are 0.1. So the same non-dimensional velocities are reached at the same real location for the same Reynolds number in every time step. Therefore, the non-dimensional velocities can be transferred directly.

3.3.2.2 Implementation of the combining method

In order to combine LBM and SIMPLE in the same problem, the computational domain is divided into two zones as shown in Fig. 3-3.

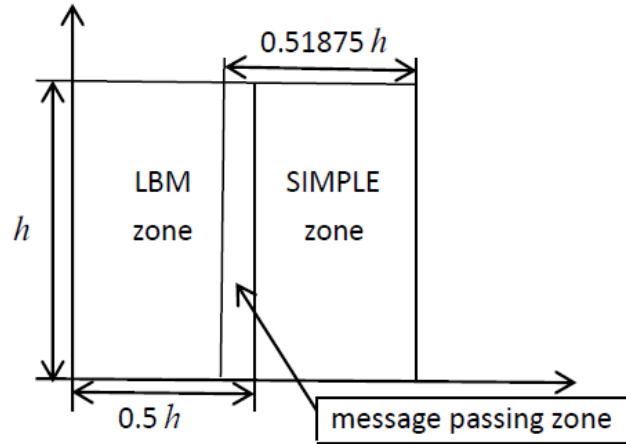


Figure 3-3 Computational domain for LBM and SIMPLE

A 160×160 uniform grid is applied to the entire computational domain. In most cases, the wider the message passing zone is, the better the accuracy is. However, enlarged message passing zone also increases the computational time in every time step. Meanwhile, although the grid is uniform in the whole domain, the locations of velocity on the grid are different for LBM and SIMPLE. So additional interpolation, which may require the information on the nearby nodes, is needed in the information sharing process. Three shared grids are selected after testing and the grid in LBM is 80×160 while that in SIMPLE is 83×160 . It is necessary to point out that it is almost impossible to transfer the pressure in LBM to that in SIMPLE because they have different ways to obtain the pressure. In LBM, the ideal gas law is used to obtain the pressure, while SIMPLE solves the pressure correction equation based on the conservation of mass. The example in this thesis does not need to transfer the pressure information in the message passing zone shown in Fig. 3-4 due to the nature of method used to combine LBM and SIMPLE. The interface between LBM and SIMPLE zone is treated as a fixed velocity boundary at every time step.

Staggered grids are used in SIMPLE and LBM, and the locations of macroscopic parameters in the computational domain are shown in Figs. 3-4 and 3-5.

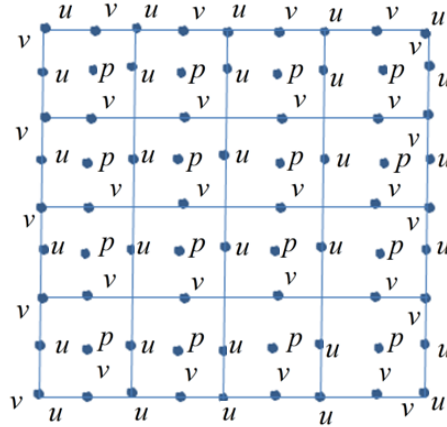


Figure 3-4 Variable locations in SIMPLE

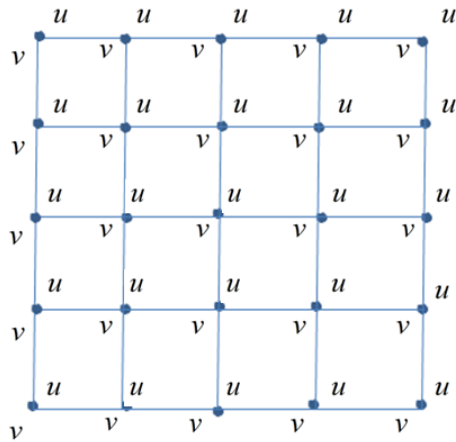


Figure 3-5 Computational nodes in LBM

It can be seen that the locations of macroscopic parameters are different in SIMPLE and LBM, even the grids are the same. Figure 3-6 gives a more clear view about that in one control volume in the message passing zone.

$$v_{i,j,S} = v_{i,j-1,L} \quad (3.33)$$

After transferring the information between the two zones, the hybrid method turns to fixed velocity problem on the interfaces l_1 and l_2 shown in Fig. 3-3 in LBM and SIMPLE. There is no need for any special treatment to the SIMPLE zone rather than setting the boundary velocity in the program. On the other hand, it is different for the LBM zone because its original variable is density distribution on the computational nodes.

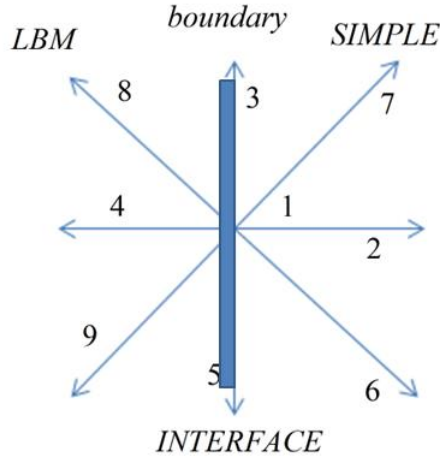


Figure 3-7 Boundary condition in LBM at the interface

The three density distributions f_4, f_8, f_9 and density ρ are unknown as shown in Fig. 3-7, while there are only three equations:

$$f_4 + f_8 + f_9 = \rho - f_1 - f_2 - f_3 - f_5 - f_6 - f_7 \quad (3.34)$$

$$f_4 + f_8 + f_9 = -\rho u_L + f_2 + f_6 + f_7 \quad (3.35)$$

$$f_8 - f_9 = \rho v_L + f_5 + f_6 - f_3 - f_7 \quad (3.36)$$

There are several methods to solve this problem on the boundary [40]. Nonequilibrium extrapolation scheme [16] and finite-difference velocity gradient method [40] are used in this thesis to replace all the density distributions on the boundary.

In the Nonequilibrium extrapolation scheme (hybrid method 1), we have the following assumption:

$$\left(f_i - f_i^{eq}\right)_{boundary} = \left(f_i - f_i^{eq}\right)_{inner} \quad i = 1, 2 \dots 9 \quad (3.37)$$

This scheme has second order accuracy and can meet the requirement of the combining method.

On the other hand, finite-difference velocity gradient method (hybrid method 2) is used to replace all the density distributions on the boundary.

Equation (2.12) can be rewritten as:

$$f_i = f_i^{(0)} + K f_i^{(1)} + O(K^2) \quad (3.38)$$

The following equations can be obtained depending on different order of K .

$$K^0: f_i^{(0)} = f^{eq} \quad (3.39)$$

$$K^1: \left(\frac{\partial}{\partial t_1} + \mathbf{e}_i \cdot \nabla_1 \right) f^{eq} + \frac{1}{\tau \Delta t} f^{(1)} = 0 \quad (3.40)$$

$$K^2: \frac{\partial f^{eq}}{\partial t_2} + \left(\frac{\partial}{\partial t_1} + \mathbf{e}_i \cdot \nabla_1 \right) \left(1 - \frac{1}{2\tau} \right) f^{(1)} + \frac{1}{\tau \Delta t} f^{(2)} = 0 \quad (3.41)$$

Then $f^{(1)}$ can be obtained from Eq. (3.40):

$$f_i^{(1)} = -\tau \Delta t \left(\frac{\partial}{\partial t_1} + \mathbf{e}_a \cdot \nabla_1 \right) f_i^{eq} \quad (3.42)$$

The hydrodynamic variables also have the relation with density distributions:

$$\Pi = \sum_{i=1}^9 \mathbf{e}_i \mathbf{e}_i f_i \quad (3.43)$$

where Π is the moment of order 2.

Assume that:

$$\mathbf{Q}_i = \mathbf{e}_i \mathbf{e}_i - c_s^2 \mathbf{I} \quad (3.44)$$

where \mathbf{I} is the identity tensor,

one obtains:

$$Kf_i^{(1)} = -\frac{\tau \omega_i}{c_s^2} \left(\mathbf{Q}_i : \rho \nabla \mathbf{u} - \mathbf{e}_i \nabla : \rho \mathbf{u} \mathbf{u} + \frac{1}{2c_s^2} (\mathbf{e}_i \cdot \nabla) (\mathbf{Q}_i : \rho \mathbf{u} \mathbf{u}) \right) \quad (3.45)$$

Substituting Eq. (3.39) to Eqs. (2.17) and (3.43) and approximating $Kf_i^{(1)}$ by the first term only [40], the density distribution can be expressed as:

$$f_i = f_i^{eq} - \frac{\tau \omega_i}{c_s^2} \mathbf{Q}_i : \rho \nabla \mathbf{u} \quad (3.46)$$

So the density distribution can be related to strain rate tensor \mathbf{S} due to the symmetry of \mathbf{Q}_i :

$$f_i = f_i^{eq} - \frac{\tau \omega_i}{c_s^2} \mathbf{Q}_i : \mathbf{S} \quad (3.47)$$

where

$$\mathbf{S} = \frac{1}{2} \left(\nabla \mathbf{u} + (\nabla \mathbf{u})^T \right) \quad (3.48)$$

Thus, the information of the strain rate tensor on l_2 is needed to be transferred to LBM zone from the FVM zone.

In addition, more information needs to be transferred from the SIMPLE zone to LBM zone besides the velocity.

$$\frac{\partial u}{\partial x}, \frac{\partial u}{\partial y}, \frac{\partial v}{\partial x} \text{ and } \frac{\partial v}{\partial y} \text{ on } l_1 \text{ are also needed in order to get the strain rate tensor. } \frac{\partial u}{\partial y}, \frac{\partial v}{\partial x}$$

and $\frac{\partial u}{\partial x}$ be approximated by a centered difference. The conservation of mass requires that

[36]:

$$\frac{\partial v}{\partial y} = -\frac{\partial u}{\partial x} \quad (3.49)$$

The following steps should be taken to transfer information between the two zones in the method to combine LBM and SIMPLE (see Fig. 3-3):

1. Assume the velocity on $x = l_2$.
2. Use SIMPLE to solve the velocity in the SIMPLE zone.
3. Transfer the information on $x = l_1$ from the SIMPLE zone to the LBM zone.
4. Use the LBM to solve the velocity in the LBM zone.
5. Transfer the information on l_2 from LBM zone to SIMPLE zone.
6. Go back to step 2 until the velocity is converged.

3.4. Results and discussions

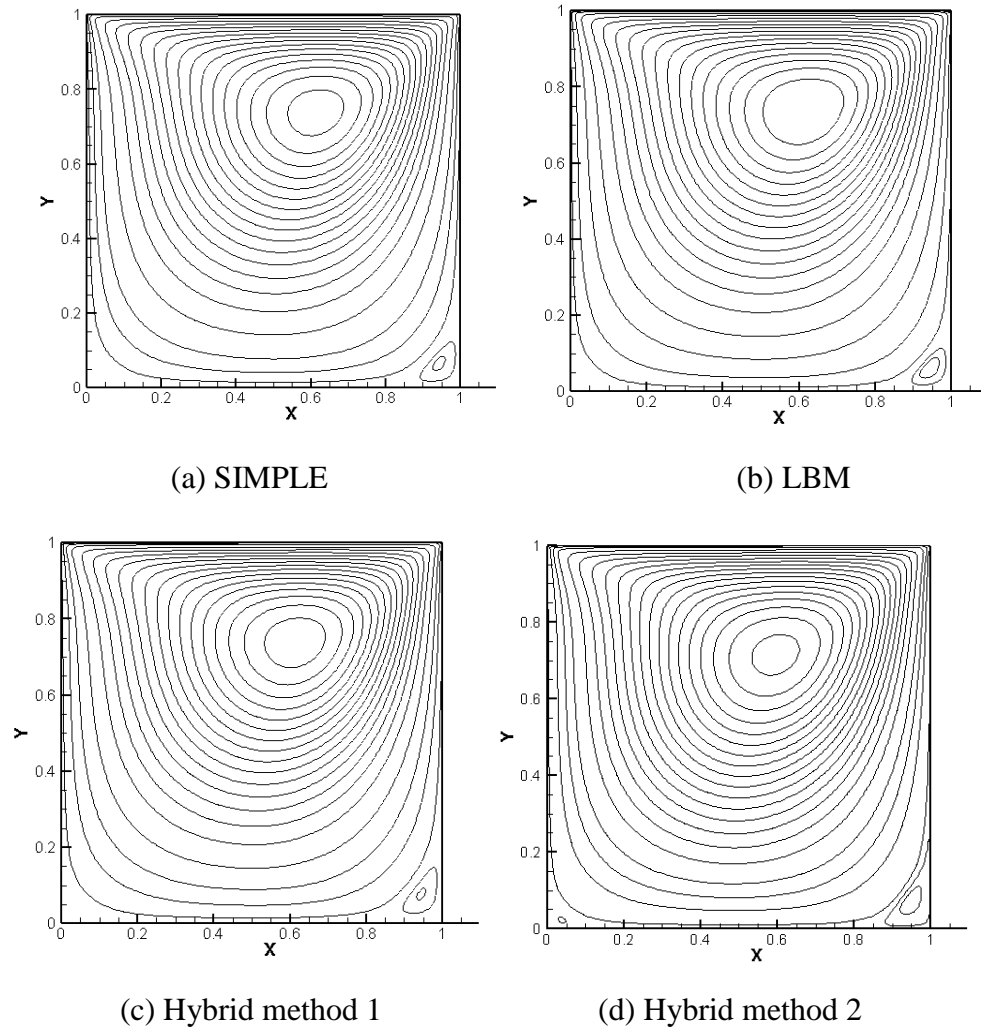
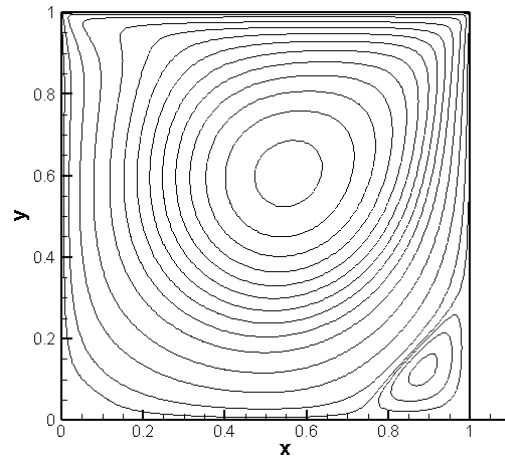
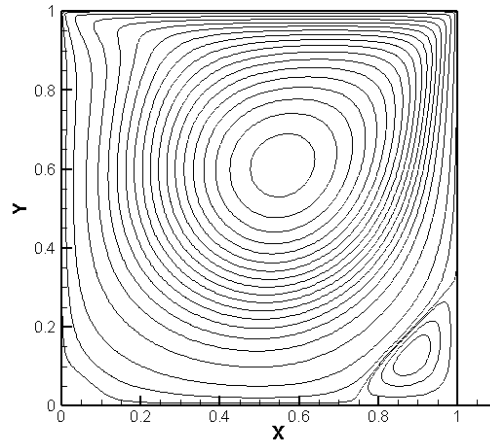


Figure 3-8 Streamlines at $Re = 100$

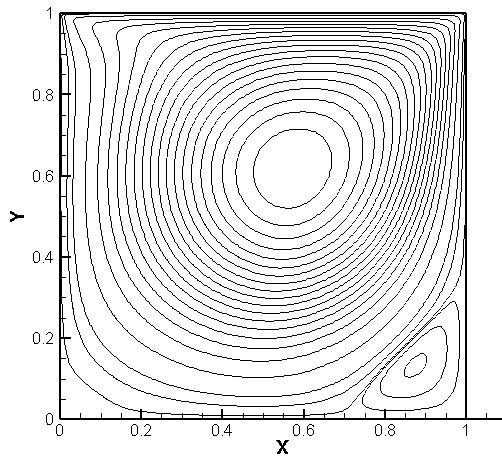
The lid driven flow is widely used as a benchmark solution to test the accuracy of a numerical method. To assess the hybrid methods, the results of reference [95] are used for comparison. The lid-driven flow is solved for three different Reynolds numbers at 100, 400, and 1000, respectively. Pure SIMPLE with QUICK scheme, LBM with nonequilibrium extrapolation boundary method, and the two methods combining SIMPLE and LBM are applied to solve this problem. As discussed above, all these four methods use the same grid of 160×160 , while the grid in the message passing zone in the hybrid method is 3×160 .



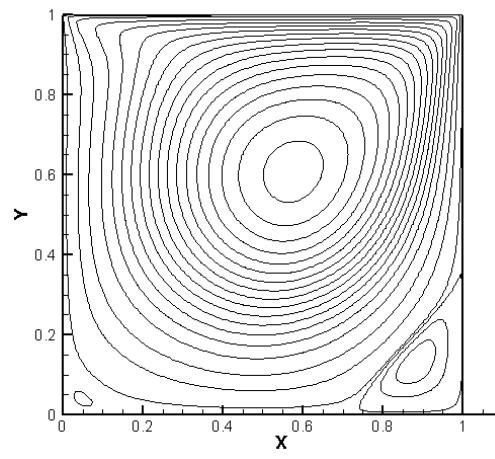
(a) SIMPLE



(b) LBM



(c) Hybrid method 1



(d) Hybrid method 2

Figure 3-9 Streamlines at $Re = 400$

Figures 3-8 to 3-10 show the streamlines at three Reynolds numbers obtained from the three methods, while Fig. 3-11 and 3-12 are the horizontal velocity profiles in the middle of the x-direction and vertical velocity profiles in the middle of the y-direction comparing with that in reference [95]. It should be pointed out that the velocities in the reference need to multiply by 0.1 because the non-dimensional processes are different.

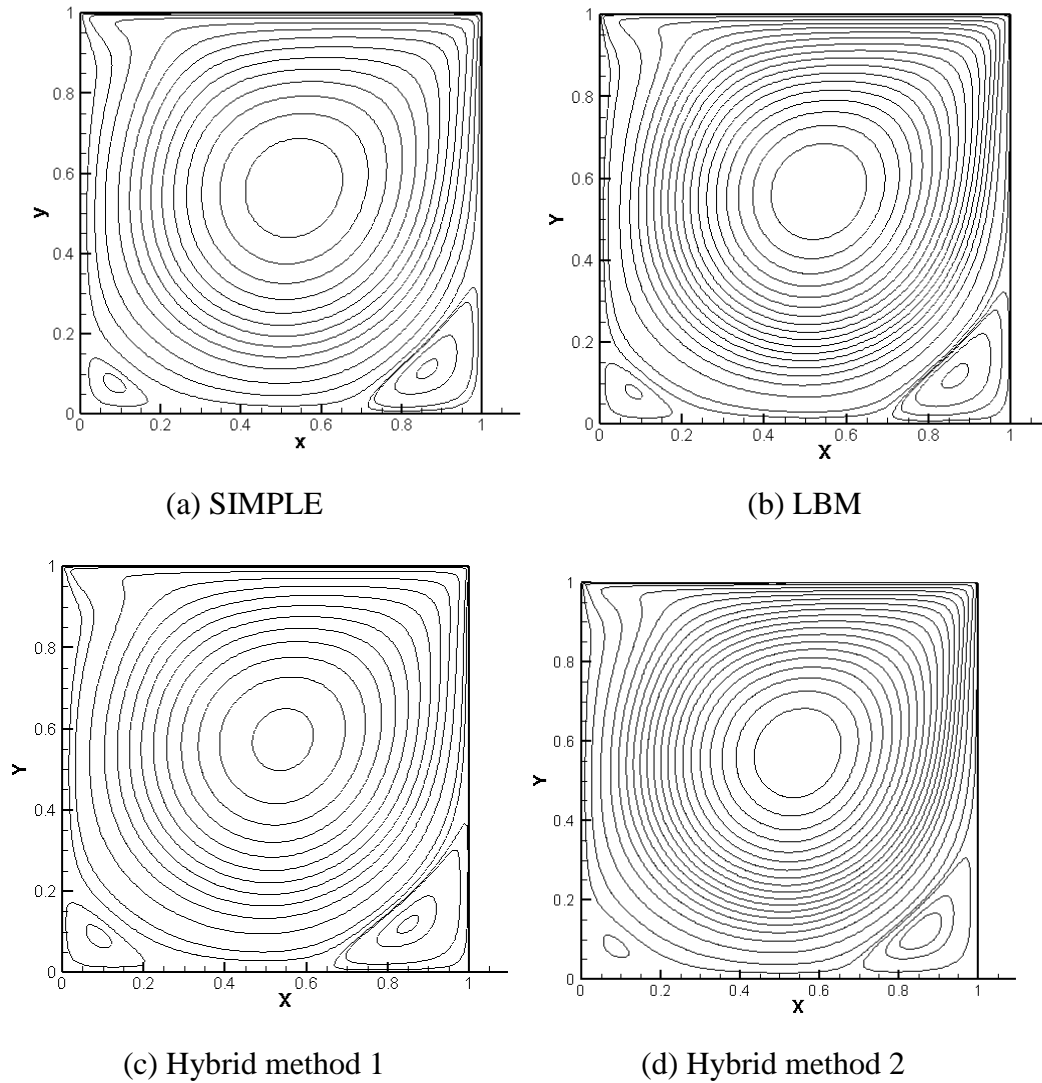
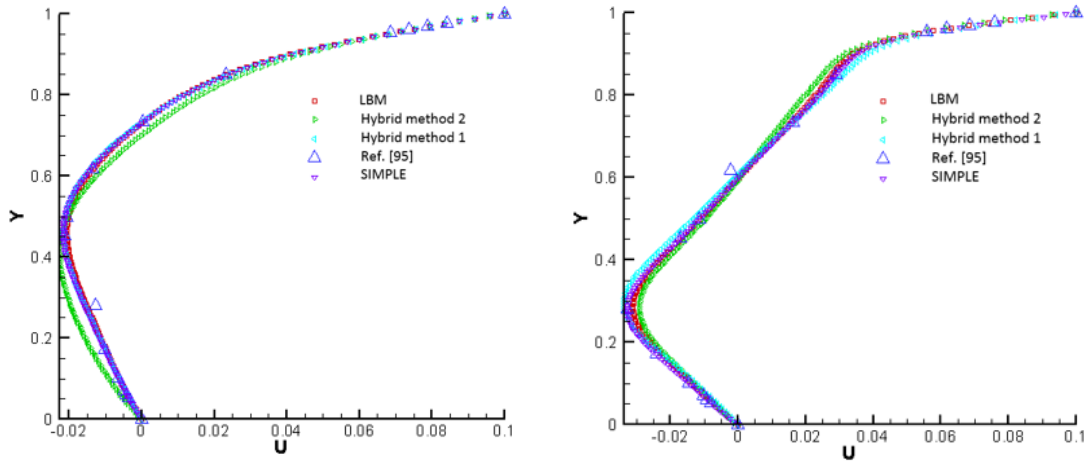


Figure 3-10 Streamlines at $Re = 1000$

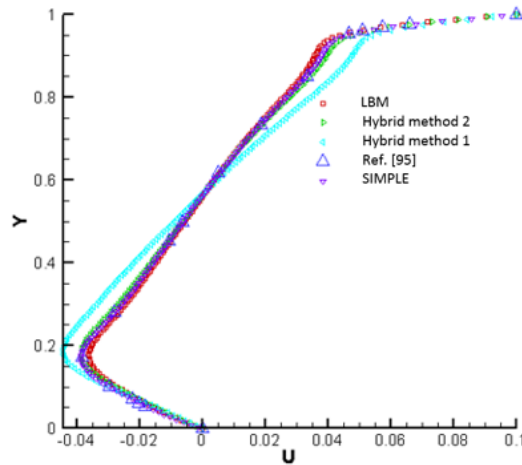
The streamlines obtained from the combined method are highly similar to that obtained from pure SIMPLE and pure LBM as shown in the Figs. 3-8 to 3-10. The positions of the centers of the primary vortices are $(0.6125, 0.7375)$ by SIMPLE, $(0.61875, 0.74375)$ by LBM, and $(0.6172, 0.7344)$ in Ref. [95] at $Re=100$. And these three locations from these three sources are $(0.5500, 0.60625)$, $(0.55625, 0.6125)$, and $(0.5547, 0.6055)$ for $Re=400$, and $(0.5250, 0.55625)$, $(0.53125, 0.56875)$, and $(0.5313, 0.5625)$ for $Re=1000$. The differences of the locations the centers of the primary vortices are insignificant in three

cases from SIMPLE and LBM. And the streamlines got from the two methods are highly similar



(a) $Re = 100$

(b) $Re = 400$



(c) $Re = 1000$

Figure 3-11 Horizontal velocity profiles

In addition to that, the horizontal velocity profiles in the middle of the x -direction and vertical velocity profiles in the middle of the y -direction obtained by SIMPLE and LBM are very close to that in reference as shown in Figs. 3-11 and 3-12. In other words, the SIMPLE and LBM used in this thesis are reliable. Due to this, the stream lines obtained from SIMPLE can be treated as standard results. Therefore, it can be concluded that the

SIMPLE and LBM used in this thesis are reliable and the accuracy of the combine method only depends on the solution of the interface itself.

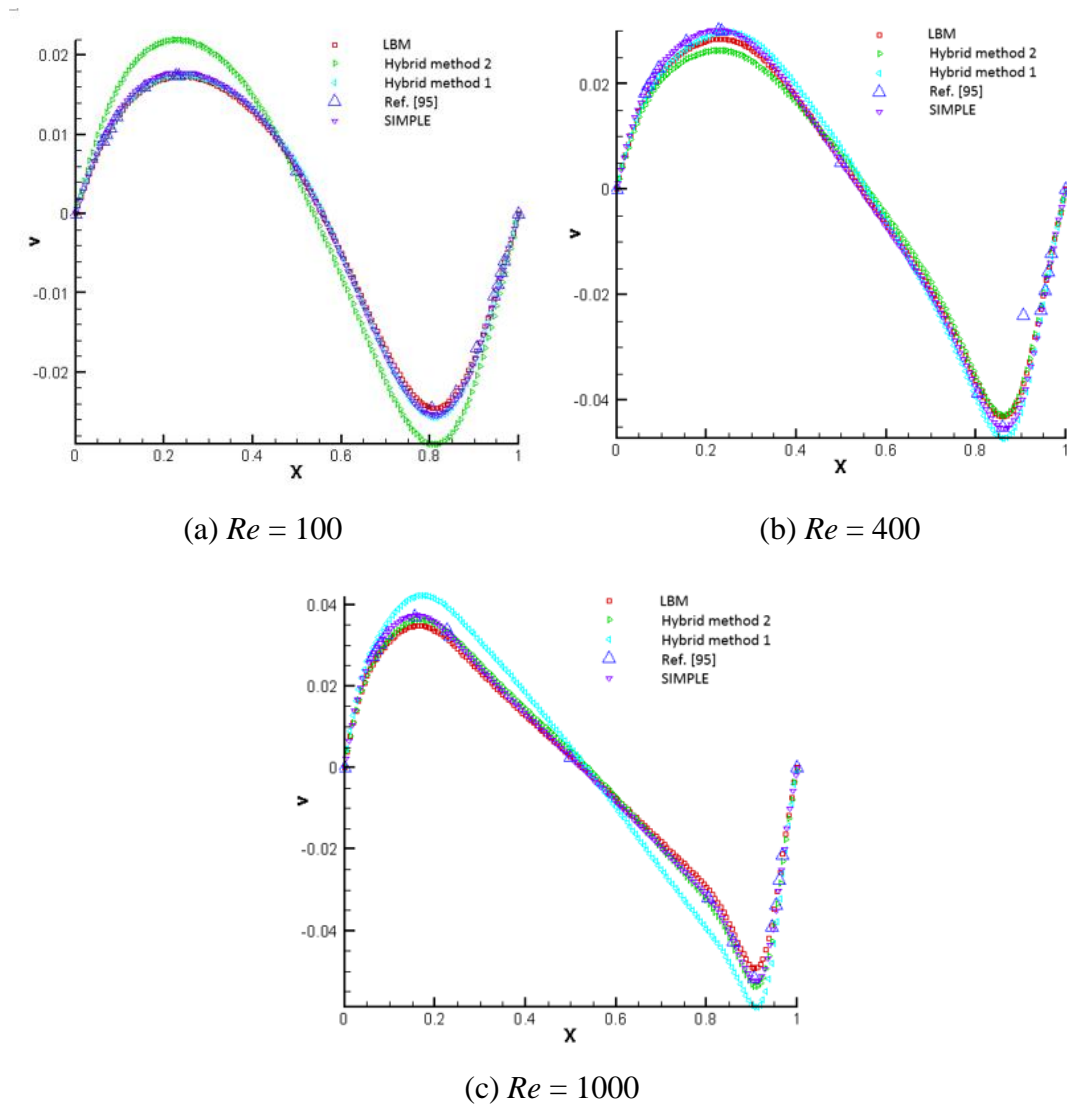


Figure 3-12 Vertical velocity profiles

On the other hand, the streamlines obtained from the hybrid method 1 and hybrid method 2 for Reynolds numbers at 100, 400 and 1000 shown in the Figs. 3-8 to 3-10 are almost the same as those obtained from SIMPLE and LBM. The positions of the centers of the primary vortices obtained from the hybrid method for three different Reynolds numbers are (0.6125, 0.7375), (0.5547, 0.6055) and (0.5313, 0.5625) for hybrid method 1 and

(0.6000, 0.71875), (0.5750, 0.60625) and (0.54375, 0.56875) for hybrid method 2 respectively. Thus, the differences from the reference are still at the same level as that from pure SIMPLE and LBM. The hybrid method can reach the same flow pattern as the other two methods. Especially the results at the message passing zone did not show any instability.

When regarding the details of the fluid field, these two hybrid methods show different accuracies in different Reynolds numbers. The horizontal velocity profiles in the middle of the x -direction and vertical velocity profiles in the middle of the y -direction obtained by hybrid method 1 satisfy the result from Ref. [95] for Reynolds number equals 100 and 400. Meanwhile, the horizontal velocity profiles in the middle of the x -direction and vertical velocity profiles in the middle of the y -direction obtained by hybrid method 2 satisfy the result from Ref. [95] for Reynolds number equals 400 and 1000. Nonequilibrium extrapolation scheme in hybrid method 1 obtain the unknown density distribution by assuming the nonequilibrium part of the density distribution equals to that on the nearby inner nodes. So the bigger the velocity gradient is, the worse the accuracy is. By contrast, the finite-difference velocity gradient method in hybrid method 2 obtains the unknown density distribution by relating the nonequilibrium part of the density distribution with the velocity distribution. So the bigger the velocity gradient is, the worse the accuracy is. Since the velocity gradient on the interface will become more valid with the increasing of Reynolds number. Hybrid method 1 is suitable for the case when Reynolds number is low while hybrid method 2 is suitable for the high Reynolds number case.

For the incompressible problem, LBM needs several times more computational time than that of the SIMPLE [30] while LBM saves a great deal of computational time in the

complex fluid flow problems [2]. The total computational time of any hybrid method always depends on the computational time of the slower one. The extra time consumption of message passing can be neglected comparing with the total computational time. Thus, the computational time in the lid-driven flow depends on that in the LBM zone when these two zones have the same grids. The computational efficiency of the hybrid methods are between those of SIMPLE and LBM. The main purpose to solve the lid-driven flow with the hybrid methods which reach the same accuracy with more time consuming comparing with SIMPLE is to certify these two hybrid methods can build a relation between LBM and FVM to solve the fluid flow problem together. These hybrid methods have the further to save time with the same accuracy for the problem including several parts that can take advantages of both SIMPLE and LBM in their subdomains. .

3.5. Conclusions

Two new methods that combine lattice Boltzmann method (LBM) and finite volume method (FVM) is proposed. The computational domain is divided into two zones with a message passing zone between them. LBGK is used in LBM while SIMPLE algorithm with QUICK scheme is used for FVM. At the interface, nonequilibrium extrapolation scheme and finite-difference velocity gradient method are utilized to transfer the macro velocities to a density distribution f_i in LBM zone from SIMPLE zone while the density distribution can be advanced in to macro velocities directly. A validation is performed by simulating the lid-driven flows for three different Reynolds numbers at 100, 400 and 1000 and comparing the results with that of the benchmark solution. The results show that hybrid method 1 is suitable for the case when Reynolds number is low while hybrid method 2 is suitable for the high Reynolds number case for the incompressible fluid flow problem.

Chapter 4 A Coupled Lattice Boltzmann and Finite Volume Method for Natural Convection Simulation

4.1 Introduction

In last chapter, LBM-FVM hybrid method for fluid flow simulation is developed. Heat transfer plays an important role in many multiscale problems. A coupled LBM-FVM method for fluid flow and heat transfer is proposed in this chapter. After taking heat transfer in consideration, three more settings are needed in LBM-FVM hybrid method comparing with that in last chapter: temperature information transfer between subdomains; temperature interpolation due to the differences between FVM and LBM in computational nodes' locations; density information transfer between subdomains regarding temperature fields are highly related with density.

Nonequilibrium extrapolation scheme has been proved to be valid in combining LBM and FVM for the low speed fluid flow simulation in last chapter. Nature convection in this chapter satisfies this speed requirement. So nonequilibrium extrapolation scheme is employed to transfer the velocity and temperature information in this chapter. Natural convections in a squared enclosure with different Rayleigh numbers are solved using the coupled method and the results are compared with those obtained from pure LBM and pure FVM for validation of the combined method.

4.2 Coupled LBM-FVM method

4.2.1 Problem statement

Natural convection of incompressible fluid in a squared enclosure as shown in Fig. 4-1 is used to test the coupled method. For the velocity field, non-slip condition is applied to

all boundaries. The left boundary is kept at a constant temperature T_h while the right boundary has a lower constant temperature of T_l . The top and bottom boundaries are adiabatic. Applying Boussinesq assumption, the problem can be described by the following governing equations:

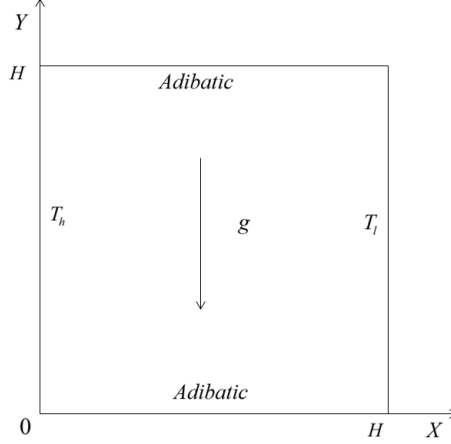


Figure 4-1 Physical model of the natural convection problem

$$\frac{\partial u}{\partial x} + \frac{\partial v}{\partial y} = 0 \quad (4.1)$$

$$\rho \left[\frac{\partial u}{\partial t} + u \frac{\partial u}{\partial x} + v \frac{\partial u}{\partial y} \right] = -\frac{\partial p}{\partial x} + \mu \left(\frac{\partial^2 u}{\partial x^2} + \frac{\partial^2 u}{\partial y^2} \right) \quad (4.2)$$

$$\rho \left[\frac{\partial v}{\partial t} + u \frac{\partial v}{\partial x} + v \frac{\partial v}{\partial y} \right] = -\frac{\partial p}{\partial y} + \mu \left(\frac{\partial^2 v}{\partial x^2} + \frac{\partial^2 v}{\partial y^2} \right) + \rho g \beta (T - T_l) \quad (4.3)$$

$$(\rho c_p) \left[\frac{\partial T}{\partial t} + u \frac{\partial T}{\partial x} + v \frac{\partial T}{\partial y} \right] = k \left(\frac{\partial^2 T}{\partial x^2} + \frac{\partial^2 T}{\partial y^2} \right) \quad (4.4)$$

Equations (4.1) – (4.4) are subject to the following boundary and initial conditions:

$$x = 0, u = 0, v = 0, T = T_h \quad (4.5)$$

$$x = H, u = 0, v = 0, T = T_l \quad (4.6)$$

$$y = 0, u = 0, v = 0, \partial T / \partial y = 0 \quad (4.7)$$

$$y = H, u = 0, v = 0, \partial T / \partial y = 0 \quad (4.8)$$

Regarding Eq. (2.18) in the view of Chapman-Enskog expansion, Eq. (4.4) can be obtained from the D2Q9 model in LBM when effective gravity acceleration \mathbf{G} is defined as:

$$\mathbf{G} = -\beta(T - T_l)\mathbf{g} \quad (4.9)$$

where β is the volume expansion coefficient of the fluid.

The SIMPLE algorithm with QUICK scheme [24] is employed to solve Eqs. (4.1) - (4.4). Prandtl number, Pr , and Rayleigh number, Ra , are the two non-dimensional parameters governing the natural convection.

$$Pr = \frac{\alpha}{\nu} \quad (4.10)$$

$$Ra = \frac{g\beta(T_h - T_l)H^3 Pr}{\nu^2} \quad (4.11)$$

For LBM Mach number, Ma , is needed:

$$Ma = \frac{u_c}{c_s} \quad (4.12)$$

where u_c is the speed of sound that equals $\sqrt{g\beta(T_h - T_l)H}$. Since the natural convection in consideration is incompressible, Ma can be any number in the incompressible region.

Applying the following non-dimensional variables

$$\begin{aligned} X &= \frac{x}{H}, Y = \frac{y}{H}, U = \frac{u}{\sqrt{3}c_s}, V = \frac{v}{\sqrt{3}c_s} \\ \tau &= \frac{t \cdot \sqrt{3}c_s}{H}, \theta = \frac{T - T_l}{T_h - T_l}, P = \frac{p}{3\rho c_s^2} \end{aligned} \quad (4.13)$$

to Eqs. (4.1)-(4.8), the dimensionless governing equations are obtained:

$$\frac{\partial U}{\partial X} + \frac{\partial V}{\partial Y} = 0 \quad (4.14)$$

$$\frac{\partial U}{\partial \tau} + U \frac{\partial U}{\partial X} + V \frac{\partial U}{\partial Y} = -\frac{\partial P}{\partial X} + Ma \sqrt{\frac{Pr}{3Ra}} \left(\frac{\partial^2 U}{\partial X^2} + \frac{\partial^2 U}{\partial Y^2} \right) \quad (4.15)$$

$$\frac{\partial V}{\partial \tau} + U \frac{\partial V}{\partial X} + V \frac{\partial V}{\partial Y} = -\frac{\partial P}{\partial Y} + Ma \sqrt{\frac{Pr}{3Ra}} \left(\frac{\partial^2 V}{\partial X^2} + \frac{\partial^2 V}{\partial Y^2} \right) + \frac{Ma^2 \theta}{3} \quad (4.16)$$

$$\frac{\partial \theta}{\partial \tau} + U \frac{\partial \theta}{\partial X} + V \frac{\partial \theta}{\partial Y} = Ma \sqrt{\frac{1}{3Ra \cdot Pr}} \left(\frac{\partial^2 \theta}{\partial X^2} + \frac{\partial^2 \theta}{\partial Y^2} \right) \quad (4.17)$$

For the heat transfer at the left boundary, Nusselt number, Nu , can be obtained by the nondimensional temperature gradient at the surface:

$$Nu = -\left. \frac{\partial \theta}{\partial X} \right|_{x=0} \quad (4.18)$$

which reflects the ratio of convection to the conduction heat transfer across the wall.

4.2.2 Description of the Coupled Method

This coupled method is designed to solve a single problem with FVM and LBM simultaneously. The computational domain is divided into LBM and FVM zones, and there

is a public area between these two zones. The artificial boundary of FVM zone is the inner nodes of LBM zone while the LBM artificial boundary is inside the FVM zone. Two kinds of geometry settings are applied to test this coupled method shown in Fig. 4-2.

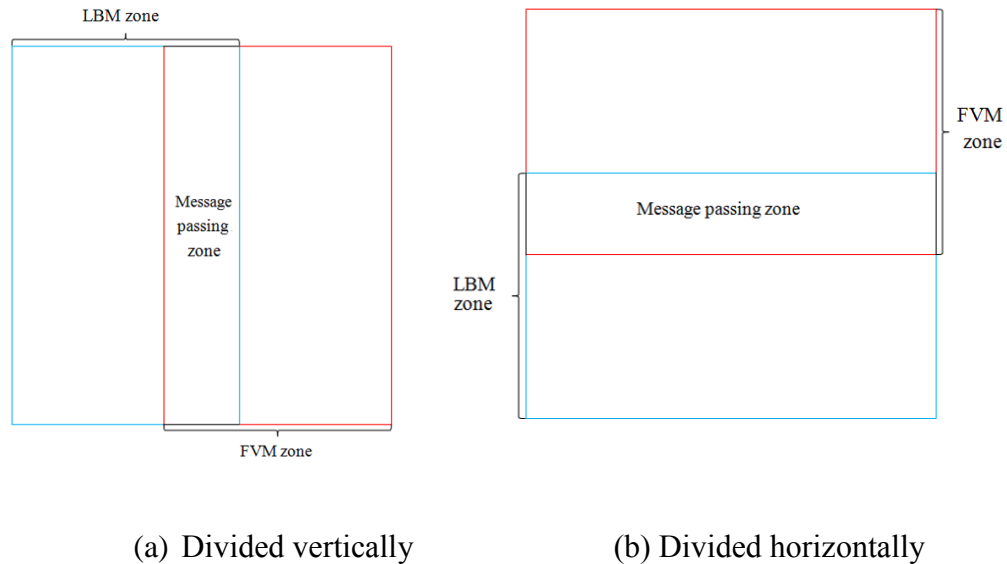


Figure 4-2 Computational domains for LBM and FVM

To fulfill the coupled method, the information on the artificial boundary needs to be obtained from the other subdomain. For the FVM zone, the velocity and temperature on the artificial boundary are needed from LBM zone. Density is not needed because FVM is solving the incompressible flow. The pressure on that boundary can be obtained directly from the FVM zone itself [24]. On the other hand, LBM needs the velocity, temperature and the density information of the artificial boundary from the FVM zone. It is not straightforward to transfer the density from an incompressible FVM zone to the compressible LBM zone. The average density in the message passing zone, ρ_0 , is calculated in the message LBM zone, and the FVM zone provides the average pressure in the message passing zone, \bar{p} . Meanwhile, the pressure on the LBM artificial boundary, p^L , can be

obtained from the FVM zone pressure, p^s . It is shown that there is very small difference between p^L and p^s in the message passing zone. But this small difference leads evident error when I tried to fulfill this combine method. It is also found that the pressure gradients differences from the two methods in the message passing zone is not evident either, Then the difference between \bar{p}^L and \bar{p} is similar as that between p^L and p^s where \bar{p}^L is average pressure in the message passing zone calculated by the LBM zone results. Therefore it is reasonable to assume that

$$p^L - \bar{p}^L = p^s - \bar{p} \quad (4.19)$$

Regarding the relation between pressure and density in LBM, it can be obtained that

$$\rho^L c_s^2 - \rho_0 c_s^2 = p^s - \bar{p} \quad (4.20)$$

Then the unknown ρ^L can be obtained that

$$\rho^L = \rho_0 \left(\frac{p^s - \bar{p}}{\rho_0 c_s^2} + 1 \right) \quad (4.21)$$

The density information on the artificial boundary of LBM can be obtained by the result of the FVM result. Staggered grid is applied to SIMPLE algorithm.

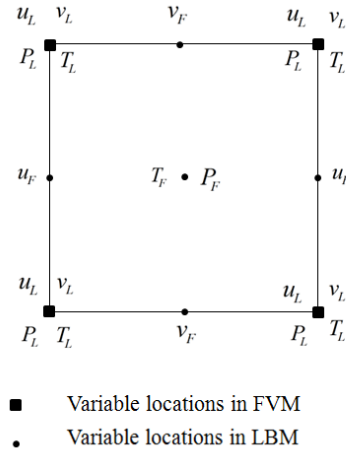


Figure 4-3 Variables locations

Figure 4-3 shows the locations of variables in a control volume for LBM and FVM. The variables in LBM all locates on the corner of the control volume while velocity, pressure and temperature in FVM have different locations in the control volume. Central difference is applied to message passing processes due to the variable location differences.

After transferring the information from each other, the FVM and LBM zones need to be solved independently for each time step. For the FVM zone, temperatures and velocities on the four boundaries are known so that the solution procedure is straightforward. There are several choices for the LBM boundary conditions. Nonequilibrium extrapolation scheme is applied to both velocity and temperature fields in the solving process. Assuming x_b is the boundary node and x_f is its nearby inner mode, the density and energy distribution at the artificial boundary are:

$$f_i(x_b, t) = f_i^{eq}(x_b, t) + f_i(x_f, t) - f_i^{eq}(x_f, t) \quad (4.22)$$

$$g_i(x_b, t) = g_i^{eq}(x_b, t) + g_i(x_f, t) - g_i^{eq}(x_f, t) \quad (4.23)$$

The temperatures on the boundaries are known in every time step, Eq. (4.23) can be applied to the thermal boundary conditions for Eq. (2.21). For the velocity field, the boundary density is only known on the artificial boundary. It is common to approximate the density on the fixed boundary by

$$\rho(x_b, t) = \rho(x_f, t) \quad (4.24)$$

4.3 Results and discussions

Natural convection in a squared enclosure is solved for three different Rayleigh numbers at 10^4 , 10^5 and 10^6 while the Prantl number is kept at 0.71. Pure LBM and pure FVM are reported in the literature to be suitable for the natural convection in a cavity. Thus, these two methods are applied to solve the test cases. If the LBM results agree with the FVM results, it can be concluded that these results can be used as standard results for comparison. It can also verify that the codes for the two subdomains are reliable in the coupled method. Then only the message passing method between the two subdomains affects the results from the coupled methods. Two coupled methods with different geometry settings are applied. When the domain is divided vertically, it is referred to as Coupled Method 1. And the Coupled Method 2 divides the domain horizontally as shown in Fig. 4-2. Temperature field, streamline and Nusselt number on the left wall obtained from these four methods are compared for the three cases. Nondimensional variables defined in Eq. (4.13) are applied in the comparisons.

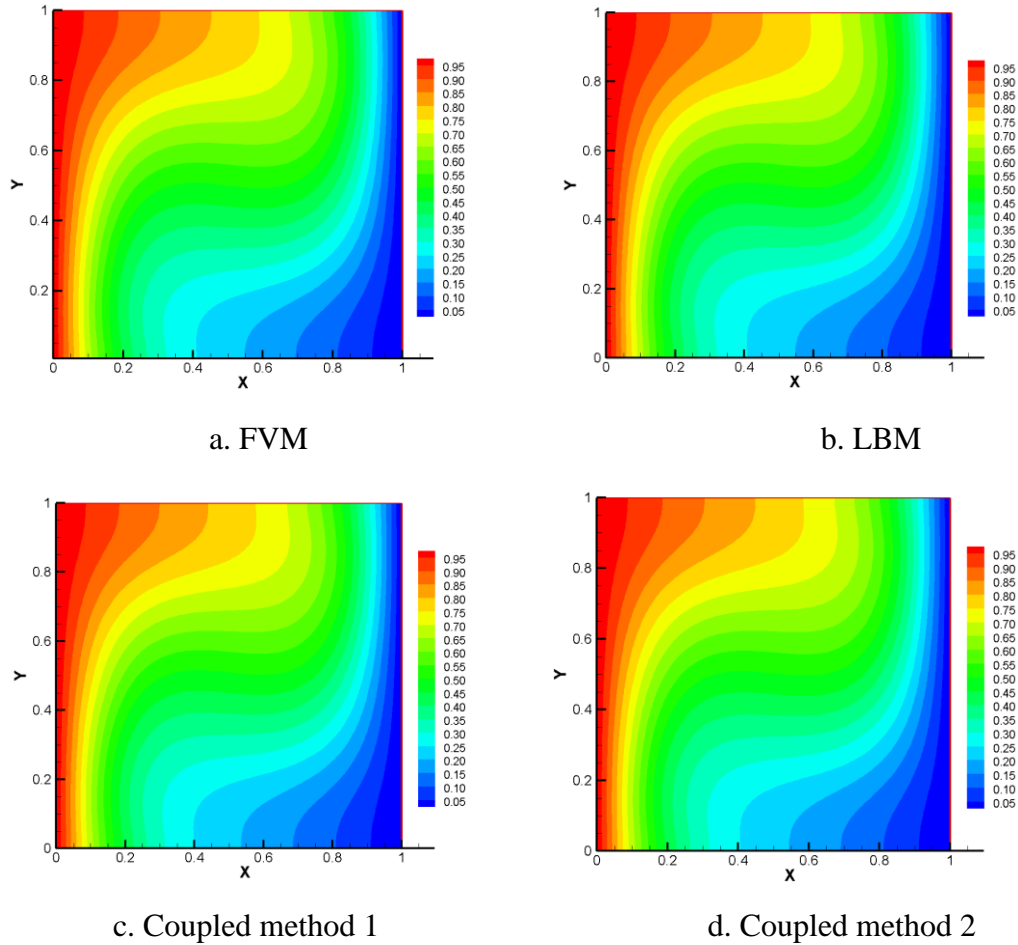
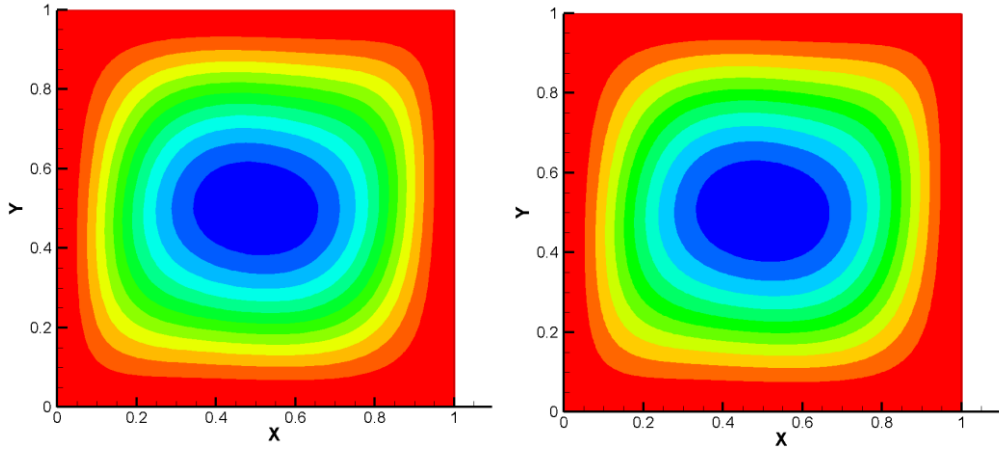


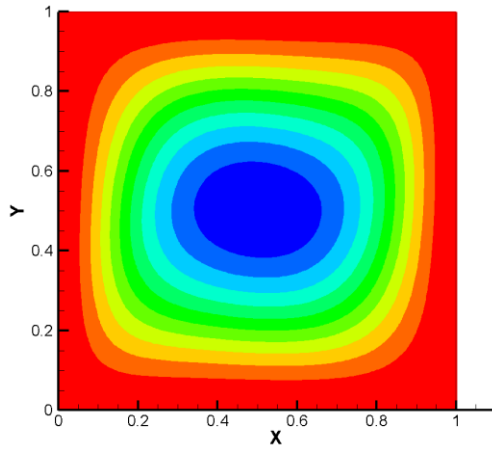
Figure 4-4 Temperature fields at $Ra=10^4$

Figures 4-4 and 4-5 show comparisons of temperature field and streamlines obtained by different methods for the case that Rayleigh number is 10^4 . It is obvious that natural convection has dominated the heat transfer process and there is a stream line vertex near the center of the cavity. Temperature fields and streamlines obtained from pure LBM and pure FVM agree with each other well as shown in Fig. 4-3 and 4-4. In addition, there is not any noticeable difference between the results obtained from coupled methods 1 and 2 and the results of coupled methods agreed with that from the pure FVM and pure LBM very well.

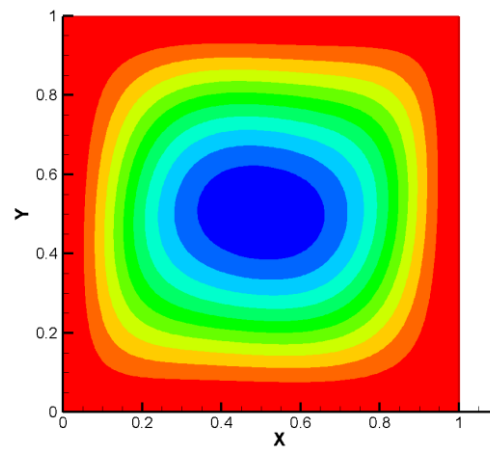


a. FVM

b. LBM



c. Coupled method 1



d. Coupled method 2

Figure 4-5 Nusselt numbers at $Ra=10^4$

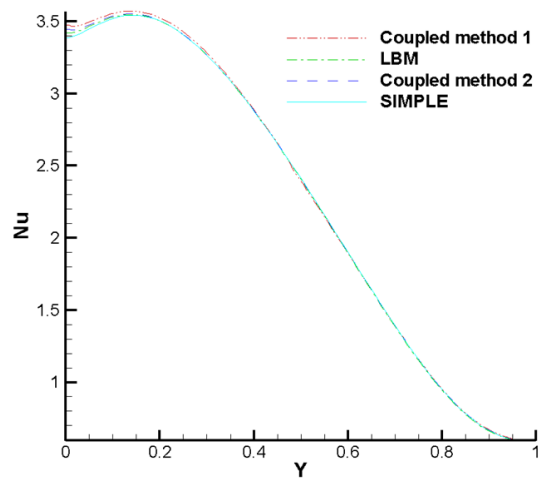


Figure 4-6 Nusselt numbers at $Ra=10^4$

Figure 4-6 shows the Nusselt number at heated wall along the vertical direction of the enclosure obtained from different methods. There is a little difference between the Nusselt numbers obtained from pure LBM and pure FVM. The cause of this difference is that FVM is based on the incompressible fluid assumption while LBM is based on compressible fluid assumption. Meanwhile the Nusselt number tendencies of the two coupled methods are very close to that of the two pure methods.

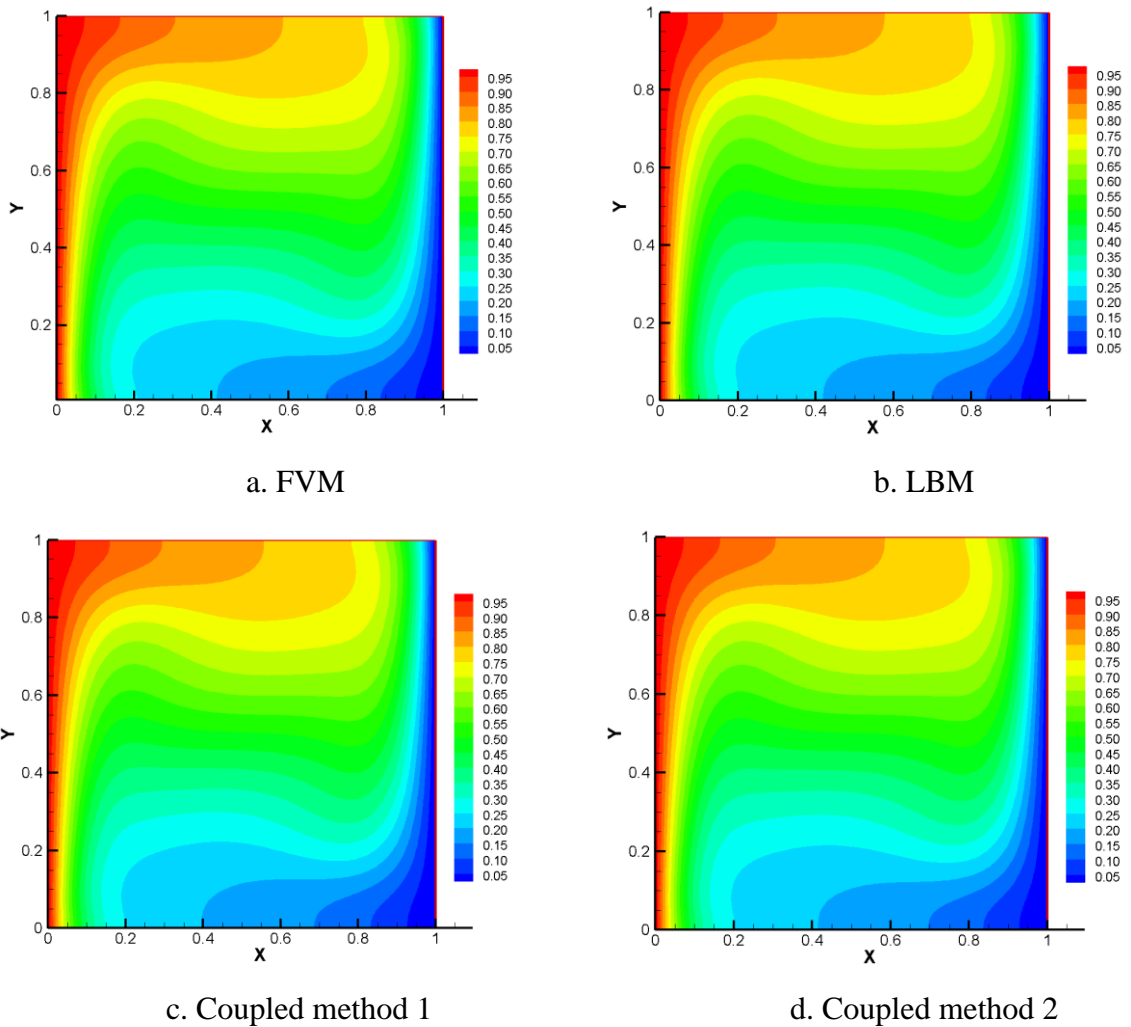


Figure 4-7 Temperature fields at $Ra=10^5$

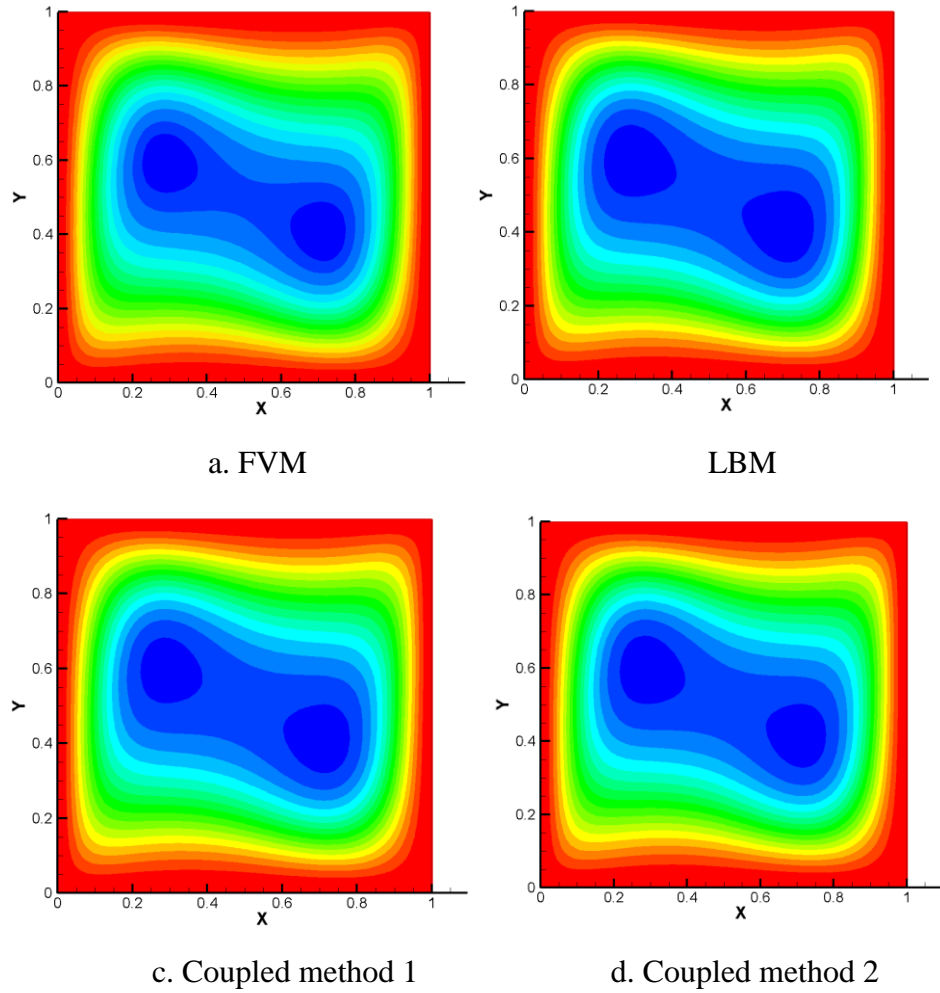


Figure 4-8 Streamlines at $Ra=10^5$

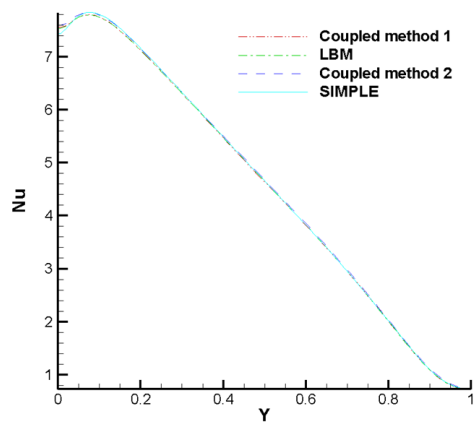


Figure 4-9 Nusselt numbers at $Ra=10^5$

Figures 4-7 and 4-8 show the temperature field and streamlines obtained by different methods for the case that Rayleigh number is 10^5 . It can be seen that the pure FVM and pure LBM reach similar temperature fields and streamlines. The convection effect becomes more pronounced as the Rayleigh number increases. Two vortices appear and the temperature gradients near the vertical boundary increase. The two coupled method results still agree very well with that in the pure methods as shown in Figs. 4-7 and 4-8. Meanwhile, Fig. 4-9 shows that the difference between Nusselt numbers obtained from pure FVM and pure LBM is larger than that in Fig. 4-6; but the largest difference is still around 2%. The Nusselt numbers from the two coupled methods are closer to the results of pure LBM than that of the pure FVM. Since both coupled methods 1 and 2 have half regions with LBM that do not have incompressible fluid assumption, the fluid in the entire computational domain of the coupled methods can be considered as compressible. The Nusselt number differences between the two coupled methods are not larger than that between the two pure methods.

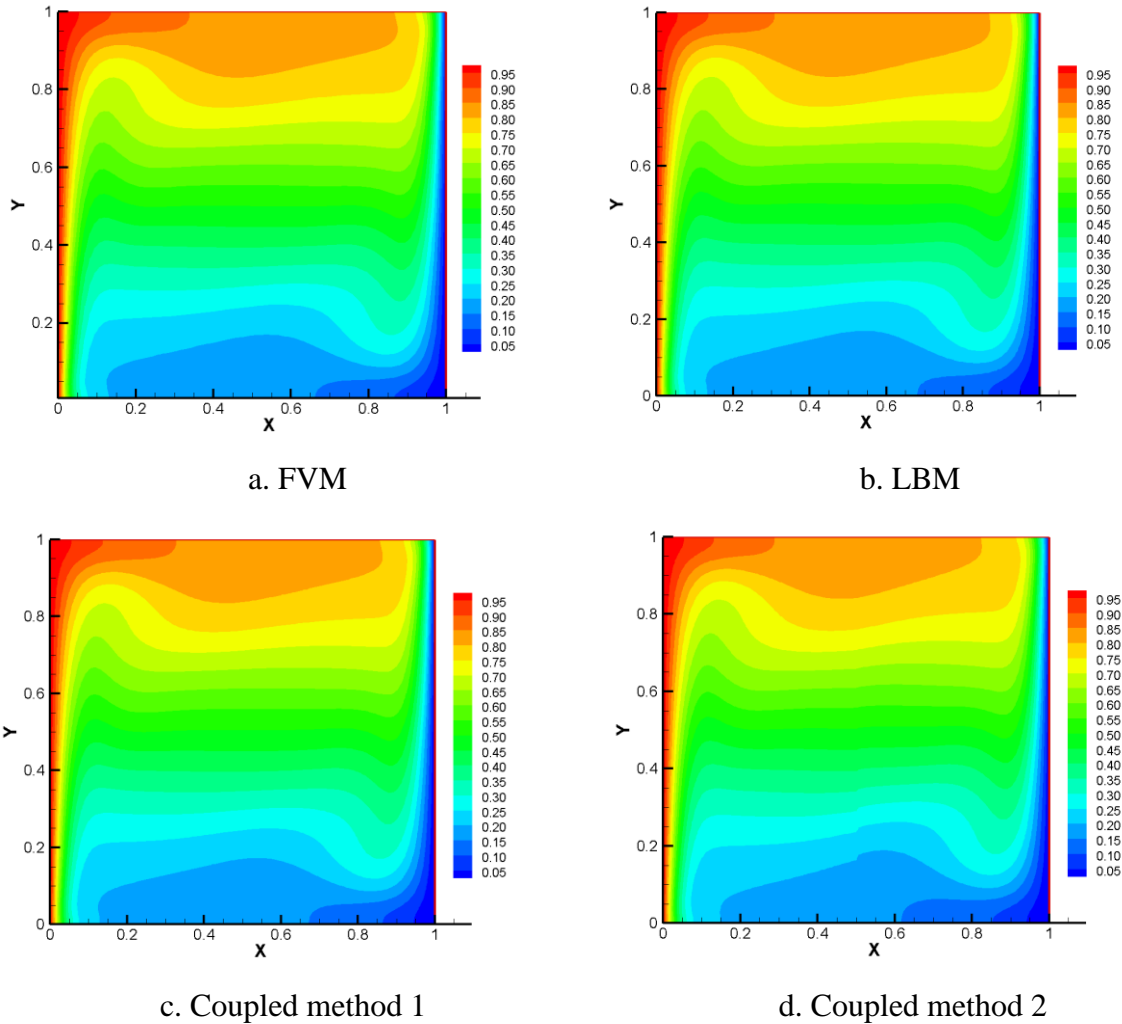


Figure 4-10 Temperature fields at $Ra=10^6$

Convection continues to become stronger when Rayleigh number is increased to 10^6 . Figures 4-10 and 4-11 show that all four methods yield the similar temperature fields and streamlines. There are still two independent stream line vertexes that are closer to the vertical boundaries; this indicates a stronger convection effect comparing with the results when Rayleigh number is 10^5 . As for the Nusselt number, Fig. 4-12 shows that the results from the coupled methods 1 and 2 are very close to that from the pure LBM. And the difference between the two coupled methods and pure FVM is still acceptable.

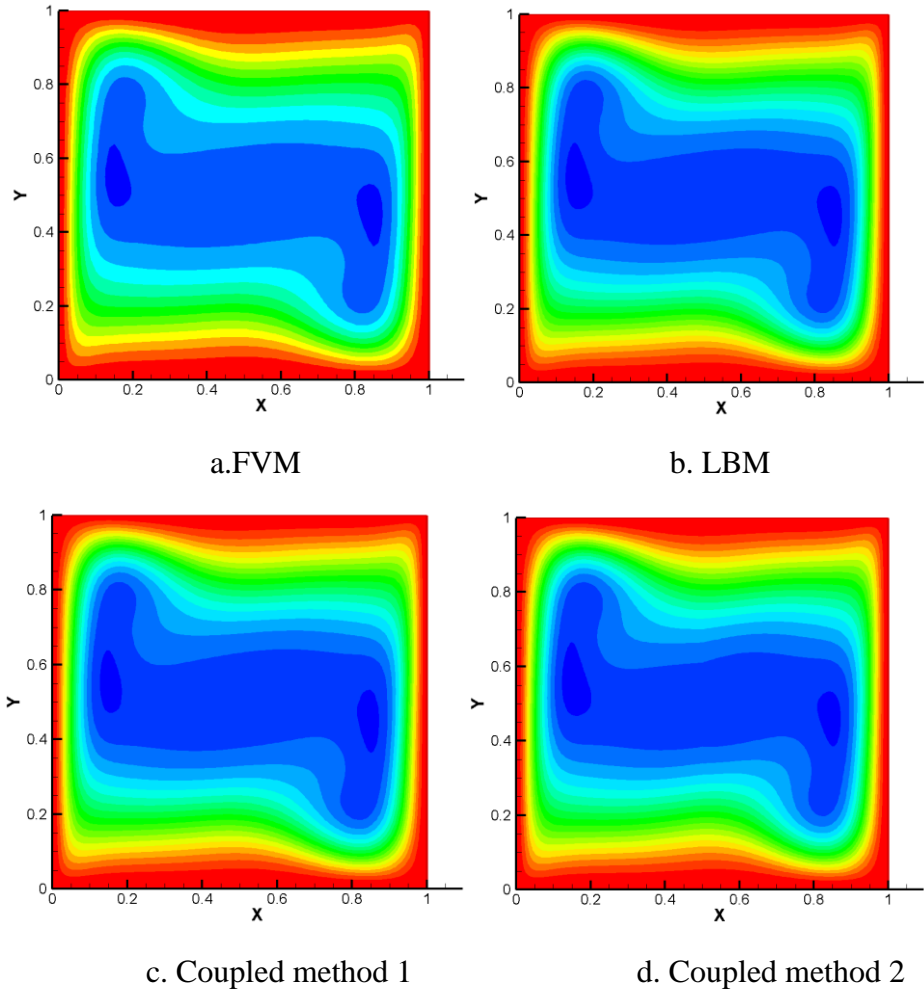


Figure 4-11 Streamlines at $Ra=10^6$

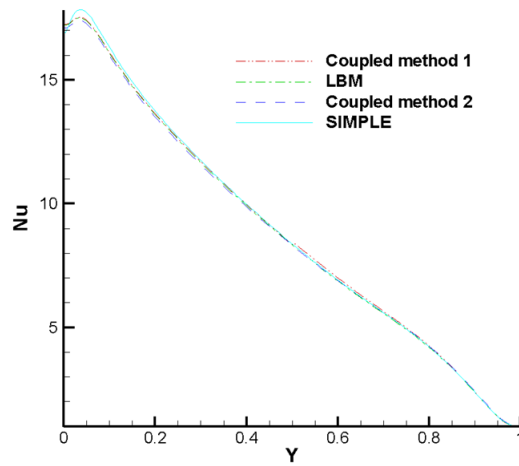


Figure 4-12 Nusselt numbers at $Ra=10^6$

4.4 Conclusions

A coupled LBM and FVM method is proposed for the fluid heat transfer problem. Nonequilibrium extrapolation scheme is used to couple the macroscopic variables in FVM region to the mesoscopic variables in LBM region. Two coupled methods with different geometric settings are employed to solve the natural convection in a squared enclosure and the results are compared with that obtained from pure FVM and LBM. The results obtained from the four methods agreed with each other very well at different Rayleigh numbers of 10^4 , 10^5 and 10^6 . The geometric settings do not affect the accuracy of the coupled method. The results of this work demonstrated that the coupled method is reliable to solve natural convection problems.

Chapter 5 A Hybrid Lattice Boltzmann and Finite Volume Method for Natural Convection

5.1 Introduction

In Chapters 3 and 4, LBM-FVM hybrid method was proposed to solve fluid flow and heat transfer problems. The whole domain is divided into two subdomains and these subdomain are solved with LBM and FVM respectively. This type of hybrid method is suitable for simulating problems involved with multiple length scales.

In another type of hybrid method – LBM-FVM, velocity, pressure and density are obtained from the density distribution solved by LBM, while the temperature field can be obtained directly using FVM based on the other solved macroscopic variables from LBM. This is a promising numerical method since the main advantages of LBM lies in obtaining velocity field. Two addition settings are needed to fulfill this LBM-FVM hybrid method: the variable locations in LBM and FVM are different and proper difference is needed in the simulation process; FVM and LBM are different time scale methods and time steps are set different in LBM and FVM.

Pure thermal LBM, pure FVM, and hybrid LBM-FVM are employed to solve the natural convection in a fixed-boundary cavity with different Rayleigh numbers. The results are compared with reference ones for validation.

5.2 Hybrid LBM-FVM approach

The velocity field is obtained by the LBM while FVM solves the temperature field in the hybrid method. They have been included in Chapter2. Different from the combined

method in Chapters 3 and 4, the LBM-FVM hybrid method in this chapter apply LBM and FVM to the whole computing domain. The locations for the temperature and velocity in the control volume are shown in Fig. 5-1.

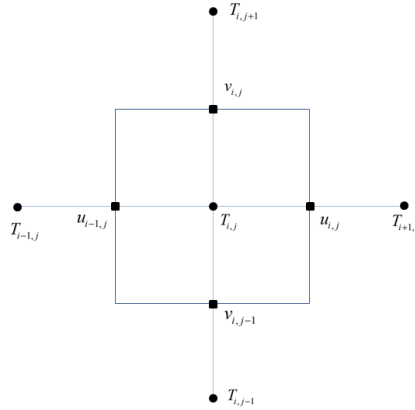


Figure 5-1 Control volume in FVM

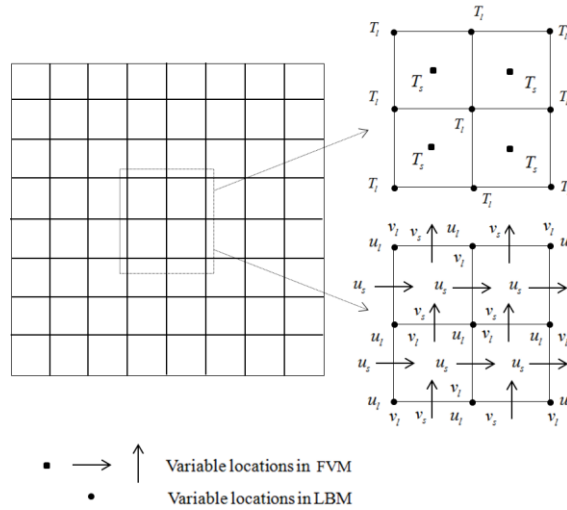


Figure 5-2 Grid setting 1

A corrected method to solve convective-diffusion equation based on SIMPLE was proposed in Ref. [96]. Based on this result, a LBM-FVM hybrid method is proposed in this chapter. The temperature field can be solved by energy balance in the control volume after the velocity field is obtained from the LBM.

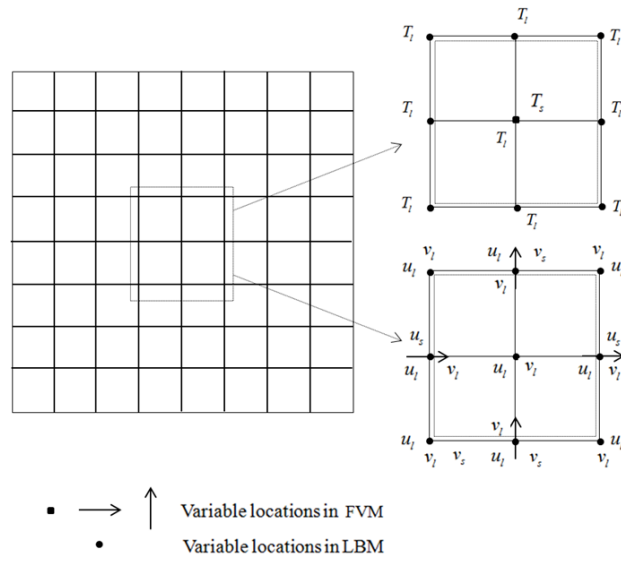


Figure 5-3 Grid setting 2

Assume the grid in LBM is $2NX \times 2NY$ after mesh independent testing for the LBM. In the natural convection cases solved in this thesis, 160×160 is the selected mesh. It is quite straightforward to assume that the grid for the temperature field is the same as that in the velocity field shown in Fig. 5-2. The velocities on the faces of control volume that are needed in the FVM are obtained by the interpolating of the LBM results. Figure 5-3 shows another method to set the grid for FVM that $NX \times NY$ grid is applied to FVM for the temperature field. The dashed lines show the new control volume for the temperature field. The obtained velocity results can be applied to FVM directly without interpolation. Then the temperature on the computing nodes of can be obtained by the interpolation of the FVM results for these two grids setting method, and they can reach the same results after comparing the results. Since the computational time for the temperature field in the second method is much shorter than that of the first one, the second method is preferred in the hybrid method.

Non-dimensional process in FVM is the same as that in Chapter 4 and $2NX \times 2NY$ is employed in LBM. Correspondently, time steps in FVM and LBM are $H / (\sqrt{3}c_s)$ and $H / (2NX \cdot \sqrt{3}c_s)$ respectively. Therefore, in every FVM time step, LBM runs $2NX$ time steps.

5.3 Results and discussions

Natural convection in squared enclosure is widely used as a benchmark problem for validation of the numerical methods. Pure LBM, pure FVM and the hybrid method are applied to simulate the natural convection independently for three different Rayleigh numbers at 10^4 , 10^5 and 10^6 , while the Prantl number is 0.71. It is reported by several groups independently that pure LBM and pure FVM are both suitable for the natural convection in this range [47, 97]. So when the results of these two methods agree with each other well, they can be treated as the benchmark results for comparison.

Under the Boussinesq assumption, variation of density with temperature is considered in the buoyancy force. In the gravitational field, there is a tendency that lighter fluid goes upward and the heavier one goes downward. The boundary layer of a vertical wall with high constant temperature turns thicker with the increasing of the height, while the boundary layer of a vertical wall with low constant temperature becomes thicker with the decreasing of the height. So the fluid near the left wall moves up but the fluid near the right wall moves down. The closer to the left boundary, the hotter the fluid is since the left boundary has the highest temperature. Therefore the upward moving fluid near the left moves towards right near the top of the cavity and the downward moving fluid moves towards left near the bottom of the cavity. And the two flows combine together as a vortex.

For the case that Rayleigh number is equal to 10^4 , the streamlines and temperature fields obtained by the pure FVM and pure LBM agreed with each other well as shown in Figs. 5-4 and 5-5, respectively. It is shown that the natural convection has governed the heat transfer process. There is a streamline vertex in the center of the cavity and the temperature field also shows the character of the convection. The streamlines and temperature field obtained from the hybrid method matches the results from the other two methods very well.

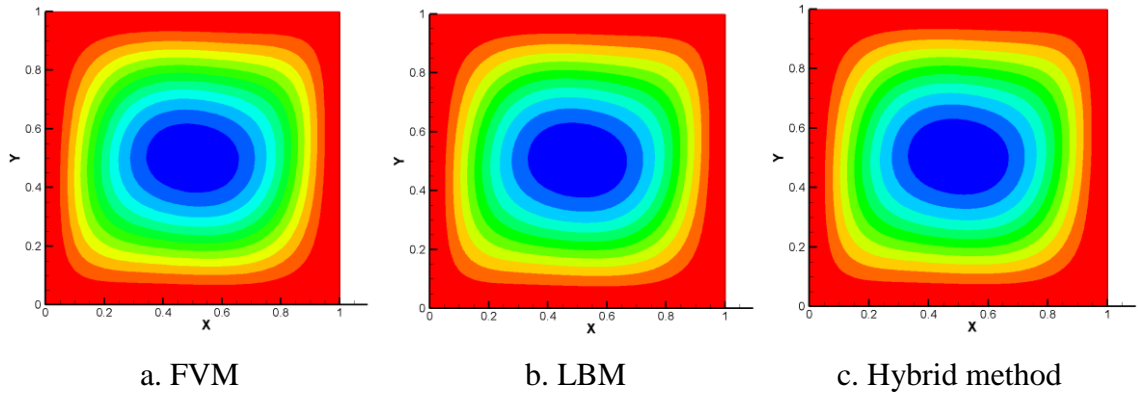


Figure 5-4 Streamlines comparison at $Ra=10^4$

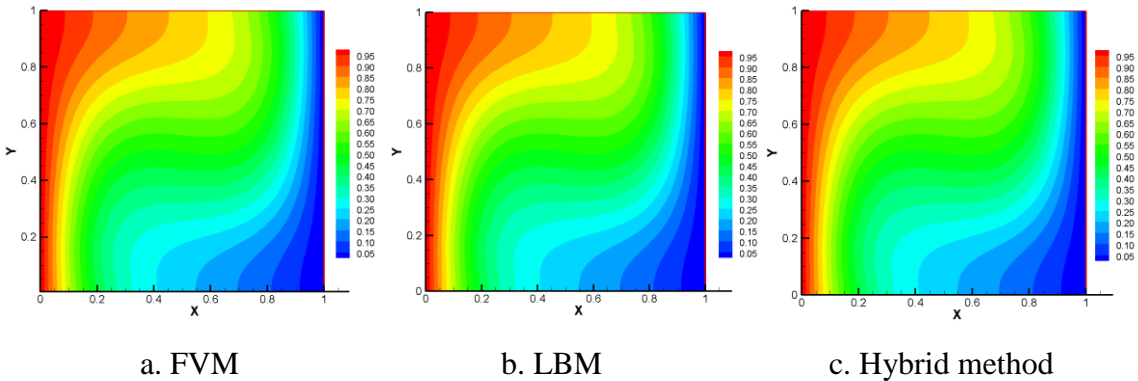


Figure 5-5 Temperature field comparison at $Ra=10^4$

The natural convection effect becomes more obvious when the Rayleigh number is increased to 10^5 . Figures 5-6 and 5-7 show that the streamlines and temperature fields from the three methods agree with each other very well. There are two vertexes in the flow field and the temperature gradient at the left and right boundaries is larger than that for the case

of $Ra = 10^4$. The differences of the streamlines and temperature fields among the three methods are still not noticeable when the Rayleigh number grows to 10^6 as shown in Figs. 5-8 and 5-9. The two streamline vertexes locate farther from the cavity center and the temperature changes turn closer to the left and right boundaries. So the streamlines and temperature fields of the hybrid method agree with those obtained by the other two methods for the three Rayleigh numbers.

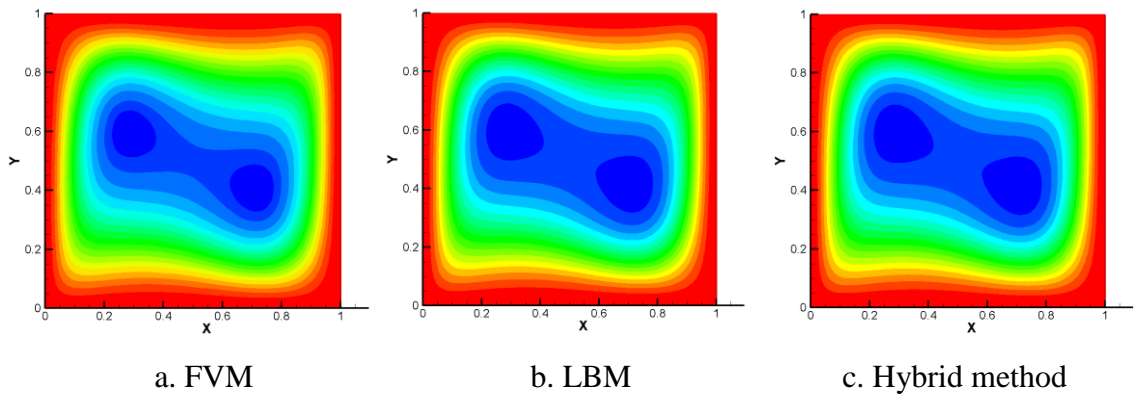


Figure 5-6 Streamlines comparison at $Ra=10^5$

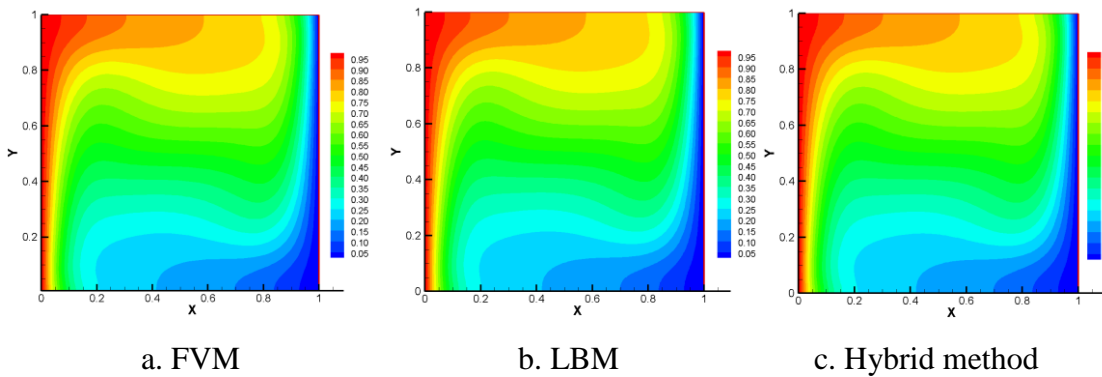
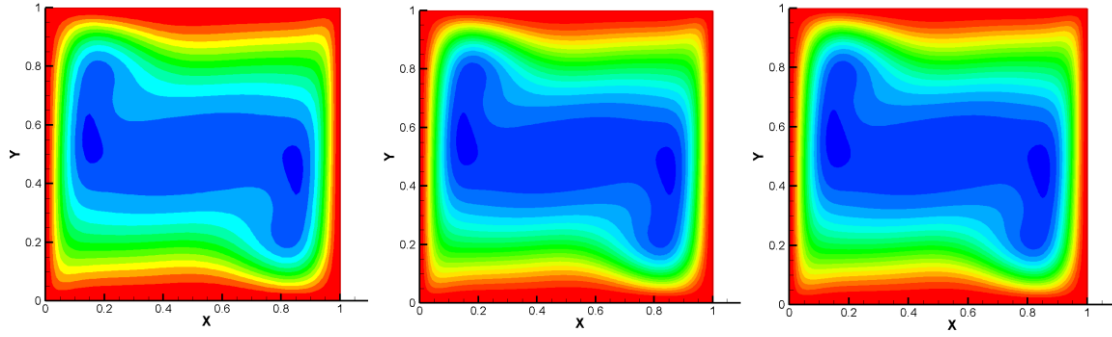


Figure 5-7 Temperature field comparison at $Ra=10^5$

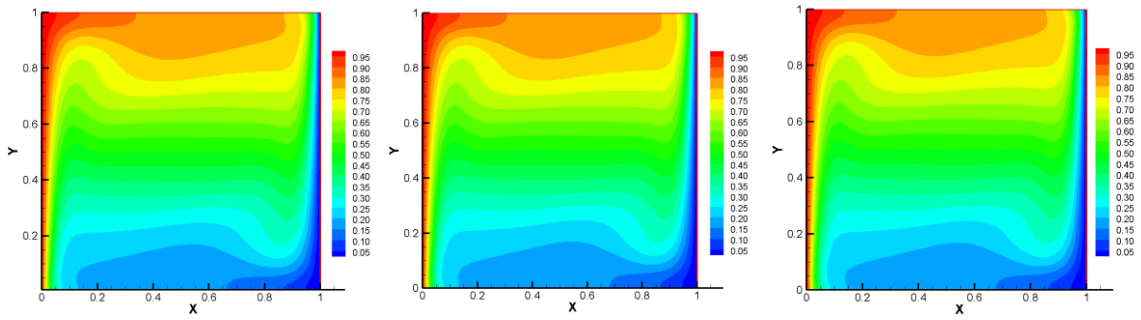


a. FVM

b. LBM

c. Hybrid method

Figure 5-8 Streamlines comparison at $Ra=10^6$



a. FVM

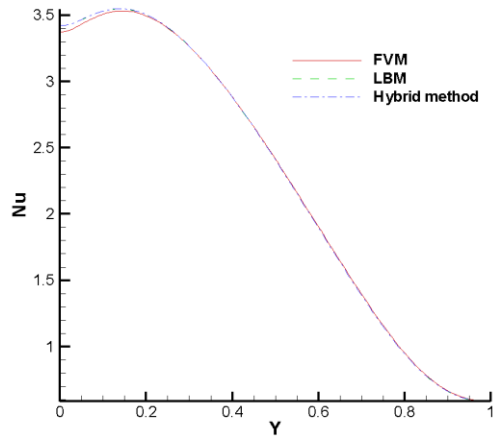
b. LBM

c. Hybrid method

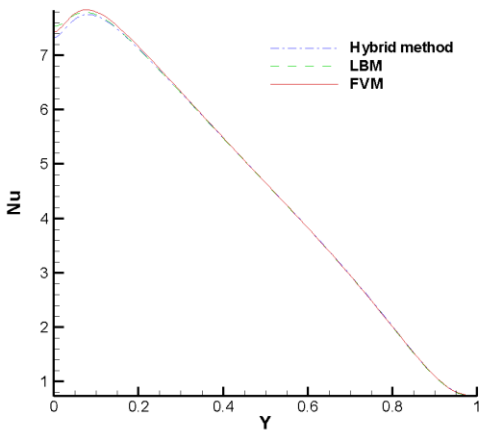
Figure 5-9 Temperature field comparison at $Ra=10^6$

Table 5-1 Comparison of the maximum Nusselt numbers

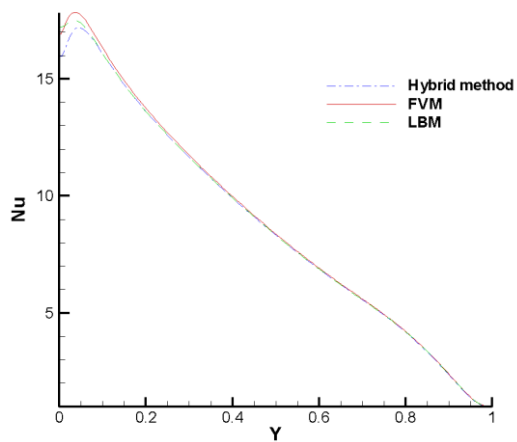
	$Ra=10^4$	$Ra=10^5$	$Ra=10^6$
Hybrid method	3.5324	7.6970	17.3354
FVM	3.5486	7.8382	17.8399
LBM	3.5481	7.7907	17.5133
Ref. [50]	3.5309	7.7201	17.5360



a. $Ra=10^4$



b. $Ra=10^5$



c. $Ra=10^6$

Figure 5-10 Comparison of Nusselt numbers

Comparison of Nusselt number obtained from the three methods is shown in the Fig. 5-10 for different cases. It can be seen that the results agree with each other very well in the three cases. The main difference locates at the maximum Nusselt number part, which is more obvious as the Rayleigh number increases. Meanwhile Table 5-1 and 5-2 give the comparisons of the maximum Nusselt number and its location for the three methods and the results from Ref. [97]. For the maximum Nusselt number, the hybrid result is closest to the reference result in the first two cases while the pure LBM has the closest result when Rayleigh number equals 10^6 . The hybrid method result is closest to the reference result in all the three cases. The largest difference between all the three methods results and the reference result is still under 3% which is acceptable.

Table 5-2 Comparison of the locations of maximum Nusselt numbers

	$Ra=10^4$	$Ra=10^5$	$Ra=10^6$
Hybrid method	0.1437	0.0812	0.0437
FVM	0.1375	0.0813	0.0334
LBM	0.1375	0.0750	0.0313
Ref. [50]	0.1439	0.0820	0.0392

5.4 Conclusions

A hybrid FVM and LBM approach is proposed for the fluid flow and heat transfer problem. LBM is applied to obtain the velocity fields and the temperature field is obtained by the FVM. The hybrid method, together with pure LBM and pure SIMPLE, are used to solve the natural convection in a squared cavity. The streamlines and temperature fields

obtained by the three methods agree with each other very well for different Rayleigh numbers at 10^4 , 10^5 and 10^6 . The hybrid method also has a good accuracy for the Nusselt number when comparing with the reference and the two pure methods results. Thus, the hybrid LBM-FVM is reliable for the natural convection simulation. This method is designed to take advantages of both LBM and FVM. It is well known that LBM has its advantage in solving complex geometry fluid flow while FVM has high efficiency for conservative laws. So this hybrid method can show its advantage in the case such as heat transfer in the complex geometry fluid flow problems.

Chapter 6 A Combined Lattice Boltzmann and Monte Carlo Method for Natural Convection Simulation

6.1 Introduction

To take advantages of both LBM and FVM, a LBM-FVM hybrid method is proposed and verified in Chapter 5. Multiscale problem may involve radiative heat transfer while MCM has valid advantages in solving it. LBM-MCM hybrid method is proposed for fluid flow and heat transfer simulation in this chapter. Velocity field is solved with LBM while temperature is obtained using MCM. Natural convection with different Rayleigh numbers are solved to verify this numerical method.

6.2 Combined LBM-MCM method

In this combined method, velocity and temperature fields are solved using LBM and Monte Carlo method, respectively. LBM for fluid field has been included in Chapter 2.

6.2.1 Monte Carlo Method (MCM) for heat transfer

A rectangular grid system of mesh size $\Delta x \times \Delta y$ is selected for the two-dimensional computing domain shown in Fig. 6-1. The inner computing node (i, j) relates to its surrounding nodes by:

$$T_{i,j} = P_{x+} T_{i+1,j} + P_{x-} T_{i-1,j} + P_{y+} T_{i,j+1} + P_{y-} T_{i,j-1} \quad (6.1)$$

where the possibilities P_{x+} , P_{x-} , P_{y+} and P_{y-} are positive; their sum has to be 1.

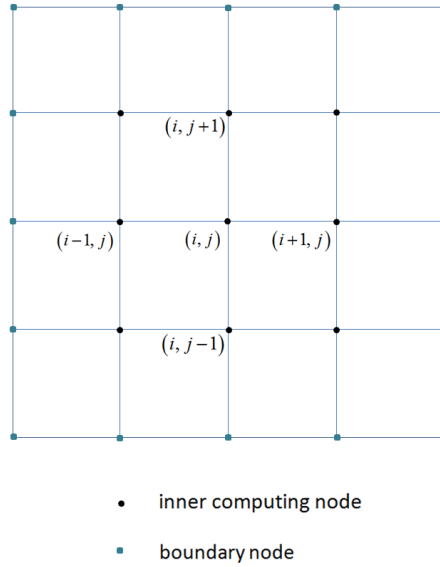


Figure 6-1 Computing grid

For the conduction heat transfer problem, these possibilities are:

$$\begin{cases} P_{x+} = P_{x-} = \frac{\Delta y / \Delta x}{2(\Delta y / \Delta x + \Delta x / \Delta y)} \\ P_{y+} = P_{y-} = \frac{\Delta x / \Delta y}{2(\Delta y / \Delta x + \Delta x / \Delta y)} \end{cases} \quad (6.2)$$

For the convection heat transfer problem, the horizontal velocity u and vertical velocity v have effects on P_{x+} , P_{x-} , P_{y+} and P_{y-} . The possibilities should be modified to the following equation:

$$\begin{cases} P_{x+} = \frac{\alpha \Delta y / \Delta x - u \Delta y}{D} & P_{x-} = \frac{\alpha \Delta y / \Delta x}{D} \\ P_{y+} = \frac{\alpha \Delta x / \Delta y - v \Delta x}{D} & P_{y-} = \frac{\alpha \Delta x / \Delta y}{D} \end{cases} \quad (6.3)$$

where

$$D = 2(\Delta y / \Delta x + \Delta x / \Delta y) - u \Delta y - v \Delta x \quad (6.4)$$

The statistical procedure MCM uses random walkers to solve the heat transfer problem [98]. A random walker locates at node (i, j) at beginning and a random number RN is chosen in the uniformly distribution set from 0 to 1. This random walker will change its position by the following rules:

$$\begin{cases} \text{if } 0 < RN < P_{x+} & \text{from } (i, j) \text{ to } (i+1, j) \\ \text{if } P_{x+} < RN < P_{x+} + P_{y+} & \text{from } (i, j) \text{ to } (i, j+1) \\ \text{if } P_{x+} + P_{y+} < RN < P_{x+} + P_{y+} + P_{x-} & \text{from } (i, j) \text{ to } (i-1, j) \\ \text{if } 1 - P_{y-1} < RN < 1 & \text{from } (i, j) \text{ to } (i, j-1) \end{cases} \quad (6.5)$$

Once the random walker has completed its first step, the procedure continues for the second step. This process goes on till that random walker reaches the boundary. Then the boundary condition $T_w(1)$ is recorded for the inner node (i, j) . This process is repeated $N-1$ times and the recorded boundary conditions are $T_w(2)$ to $T_w(N)$. With these N results, the MCM estimation for $T(i, j)$ can be expressed as:

$$T(i, j) = \frac{1}{N} \sum_{n=1}^N T_w(n) \quad (6.6)$$

Then all the inner computing nodes can be obtained by this method. The treatments to different kind boundaries can be found in Ref. [98].

6.2.2 Description of the combined method

A combined LBM-MCM method is designed to solve a fluid flow and heat transfer problem with LBM and MCM simultaneously. Same grid system is used in both LBM and MCM. The velocity field is obtained by LBM and MCM solves the temperature field.

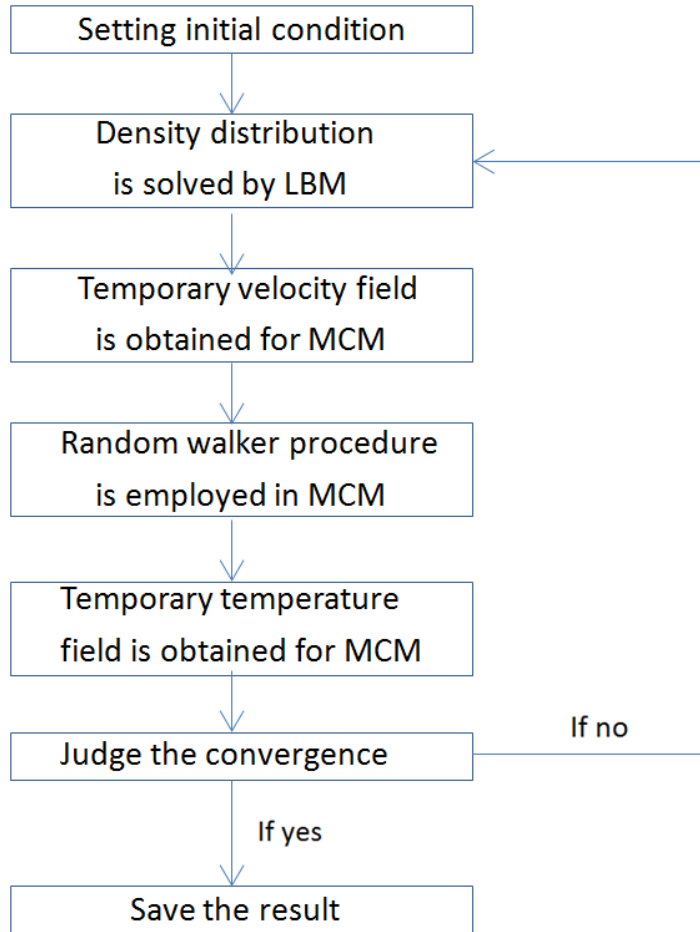


Figure 6-2 Flowchart

Figure 6-2 shows the flowchart for the combined method. For the natural convection problem in consideration, temperature and velocity have effects on each other. Therefore this method needs to run LBM and MCM in consequence for each step. After setting the initial condition, LBM solves the velocity field with the initial temperature field. Then the temperature field is obtained by MCM with the LBM velocity result. This temperature can be applied to LBM in next step. This process is repeated till converged results are reached.

6.3 Results and discussions

6.3.1 Validation of MCM

In Chapter 3, LBM has been proved to be valid in solving incompressible fluid flow problems. In this section, MCM is verified for heat transfer simulation. As discussed in section 3.2, MCM has the same approach in solving conduction and convection heat transfer problems. A pure conduction problem is solved to test the MCM. In Fig. 6-3, the left, right and bottom of the two-dimensional domain are kept at T_c and the top boundary has a higher temperature of T_h . It is assumed that the thermal conductivity is independent from the temperature. The energy equation for this problem is

$$\frac{\partial^2 T}{\partial x^2} + \frac{\partial^2 T}{\partial y^2} = 0, \quad 0 < x < H, 0 < y < H \quad (6.7)$$

with the following boundary conditions:

$$T = T_c, \quad x = 0 \text{ or } H, 0 < y < H \quad (6.8)$$

$$T = T_c, \quad y = 0, 0 < x < H \quad (6.9)$$

$$T = T_h, \quad y = H, 0 < x < H \quad (6.10)$$

Defining the following non-dimensional variables

$$\begin{cases} X = \frac{x}{H}, Y = \frac{y}{H}, \\ \theta = \frac{T - T_c}{T_h - T_c} \end{cases} \quad (6.11)$$

Equations. (6.7)-(6.10) become

$$\frac{\partial^2 \theta}{\partial X^2} + \frac{\partial^2 \theta}{\partial Y^2} = 0, \quad 0 < X < 1, 0 < Y < 1 \quad (6.12)$$

with the following boundary conditions:

$$\theta = 0, \quad X = 0 \text{ or } 1, 0 < Y < 1 \quad (6.13)$$

$$\theta = 0, \quad Y = 0, 0 < X < 1 \quad (6.14)$$

$$\theta = 1, \quad Y = 1, 0 < X < 1 \quad (6.15)$$

This problem can be solved analytically by separation of variable method [99].

$$\theta = \frac{2}{\pi} \sum_{n=1}^{\infty} \frac{(-1)^{n+1} + 1}{n} \frac{\sinh(n\pi Y)}{\sinh(n\pi)} \sin(n\pi X) \quad (6.16)$$

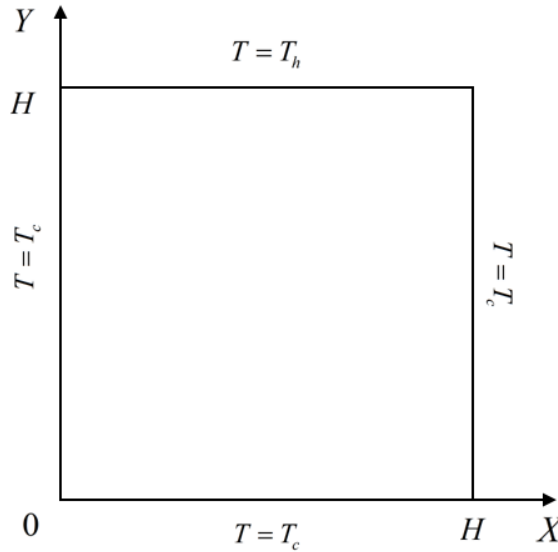


Figure 6-3 Two-dimensional steady state heat conduction

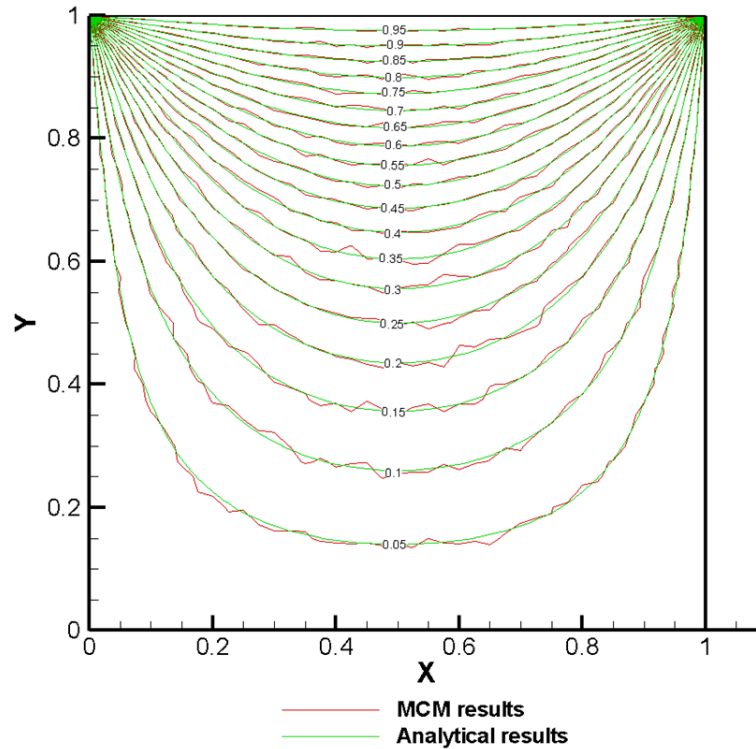


Figure 6-4 Conduction temperature field comparison

Figure 6-4 shows the comparison of the analytical and MCM temperature fields. As discussed in section 6.2, MCM is a statistical method to simulate the heat transfer process. Its results are based on a large number of random walkers' results. The MCM isothermal lines are not that smooth due to its procedure nature. These two methods isothermal lines agree with each other well. Therefore, MCM in this thesis is valid for the heat transfer problem.

6.3.2 Natural convection in rectangular enclosure

In case 1, Figure 6-5 shows the streamlines for Case 1 that Ra and Pr are 10^4 and 0.71, respectively. There is a vortex in the cavity due to the convection effect. Figure 6-6 is the temperature field obtained from the combined method.

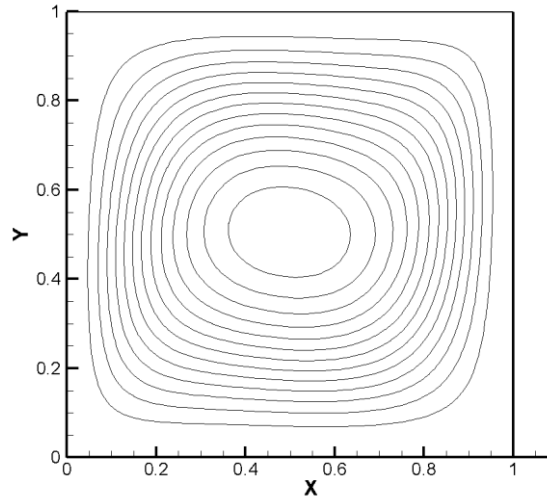


Figure 6-5 Streamlines in case 1

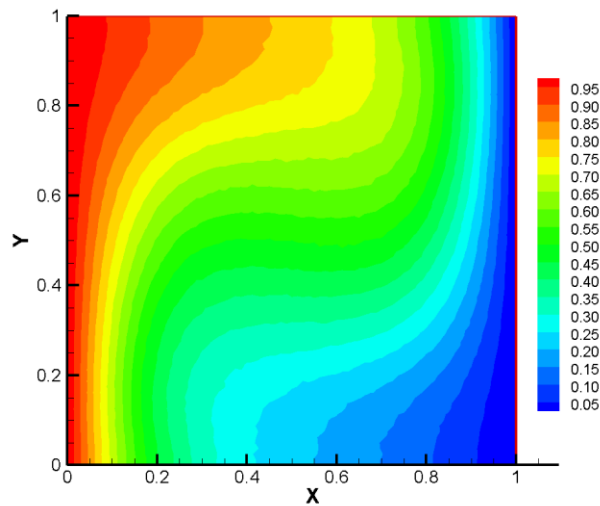


Figure 6-6 Temperature field in case 1

Both streamlines and temperature field agree with the benchmark solutions very well except the unsmoothness of some isothermal lines. As discussed in the pure conduction problem, the unsmoothness is led by the nature of MCM and its effect to the streamlines is insignificant. Meanwhile, Table 1 summarize maximum Nusselt number Nu_{max} , maximum Nusselt number location $Y_{Nu_{max}}$ and average Nusselt number Nu_{ave} obtained from the LBM-MCM and Ref. [100]. It can be seen that the combined LBM-MCM method has a good agreement with benchmark standard solutions for these three parameters for Case 1.

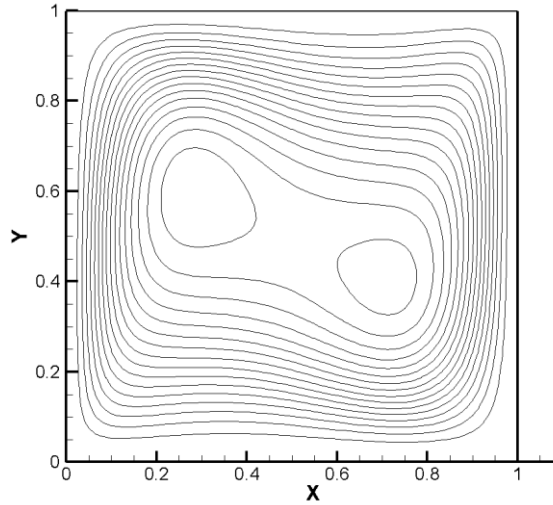


Figure 6-7 Streamlines in case 2

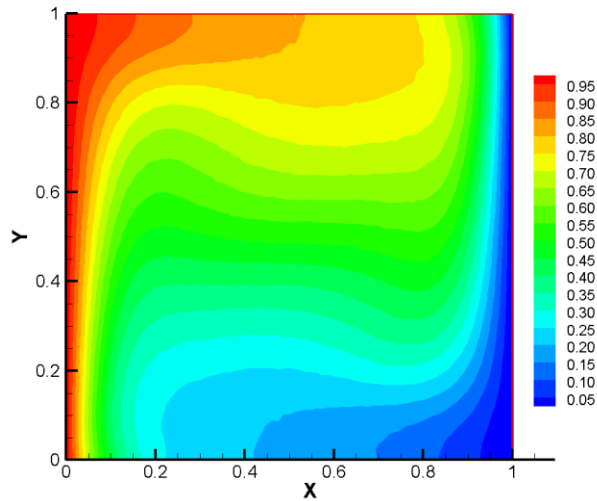


Figure 6-8 Temperature field in case2

Case 2 is also studied when Ra grows to 10^5 and Pr is kept 0.71. Convection plays a more important role due to the increased Ra . Two vortices locate in the cavity are shown in Fig. 6-7. And the temperature field in Fig. 6-8 also indicates a pronounced convection effect.

Table 6-1 also showed the comparison of Nu_{max} , $Y_{Nu_{max}}$ and Nu_{ave} obtained from the present LBM-MCM with the benchmark solutions for this case. The streamlines,

temperature field and Nusselt number results in combined LBM-MCM method all agree with the benchmark solutions well. Similar to Case 1, the unsmooth isothermal lines effect is insignificant. Therefore the combined LBM-MCM method can give good predictions to these two natural convection cases.

Table 6-1 Comparison of Nusselt number

Results		Nu_{max}	$Y_{Nu_{max}}$	Nu_{ave}
$Ra = 10^4$	LBM-MCM	3.50	0.15	2.21
	Ref. [100]	3.53	0.15	2.24
	Error	1.0%	0	1.4%
$Ra = 10^5$	LBM-MCM	7.38	0.08	4.38
	Ref. [100]	7.72	0.08	4.52
	Error	4.4%	0	3.1%

6.4 Conclusions

A pure incompressible fluid flow and a pure conduction problem are solved by LBM and MCM respectively. The results indicate LBM and MCM are valid for those problems. Then, a combined LBM-MCM approach is proposed for the fluid flow and heat transfer problem. The LBM is applied to solve the velocity field and the temperature field is obtained by the MCM. This combined method is employed to solve two cases natural convection in a cavity. The streamlines temperature field and Nusselt number obtained from the present LBM-MCM approach agree with that of the benchmark solutions well. Thus, the combined LBM-MCM is reliable for the natural convection simulation.

Chapter 7 Double MRT Thermal Lattice Boltzmann Method for Simulating Natural Convection of Low Prandtl Number Fluids

7.1 Introduction

Various hybrid methods have been discussed in Chapter 3 to 6 for natural convection simulation. Another objective of this dissertation is solving various melting problems with different numerical methods. Melting problem can involve various phase change materials (PCM). Their Prandtl numbers vary from 10^{-3} (liquid metal) to 10^5 (functional oil) [92]. Low Prandtl number fluid flow and heat transfer problem may reach oscillation results. In this chapter low Prandtl fluid natural convection is discussed with LBM, and low Prandtl melting problems will be solved in the next chapter based on these results.

Instead of solving the macroscopic continuum and momentum equations as the traditional computational fluid dynamics (CFD), the LBM is based on solving the discrete Boltzmann equation in statistical physics via two basic steps: collision step and streaming step. There are different LBM models for fluid flow problems. Lattice Bhatnagar-Gross-Krook simplifies the collision term with one relaxation time [101, 102]. Although it is widely used, LBGK is limited by the numerical instability [103]. To overcome this limitation, entropy LBM (ELBM) [104, 105], two-relaxation-time model (TRT) [106, 107] and multiple relaxation time model (MRT) [68, 108] have been proposed. The difference among these models lies in the ways to simplify the collision term while their streaming steps are the same. Luo et al. [109] compared these models by using them to solve the lid driven flow problem. It was concluded that the MRT was preferred due to its advantages

in accuracy and numerical stability. The objective of this chapter is to employ the double MRT model to analyze the low Prandtl number natural convection problems.

7.2 Double MRT thermal lattice Boltzmann model

Double MRT thermal LBM model [110] is selected to solve the natural convection problem. Wang et al. [110] discussed the convective flow for Prandtl number of 0.71 and 7.0 with the double MRT thermal LBM. Mezhahab et al. [111] used double MRT thermal LBM for simulating air convective flow in a cavity respectively for Rayleigh number up to 10^8 . D2Q9-MRT is applied to analyze the velocity field and the temperature field is solved by D2Q5-MRT.

7.2.1 D2Q9-MRT for fluid flow

In Chapter 2, LBGK model has been introduced. The difference between LBGK and MRT locates in the way to simplify the collision term. To satisfy the continuum and momentum conservations, the collision term in MRT is:

$$\Omega_i = -M^{-1} \cdot S \cdot [m_i(\mathbf{r}, t) - m_i^{eq}(\mathbf{r}, t)], \quad i = 1, 2, \dots, 9 \quad (7.1)$$

where $m_i(\mathbf{r}, t)$ and $m_i^{eq}(\mathbf{r}, t)$ are moments and their equilibrium functions; M and S are the transform matrix and collision matrix respectively [111]. For the D2Q9 model the nine macroscopic moments are:

$$\begin{aligned} \mathbf{m} &= (m_1, m_2, m_3, m_4, m_5, m_6, m_7, m_8, m_9)^T \\ &= (\rho, j_x, j_y, e, p_{xx}, p_{xy}, q_x, q_y, \varepsilon)^T \end{aligned} \quad (7.2)$$

Consequently, the transform matrix M and is:

$$M = \begin{pmatrix} 1 & 1 & 1 & 1 & 1 & 1 & 1 & 1 & 1 \\ 0 & 1 & 0 & -1 & 0 & 1 & -1 & -1 & 1 \\ 0 & 0 & 1 & 0 & -1 & 1 & 1 & -1 & -1 \\ -4 & -1 & -1 & -1 & -1 & 2 & 2 & 2 & 2 \\ 0 & 1 & -1 & 1 & -1 & 0 & 0 & 0 & 0 \\ 0 & 0 & 0 & 0 & 0 & 1 & -1 & 1 & -1 \\ 0 & -2 & 0 & 2 & 0 & 1 & -1 & -1 & 1 \\ 0 & 0 & -2 & 0 & 2 & 1 & 1 & -1 & -1 \\ 4 & -2 & -2 & -2 & -2 & 1 & 1 & 1 & 1 \end{pmatrix} \quad (7.3)$$

Correspondingly, the collision matrix S is:

$$S = \text{diag}(0, 1, 1, s_e, s_v, s_v, s_q, s_q, s_\varepsilon) \quad (7.4)$$

In the present simulations, the unknown parameters in Eq. (7.4) are defined as following:

$$\begin{cases} s_e = s_\varepsilon = s_v = \frac{2}{6\nu+1} \\ s_q = 8 \frac{(2-s_v)}{(8-s_v)} \end{cases} \quad (7.5)$$

Then ρ , j_x and j_y are related with density distribution f_i by the following equation:

$$\begin{cases} \rho = \delta\rho + \rho_0, \rho_0 = 1, \delta\rho = \sum_{i=1}^9 f_i \\ \mathbf{j} = \rho_0 \mathbf{u} = \rho_0(u, v), \rho_0 \mathbf{u} = \sum_{i=1}^9 f_i \mathbf{e}_i \end{cases} \quad (7.6)$$

Adding ρ_0 can reduce round-off errors in the simulation process [110]. Accordingly, the equilibrium functions m_i^{eq} are

$$\begin{cases} m_1^{eq} = \delta\rho, m_2^{eq} = \rho_0 u, m_3^{eq} = \rho_0 v, m_4^{eq} = -2\delta\rho + \rho_0 \mathbf{u} \cdot \mathbf{u}, m_5^{eq} = \rho_0 (u^2 - v^2) \\ m_6^{eq} = \rho_0 uv, m_7^{eq} = -\rho_0 u, m_8^{eq} = -\rho_0 v, m_9^{eq} = \delta\rho - 3\rho_0 \mathbf{u} \cdot \mathbf{u} \end{cases} \quad (7.7)$$

Bounce-back scheme is employed for the no-slip boundary conditions [40].

7.2.2 D2Q5-MRT for heat transfer

The D2Q5 model is used to obtain the temperature field. Each computing node has five discrete velocities shown in Fig. 2-3:

$$\mathbf{u}_i = \begin{cases} (0, 0) & i = 1 \\ c(-\cos \frac{i\pi}{2}, -\sin \frac{i\pi}{2}) & i = 2, 3, 4, 5 \end{cases} \quad (7.8)$$

Similar to the density distribution, the energy distribution g_i can be obtained by:

$$g_i(\mathbf{r} + \mathbf{u}_i \Delta t, t + \Delta t) - g_i(\mathbf{r}, t) = -N^{-1} \cdot Q \cdot [n_i(\mathbf{r}, t) - n_i^{eq}(\mathbf{r}, t)], \quad i = 1, 2, \dots, 5 \quad (7.9)$$

where $n_i^{eq}(\mathbf{r}, t)$ are the equilibrium functions for $n_i(\mathbf{r}, t)$, N and Q are the transform matrix and collision matrix for the energy distribution [110]:

$$N = \begin{pmatrix} 1 & 1 & 1 & 1 & 1 \\ 0 & 1 & 0 & -1 & 0 \\ 0 & 0 & 1 & 0 & -1 \\ -4 & 1 & 1 & 1 & 1 \\ 0 & 1 & -1 & 1 & 1 \end{pmatrix} \quad (7.10)$$

$$Q = \text{diag}(0, \sigma_k, \sigma_k, \sigma_e, \sigma_v) \quad (7.11)$$

$$\text{where } \left(\frac{1}{\sigma_v} - \frac{1}{2} \right) \left(\frac{1}{\sigma_k} - \frac{1}{2} \right) = \frac{1}{6} \quad (7.12)$$

The unknown parameters in Eq. (7.11) are defined as following [110]:

$$\begin{cases} \frac{1}{\sigma_e} - \frac{1}{2} = \frac{1}{\sigma_v} - \frac{1}{2} = \frac{\sqrt{3}}{3} \\ \frac{1}{\sigma_k} - \frac{1}{2} = \frac{\sqrt{3}}{6} \end{cases} \quad (7.13)$$

The temperature at each computing node can be obtained as:

$$\theta = \sum_{i=1}^5 g_i \quad (7.14)$$

Then the equilibrium functions $n_i^{eq}(\mathbf{r}, t)$ are:

$$n_1^{eq} = T, n_2^{eq} = uT, n_3^{eq} = vT, n_4^{eq} = aT, n_5^{eq} = 0 \quad (7.15)$$

where a is related to the thermal diffusivity α by:

$$\alpha = \frac{(4+a)}{10} \left(\frac{1}{\sigma_k} - \frac{1}{2} \right) \quad (7.16)$$

It is necessary that $a < 1$ to avoid instability [112]. The natural convection problem under consideration involves two types of boundary conditions: constant temperature and adiabatic. Assuming x_f is a fluid computing node adjacent to the boundary, only one direction energy distribution $g_i(x_f, t)$ among the five directions in D2Q5 model is unknown on each boundary nodes. On its opposite direction, energy distribution $g_i(x_f, t)$ is known after the streaming process. The top and bottom of the cavity are adiabatic and bounce-back scheme [110] is employed to fulfill them:

$$g_i(x_f, t) = g_i(x_f, t) \quad (7.17)$$

For the boundary with constant temperature θ_w , the anti-bounce-back boundary condition is employed [111].

$$g_i(x_f, t) = 2\sqrt{3}\alpha\theta_w - g_i(x_f, t) \quad (7.18)$$

7.3 Results and discussions

The natural convection problem is governed by Rayleigh number and Prandtl number. The Rayleigh number, Ra is depending on the temperature difference $T_h - T_c$, cavity height H and thermal properties of fluid. Meanwhile, the Prandtl number, Pr is a fluid thermal property that varies from 10^{-3} (liquid metal) to 10^5 (functional oil) [92]. The objective of this thesis is to study natural convection of low Pr (orders of magnitude from 10^{-3} to 10^{-2}) fluid.

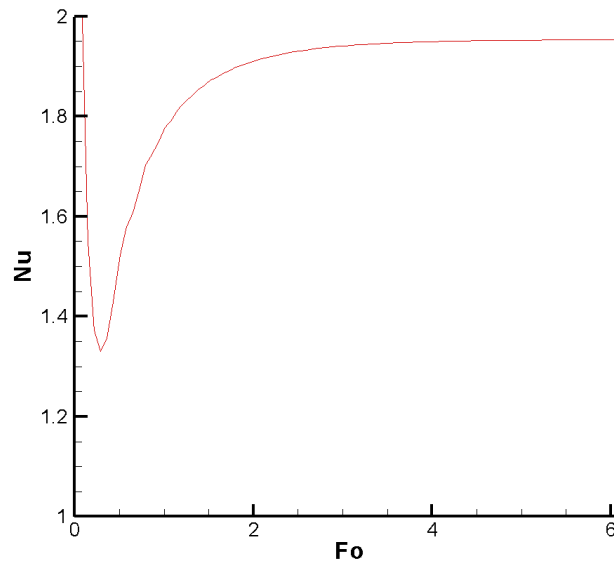


Figure 7-1 Case 1: average Nusselt number

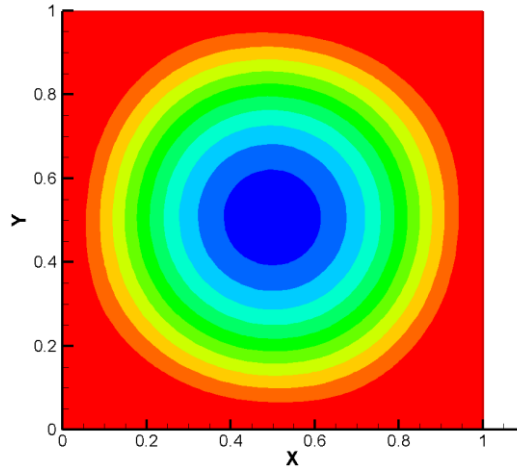


Figure 7-2 Case 1: streamlines

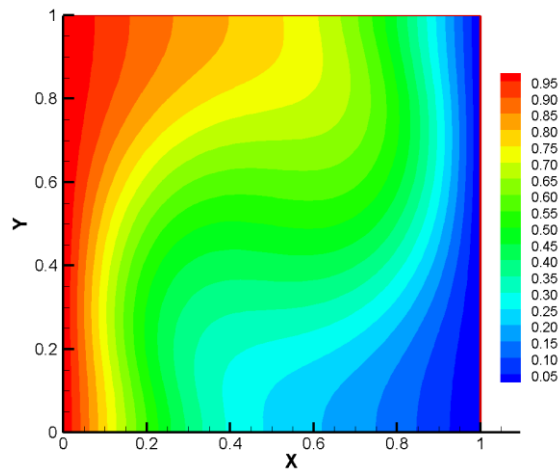


Figure 7-3 Case 1: temperature field

Natural convection in a square enclosure with $Ra = 10^4$ and $Pr = 0.01$ is considered first (referred to as Case 1 thereafter). Figure 7-1 shows the variation of the average Nusselt number with time. It can be seen that the average Nusselt number become a constant after $Fo = 3$; this indicates the heat transfer rate through the left heat wall reaches a fixed value of 1.95 which agrees with that in Ref. [92] well. Figure 7-2 shows the streamlines for Case 1 that one vortex exists in the center of cavity due to the convection effect; it agrees with that in Ref. [92] as well. This convection effect is also evident in the temperature field

shown in Fig. 7-3. The local Nusselt number along the vertical direction is shown in Fig.

7-4. The maximum Nusselt number Nu_{\max} of 3.02 occurs at the location of $Y_{Nu_{\max}} = 0.30$.

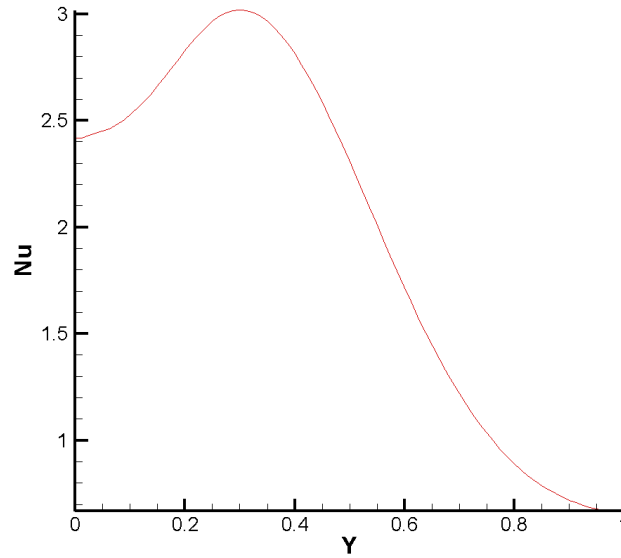


Figure 7-4 Case 1: Nusselt number

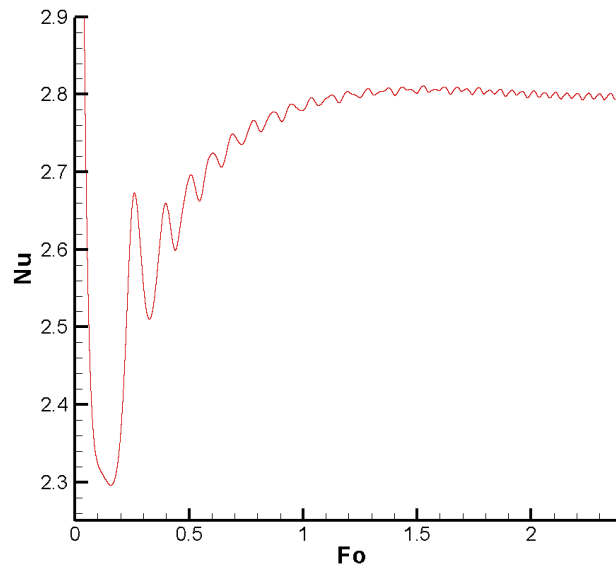


Figure 7-5 Case 2: average Nusselt number

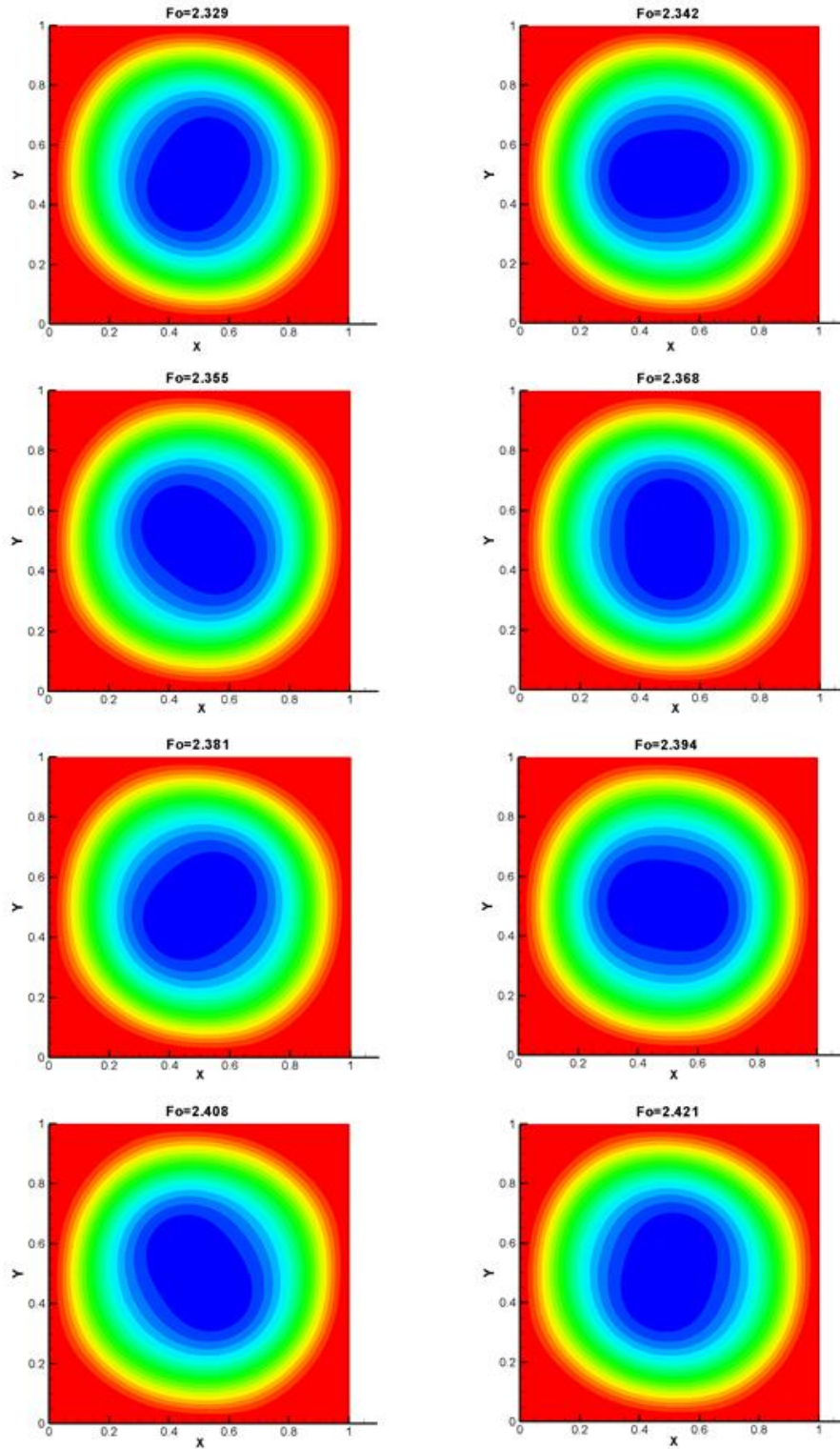


Figure 7-6 Case 2: streamlines

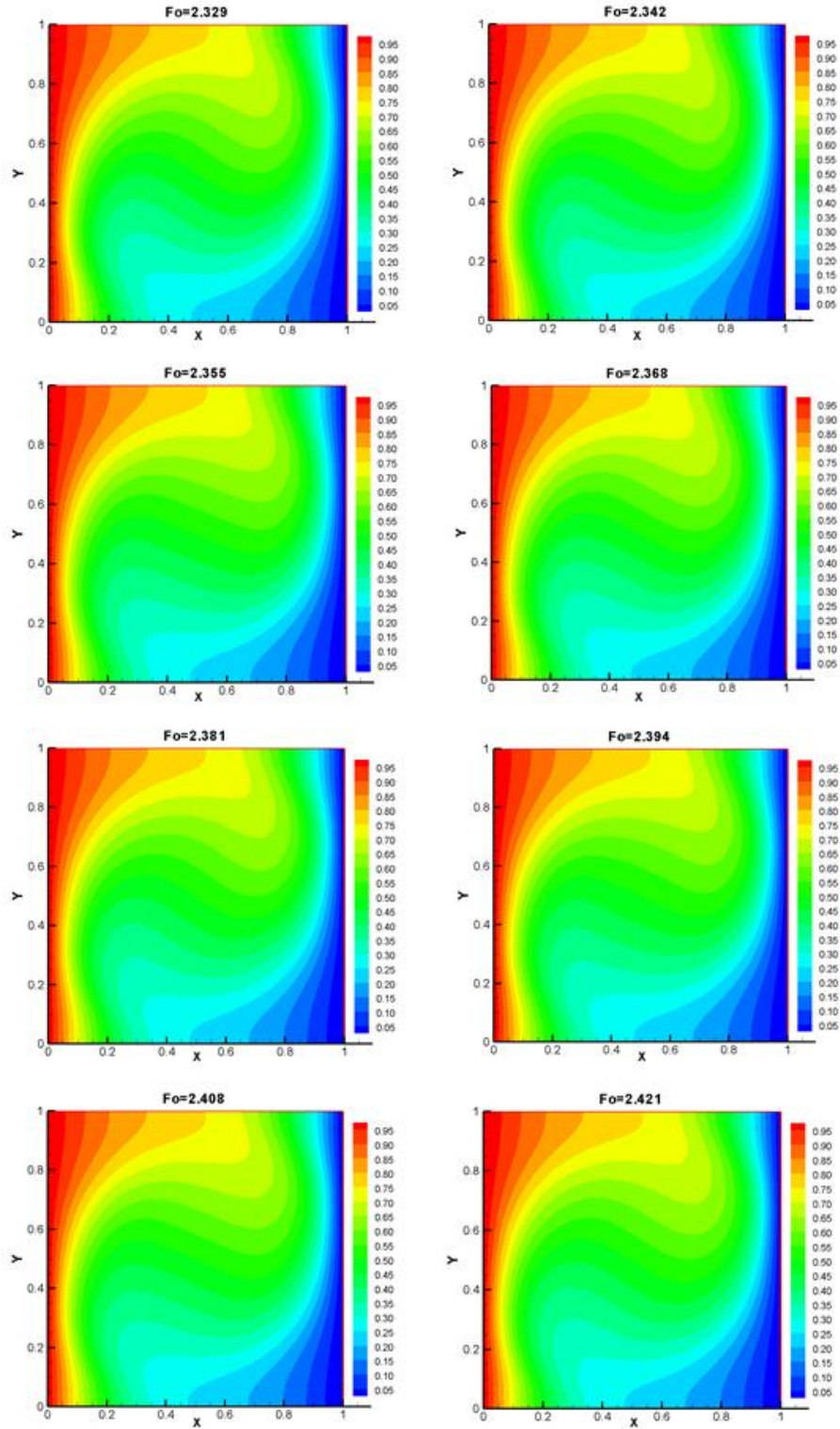


Figure 7-7 Case 2: temperature field

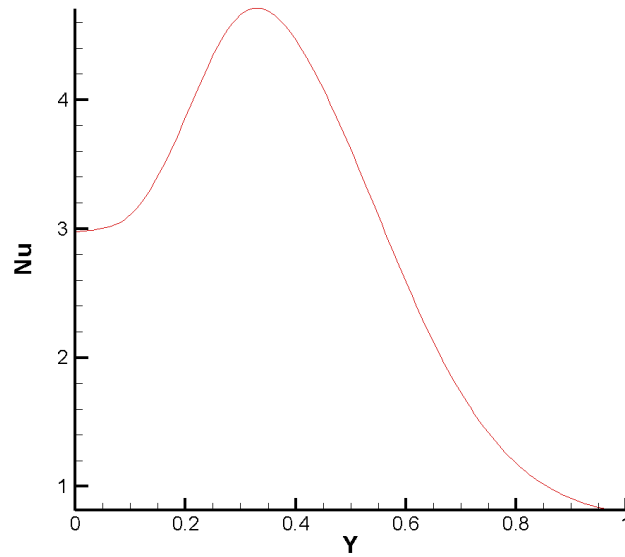


Figure 7-8 Case 2: Nusselt number

Simulation is then carried out for Case 2 that Rayleigh number increases to 5×10^4 while the Prandtl number is kept at 0.01. Figure 7-5 shows the variation of the average Nusselt number with time. It is different from the Case 1 that steady state cannot be reached; After $Fo = 1$, the average Nusselt number oscillates around 2.80, which agrees with that in Ref. [92]. The amplitudes and periods of the oscillations turn to be constant (0.01 and 0.092) as the time increasing. The streamlines and temperature fields in one oscillation at different times are presented in Figs. 7-6 and 7-7, respectively. Convection effect is more evident than that in Case 1 due to the higher Rayleigh number. A stronger vortex exists in the cavity and changes with time. It leads to various temperature fields at different times. The streamlines difference is more evident than that in temperature fields. The local Nusselt number in Fig. 7-8 is the mean value in one oscillation. The maximum Nusselt number Nu_{\max} is 4.71 and it occurs at the location of $Y_{Nu_{\max}} = 0.33$.

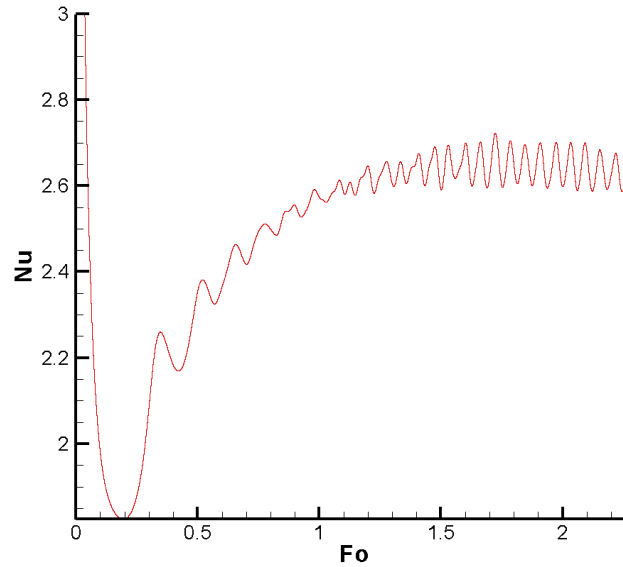


Figure 7-9 Case 3: average Nusselt number

Simulation is now carried out for a lower Prandtl number of 0.005 with $Ra = 5 \times 10^4$. Similar to Case 2, it can still reach oscillatory solution. The variation of average Nusselt number with time is shown in Fig. 7-9. It oscillates around 2.65 after $Fo = 1.5$, and the mean value of the Nusselt number is lower than that of Case 2. In other words, the convection effect weakens as Prandtl number decreases. The amplitude and period of oscillation are 0.05 and 0.093, respectively. Figures 7-10 and 7-11 show streamlines and temperature fields in one oscillation at different times. It is evidence that lower Prandtl number leads to a lower convection effect, longer oscillation period and higher oscillation amplitude.

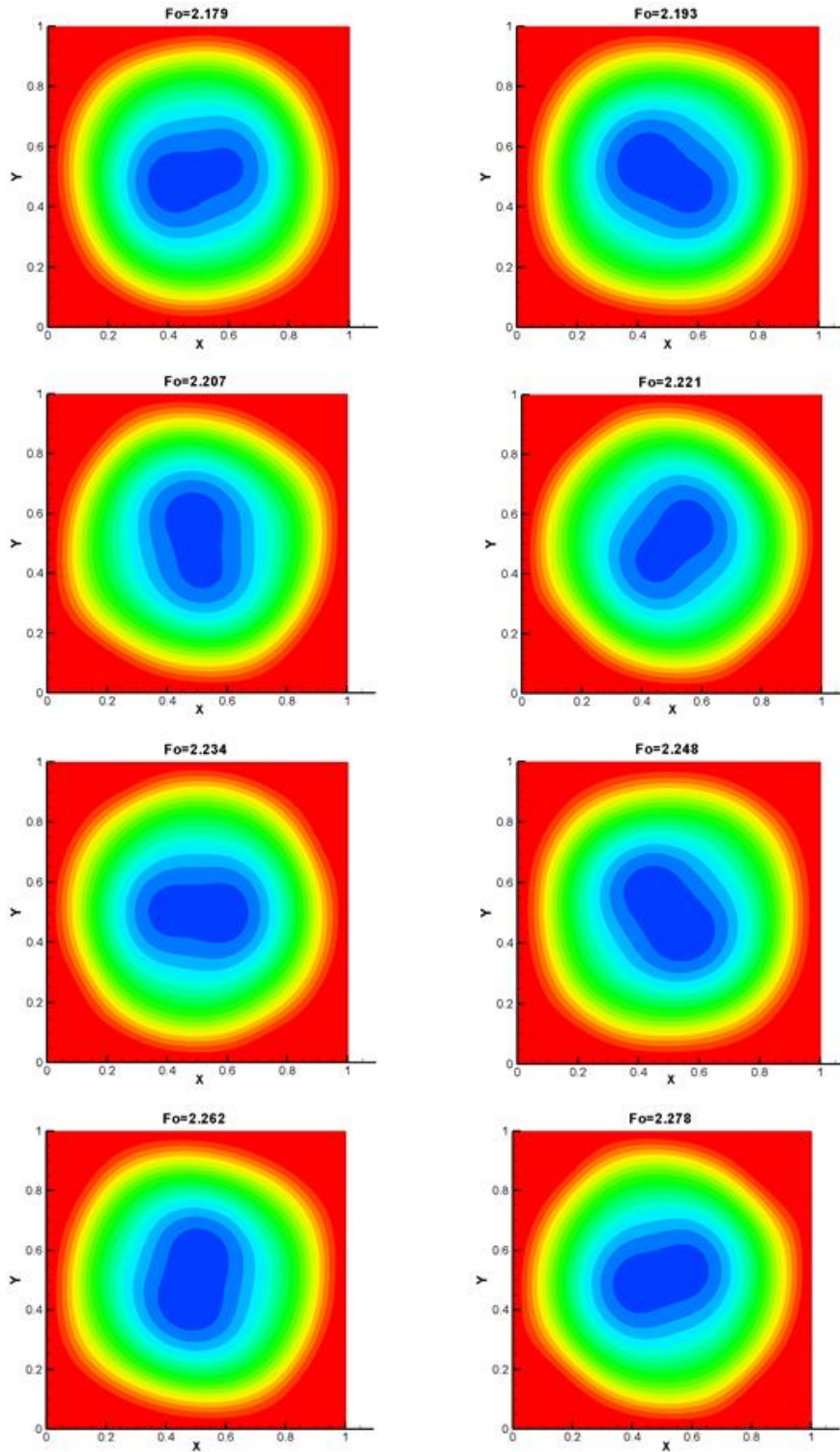


Figure 7-10 Case 3: streamlines

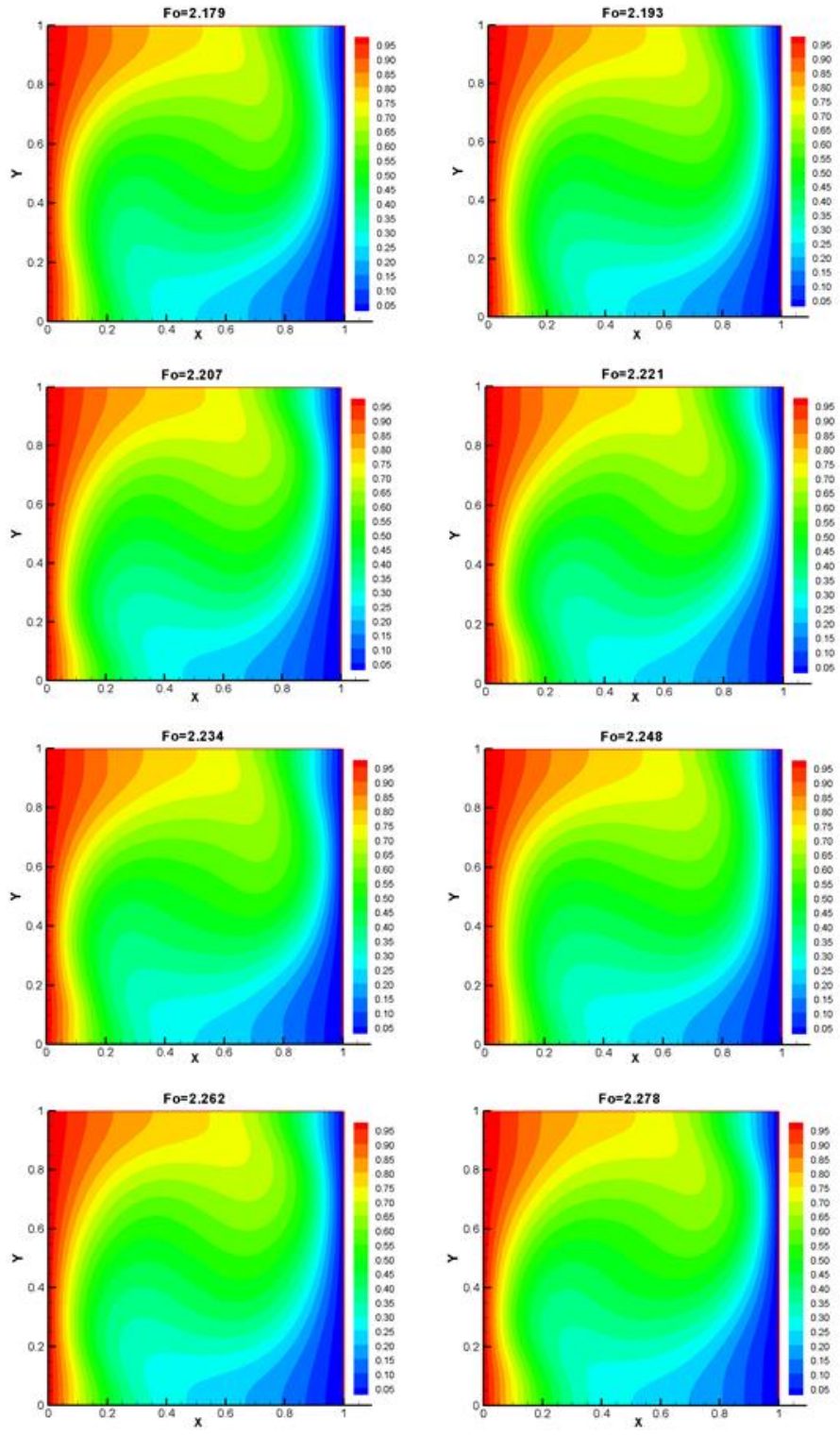


Figure 7-11 Case 3: temperature field

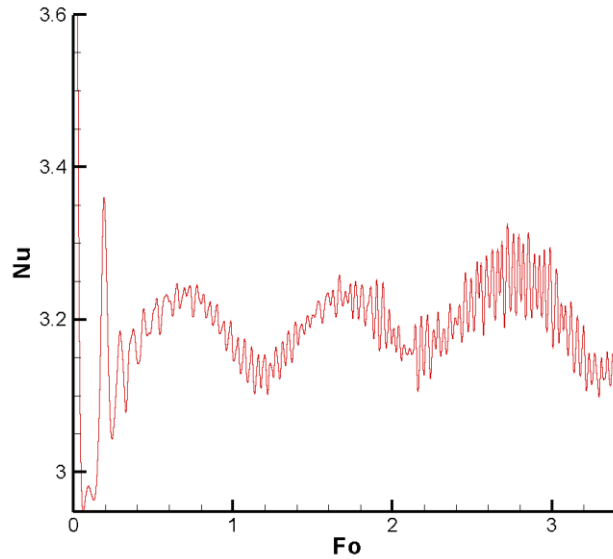


Figure 7-12 Case 4: average Nusselt number

To further study the effects of Rayleigh number on the natural convection, another case is studied for $Ra = 1 \times 10^5$ and $Pr = 0.01$ (Case 4). This case also reaches the oscillatory solution. Instead of oscillating round a constant value as that in Cases 2 or 3, average Nusselt number for Case 4 varies round a wave as shown in Fig. 7-12. The streamlines and temperature fields in one period (0.073) at different times are shown in Figs. 7-13 and 7-14, respectively. Comparing with case 2, the convection effect is more notable because of the higher Rayleigh number. And the oscillation period is also longer than that for Case 2.

These oscillation results in numerical simulations are common and researchers haven't reach agreements on them. Some researchers believe these oscillations are caused by the numerical method while other ones support they are leaded by the problem themselves. I also discussed the sources of these oscillations based on heat pipe [113], which is not included in this diddertation.

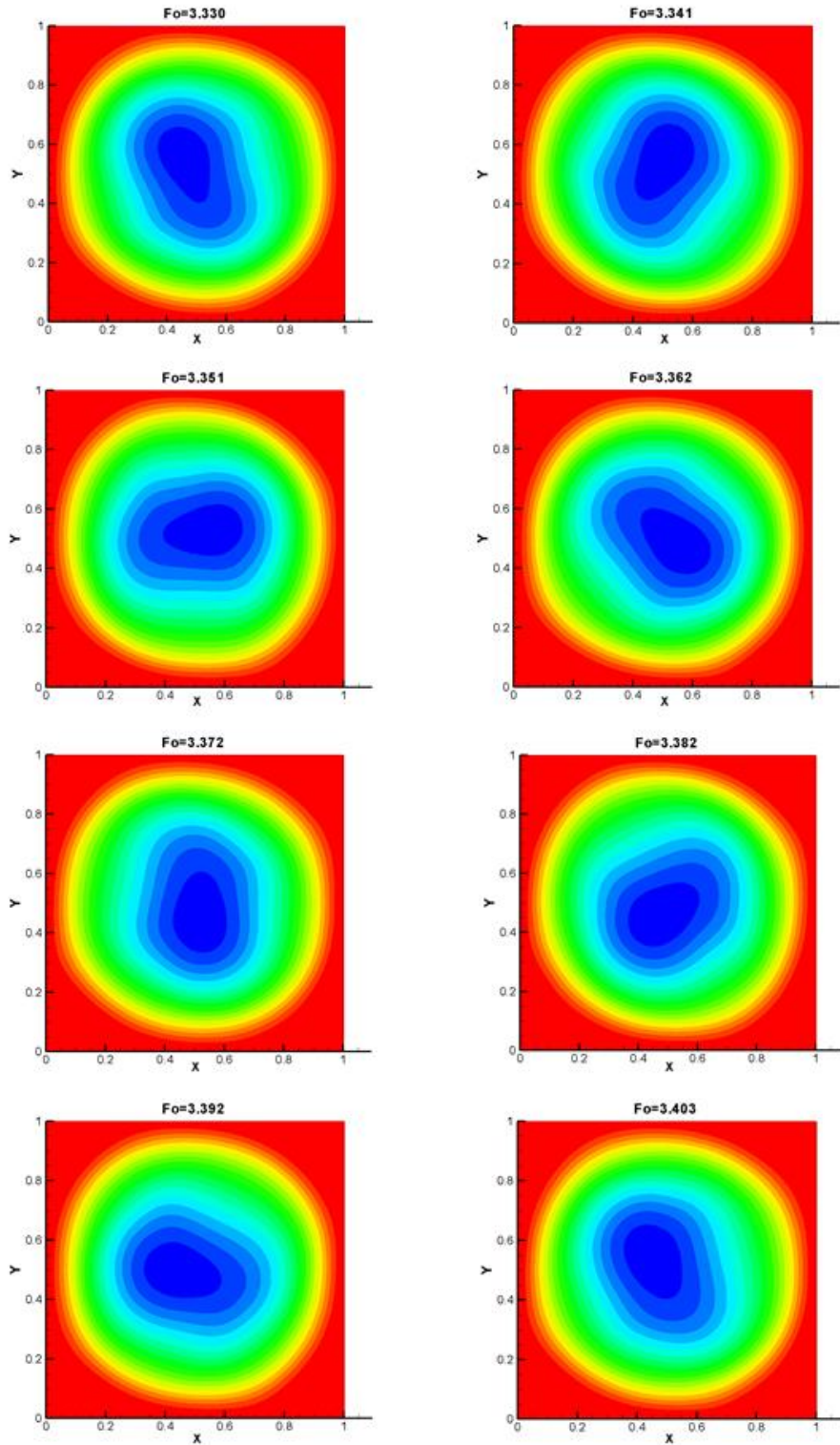


Figure 7-13 Case 4: streamlines

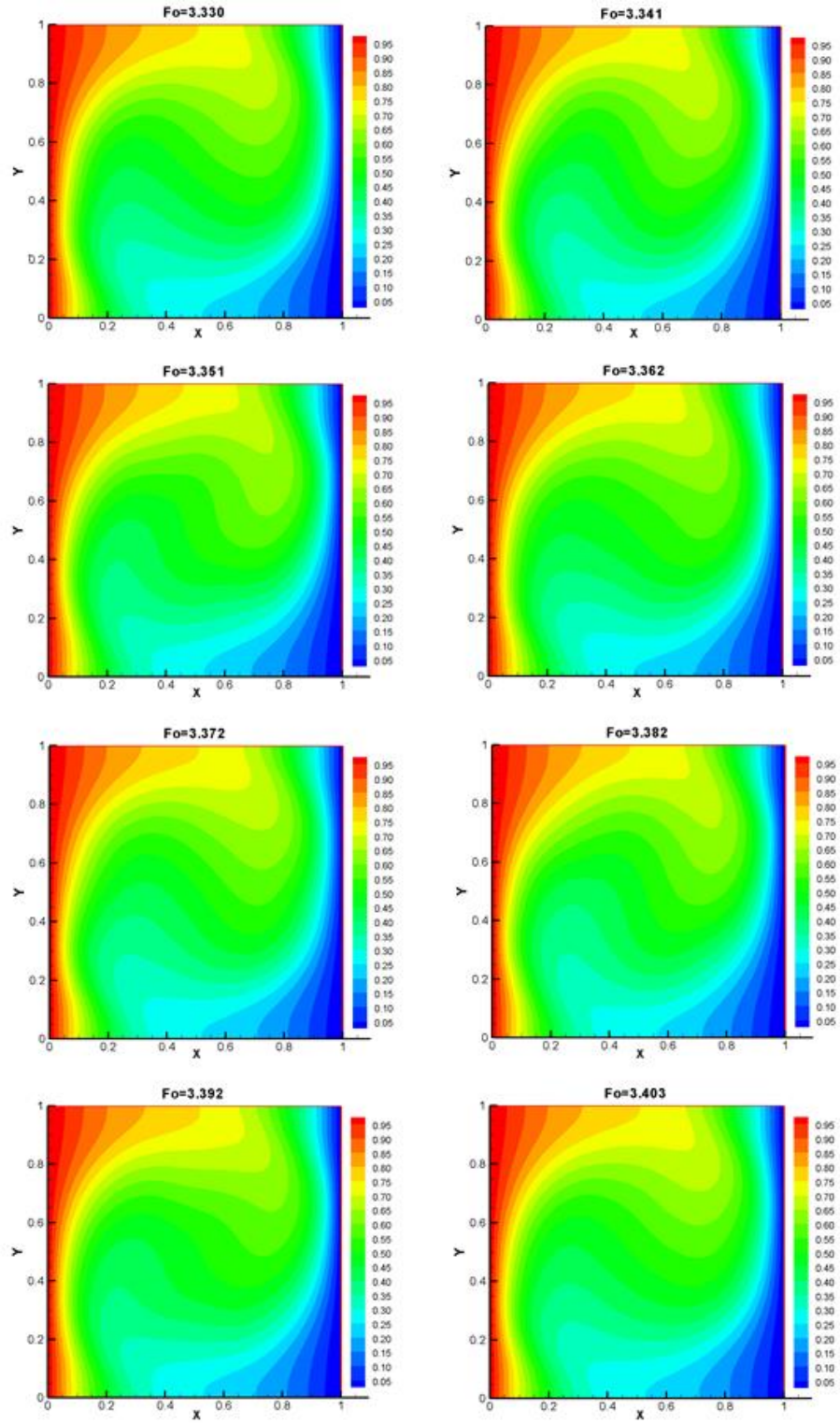


Figure 7-14 Case 4: temperature field

7.4 Conclusions

Double MRT thermal LBM is applied to simulate the natural convection of fluid with low Prandtl number ($10^{-3} - 10^{-2}$). The natural convection can reach to steady state or oscillate, which agree with the reference results well. Therefore, the double MRT thermal LBM is valid for simulation of natural convection of the fluid with low Prandtl numbers. With fixed Rayleigh number, lower Prandtl number leads to a weaker convection effect, longer oscillation period and higher oscillation amplitude for the cases reaching oscillatory solutions. At fixed Prandtl number, higher Rayleigh number leads to a more notable convection effect and longer oscillation period.

Chapter 8 Numerical Simulation of Melting Problems Using Lattice Boltzmann Method with Interfacial Tracking Method

8.1 Introduction

Melting problems appear in different areas such as thermal energy storage, electronics cooling, and food processing. These problems always involve nonlinearities, strong couplings and a moving boundary. As discussed in last chapter, low Prandtl natural convection can reach steady state or oscillation results. Based on these results, low Prandtl number melting problems are solve in this chapter.

The key point for the numerical simulation of a melting problem is the methods to obtain the location of the melting front. In this chapter, pure LBM using interfacial tracking method is developed firstly for simulating transport phenomena during melting process. This method treats melting front as a moving boundary. Velocity and temperature settings are different on that boundary. Both conduction and convection the melting problems are solved for validation.

8.2 Problem Statement

Figure 8-1 shows the physical model of melting process in an enclosure filled with a phase change material (PCM). The left wall is kept at a constant temperature T_h , which is higher than the melting temperature T_m . The right wall is also kept at a constant T_c that is below or equal to T_m . Meanwhile the top and the bottom of the enclosure are adiabatic. No slip conditions are applied to all the boundaries. The initial temperature of the system is at

T_c . The temperature difference in the liquid phase can cause natural convection due to the buoyance effect.

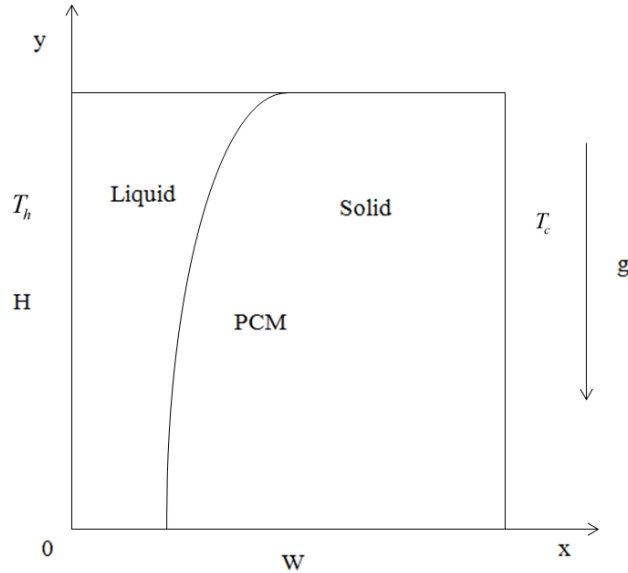


Figure 8-1 Phase change model

The following additional assumptions are made for convection controlled melting problem:

1. The PCM is pure and homogeneous.
2. The volume change due to the phase change is negligible.
3. The liquid phase of the PCM is Newtonian and incompressible
4. Boussinesq approximation is applied to the liquid phase.
5. Natural convection of the liquid phase is laminar.

Then the liquid PCM can be described by the following governing equations:

$$\frac{\partial u}{\partial x} + \frac{\partial v}{\partial y} = 0 \tag{8.1}$$

$$\rho \left(\frac{\partial u}{\partial t} + u \frac{\partial u}{\partial x} + v \frac{\partial u}{\partial y} \right) = -\frac{\partial p}{\partial y} + \mu \left(\frac{\partial^2 u}{\partial x^2} + \frac{\partial^2 u}{\partial y^2} \right) \quad (8.2)$$

$$\rho \left(\frac{\partial v}{\partial t} + u \frac{\partial v}{\partial x} + v \frac{\partial v}{\partial y} \right) = -\frac{\partial p}{\partial x} + \mu \left(\frac{\partial^2 v}{\partial x^2} + \frac{\partial^2 v}{\partial y^2} \right) + \rho g \beta (T - T_m) \quad (8.3)$$

$$(\rho c_p) \left(\frac{\partial T}{\partial t} + u \frac{\partial T}{\partial x} + v \frac{\partial T}{\partial y} \right) = k \left(\frac{\partial^2 T}{\partial x^2} + \frac{\partial^2 T}{\partial y^2} \right) \quad (8.4)$$

Equations (8.1) – (8.4) are subject to the following boundary and initial conditions:

$$x = 0, u = 0, v = 0, T = T_h \quad (8.5)$$

$$x = W, u = 0, v = 0, T = T_c \quad (8.6)$$

$$y = 0, u = 0, v = 0, \partial T / \partial y = 0 \quad (8.7)$$

$$y = H, u = 0, v = 0, \partial T / \partial y = 0 \quad (8.8)$$

Melting front:

$$x = s, T = T_m \quad (8.9)$$

$$x = s, \left[1 + \left(\frac{\partial s}{\partial y} \right)^2 \right] \left(k_s \frac{\partial T_s}{\partial x} - k_l \frac{\partial T_l}{\partial x} \right) = \rho_l h_{sl} \frac{\partial s}{\partial t} \quad (8.10)$$

Initial condition:

$$t = 0, T = T_c \quad (8.11)$$

For a two-dimensional problem, Eq. (8.10) represents the melting front moving velocity in the x direction [74].

Assuming c_s is the speed of sound and defining the following non-dimensional variables

$$\left\{ \begin{array}{l} X = \frac{x}{H}, Y = \frac{y}{H}, u_c = \sqrt{g\beta(T_h - T_m)H}, Ma = \frac{u_c}{c_s}, U = \frac{u}{\sqrt{3}c_s}, \\ V = \frac{v}{\sqrt{3}c_s}, \tau = \frac{t \cdot \sqrt{3}c_s}{H}, \theta = \frac{T - T_m}{T_h - T_m}, P = \frac{p}{3\rho c_s^2}, Pr = \frac{\nu}{\alpha}, \\ Sc = \frac{T_m - T_c}{T_h - T_m}, Ste = \frac{c_{pl}(T_h - T_c)}{h_{sl}}, Ra = \frac{g\beta(T_h - T_m)H^3 Pr}{\nu^2} \end{array} \right. \quad (8.12)$$

Eqs. (8.1) to (8.11) can be rewritten as:

$$\frac{\partial U}{\partial X} + \frac{\partial V}{\partial Y} = 0 \quad (8.13)$$

$$\frac{\partial U}{\partial \tau} + U \frac{\partial U}{\partial X} + V \frac{\partial U}{\partial Y} = -\frac{\partial P}{\partial X} + Ma \sqrt{\frac{Pr}{3Ra}} \left(\frac{\partial^2 U}{\partial X^2} + \frac{\partial^2 U}{\partial Y^2} \right) \quad (8.14)$$

$$\frac{\partial V}{\partial \tau} + U \frac{\partial V}{\partial X} + V \frac{\partial V}{\partial Y} = -\frac{\partial P}{\partial Y} + Ma \sqrt{\frac{Pr}{3Ra}} \left(\frac{\partial^2 V}{\partial X^2} + \frac{\partial^2 V}{\partial Y^2} \right) + \frac{Ma^2 \theta}{3} \quad (8.15)$$

$$\frac{\partial \theta}{\partial \tau} + U \frac{\partial \theta}{\partial X} + V \frac{\partial \theta}{\partial Y} = Ma \sqrt{\frac{1}{3Ra \cdot Pr}} \left(\frac{\partial^2 \theta}{\partial X^2} + \frac{\partial^2 \theta}{\partial Y^2} \right) \quad (8.16)$$

$$X = S, \theta = 0 \quad (8.17)$$

$$X = S, \frac{Ma \cdot Ste}{\sqrt{3Ra Pr}} \left[1 + \left(\frac{\partial S}{\partial Y} \right)^2 \right] \left[\frac{k_s}{k_l} \frac{\partial \theta_s}{\partial X} - \frac{\partial \theta_l}{\partial X} \right] = \frac{\partial S}{\partial \tau} \quad (8.18)$$

$$X = 0, U = 0, V = 0, \theta = 1 \quad (8.19)$$

$$X = W/H, U = 0, V = 0, \theta = -Sc \quad (8.20)$$

$$Y = 0, U = 0, V = 0, \partial\theta / \partial Y = 0 \quad (8.21)$$

$$Y = 1, U = 0, U = 0, \partial\theta / \partial Y = 0 \quad (8.22)$$

Initial condition:

$$\tau = 0, \theta = -Sc \quad (8.23)$$

8.3 LBM with Interfacial Tracking Method

Lattice Boltzmann method has been used to solve different fluid flow and heat transfer problems, including melting process. Miller et al. [88] proposed a LBM model for anisotropic liquid-solid phase transition. Eshraghi and Felicelli [89] solved a conduction with phase change problem using an implicit LBM model. Chakraborty and Chatterjee [114] and Huber et al. [17] solved natural convection governed melting problems with hybrid LBM-FDM and pure LBM respectively. Double distributions model in LBM is employed in this chapter and it has been included in chapters above. The key point is the way to handle the moving melting front and interfacial tracking method is used to fulfill it.

8.3.1 Interfacial Tracking Method

The melting front location is obtained by the interfacial tracking method. The melting front location in the fixed grid X_n satisfies the following equation.

$$-\frac{\Delta X}{2} \leq S - X_n < \frac{\Delta X}{2} \quad (8.24)$$

where S is the melting front location, and X_{n-1} is the location of the computing nodes beside the melting front (in the liquid side) shown in Fig. 8-2.

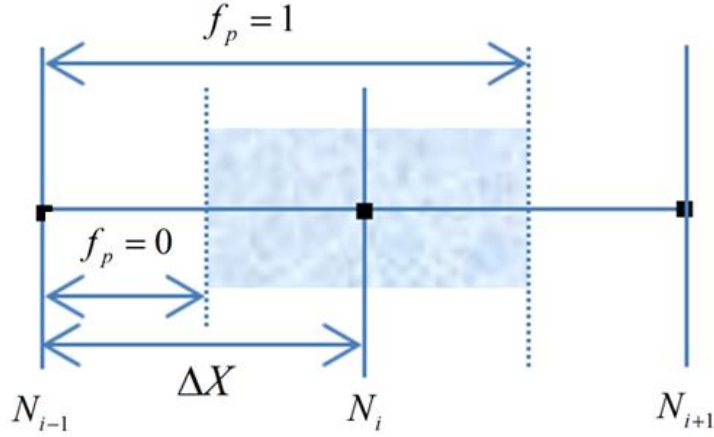


Figure 8-2 Melting front

Then the liquid fraction f_p in the control volume is related to the location of the solid-liquid interface by:

$$f_p = \frac{S - X_{n-1} - 0.5 \times \Delta X}{\Delta X} \quad (8.25)$$

where $0 \leq f_p < 1$. The following equation expresses the melting front moving velocity at Y_m when the temperature field is known:

$$\frac{\partial S}{\partial \tau} = \frac{Ma \cdot Ste}{\sqrt{3RaPr}} \left[1 + \left(\frac{S_{Y_m} - S_{Y_{m-1}}}{\Delta Y} \right)^2 \right] \left[\frac{k_s}{k_l} \frac{\theta_{X_{n+1}} - \theta_m}{\Delta X \cdot (1.5 - f_p)} - \frac{\theta_m - \theta_{X_{n-1}}}{\Delta X \cdot (0.5 + f_p)} \right] \quad (8.26)$$

With these settings, interfacial tracking model can be used in simulating the melting process. Then the interface location can be obtained by:

$$S = S^0 + \frac{\partial S}{\partial \tau} \Delta \tau \quad (8.27)$$

where S^0 is the interface location in the last time step and $\Delta\tau$ is the time step. Once f_p is no less than 1, the melting front moves to the next grid. Fixed LBM lattice grids are employed in the solving process.

8.3.2 Boundary condition

No slip boundary condition is applied to the fixed boundaries and melting front. The macroscopic variables on them are known from the problem statement. Fixed grid is employed in the model, therefore X_n in Fig. 4 is the right moving boundary in LBM. Its velocity U_{X_n} and temperature θ_{X_n} can be obtained by the following steps.

The velocity and temperature on the melting front are:

$$U_m = 0, \quad \theta_m = 0 \quad (8.28)$$

Then the velocity at X_n is

$$U_{X_n} = \frac{f_p - 0.5}{f_p + 0.5} U_{X_{n-1}} \quad (8.29)$$

Similar to the velocity field, the temperature at X_n is also not zero.

$$\theta_{X_n} = \frac{f_p - 0.5}{f_p + 0.5} \theta_{X_{n-1}} \quad (8.30)$$

If Eq. (8.30) is applied to the solving process, there might be negative value for θ_{X_n} regarding the f_p value. The force in Eq. (2.18) changes direction when θ_{X_n} turns to negative value from the positive value. This leads to the divergence after testing. Then we assume the moving boundary X_n temperature is θ_m for the whole solving process. This

setting does not have effect on the melting front moving velocity $\partial S / \partial \tau$ directly regarding Eq. (8.26). But it may lead to a higher $\theta_{x_{n-1}}$ when f_p is lower than 0.5. Then it will predict a higher melting front moving velocity $\partial S / \partial \tau$. Similarly, the case that f_p is higher than 0.5 has a lower $\partial S / \partial \tau$. These two errors tend to cancel each other since the possibilities for f_p is higher or lower than the 0.5 are the same. Though there is still error due to this assumption, the test case results indicate that error is acceptable. Then the velocity and temperature on three fixed boundaries and moving melting front are known. It is necessary to pay attention to the computing nodes which newly change from solid to liquid. The ways to obtain their velocity and temperature have been described above. Their densities are set as the initial density in LBM.

Nonequilibrium extrapolation scheme [16] is applied to both velocity and temperature fields in the solving process. Assuming x_b is the boundary node and x_f is its nearby inner mode, the density and energy distribution at the boundaries are:

$$f_i(x_b, t) = f_i^{eq}(x_b, t) + f_i(x_f, t) - f_i^{eq}(x_f, t), \quad i = 1, 2, \dots, 9 \quad (8.31)$$

$$g_i(x_b, t) = g_i^{eq}(x_b, t) + g_i(x_f, t) - g_i^{eq}(x_f, t), \quad i = 1, 2, \dots, 5 \quad (8.32)$$

8.4 Results and discussions

The conduction and convection melting problems are solved by LBM with interfacial tracking method to investigate its applicability and accuracy. The results are compared with analytical results for the conduction melting problem and convection melting results in Ref. [73] for validation of the model.

8.4.1 Conduction Controlled Melting

For the case that natural convection is negligible, the melting front moves at a same velocity at any height. Then this problem can be simplified to a 1-D problem governed by conduction. There is an analytical solution for this problem when Sc is equal to 0 [74]. The following non-dimensional variables are applied to the governing Eqs. (8.1-8.11).

$$\begin{cases} X = \frac{x}{W}, S = \frac{s}{W}, Fo = \frac{\alpha t}{W^2} \\ \theta = \frac{T - T_m}{T_h - T_m}, Ste = \frac{c_p(T_h - T_m)}{h_{sl}} \end{cases} \quad (8.33)$$

The melting front location can be obtained from:

$$S = 2\lambda\sqrt{Fo} \quad (8.34)$$

where λ is a function of the Stefan number and can be obtained from.

$$\lambda e^{\lambda^2} \operatorname{erf}(\lambda) = \frac{Ste}{\sqrt{\pi}} \quad (8.35)$$

The temperature distribution in the liquid PCM is.

$$\theta(X, Fo) = 1 - \frac{\operatorname{erf}(X / 2Fo^{1/2})}{\operatorname{erf}(\lambda)} \quad (8.36)$$

The cases for Stefan number equals 0.1, 0.5 and 1 are solved for validation. The corresponding λ obtained from Eq. (8.35) are equal 0.220, 0.465, and 0.620, respectively. The melting front moves at the uniform velocity (not a function of Y) and the non-dimensional computational domain is 1 in the conduction controlled melting. Meanwhile, the temperature distribution in the computational domain can be obtained in Eq. (8.36). For

the numerical solution, only energy equation in LBM is solved for the conduction controlled melting problem and 80×10 grids are employed.

Figure 8-3 shows comparison of melting fronts obtained from analytical solution and the LBM. The melting front moves faster with increasing Stefan number. The LBM results agreed with the results from the analytical solutions very well.

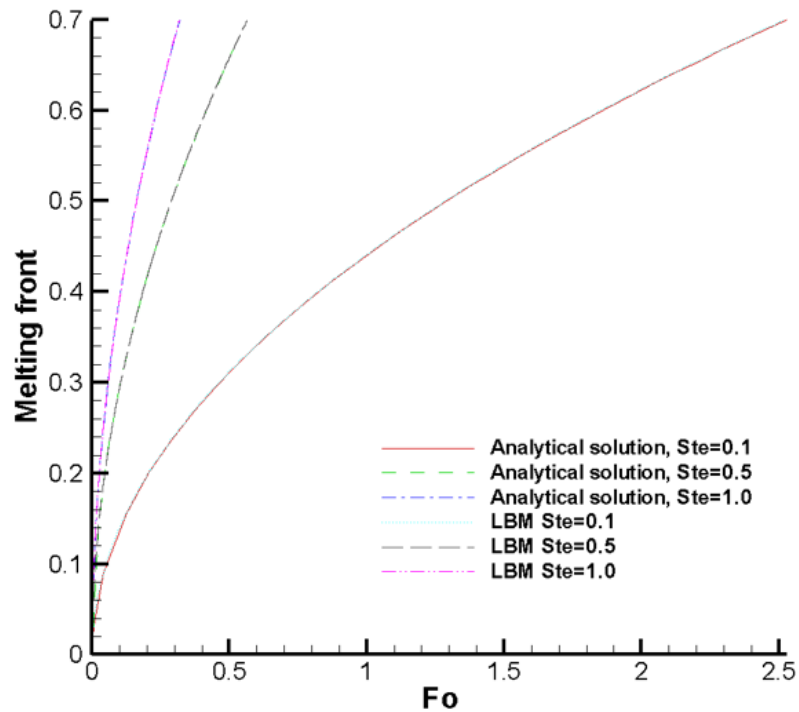


Figure 8-3 Liquid fraction comparison in conduction melting

Figure 8-4 shows the comparison of the temperature distributions for the three cases when Fo equals 0.3. As discussed above, the case with higher Stefan number has shorter time to reach the same interfacial location. The temperature distribution is closer to a straight line with lower Stefan number. And it is difficult to distinguish the LBM results from the analytical result for all three cases in Fig. 8-4.

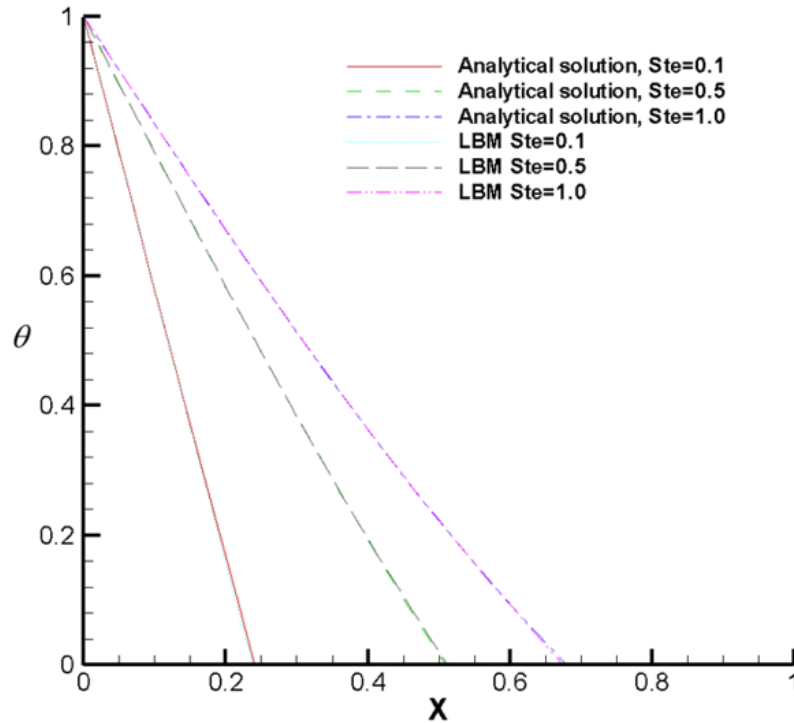


Figure 8-4 Temperature comparison in conduction melting

Three conduction melting problem results agree with the analytical results well. The LBM with interfacial tracking method is reliable for the conduction controlled melting problem.

8.4.2 Convection Controlled Melting

The convection controlled melting problem can be described by Eqs. (8.13) to (8.23). No subcooling is considered and the height of the enclosure equals to its width. Two melting cases are solved by the LBM with interfacial tracking method. The temperature field, melting front location and liquid fraction are discussed in two cases to verify the proposed numerical method. The Rayleigh number, Prandtl number and Stefan number are 2.5×10^4 , 0.02, and 0.01, respectively in case 1 while these parameters in case 2 are 2.5×10^5 , 0.02, and 0.01, respectively. After grid number testing, 200×200 grids are chosen for these two cases.

Bertrand et al. compared results obtained from different numerical methods for the convection controlled melting problem. The Fourier number Fo was used in Ref. [73] and it is related to the non-dimensional time τ in LBM by:

$$Fo = \tau \cdot Ma / \sqrt{3Ra \cdot Pr} \quad (8.37)$$

These results of these two cases are recorded for Fo equaling 4 and 10 in Ref. [73]. The corresponding τ are 1549 and 3872 for Case 1 and they are 4900 and 12250 for Case 2.

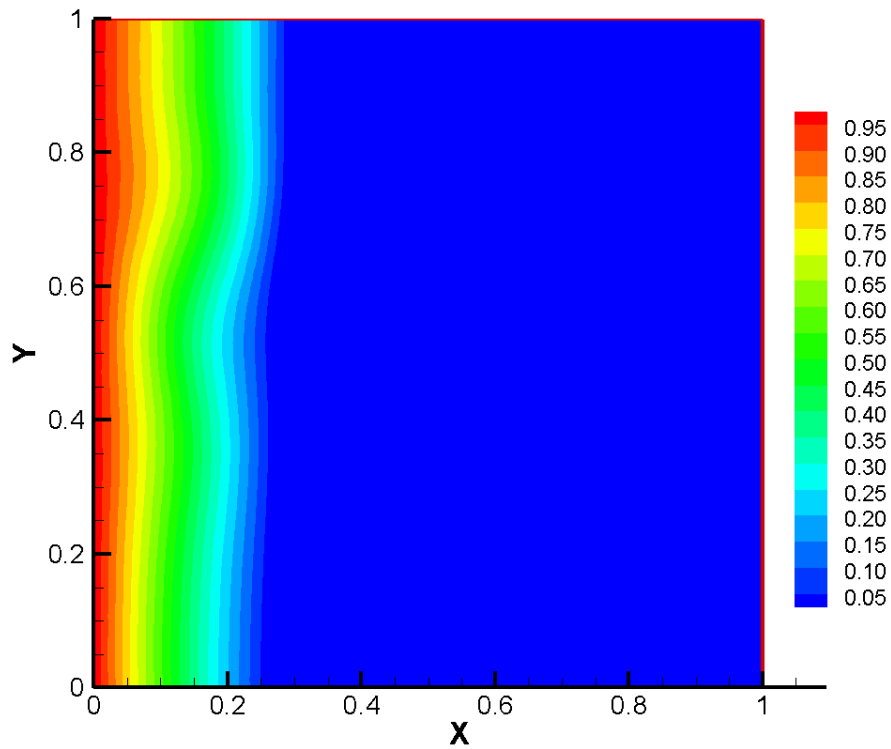


Figure 8-5 Case 1: temperature field ($Fo = 4$)

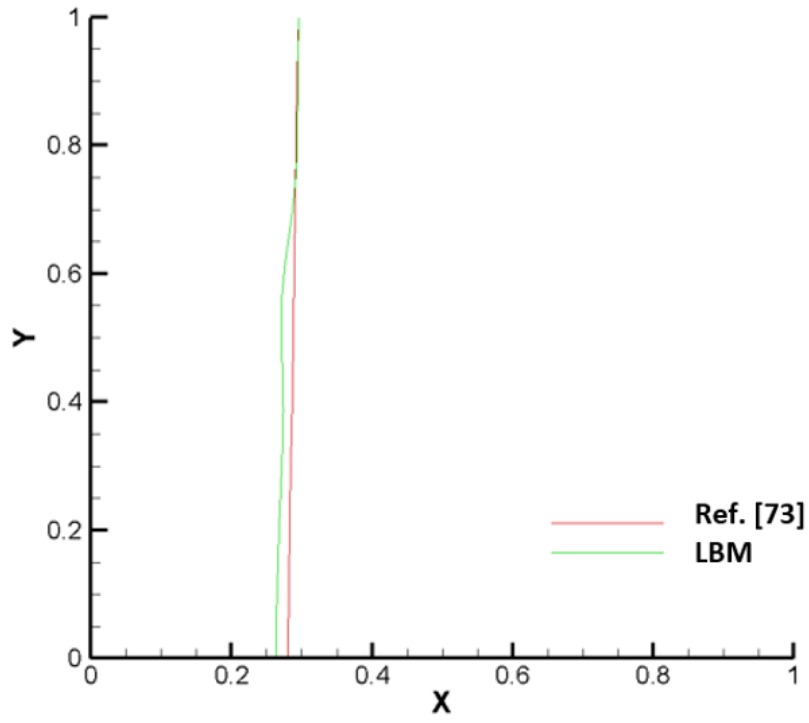


Figure 8-6 Case 1: melting front comparison ($Fo = 4$)

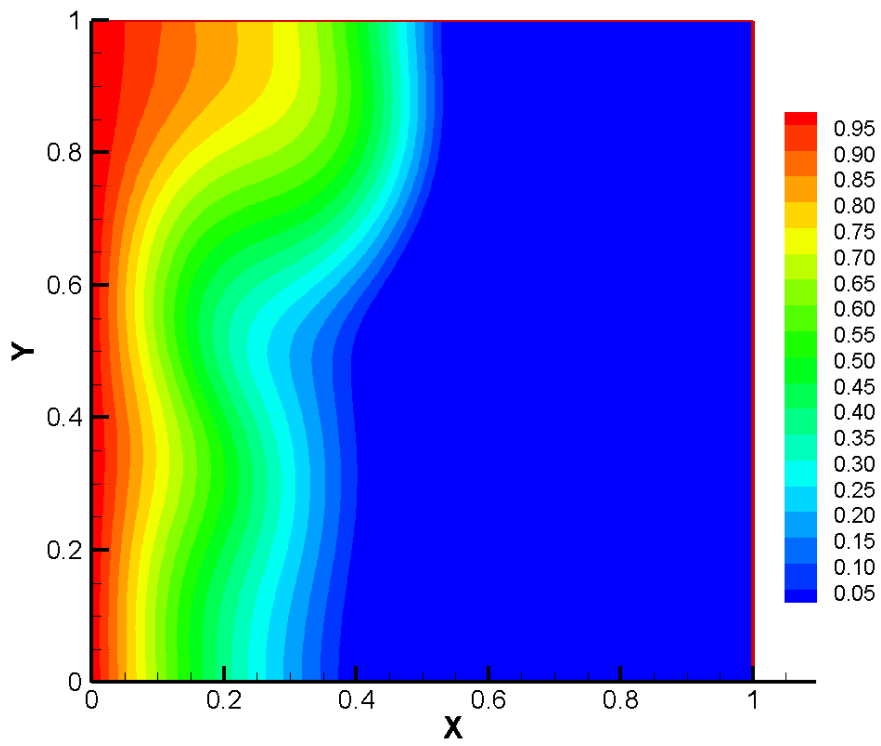


Figure 8-7 Case 1: temperature field ($Fo = 10$)

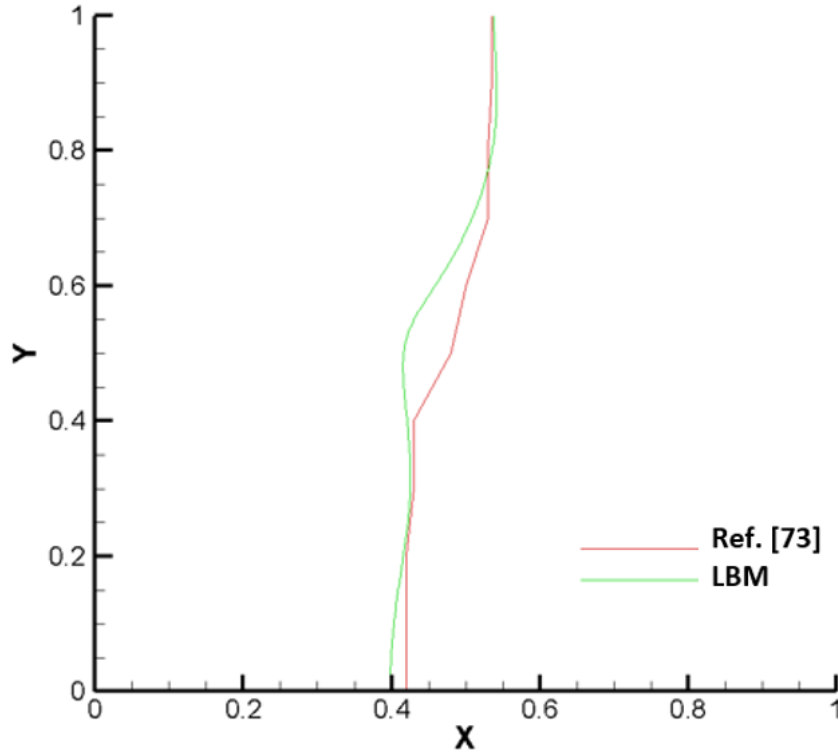
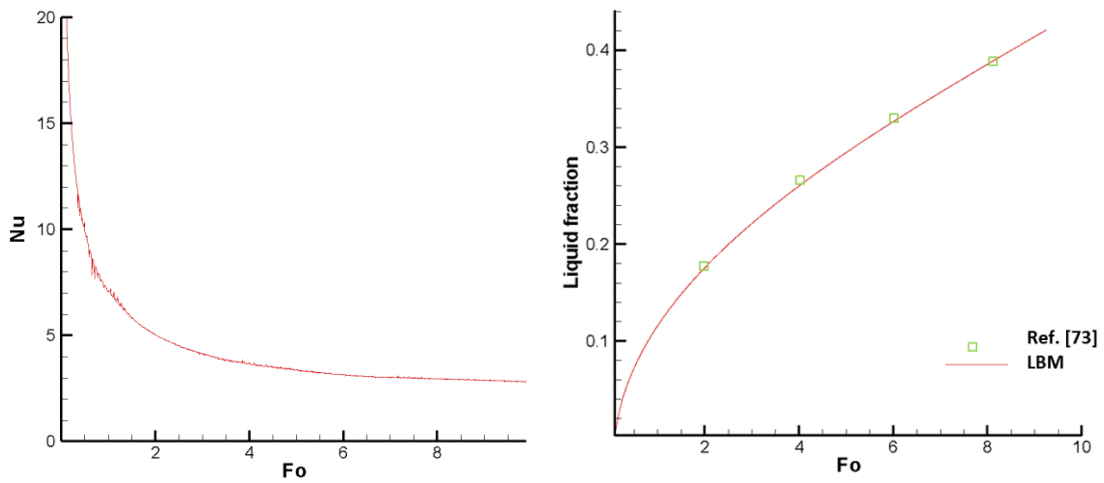


Figure 8-8 Case 1: melting front comparison ($Fo = 10$)



(a) Nusselt number

(b) liquid fractions

Figure 8-9 Case 1: Nusselt number and liquid fractions

Figure 8-5 shows the temperature field for Case 1 for $Fo = 4$. All the isotherms are all close to straight line normal to the bottom. The region with θ higher than 0 is the liquid PCM region. The temperature is linear to X in the liquid PCM region basically. It shows

the melting process is still governed by conduction at $Fo = 4$. Figure 8-6 compares the numerical melting front with that in Ref. [73]. They are both nearly constant to Y and agree with each other well. It also supports the melting process is still governed by conduction. The temperature field for Fo equaling 10 is shown in Fig. 8-7. The temperature in the liquid PCM zone increases with increasing Y . It indicates convection has dominated the melting process. Figure 8-8 shows the comparison of the melting fronts obtained from the numerical method and those from the reference. The LBM melting front moves faster in the higher location due to convection effect. And these two results agree with each other well. The liquid fraction is the percentage of liquid PCM in the total PCM and it indicates the melting ratio. The Nusselt number Nu that represents the heat transfer rate from the heated wall to the liquid PCM.

Average Nusselt number changing with time is shown in Fig. 8-9 (a). It turns to be a constant when Fo is greater than 4. This indicates the heat transfer rate through the left heat wall reaches a fixed value. Figure 8-9 (b) shows comparison of the liquid fraction obtained from different methods. The liquid fraction is linear to Fo when Fo is greater than 4. It means the melting reaches to the quasi-steady state. And the numerical and reference results agree with each other very well.

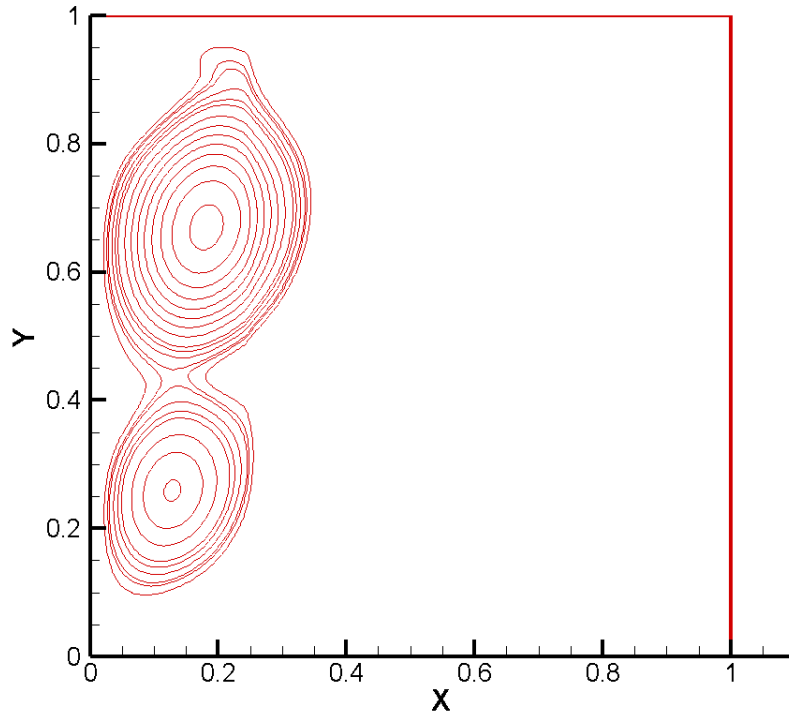


Figure 8-10 Case 2: streamlines ($Fo = 4$)

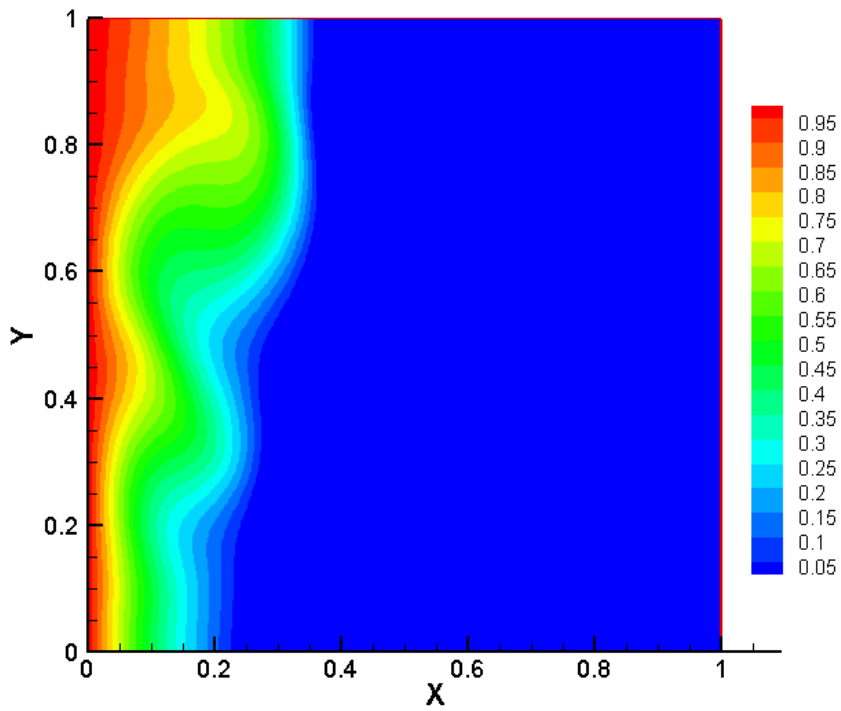


Figure 8-11 Case 2: temperature field ($Fo = 4$)

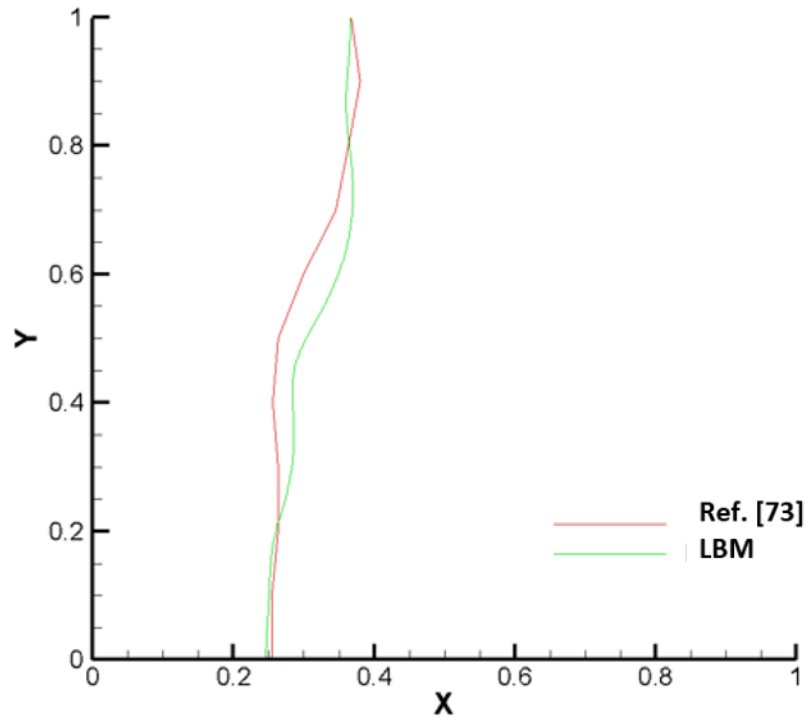


Figure 8-12 Case 2: melting front comparison ($Fo = 4$)

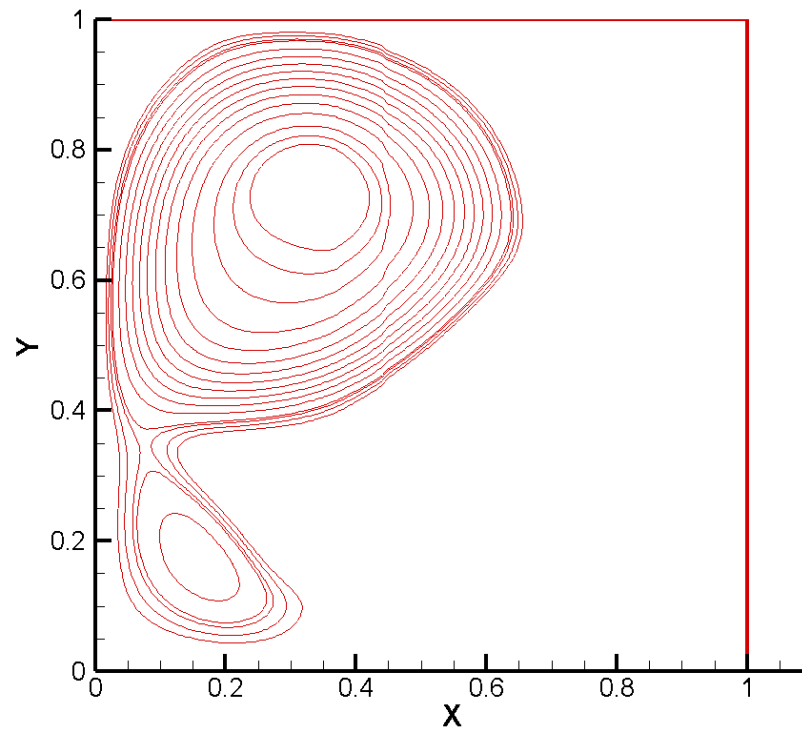


Figure 8-13 Case 2: streamlines ($Fo = 10$)

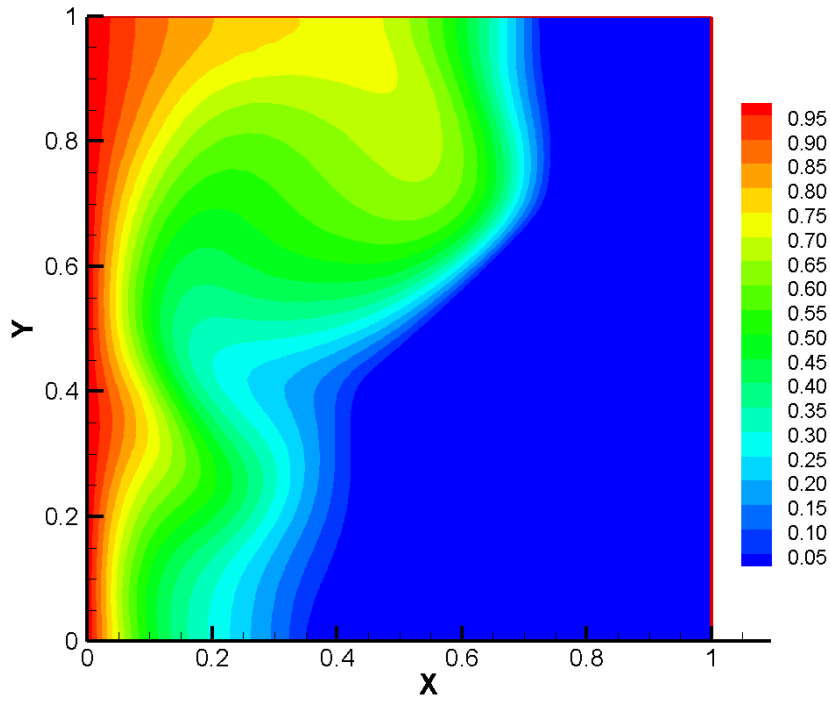


Figure 8-14 Case 2 temperature field ($Fo = 10$)

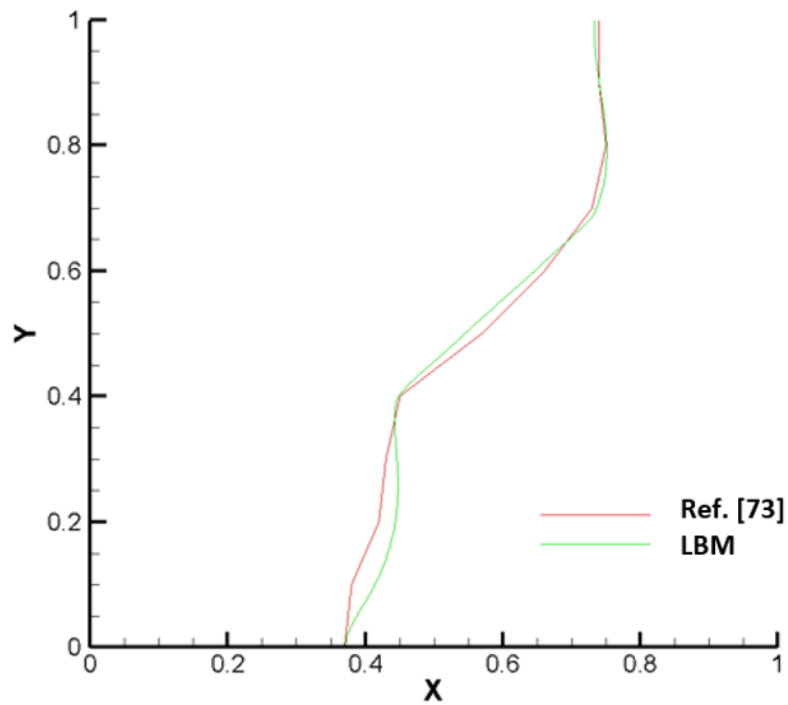


Figure 8-15 Case 2: melting front comparison ($Fo = 10$)

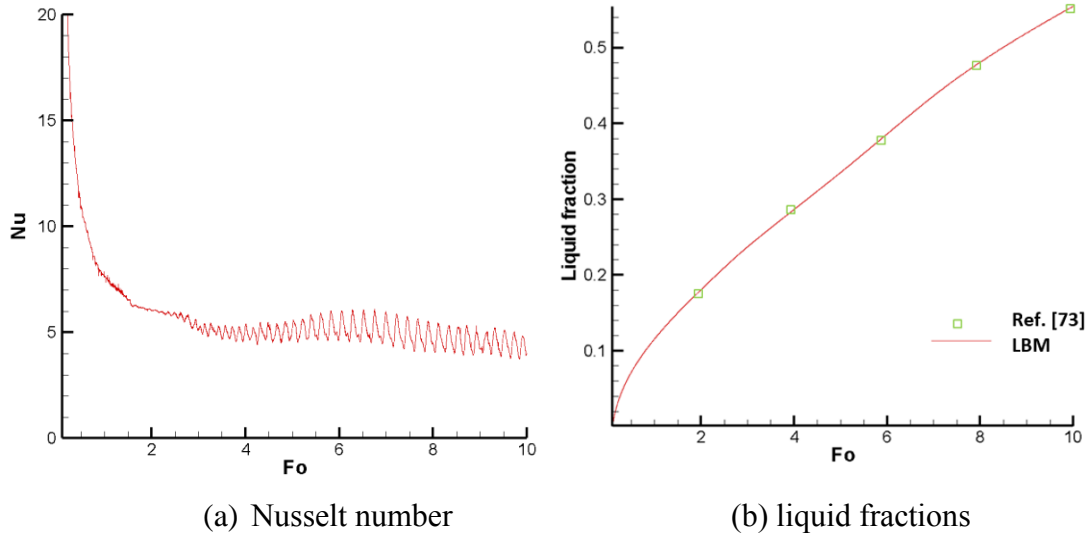


Figure 8-16 Case 2: Nusselt number and liquid fractions

The melting front location and liquid fraction for Case 2 were also reported for Case 2. Meanwhile, Hannoun et al. discussed the fluid field bifurcation for the same case [59]. It was reported that two vortexes are in the liquid PCM region when Fo is greater than 2.8 in case 2. Figure 8-10 shows the streamlines for Case 2 for $Fo = 4$. There are two vortexes in the liquid PCM zone which agree the results in Ref. [93] well. On the other hand, Fig. 8-11 shows the temperature field for the same Fo . There are two curves on most isotherms, led by the velocity results. The LBM melting front agrees with the Ref. [73] very well as shown in Fig. 8-12. Basically the melting front moves faster as the height increasing even there are two vortexes in the liquid PCM zone. When Fo increases to 10, the streamlines and temperature field are shown in Fig. 8-13 and Fig. 8-14, respectively. Two vortexes still appear in the liquid PCM zone and the upper one is much stronger than the other one. The LBM melting front agrees with that in Ref. [73] as shown in Fig. 6-15 for $Fo = 10$. Ref. [92] reported the average Nusselt oscillation phenomena in low Prandtl natural convection problem. They reported that the left heat boundary average Nusselt number reached a

constant number for the case $Ra = 1 \times 10^4$, $Pr = 0.01$ while it oscillated round a fixed number for the case $Ra = 5 \times 10^4$, $Pr = 0.01$. It is reasonable to believe when Ra equals to 1×10^5 , the average Nusselt number would also oscillate because the higher Ra gives a nonlinear effect to the governing equations. Figure 8-16 (a) shows the variation of the Case 2 average Nusselt number with time. After $Fo=4$, the average Nusselt number oscillates around 5. For the Figure 8-16 (b) shows the variation of the liquid fraction for the entire enclosure with time. The liquid fraction result tendency is not linear to the Fo at the very beginning (conduction controlled stage). It then turns to be linear to the time when Fo is above 2. It means that the melting process reaches quasi-steady state. And it has a good agreement with the reference result.

These two case convection results agree with the reference well. The LBM with interfacial tracking method is reliable for the convection controlled melting problem.

8.5 Conclusions

LBM with interfacial tracking method is applied to simulate the melting problem. Both conduction and convection controlled melting problems are solved for validation. The numerical results agreed with the analytical results for conduction controlled melting. For convection controlled melting, the agreement between the results from the present method agreed with that in the reference very well. Therefore the proposed numerical method is valid for the melting problem simulation.

Chapter 9 Numerical Solution of Melting in a Discretely Heated Enclosure using an Interfacial Tracking Method

9.1 Introduction

In last chapter, low Prandtl melting problem has been discussed using LBM with interfacial tracking method. On the other hand, high Prandtl number melting problem is very important, such as electronic cooling. Effective cooling is very critical for the reliable operation of the electronic components and devices. Natural [115, 116] and forced [117, 118] convection with air, forced convection with water [119, 120] and many other methods can be applied to tackle this problem. While all these methods have their own merits, melting of phase change material (PCM) is distinguished from others for the huge endothermic capability in the melting process [121, 122]. Electronic cooling using PCM can be modeled as melting in a discretely heated enclosure.

In this chapter, melting in a discretely heated enclosure from the side wall will be solved using the interfacial tracking method, and the numerical results will be validated with the experiment results. Effect of Stefan number and geometry of the heaters on the melting process will also be investigated.

9.2 Problem statement

Figure 9-1 shows an enclosure with heaters flush-mounted to the left wall made of Plexiglas and filled with phase change material (PCM). The heaters located in the red part are made of constantan wires while the covers colored yellow are made of coppers. These heaters provide heat at constant rate while the four boundaries are all adiabatic. The top of PCM is free surface while no slip conditions are applied to all other boundaries.

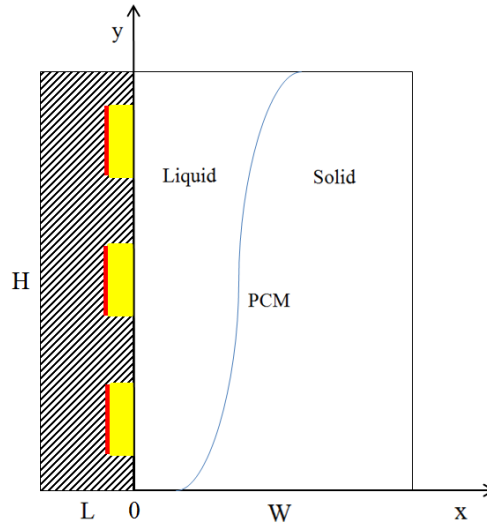


Figure 9-1 Physic model

The following assumptions are made:

1. The PCM is pure and homogeneous.
2. The liquid phase of the PCM is Newtonian and incompressible.
3. Boussinesq approximation is applied to the liquid phase.
4. The volume change due to the phase change is negligible.
5. Natural convection of the liquid phase is laminar.

This problem can be described by the following equations:

Continuity equation:

$$\frac{\partial u}{\partial x} + \frac{\partial v}{\partial y} = 0 \quad (9.1)$$

Momentum equations:

$$\rho \left[\frac{\partial u}{\partial t} + u \frac{\partial u}{\partial x} + v \frac{\partial u}{\partial y} \right] = - \frac{\partial p}{\partial x} + \mu \left(\frac{\partial^2 u}{\partial x^2} + \frac{\partial^2 u}{\partial y^2} \right) \quad (9.2)$$

$$\rho \left[\frac{\partial v}{\partial t} + u \frac{\partial v}{\partial x} + v \frac{\partial v}{\partial y} \right] = -\frac{\partial p}{\partial y} + \mu \left(\frac{\partial^2 v}{\partial x^2} + \frac{\partial^2 v}{\partial y^2} \right) + \rho g \beta (T - T_m) \quad (9.3)$$

Energy equation:

$$(\rho c_p) \left[\frac{\partial T}{\partial t} + u \frac{\partial T}{\partial x} + v \frac{\partial T}{\partial y} \right] = k \left(\frac{\partial^2 T}{\partial x^2} + \frac{\partial^2 T}{\partial y^2} \right) + q''' \quad (9.4)$$

where q''' is the internal heat generation which only exists in the regions of heaters.

Equations (9.1) – (9.4) are subject to the following boundary and initial conditions:

$$x = -L, u = 0, v = 0, \partial T / \partial x = 0 \quad (9.5)$$

$$x = W, u = 0, v = 0, \partial T / \partial x = 0 \quad (9.6)$$

$$y = 0, u = 0, v = 0, \partial T / \partial y = 0 \quad (9.7)$$

$$y = H, \partial u / \partial y = 0, v = 0, \partial T / \partial y = 0 \quad (9.8)$$

Melting front:

$$x = s, T = T_m \quad (9.9)$$

$$x = s, \left[1 + \left(\frac{\partial s}{\partial y} \right)^2 \right] \left[k_s \frac{\partial T_s}{\partial x} - k_l \frac{\partial T_l}{\partial x} \right] = \rho_l h_{sl} \frac{\partial s}{\partial t} \quad (9.10)$$

Initial condition:

$$t = 0, T = T_i \quad (9.11)$$

Assuming Q is the rate of total heat generation provided by the heaters and defining the following non-dimensional variables:

$$\left. \begin{aligned} X = \frac{x}{H}, Y = \frac{y}{H}, S = \frac{y}{H}, u_c = \frac{\mu_l}{\rho H}, \tau = \frac{u_c t}{H}, P = \frac{p + \rho_0 g y}{\rho u_c^2} \\ U = \frac{u}{u_c}, \theta = \frac{k_l (T - T_m)}{Q}, Ste = \frac{c_{pl} (Q / k_l)}{h_{sl}}, Sc = \frac{c_{pl} (T_m - T_i)}{h_{sl}} \end{aligned} \right\} \quad (9.12)$$

Equations (9.1) – (9.4) become:

$$\frac{\partial U}{\partial X} + \frac{\partial V}{\partial Y} = 0 \quad (9.13)$$

$$\frac{\partial U}{\partial F} + U \frac{\partial U}{\partial X} + V \frac{\partial U}{\partial Y} = -\frac{\partial P}{\partial X} + \frac{\partial^2 U}{\partial X^2} + \frac{\partial^2 U}{\partial Y^2} \quad (9.14)$$

$$\frac{\partial V}{\partial F} + U \frac{\partial V}{\partial X} + V \frac{\partial V}{\partial Y} = -\frac{\partial P}{\partial Y} + \frac{\partial^2 V}{\partial X^2} + \frac{\partial^2 V}{\partial Y^2} + \frac{Ra}{Pr} \theta \quad (9.15)$$

$$\frac{\partial \theta}{\partial F} + U \frac{\partial \theta}{\partial X} + V \frac{\partial \theta}{\partial Y} = A \frac{1}{Pr} \left(\frac{\partial^2 \theta}{\partial X^2} + \frac{\partial^2 \theta}{\partial Y^2} \right) + Q''' \quad (9.16)$$

where A is non-dimensional parameter depending on different materials, and Q''' is the non-dimensional internal heat generation. The Rayleigh number is defined as:

$$Ra = \frac{g \beta H^3 Pr Q}{\nu^2 k_l} \quad (9.17)$$

Boundary conditions:

$$X = -A_1, U = 0, V = 0, \partial \theta / \partial X = 0 \quad (9.18)$$

$$X = A_0, U = 0, V = 0, \partial \theta / \partial X = 0 \quad (9.19)$$

where A_0 and A_1 are the aspect ratios of the enclosure and the left wall that are equal to W/H and L/H , respectively.

$$Y = 0, U = 0, V = 0, \partial \theta / \partial Y = 0 \quad (9.20)$$

$$Y = 1, \partial U / \partial Y = 0, V = 0, \partial \theta / \partial Y = 0 \quad (9.21)$$

$$X = S, \theta = 0 \quad (9.22)$$

$$X = S, \frac{Ste}{Pr} \left[1 + \left(\frac{\partial S}{\partial Y} \right)^2 \right] \left[\frac{k_s}{k_l} \frac{\partial T_s}{\partial x} - \frac{\partial T_l}{\partial x} \right] = \frac{\partial S}{\partial \tau} \quad (9.23)$$

Initial condition:

$$\tau = 0, \theta = \theta_i \quad (9.24)$$

where θ_i is the dimensionless initial temperature which equals to $k_l (T_i - T_m) / Q$.

9.3 Numerical method

The SIMPLE algorithm is used to solve the fluid flow and heat transfer in the liquid zone while interfacial tracking method is applied to solve solid-liquid interface. For this 2-D melting problem, the location of melting front in the control volume where melting takes place changes every time step.

Figure 9-2 shows three possible locations of the melting front in the control volume. Assuming the size of the control volume in the x - direction is $(\Delta x)_p$, the liquid fraction,

f_p , can be obtained by:

$$f_p = \frac{S - x_p - (\Delta x)_p / 2}{(\Delta x)_p} \quad (9.25)$$

where x_p is the center of the control volume in the x -direction.

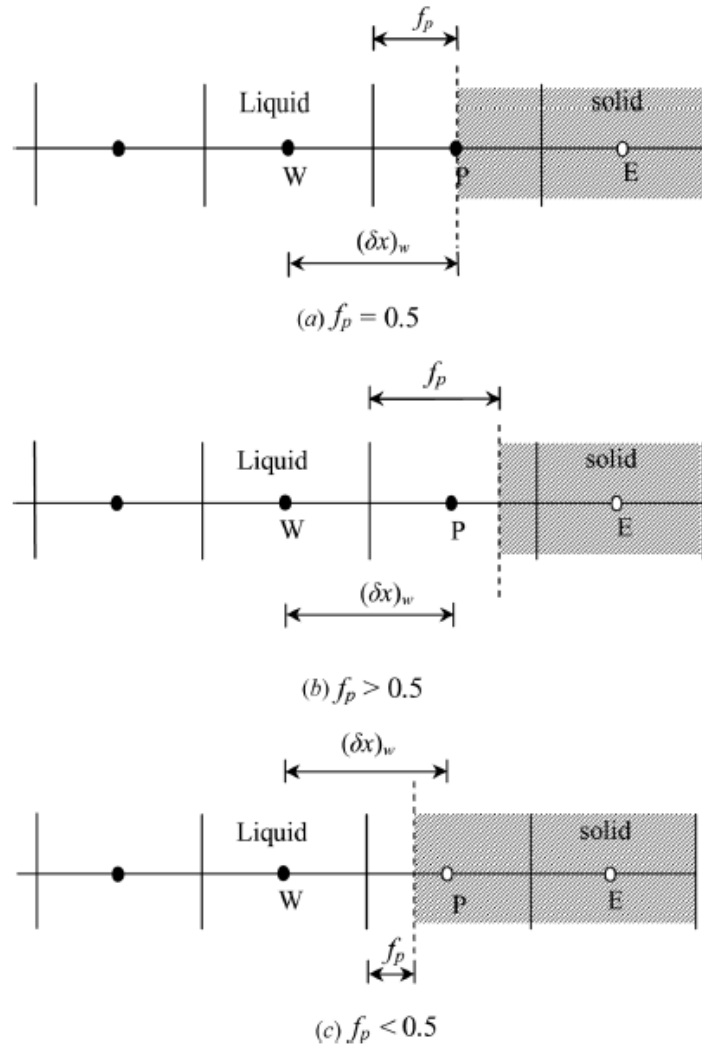


Figure 9-2 Location of the liquid-solid interface

The temperature at the center of the control volume P in which melting takes place is assumed to be at the melting temperature. This assumption will cause an error when the melting front is not at P as shown in Figs. 9-2 (b) and (c). Since this mainly affects the energy balance, a correction to the conductivity can be applied to fix this error. Interfacial tracking method uses the following corrections to \bar{k}_e and \bar{k}_w in the melting control volume:

$$\bar{k}_e = \frac{(\delta X)_e}{(\delta X)_e + (0.5 - f_p)(\Delta x)_P} k_e \quad (9.26)$$

$$\bar{k}_w = \frac{(\delta X)_w}{(\delta X)_w - (0.5 - f_p)(\Delta x)_p} k_w \quad (9.27)$$

Apply Eqs. (9.26) and (9.27) to Eq. (9.24), one obtains:

$$U_s = \frac{Ste}{Pr} \left[1 + \left(\frac{\partial S}{\partial Y} \right)^2 \right] \left[\frac{k_s}{k_l} \frac{(\theta_w - \theta_p)}{(\delta X)_w - (0.5 - f_p)(\Delta x)_p} - \frac{(\theta_p - \theta_e)}{(\delta X)_e + (0.5 - f_p)(\Delta x)_p} \right] \quad (9.28)$$

Then the interface location can be obtained by:

$$S = S^0 + U_s \Delta \tau \quad (9.29)$$

where $\Delta \tau$ is the non-dimension time step.

9.4 Results and discussions

The interfacial tracking method is validated by comparing its results with the experimental results in Ref. [68]. In the experimental system, a 60mm×90mm enclosure is filled with n-octadecane with the initial temperature at melting point. Three discrete heaters are flush mounted to the left wall that is made of Plexiglas with a thickness of 20 mm. The heaters are made of constantan wires covered with 4 mm thick copper blocks. The height and thickness of the heater are 15 and 5 mm, respectively. Meanwhile, the locations of the center of the heaters are $H/6$, $H/2$ and $5H/6$ at the left wall. These heaters can provide different amount of constant heating rates to the system.

Table 9-1 Thermophysical properties

	Thermal conductivity (W/m·K)	Specific heat (J/kg·K)	Density (kg/m ³)
n-octadecane (liquid)	0.152	2180	774
n-octadecane (solid)	0.358	2150	814
copper	401	390	8960
plexiglas	0.193	1445	1188

The melting point of the n-octadecane is 300.7 K and its latent heat is 244 kJ/kg. The viscosity is 0.0039 Ns/m² and the thermal expansion coefficient is 0.00085 K⁻¹. The Prandtl number of the liquid PCM is 55.93. The other thermophysical properties of the PCM, copper and Plexiglas are tabulated in Table 9-1.

The results of numerical solution for Stefan number equals 1.96 and 2.36 are compared with the experimental results in Ref. [68]. The corresponding total heating rates for these two cases are 32.9 and 39.6 W/m, respectively. The Rayleigh numbers for these two cases are equal 2.9346×10^9 and 3.5335×10^9 as obtained from Eq. (9.17). In order to compare with the experimental result, the non-dimensional temperature and time are converted back to dimensional ones using Eq. (9.12).

For the case that Stefan number Ste is equal to 2.36, the melting process is initiated separately near the three copper blocks. After around thirty minutes, the separated regions merge to one liquid region. Then natural convection has a more pronounced effect on the melting process after three regions are merged. Figure 9-3 shows the temperature fields at different times. The copper blocks are the hottest part which distinguishes the heating region and the melt region in the computational domain. Meanwhile, the coldest region is where the solid n-octadecane is located. Generally, the higher the location is in the liquid region, the higher the temperature is due to natural convection. Consequently, the upper part of the PCM melts faster than the lower part; this trend grows as the time growing. Meanwhile, the temperature of the free surface on the top of the PCM decreases with the growing of the distance to the heaters. As the surface tension decreases with increasing temperature, the liquid near the interface with lower surface tension will be pulled to the higher surface tension zone due to Marangoni effect [74]. This effect provides an additional

driven force to accelerate the melt process on the top. Then the melting front has a stepwise shape due to the natural convection and Marangoni effect.

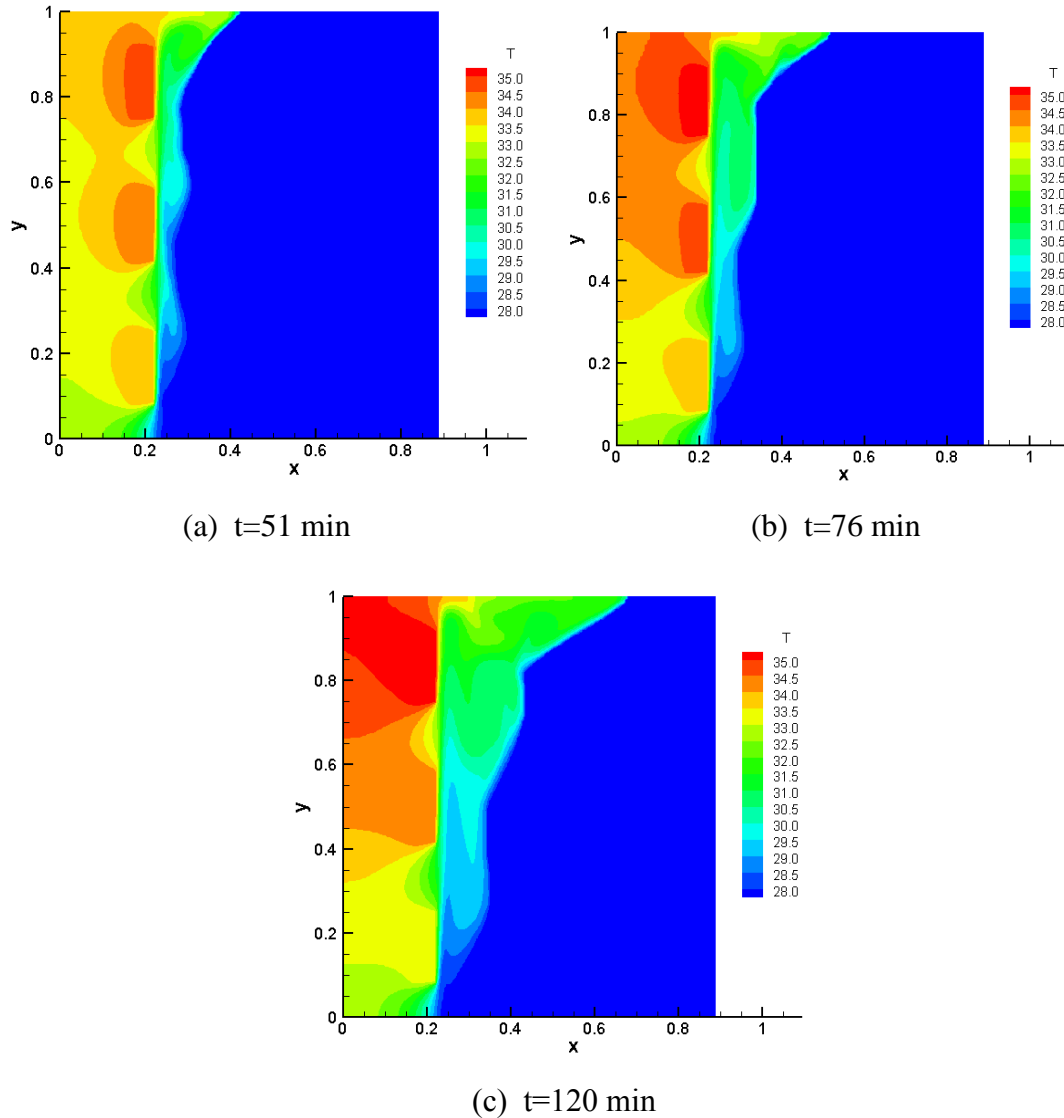


Figure 9-3 Temperature field $Ste=2.36$

Figure 9-4 shows the comparison of the melting fronts obtained from numerical solution and experiment. It can be seen that the numerical results agreed with the experiment result well. Several facts may cause the slight differences between the numerical and experimental results. For example, the density change of n-octadecane from

solid to liquid is not considered in the numerical solution. In addition, to keep the heating rate constant in the experiment is also very challenging.

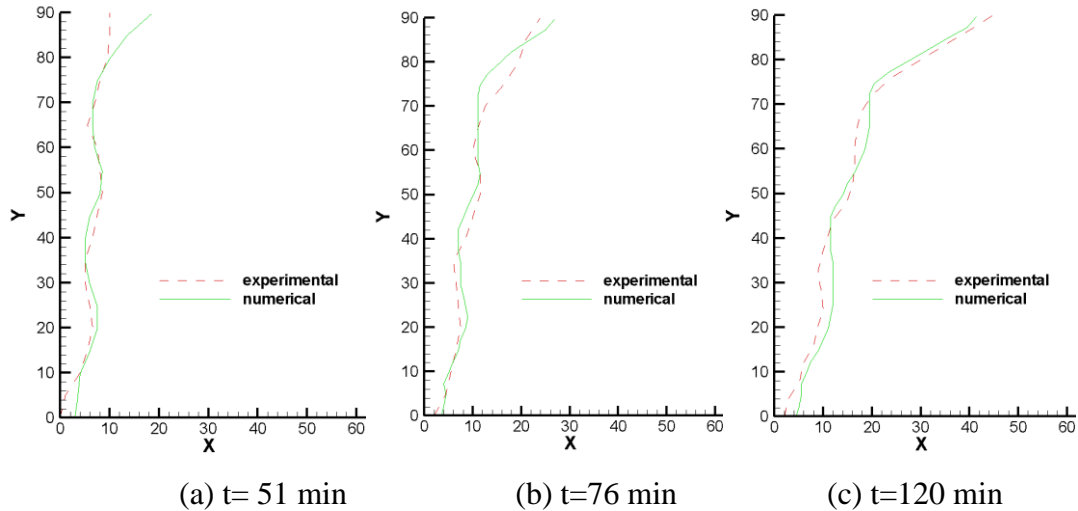


Figure 9-4 Melting front comparison $Ste=2.36$

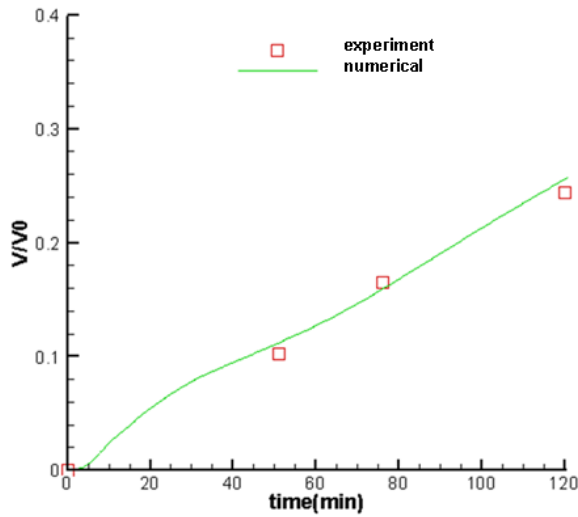


Figure 9-5 Comparison of melting volume fraction $Ste=2.36$

The melting volume fraction is the ratio obtained by the volume of liquid phase divided by the total volume of the PCM. Figure 9-5 shows the comparison of the melting volume fraction between numerical and experimental results. It can be seen that the numerical results are almost linear function of time because the constant heating rate is mainly used

to melt the n-octadecane. The melting volume fraction obtained from numerical solution agreed with that from the experiment very well.

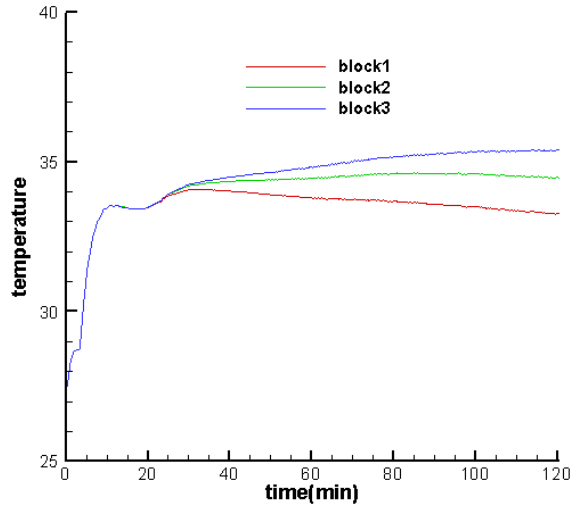


Figure 9-6 Temperature on the heat blocks changing with time $Ste=2.36$

The three copper heat blocks are block 1, block 2 and block 3 from bottom to up in the system. In the experiment, it is observed that after 50 minutes, the surface temperatures of the three heat blocks are almost constant with the change of time while temperature on the block 3 is highest and temperature on block 1 is the lowest. Figure 9-6 shows the temperature history on the heating blocks. In the beginning, the temperatures on the three blocks are identical and increase quickly together. During this stage the conduction in the liquid regions plays the dominate role in the process. At the time that the temperature slightly drops, the natural convection become more and more dominate in the heat transfer process. This trend is consistent with the experimental work reported by Zhang and Bejan [67]. As the time further increases, the surface temperatures on the three heat blocks slightly change and block 3 is hottest and block 1 is coldest. Meanwhile the temperature on the block 2 is $35^{\circ}C$ which is close to the experiment results. This result predict the

quasi-steady phenomenon very well which means the all the energy put in the system is used for the melting process.

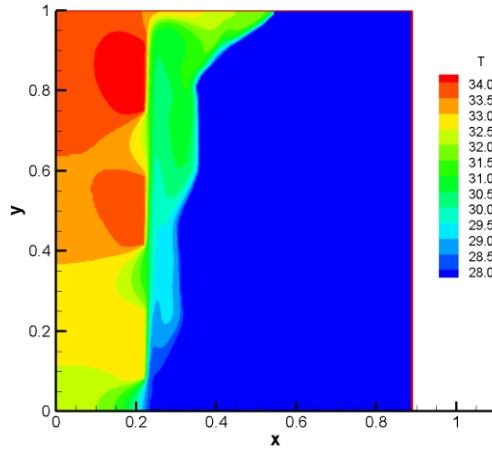


Figure 9-7 Temperature field $t=92$ min, $Ste=1.96$

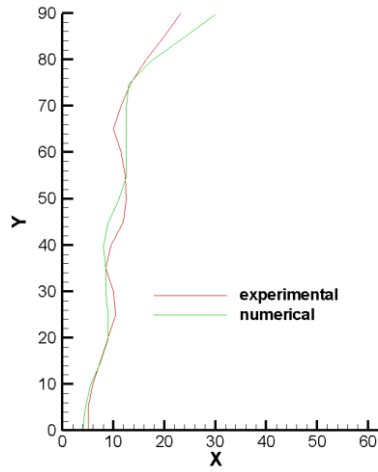


Figure 9-8 Melting volume fraction comparison $t=92$ min, $Ste=1.96$

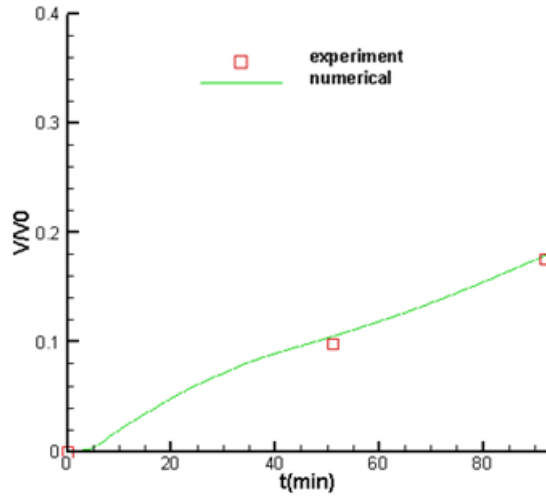


Figure 9-9 Melting front comparison $t=92$ min, $Ste=1.96$

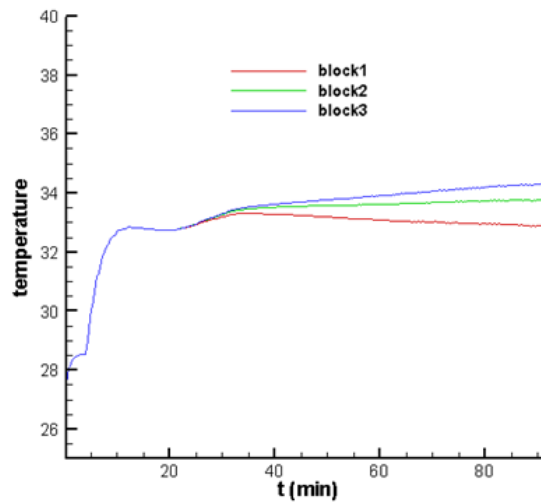


Figure 9-10 Temperature on the heat blocks changing with time $t=92$ min, $Ste=1.96$

Figures 9-7 to 9-10 show temperature field, melting front, melting volume fraction and temperature on the heat blocks for $Ste = 1.96$. The temperature field also showed that the results are governed by the natural convection. The numerical results agreed with experimental results very well in Fig. 9-8 and 9-9. The numerical solution also can also predict temperatures on the heat blocks correctly (see Fig. 9-10).

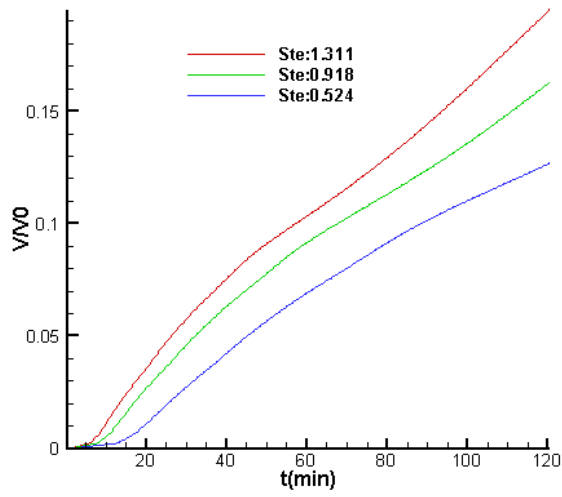


Figure 9-11 Melting volume fraction comparison with different Ste

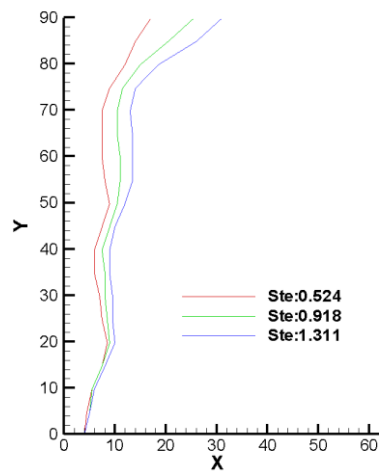
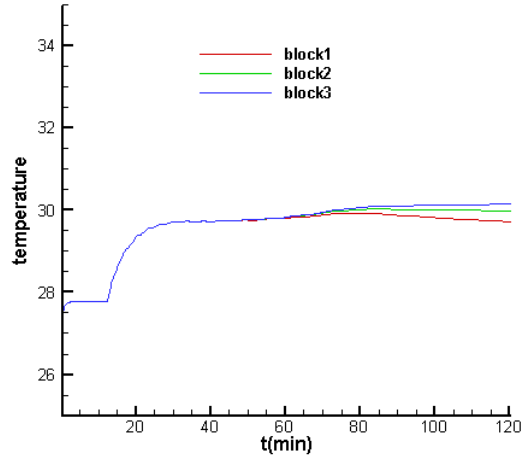
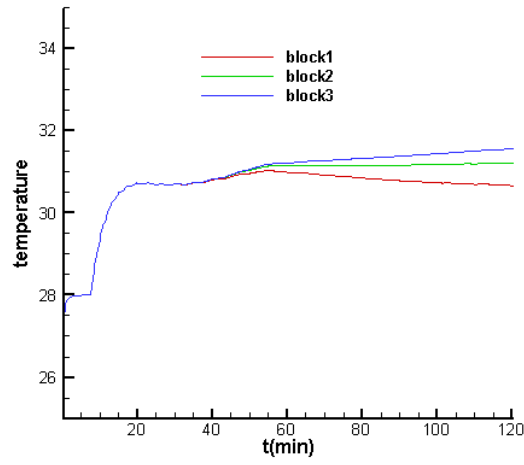


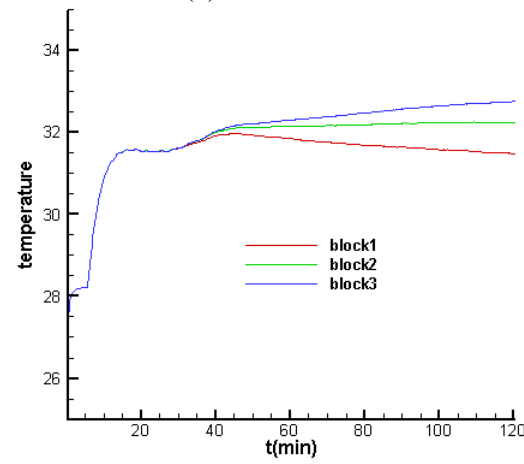
Figure 9-12 Melting front comparison with different Ste



(a) $Ste=0.524$



(b) $Ste=0.918$



(c) $Ste=1.311$

Figure 9-13 Temperature on the heat blocks changing with time

Numerical solutions are then carried out for the heating rates of 22.0, 15.4 and 8.8 W/m, respectively. The corresponding Stefan numbers are 1.311, 0.918 and 0.524, respectively; the Rayleigh numbers are 1.96×10^9 , 1.37×10^9 and 7.85×10^8 , respectively. Figure 9-11 shows the melting volume fraction at different Stefan numbers. The melting volume fraction still appears to be nearly linear functions of the time. The higher the Stefan number is, the larger the slope is. But this slope change is not linear to the Stefan number because part of the heat is transferred to the other components in the system. This part of the energy plays more important role for higher Stefan number. Figure 9-12 shows the melting fronts at different Stefan number when time is equal to 120 minutes. The melting front appears to have similar shapes for different Stefan number. It can also be seen that natural convection has a pronounced effect on all these three cases and the one with higher Stefan number is steeper than that with lower Stefan number. This indicates that natural convection plays a more important role with increasing Stefan number.

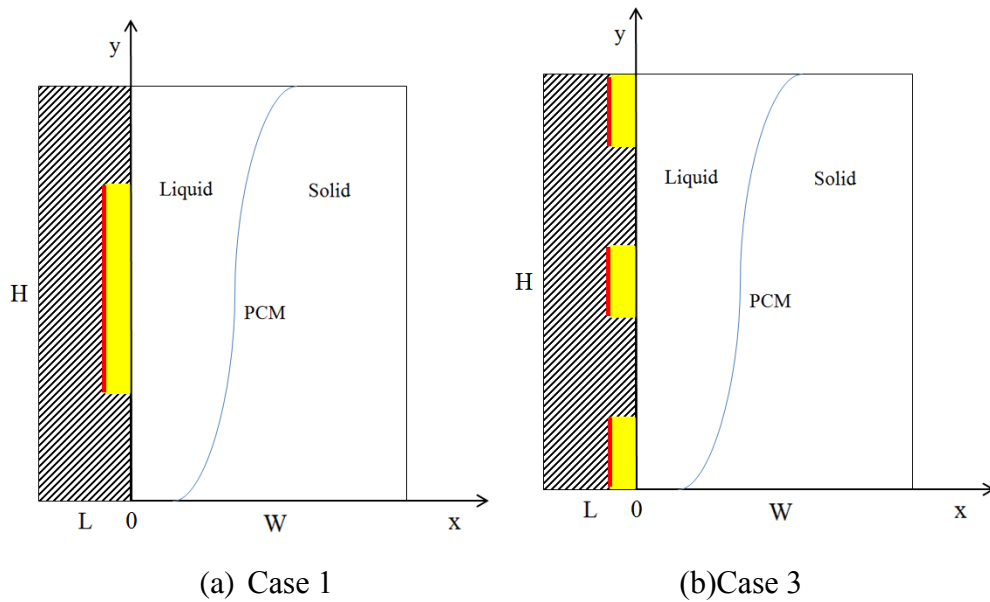


Figure 9-14 Different locations of the heaters

Figure 9-13 shows the temperature histories on the heating blocks with different Stefan numbers. The results show the quasi-steady phenomena exist in these three cases and the higher Stefan number is, the higher the temperatures on the heat blocks are. For the case of $Ste = 0.524$, the temperature on the heat blocks turns different after 60 minutes while this turning point is approximately 40 and 25 minutes in the other two cases with higher Stefan numbers. This turning point indicates that natural convection begins to domain the melting process. So with increasing Stefan number, the natural convection takes affects more quickly and significantly. Numerical simulations are carried out for different locations of the heaters. Cases 1 and 3 are shown in the Fig. 9-14 while Case 2 has the same geometry as that in Fig. 9-1. The heating rates are the same for all three cases since the Stefan numbers for all cases are 2.36. Table 9-2 shows the temperatures on the heaters at 120 minutes.

Table 9-2 Temperatures on the heat blocks

	Temperature (°C)		
	Heat block 1	Heat block 2	Heat block 3
Case 1	35.2	35.2	35.2
Case 2	33.0	34.5	35.4
Case 3	33.3	34.4	35.7

Since the three heaters are combined together in case 1, the temperatures on the three blocks are all equal to 35.2 °C. The locations of the center of the heaters are $H/6$, $H/2$ and $5H/6$ at the left wall in Case 2 (see Fig. 9-14 (a)), the temperatures of the three blocks are 33.0, 34.5 and 35.4 °C, respectively. For Case 3, the heaters 1 and 3 are at the bottom and top of the cavity while the center of the heater 2 is $H/2$ at the left wall. The temperatures at the three blocks are 33.0, 34.5 and 35.4 °C, respectively. However, the maximum difference between the highest temperatures (block 3) for the three cases is only 0.5 °C.

9.5 Conclusions

Interfacial tracking method is applied to solve a melting problem in an enclosure with discrete heating at a constant rate. The location of melting fronts, melting volume fraction and surface temperature at the surface of the heat blocks in the numerical results agreed with the experiment results well. With increasing Stefan numbers, the natural convection affects the results more quickly and significantly. The effect of the locations of the heater on the maximum temperatures is not significant.

Chapter 10 A Hybrid Lattice Boltzmann and Finite Volume Method for Melting with Convection

10.1 Introduction

Low Prandtl number and high Prandtl number melting problems has been solved in Chapters 8 and 9 with LBM and FVM respectively. And in these two chapters, the melting front locations are obtained with interfacial tracking method. Fix grids are employed and the melting fronts don't always locate at the computational nodes. Thermal conductivity settings are included to fix the errors caused by it. In this chapter, interfacial tracking method is advanced by adding corrections to velocity field simulation process with porous media assumptions. Comparing with FVM, LBM has advantages in solving fluid flow in porous media. LBM-FVM hybrid method discussed in Chapter 5 uses LBM and FVM to solve velocity field and temperature field respectively. The objective of this chapter is to apply the hybrid method to solve melting with natural convection based on advanced interfacial tracking method. The results will be compared with experimental results for validation.

10.2 Problem statement

Figure 10-1 shows an enclosure filled with phase change material (PCM). The left vertical wall is kept at a constant temperature, T_h , which is above the melting temperature, T_m , while the right cold wall is kept at a constant temperature, T_c , which is below T_m . Meanwhile, the top and bottom of the enclosure are adiabatic. Non-slip conditions are applied to all the boundaries. The initial temperature of the system is at T_c .

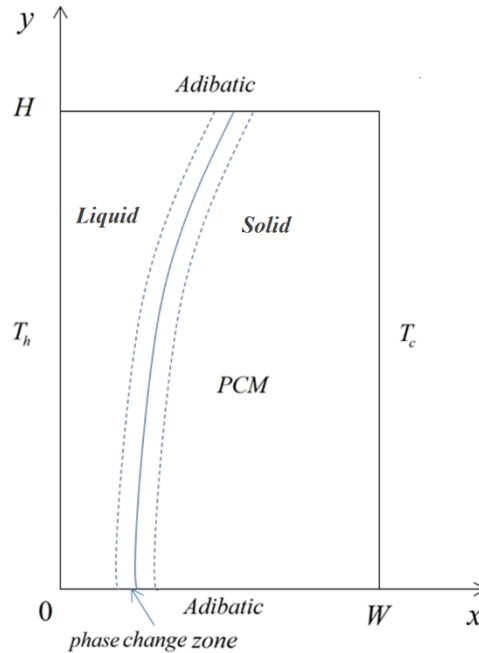


Figure 10-1 Phase change model

The problem can be described by the following governing equations in Section 8.2

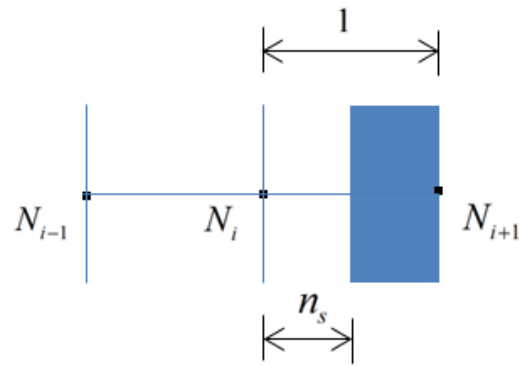
10.3 Hybrid LBM and FVM method for melting problem

Ganaoui and Semma [83] reported the results of phase change problem obtained by hybrid method based on entropy model. Hybrid LBM and FVM method for natural convection has been included in Chapter 5. Interfacial tracking method in Section 6.3.1 is also employed to handle the moving melt front.

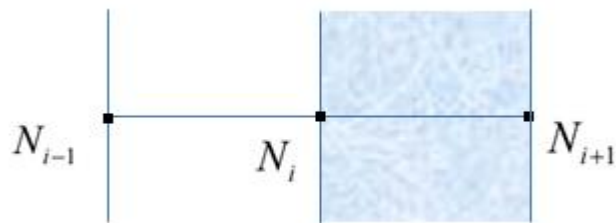
10.3.1 Porous media model

Melting of pure PCM takes place at a fixed temperature and the solid and liquid phases are separated by a clear interface. In order to obtain reasonable velocity field near solid-liquid interface, it is assumed that there is a phase change zone between the solid and the liquid zones as shown in Fig. 10-1. Both liquid and solid exist in the one control volume in the phase change zone and the fractions of liquid and solid depend on the degree of

melting (solid-liquid interface within the control volume). Semma et al. [123] suggested that the phase change zone can be considered as a porous medium and solved the phase change problem with pure LBM. There are several methods for the fluid flow in porous media using LBM. Spaid and Phelan [124] proposed a model for microscale flow in fibrous media by solving the Brinkman Equation directly while Dardis and McCloskey [125] to avoid solving Brinkman Equation by adding the porous media effect term in the collision term. Guo and Zhao [8] fulfilled the fluid flow simulation by introducing another force term depending on the parameters of the porous media.



(a) real interface location



(b) assumption

Figure 10-2 Porous media assumption

In this work, the velocity field in the phase change zone is obtained using the porous media model [125]. It is assumed that the density distribution in each node is uniform throughout the volume of each node and each particle only moves 1 or $\sqrt{2}$ lattice spacing in one step in the nine directions as shown in Fig. 10-1.

The real situation of the computing node N_i in the phase change zone is shown in Fig. 10-2(a). The interface location is not right on the node N_{i+1} and the liquid fraction on node N_i is n_s . Then the volume of node N_i is assumed to be filled with a porous with permeability of $1-n_s$ as shown in Fig. 10-2(b). The density distribution in the phase change zone can be expressed as:

$$f_i(\mathbf{r} + \mathbf{e}_i \Delta t, t + \Delta t) - f_i(\mathbf{r}, t) = \frac{1}{\tau_v} (f_i^{eq}(\mathbf{r}, t) - f_i(\mathbf{r}, t)) + F_i + \Delta^{PCM}, \quad (10.1)$$

$$\Delta^{PCM} = (1 - n_s) (f_i(\mathbf{r} + \mathbf{e}_i \Delta t, t) - f_i(\mathbf{r}, t)), \quad i = 1, 2, \dots, 9$$

where Δ^{PCM} is the porous media effect term. When n_s equals 1, it means that the node N_i is pure free fluid node so that Δ^{PCM} has no effect on the simulation process. When n_s equals 0, it means the node N_i is solid boundary node and Eq. (10-1) is reduced to a standard bounce-back boundary condition [83].

10.4 Results and discussions

The hybrid method is validated by comparing the results with the experimental results in Ref. [66]. In the experimental system, a $15\text{mm} \times 15\text{mm}$ enclosure is filled with n-octadecane as PCM. The melting point of the n-octadecane is 300.7 K and its latent heat is 244 kJ/kg . The viscosity is 0.0039 Ns/m^2 and the density is 774 kg/m^3 . The thermal

conductivity, specific heat, and thermal expansion coefficient are $0.152W/(m \cdot K)$, $2180J/(kg \cdot K)$ and $0.00085 K^{-1}$, respectively. The Prandtl number equals 56.2 and the subcooling is zero. Regarding the definition of Rayleigh number and Stefan number, they only change with the temperature difference $T_h - T_m$ linearly when the other parameters are all fixed in the system.

The results of numerical solution for Stefan number Ste equals 0.0451 and 0.0959 are compared with the results in Ref. [66]. The corresponding temperature differences are 5.3 K and 11.2 K respectively. The Rayleigh numbers for these two cases are 3.27×10^5 and 6.95×10^5 , respectively.

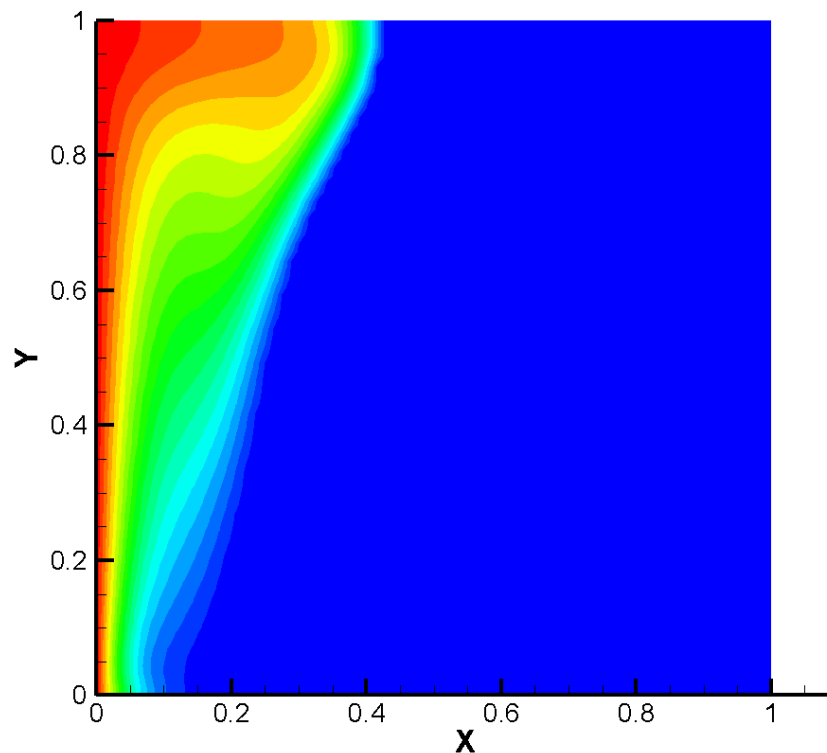


Figure 10-3 Temperature field $Ste=0.0451$, $\tau=52700$

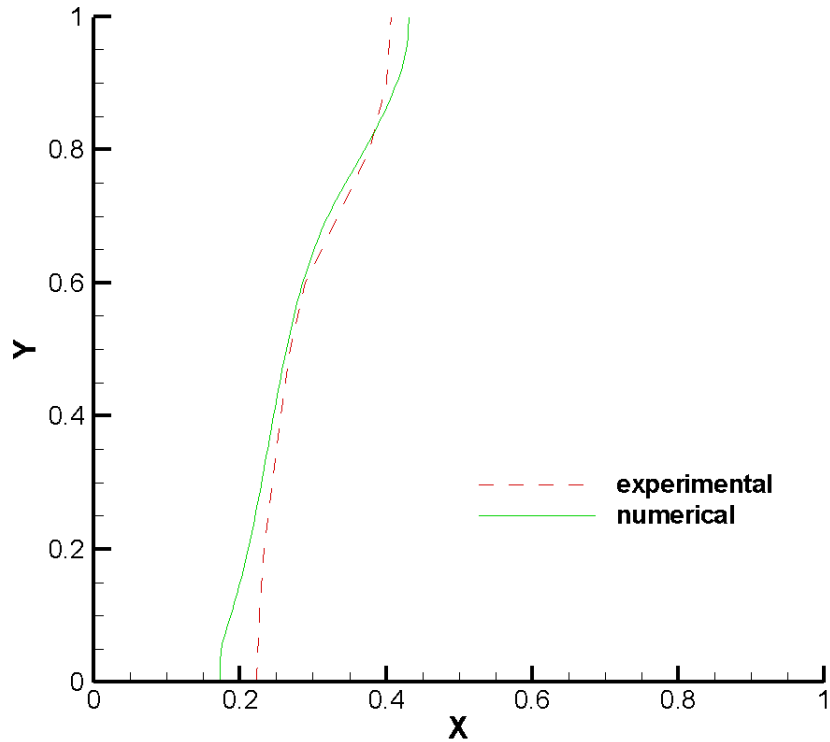


Figure 10-4 Melting front comparison $Ste=0.0451$, $\tau=52700$

For the case that Ste equals 0.0451, the melting process is governed by the conduction at the beginning. The melting interface is almost a vertical straight line during that period. After the non-dimensional time τ turning greater than 7500, the melting velocity varies depending on the Y location in the enclosure. The PCM closer to the top of the enclosure melts faster than that closer to the bottom. And this difference turns bigger as time grows. The temperature field of this case when τ equals 52700 is shown in Fig. 10-3. Generally, the higher the location is, the higher temperature is due to the natural convection. This temperature field governed by the natural convection leads to the sloping interface. Figure 10-4 shows the comparison of melting fronts between the numerical results and the experimental results when τ equals 52700 for the case of $Ste = 0.0451$. It can be seen that the numerical results agree with the experimental results very well.

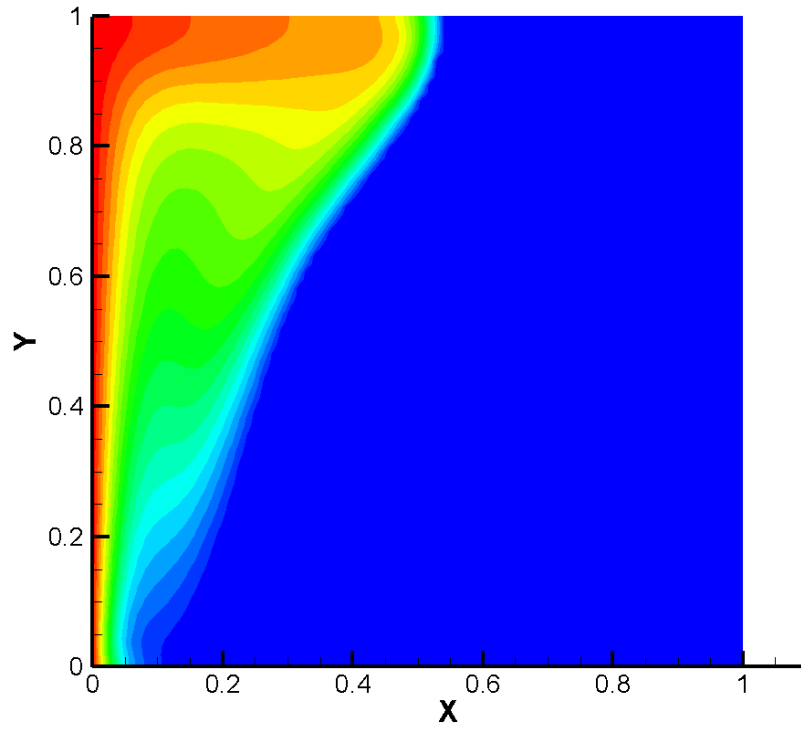


Figure 10-5 Temperature field $Ste=0.0959$, $\tau = 37250$

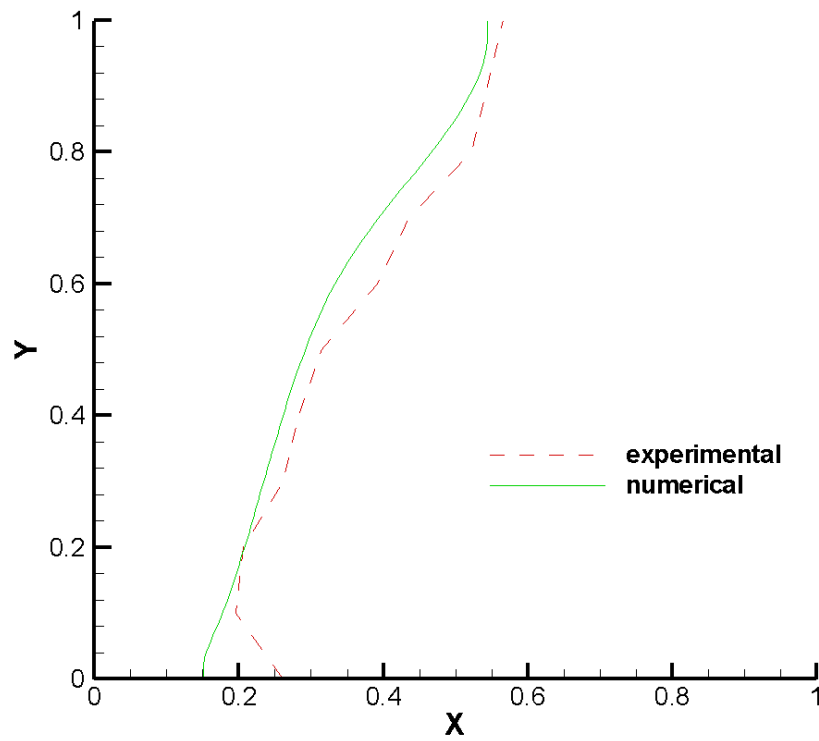


Figure 10-6 Melting front comparison $Ste=0.0959$, $\tau = 37250$

The case that Ste equals 0.0959 is also studied. The temperature difference is larger than the previous case. Therefore the natural convection effect is more pronounced. The liquid PCM zone begins to be governed by the natural convection when τ is around 5700. The temperature field is shown in Fig. 10-5 when τ equals 37250. Similar to the previous case, basically the higher temperature locates in the higher location due to the natural convection. It can also be seen that the non-dimensional temperature gradient near the interface is larger than the previous case. Since this case has a larger temperature difference, it has a larger temperature gradient which can lead to higher melting rate. Figure 10-6 shows the comparison of melting fronts between the numerical and the experimental results when τ is 37250 for the case that $Ste = 0.0959$. The numerical results agree with the experimental results very well. Several facts may cause the slight difference between the numerical and experimental results. The discrepancies may be caused by the facts that the volume change due to the phase change is assumed to be negligible in the numerical method and keep the heated wall at a constant temperature during experiments is also challenging.

More numerical solutions are carried out for the cases that Stefan numbers are 0.0658, 0.0309 and 0.0212, respectively. The corresponding Rayleigh numbers are 4.77×10^5 , 2.24×10^5 and 1.54×10^5 , respectively. Figure 10-7 shows the comparisons of Nusselt numbers for different Stefan numbers. The Nusselt number Nu represents the heat transfer rate from the heated wall to the liquid PCM.

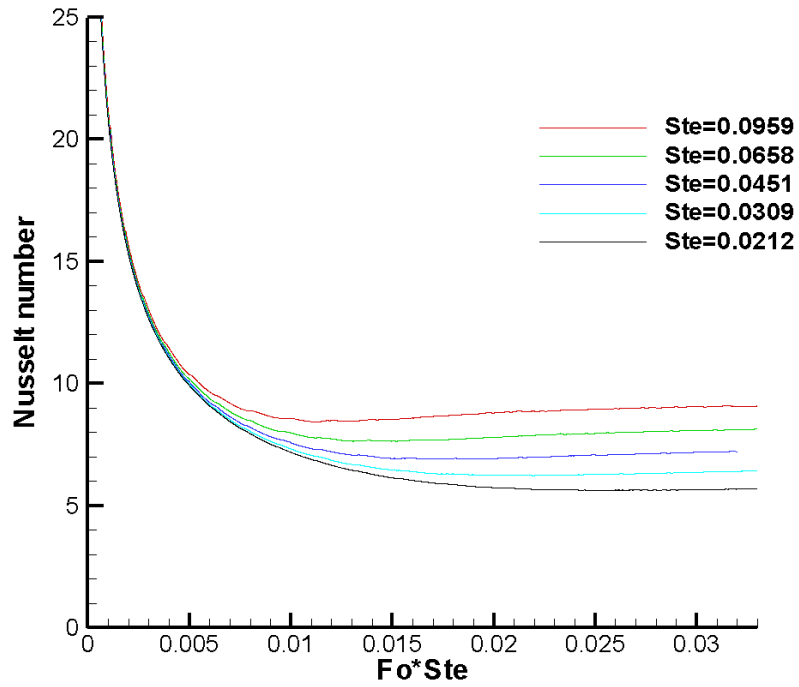


Figure 10-7 Nusselt number comparison

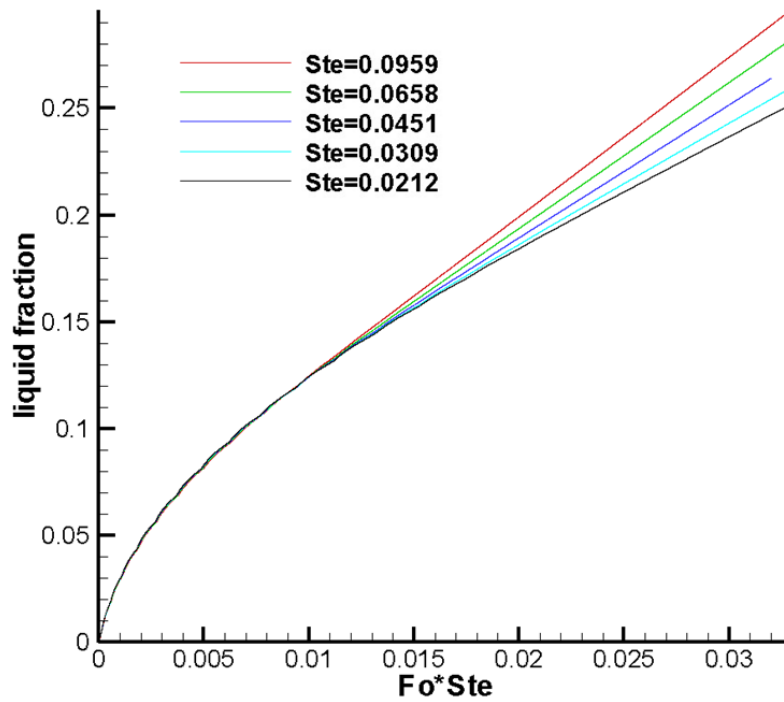


Figure 10-8 Comparison of liquid fractions

The parameter $Fo \times Ste$ is an important time measure in the melting problem. For the conduction governed melting problem we can reach [17]:

$$Nu_{avg} \sim (Fo \times Ste)^{-1/2} \quad (10.2)$$

Slopes to $Fo \times Ste$ since the higher Stefan number case has higher Nusselt number.

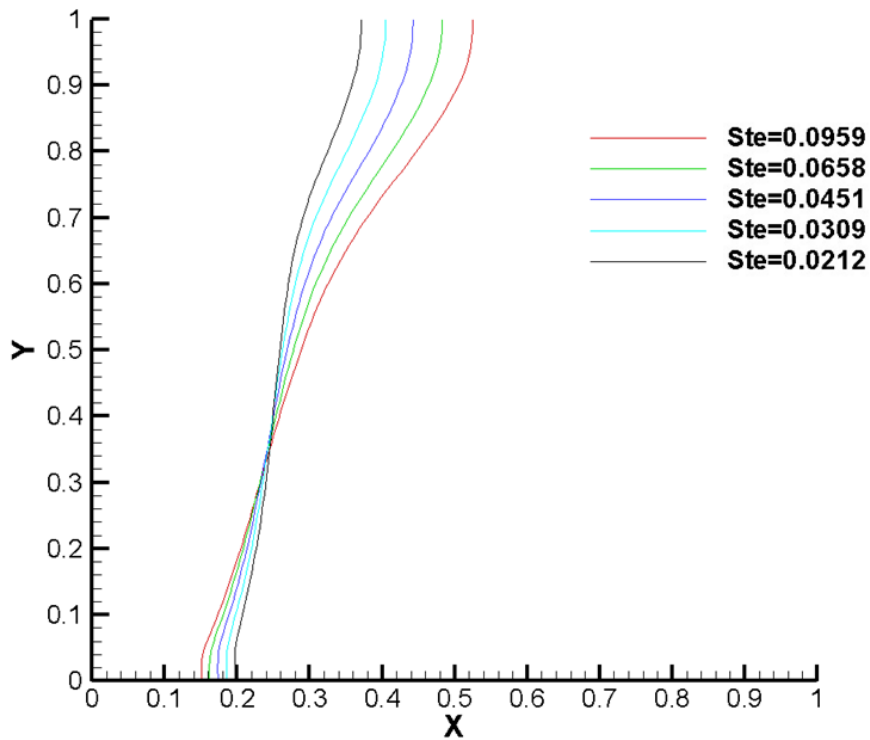


Figure 10-9 Comparison of melting fronts

For all the five cases considered, the conduction dominates the melting process at the beginning. When $Fo \times Ste$ is less than 0.005, the Nusselt numbers are almost the same in the five cases; this means that the melting processes for all five cases are governed by the conduction during that period. Then Nusselt numbers turn different and they are higher for higher Stefan numbers. Natural convection is more pounced with larger temperature difference that leads to higher Stefan number. After some time the Nusselt numbers

approach to different constant numbers, which means that the melting processes reach to quasi-steady state. After reaching this state, the liquid fraction becomes linear to the time which agrees with the Fig. 10-8 well. And the liquid fractions have different

The melting front comparison is shown in Fig. 10-9 when $Fo \times Ste$ equals 0.033. As discussed above, the natural convection has governed the melting process at that instance. We can see that the melting rate close to the top of the enclosure is higher for the case with higher Ste and the melting rate close to the bottom of the enclosure is higher for the case with lower Ste . It indicates that the natural convection effect is more important for the higher Ste case which agrees with the discussions above.

10.5 Conclusions

A hybrid lattice Boltzmann and finite volume method is developed for the melting problems. The interfacial tracking method is applied to obtain the location of the interface. Natural convection governed melting problems with different Stefan numbers are solved for validation. The numerical results agreed with the experimental results very well. Therefore the proposed numerical method is valid for the melting problem simulation.

Chapter 11 Lattice Boltzmann Method Simulation of 3-D Natural Convection with Double MRT Model

11.1 Introduction

In Chapters 3 to 10, two-dimensional natural convection and melting problem with various conditions are solved. The research on three-dimensional cases are scant although they are more general. Leong et al. [126] provided experimental Nusselt numbers for a cubical-cavity benchmark problem in three-dimensional natural convection. Tric et al. [127] solved three-dimensional natural convection at different Rayleigh numbers numerically. Wakashima and Saitoh [128] obtained Benchmark solutions for natural convection in a cubic cavity using the high-order time-space method. Salat et al. [129] did experimental and numerical investigation of turbulent natural convection in a large air-filled cavity. This problem was also investigated using LBM [130]. Azwadi and Syahrullall [131] employed a double LBGK model to simulate natural convection in a cubic cavity. LBM models in DDF can be different from each other. MRT and LBGK were applied to solve velocity and temperature fields respectively in a cubic cavity mix convection flow [132, 133]. This article proposed a double MRT model, which has not been reported by our knowledge, for three-dimensional fluid flow and heat transfer simulation. The objective of this chapter is to discuss three-dimensional natural convections with proposed double MRT model.

11.2 Natural convection in cubic cavity

Physical model of natural convection in a cubic cavity is shown in Fig. 11-1. The cubic cavity with an edge length of H is filled with working fluid of air.

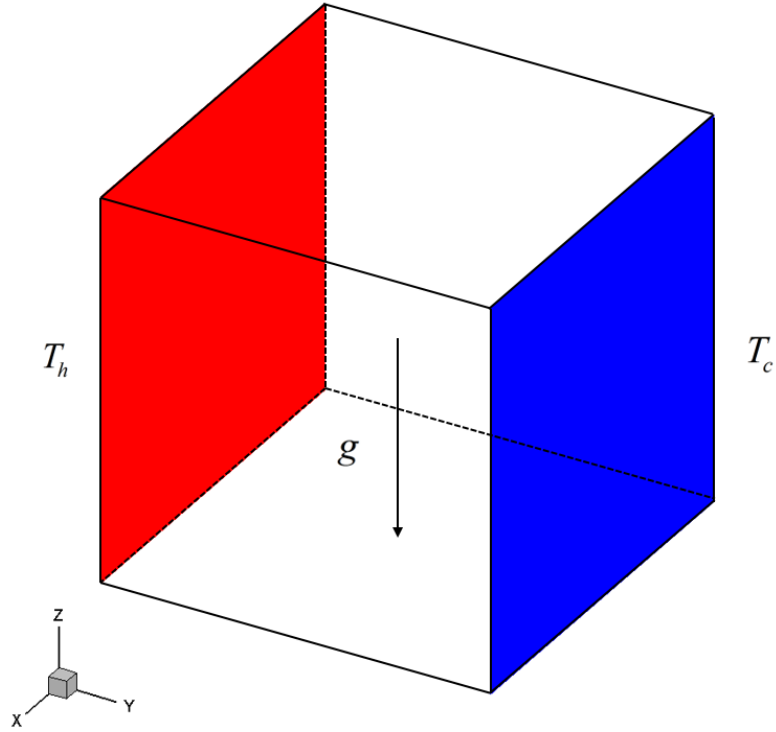


Figure 11-1 Cubic natural convection

The Prandtl number is fixed at 0.71. Boussinesq assumption is employed. Then the governing equations are

$$\frac{\partial u}{\partial x} + \frac{\partial v}{\partial y} + \frac{\partial w}{\partial z} = 0 \quad (11.1)$$

$$\rho \left(\frac{\partial u}{\partial t} + u \frac{\partial u}{\partial x} + v \frac{\partial u}{\partial y} + w \frac{\partial u}{\partial z} \right) = -\frac{\partial p}{\partial x} + \mu \left(\frac{\partial^2 u}{\partial x^2} + \frac{\partial^2 u}{\partial y^2} + \frac{\partial^2 u}{\partial z^2} \right) \quad (11.2)$$

$$\rho \left(\frac{\partial v}{\partial t} + u \frac{\partial v}{\partial x} + v \frac{\partial v}{\partial y} + w \frac{\partial v}{\partial z} \right) = -\frac{\partial p}{\partial y} + \mu \left(\frac{\partial^2 v}{\partial x^2} + \frac{\partial^2 v}{\partial y^2} + \frac{\partial^2 v}{\partial z^2} \right) \quad (11.3)$$

$$\rho \left(\frac{\partial w}{\partial t} + u \frac{\partial w}{\partial x} + v \frac{\partial w}{\partial y} + w \frac{\partial w}{\partial z} \right) = -\frac{\partial p}{\partial z} + \mu \left(\frac{\partial^2 w}{\partial x^2} + \frac{\partial^2 w}{\partial y^2} + \frac{\partial^2 w}{\partial z^2} \right) + \rho g \beta (T - T_l) \quad (11.4)$$

$$\rho \left(\frac{\partial T}{\partial t} + u \frac{\partial T}{\partial x} + v \frac{\partial T}{\partial y} + w \frac{\partial T}{\partial z} \right) = k \left(\frac{\partial^2 T}{\partial x^2} + \frac{\partial^2 T}{\partial y^2} + \frac{\partial^2 T}{\partial z^2} \right) \quad (11.5)$$

Three types of natural convections are in consideration in this article. They differ from each other with the thermal boundary settings. In all these cubic cavity natural convections, the vertical walls ($y = 0$ and $y = H$) are kept at T_h and T_c respectively. u , v and w are velocities in the x-, y- and z-directions. Non-slip boundary conditions are employed.

$$y = 0, T = T_h \quad (11.6)$$

$$y = H, T = T_c \quad (11.7)$$

$$u = v = w = 0 \text{ for all boundaries} \quad (11.8)$$

In the first type cubic cavity natural convection, the remained four walls are all adiabatic. Natural convection with this setting is solved as benchmark problem in Refs. [127-130]. Leong et al. [126] argued that this setting was not physically-realizable because adiabatic boundary condition was hard to be reached.

The second type of cubic cavity natural convection is a physically-realizable benchmark problem. Its remained four walls have a linear temperature variation from the cold surface to hot surface. Experimental results are reported in Refs. [126, 134]. In this article, we use:

$$\begin{cases} x = 0, T = T_h + (T_c - T_h) \cdot y / H \\ x = H, T = T_h + (T_c - T_h) \cdot y / H \\ z = 0, T = T_h + (T_c - T_h) \cdot y / H \\ z = H, T = T_h + (T_c - T_h) \cdot y / H \end{cases} \quad (11.9)$$

The following boundary conditions are applied to the third type cubic natural convection.

$$\begin{cases} x = 0, T = T_h + (T_c - T_h) \cdot y / H \\ x = H, T = T_h + (T_c - T_h) \cdot y / H \\ z = 0, \partial T / \partial z = 0 \\ z = H, \partial T / \partial z = 0 \end{cases} \quad (11.10)$$

In the remained parts of this article, these three types of problems are referred to as Type 1, Type 2 and Type 3.

11.3 Lattice Boltzmann method for 3-D problems

The DDF in LBM will be used to solve velocity and temperature fields, respectively. MRT is selected due to its advantages in accuracy and numerical stability. To the best of the authors' knowledge, double MRT model for three-dimensional fluid flow and heat transfer simulation has not been reported by now. In this article, 3-D double MRT model is proposed and three types of natural convections are solved with it for validation.

11.3.1 D3Q19-MRT-LBM Model for Fluid Flow

Lattice Boltzmann equation can describe the statistical behavior of a fluid flow.

$$f(\mathbf{r} + \mathbf{e}\Delta t, t + \Delta t) - f(\mathbf{r}, t) = \mathbf{\Omega} + F \quad (11.11)$$

where f is the density distribution, Δt is the time step, $\mathbf{\Omega}$ is the collision term and F is the body force. To simplify this equation, it is assumed that each computing nodes has 19 directions as shown in Fig. 11-2 and these velocities are given by:

$$\mathbf{e}_i = c \begin{bmatrix} 0 & 1 & -1 & 0 & 0 & 0 & 0 & 1 & -1 & 1 & -1 & 1 & -1 & 1 & -1 & 0 & 0 & 0 & 0 \\ 0 & 0 & 0 & 1 & -1 & 0 & 0 & 1 & 1 & -1 & -1 & 0 & 0 & 0 & 0 & 1 & -1 & 1 & -1 \\ 0 & 0 & 0 & 0 & 0 & 1 & -1 & 0 & 0 & 0 & 0 & 1 & 1 & -1 & -1 & 1 & 1 & -1 & -1 \end{bmatrix} \quad (11.12)$$

where c is the lattice speed and it relates to the sound speed c_s as:

$$c^2 = 3c_s^2 \quad (11.13)$$

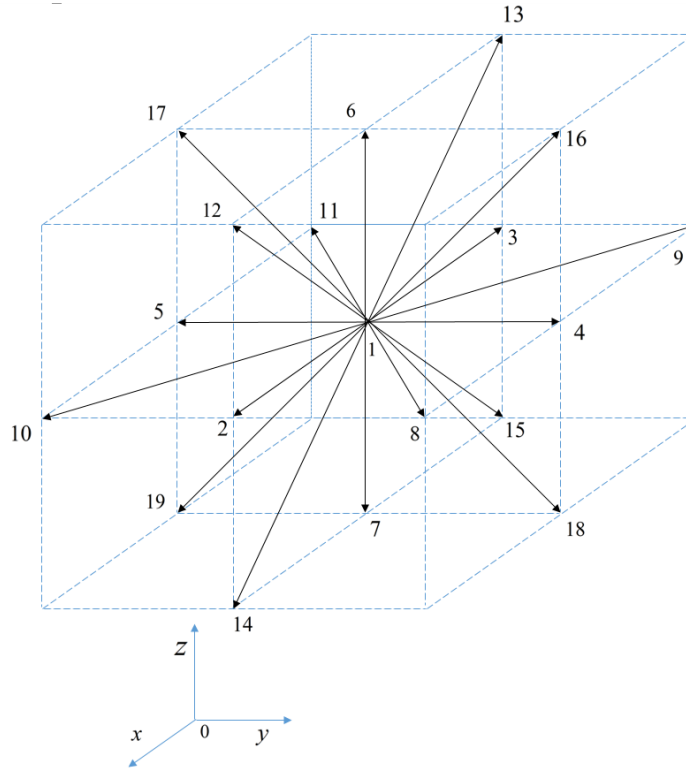


Figure 11-2 D3Q19 model

In this D3Q19 model, Eq. (11.11) can be expressed as:

$$f_i(\mathbf{r} + \mathbf{e}_i \Delta t, t + \Delta t) - f_i(\mathbf{r}, t) = \Omega_i + F_i, \quad i = 1, 2, \dots, 19 \quad (11.14)$$

where the force term in the equation can be obtained as:

$$F_i = \Delta t \mathbf{G} \cdot \frac{(\mathbf{e}_i - \mathbf{V})}{p} f_i^{eq}(\mathbf{r}, t) \quad (11.15)$$

where \mathbf{G} is the effective gravitational force:

$$\mathbf{G} = -\beta(T - T_l)\mathbf{g} \quad (11.16)$$

The equilibrium distribution function $f_i^{eq}(\mathbf{r}, t)$ is expressed as:

$$f_i^{eq}(\mathbf{r}, t) = \rho\omega_i \left[1 + \frac{\mathbf{e}_i \cdot \mathbf{V}}{c_s^2} + \frac{(\mathbf{e}_i \cdot \mathbf{V})^2}{2c_s^4} - \frac{\mathbf{V} \cdot \mathbf{V}}{2c_s^2} \right], \quad i = 1, 2, \dots, 19 \quad (11.17)$$

The density weighting factors ω_i are:

$$\omega_i = \begin{cases} 1/3, & i = 1 \\ 1/18, & i = 2, 3, \dots, 7 \\ 1/36, & i = 8, 9, \dots, 19 \end{cases} \quad (11.18)$$

To satisfy the continuum and momentum conservations, the collision term in MRT is:

$$\Omega_i = -M^{-1} \cdot \mathbf{S} \cdot [m_i(\mathbf{r}, t) - m_i^{eq}(\mathbf{r}, t)], \quad i = 1, 2, \dots, 19 \quad (11.19)$$

where $m_i(\mathbf{r}, t)$ and $m_i^{eq}(\mathbf{r}, t)$ are moments and their equilibrium functions; M and S are the transform matrix and collision matrix respectively. d'Humieres et al. [135] introduced the detailed parameter settings in D3Q19-MRT model.

Macroscopic parameters are relate to the density distributions as:

$$\begin{cases} \rho = \sum_{i=1}^{19} f_i(\mathbf{r}, t), \quad \rho\mathbf{V} = \sum_{i=1}^{19} f_i(\mathbf{r}, t)\mathbf{e}_i \\ \mathbf{m} = M \cdot [f_1, \quad f_2, \quad \dots \quad f_{19}]^T \end{cases} \quad (11.20)$$

In this model, transform matrix M is:

$$\mathbf{M} = \begin{bmatrix}
1 & 1 & 1 & 1 & 1 & 1 & 1 & 1 & 1 & 1 & 1 & 1 & 1 & 1 & 1 & 1 & 1 & 1 \\
-30 & -11 & -11 & -11 & -11 & -11 & -11 & 8 & 8 & 8 & 8 & 8 & 8 & 8 & 8 & 8 & 8 & 8 \\
12 & -4 & -4 & -4 & -4 & -4 & -4 & 1 & 1 & 1 & 1 & 1 & 1 & 1 & 1 & 1 & 1 & 1 \\
0 & 1 & -1 & 0 & 0 & 0 & 0 & 1 & -1 & 1 & -1 & 1 & -1 & 1 & -1 & 0 & 0 & 0 \\
0 & -4 & 4 & 0 & 0 & 0 & 0 & 1 & -1 & 1 & -1 & 1 & -1 & 1 & -1 & 0 & 0 & 0 \\
0 & 0 & 0 & 1 & -1 & 0 & 0 & 1 & 1 & -1 & -1 & 0 & 0 & 0 & 0 & 1 & -1 & 1 \\
0 & 0 & 0 & -4 & 4 & 0 & 0 & 1 & 1 & -1 & -1 & 0 & 0 & 0 & 0 & 1 & -1 & 1 \\
0 & 0 & 0 & 0 & 0 & 1 & -1 & 0 & 0 & 0 & 0 & 1 & 1 & -1 & -1 & 1 & 1 & -1 \\
0 & 0 & 0 & 0 & 0 & -4 & 4 & 0 & 0 & 0 & 0 & 1 & 1 & -1 & -1 & 1 & 1 & -1 \\
0 & 2 & 2 & -1 & -1 & -1 & -1 & 1 & 1 & 1 & 1 & 1 & 1 & 1 & 1 & -2 & -2 & -2 \\
0 & -4 & -4 & 2 & 2 & 2 & 2 & 1 & 1 & 1 & 1 & 1 & 1 & 1 & 1 & -2 & -2 & -2 \\
0 & 0 & 0 & 1 & 1 & -1 & -1 & 1 & 1 & 1 & 1 & -1 & -1 & -1 & -1 & 0 & 0 & 0 \\
0 & 0 & 0 & -2 & -2 & 2 & 2 & 1 & 1 & 1 & 1 & -1 & -1 & -1 & -1 & 0 & 0 & 0 \\
0 & 0 & 0 & 0 & 0 & 0 & 0 & 1 & -1 & 1 & -1 & 0 & 0 & 0 & 0 & 0 & 0 & 0 \\
0 & 0 & 0 & 0 & 0 & 0 & 0 & 0 & 0 & 0 & 0 & 0 & 0 & 0 & 0 & 1 & -1 & -1 \\
0 & 0 & 0 & 0 & 0 & 0 & 0 & 0 & 0 & 0 & 0 & 1 & -1 & -1 & 1 & 0 & 0 & 0 \\
0 & 0 & 0 & 0 & 0 & 0 & 0 & 1 & -1 & 1 & -1 & -1 & 1 & -1 & 1 & 0 & 0 & 0 \\
0 & 0 & 0 & 0 & 0 & 0 & 0 & -1 & -1 & 1 & 1 & 0 & 0 & 0 & 0 & 1 & -1 & 1 \\
0 & 0 & 0 & 0 & 0 & 0 & 0 & 0 & 0 & 0 & 0 & 1 & 1 & -1 & -1 & -1 & -1 & 1
\end{bmatrix} \quad (11.21)$$

The corresponding macroscopic moments are:

$$\mathbf{m} = (\rho, e, \varepsilon, j_x, q_x, j_y, q_y, j_z, q_z, 3p_{xx}, 3\pi_{xx}, p_{ww}, \pi_{ww}, p_{xy}, p_{yz}, p_{xz}, m_x, m_y, m_z)^T \quad (11.22)$$

The collision matrix \mathbf{S} in moment space is the diagonal matrix

$$\mathbf{S} = \text{diag}(s_1, s_2, s_3, s_4, s_5, s_6, s_7, s_8, s_9, s_{10}, s_{11}, s_{12}, s_{13}, s_{14}, s_{15}, s_{16}, s_{17}, s_{18}, s_{19}) \quad (11.23)$$

With s_9 equaling to s_{13} , the equilibrium moments are:

$$\mathbf{m}^{eq} = \left(\rho, -11\rho + 19 \frac{j_x^2 + j_y^2 + j_z^2}{\rho_0}, 3\rho - \frac{11}{2} \frac{j_x^2 + j_y^2 + j_z^2}{\rho_0}, j_x, -\frac{2}{3}j_x, j_y, -\frac{2}{3}j_y, j_z, -\frac{2}{3}j_z, \right. \\
\left. \frac{2j_x^2 - (j_y^2 + j_z^2)}{\rho_0}, -\frac{1}{2} \frac{2j_x^2 - (j_y^2 + j_z^2)}{\rho_0}, \frac{j_y^2 - j_z^2}{\rho_0}, -\frac{1}{2} \frac{j_y^2 - j_z^2}{\rho_0}, \frac{j_x j_y}{\rho_0}, \frac{j_y j_z}{\rho_0}, \frac{j_x j_z}{\rho_0}, 0, 0, 0 \right)^T \quad (11.24)$$

where

$$j_x = \rho u_x, \quad j_y = \rho u_y, \quad j_z = \rho u_z \quad (11.25)$$

The constant ρ_0 in Eq. (11.24) is the mean density in the system and it is usually set to be unity. Taking ρ_0 in to account can reduce compressible effect in the model [136].

Then the unknown parameters in collision matrix S are:

$$\begin{cases} s_1 = s_4 = s_6 = s_8 = 1.0, & s_2 = 1.19, & s_3 = s_{11} = s_{13} = 1.4, & s_5 = s_7 = s_9 = 1.2 \\ s_{17} = s_{18} = s_{19} = 1.98, & s_{10} = s_{12} = s_{14} = s_{15} = s_{16} = 1 / (3\nu + 0.5) \end{cases} \quad (11.26)$$

The velocity field is solved using this D3Q19-MRT model. Non-slip boundary conditions in this article are fulfilled using bounce-back boundary conditions [135].

11.3.2 D3Q7-MRT-LBM Model for Heat Transfer

Yoshida and Nagaoka [137] proposed a Multiple-relaxation-time lattice Boltzmann model for convection and anisotropic diffusion equation. In this D3Q7 model, seven discrete velocities are needed for a three-dimensional problem. Li et al. [138] discussed boundary conditions for this thermal LBM model. This model has not been involved by any DDF model in LBM. In this article, we propose a double MRT model for fluid flow and heat transfer problem simulation. Velocity and temperature fields are solved with D3Q19-MRT and D3Q7-MRT, respectively.

D3Q7-MRT model is valid to solve the following standard convection-diffusion equation.

$$\frac{\partial \phi}{\partial t} + \frac{\partial}{\partial x_j} (v_j \phi) = \frac{\partial}{\partial x_i} \left(D_{ij} \frac{\partial \phi}{\partial x_j} \right) \quad (11.27)$$

where ϕ is a scalar variable and D_{ij} is the diffusion coefficient. Energy equation for the benchmark problem in this article is shown in Eq. (11.5), which is a special case of Eq. (11.27). Therefore, D3Q7 model can be used to solve the energy equation in this article.

Each computing nodes have seven discrete velocities shown in Fig. 11-3:

$$\mathbf{u}_i = c \begin{bmatrix} 0 & 1 & -1 & 0 & 0 & 0 & 0 \\ 0 & 0 & 0 & 1 & -1 & 0 & 0 \\ 0 & 0 & 0 & 0 & 0 & 1 & -1 \end{bmatrix} \quad (11.28)$$

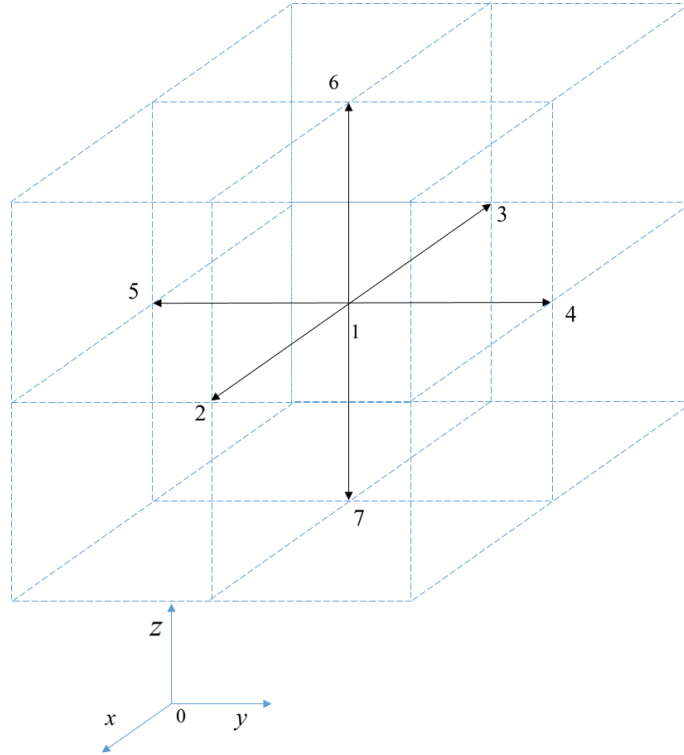


Figure 11-3 D3Q7 model

Similar to the density distribution, energy distribution g_i can be obtained by:

$$g_i(\mathbf{r} + \mathbf{u}_i \Delta t, t + \Delta t) - g_i(\mathbf{r}, t) = -N^{-1} \cdot Q \cdot [n_i(\mathbf{r}, t) - n_i^{eq}(\mathbf{r}, t)], \quad i = 1, 2, \dots, 7 \quad (11.29)$$

where $n_i^{eq}(\mathbf{r}, t)$ is the equilibrium function for $n_i(\mathbf{r}, t)$, N and Q are the transform matrix and collision matrix for the energy distribution [137].

Macroscopic parameters relate to the energy distributions as:

$$\begin{cases} T = \sum_{i=1}^7 g_i(\mathbf{r}, t), \\ \mathbf{n} = \mathbf{N} \cdot [g_1, g_2, \dots, g_7]^T \end{cases} \quad (11.30)$$

The energy weight factors $\omega_{T,i}$ are:

$$\omega_{T,i} = \begin{cases} 1/4, & (i=1), \\ 1/8, & (i=2,3,\dots,7) \end{cases} \quad (11.31)$$

Transform matrix in D3Q7 model is defined as:

$$\mathbf{N} = \begin{bmatrix} 1 & 1 & 1 & 1 & 1 & 1 & 1 \\ 0 & 1 & -1 & 0 & 0 & 0 & 0 \\ 0 & 0 & 0 & 1 & -1 & 0 & 0 \\ 0 & 0 & 0 & 0 & 0 & 1 & -1 \\ 6 & -1 & -1 & -1 & -1 & -1 & -1 \\ 0 & 2 & 2 & -1 & -1 & -1 & -1 \\ 0 & 0 & 0 & 1 & 1 & -1 & -1 \end{bmatrix} \quad (11.32)$$

and its corresponding equilibrium moments are:

$$\mathbf{n}^{eq} = [T, uT, vT, wT, aT, 0, 0]^T \quad (11.33)$$

where a is a constant relating to the coefficient $\omega_{T,1}$ by:

$$a = (7\omega_{T,1} - 1) = 3/4 \quad (11.34)$$

The definition of collision matrix \mathbf{Q} is:

$$\mathbf{Q}^{-1} = \begin{bmatrix} \tau_1 & 0 & 0 & 0 & 0 & 0 & 0 \\ 0 & \bar{\tau}_{xx} & \bar{\tau}_{xy} & \bar{\tau}_{xz} & 0 & 0 & 0 \\ 0 & \bar{\tau}_{xy} & \bar{\tau}_{yy} & \bar{\tau}_{yz} & 0 & 0 & 0 \\ 0 & \bar{\tau}_{xz} & \bar{\tau}_{yz} & \bar{\tau}_{zz} & 0 & 0 & 0 \\ 0 & 0 & 0 & 0 & \tau_5 & 0 & 0 \\ 0 & 0 & 0 & 0 & 0 & \tau_6 & 0 \\ 0 & 0 & 0 & 0 & 0 & 0 & \tau_7 \end{bmatrix} \quad (11.35)$$

The off-diagonal components correspond to the rotation of principal axis of anisotropic diffusion [137]. The relaxation coefficients $\bar{\tau}_{ij}$ are related to the diffusion coefficient matrix by:

$$\bar{\tau}_{ij} = \frac{1}{2} \delta_{ij} + \frac{\Delta t}{\varepsilon \Delta x^2} D_{ij} \quad (11.36)$$

where ε is a constant 0.25 in a three-dimensional problem, and δ_{ij} is the Kronecker's delta:

$$\delta_{ij} = \begin{cases} 0 & \text{if } i \neq j, \\ 1 & \text{if } i = j. \end{cases} \quad (11.37)$$

The relaxation coefficient τ_1 for the conserved quantity does not affect the numerical solution, and τ_5 , τ_6 and τ_7 only affect error terms. After testing, this article use 1 for these four coefficients.

Temperature field is solved using this D3Q7-MRT model and thermal boundary conditions are solved based on the settings in Ref. [138].

11.4 Results and discussions

Natural convection problem is fully defined with Pr and Ra . LBM includes the speed of sound, c_s . So we have to include Ma to fulfill this non-dimensional process for lattice

unit. Wang et al. [139] demonstrated that Ma has little effect on accuracy of MRT simulation. Incompressible air is the working fluid. Ma is 0.1 while Pr is 0.71 for all the cases in this article. Three types of natural convections in Section 2 are solved for various Rayleigh numbers ranged from 1×10^4 to 1×10^5 .

The two vertical walls ($Y = 0$ and $Y = 1$) are kept at T_h and T_c for all the cases in consideration. The local Nusselt number is defined as

$$Nu = \frac{h}{k/H} \Big|_{Y=0} = - \frac{\partial \theta}{\partial Y} \Big|_{Y=0} \quad (11.38)$$

The average Nusselt number \overline{Nu}_{3D} :

$$\overline{Nu}_{3D} = \int_0^1 \int_0^1 (Nu) dX dZ \quad (11.39)$$

and the maximum Nusselt number Nu_{\max} on the heat wall are important parameters to discuss three-dimensional natural convection problems. Due to the symmetry of the cubic natural convection, the mid-plane of the cubic ($X=0.5$) plays an important role in this problem and the average Nusselt number \overline{Nu}_{2D} at mid-plane is also in consideration.

$$\overline{Nu}_{2D} = \int_0^1 (Nu_{X=0.5}) dZ \quad (11.40)$$

Besides \overline{Nu}_{2D} , \overline{Nu}_{3D} and Nu_{\max} , the maximum velocities in all directions are also discussed.

11.4.1 Type 1 natural convection

For type 1 natural convection, two different sets of grids ($50 \times 50 \times 50$ and $60 \times 60 \times 60$) are employed. Refs. [127, 128, 129 and 140] reported $\overline{Nu_{3D}}$ for $Ra = 1 \times 10^4$ and $Ra = 1 \times 10^5$. Table 11-1 shows the comparison between present results and that in references.

Table 11-1 Type 1, $\overline{Nu_{3D}}$ comparison

	Ref. [127]	Ref. [128]	Ref. [128]	Ref. [140]	$50 \times 50 \times 50$	$60 \times 60 \times 60$
$Ra = 1 \times 10^4$	2.05	2.06	2.08	2.10	2.07	2.08
$Ra = 1 \times 10^5$	4.34	4.37	4.38	4.36	4.42	4.39

These references results agree with each other well and their averages (2.07 for $Ra = 1 \times 10^4$ and 4.36 for $Ra = 1 \times 10^5$) can be viewed as standard results. For the case of $Ra = 1 \times 10^4$, the present numerical results in different grids are both close to the standard one. For the case of $Ra = 1 \times 10^5$, however, the results obtained using grid of $60 \times 60 \times 60$ agreed better with the results in the literature. Refs. [128 and 131] reported $\overline{Nu_{2D}}$ for this type of natural convection. Table 2 is the comparison between results obtained from the present LBM and those from the references. The mean values from the references (2.28 for $Ra = 1 \times 10^4$ and 4.64 for $Ra = 1 \times 10^5$) are taken as standard ones.

For the case of $Ra = 1 \times 10^4$, the results from the two grid number are the same and their differences between standard one are negligible. For the case of $Ra = 1 \times 10^5$, the differences between two the results from the two grid numbers and standard one are within 2% and the result from grid number of $60 \times 60 \times 60$ grids is closer to the standard one. Refs.

[127 and 130] reported the Nu_{\max} and maximum velocities, respectively. Non-dimensional process in these references is different from that in article. We can get the velocity U_s in reference unit with the numerical results U_l using the following equation:

$$U_s = U_l \sqrt{3Pr \cdot Ra} / Ma \quad (11.41)$$

Table 11-2 Type 1, Nu_{\max} comparison

	Ref. [128]	Ref. [131]	50×50×50	60×60×60
$Ra = 1 \times 10^4$	2.25	2.30	2.27	2.27
$Ra = 1 \times 10^5$	4.61	4.67	4.72	4.69

Tables 11-3 to 11-5 are the comparisons between numerical and reference results. They indicate that the results from different grid numbers agreed well with those from the references. The above comparisons indicated that $\overline{Nu_{2D}}$, $\overline{Nu_{3D}}$, Nu_{\max} and maximum velocities in different directions results all agreed well with reference ones; thus the proposed double MRT model is valid for the Type 1 cubic natural convection simulation. Considering the computational efficiency and accuracy, the grid number of 50×50×50 is suitable for the case of $Ra = 1 \times 10^4$ while 60×60×60 is more appropriate for the case of $Ra = 1 \times 10^5$. The other two types of natural convection simulations for various Rayleigh numbers also have the same grid settings.

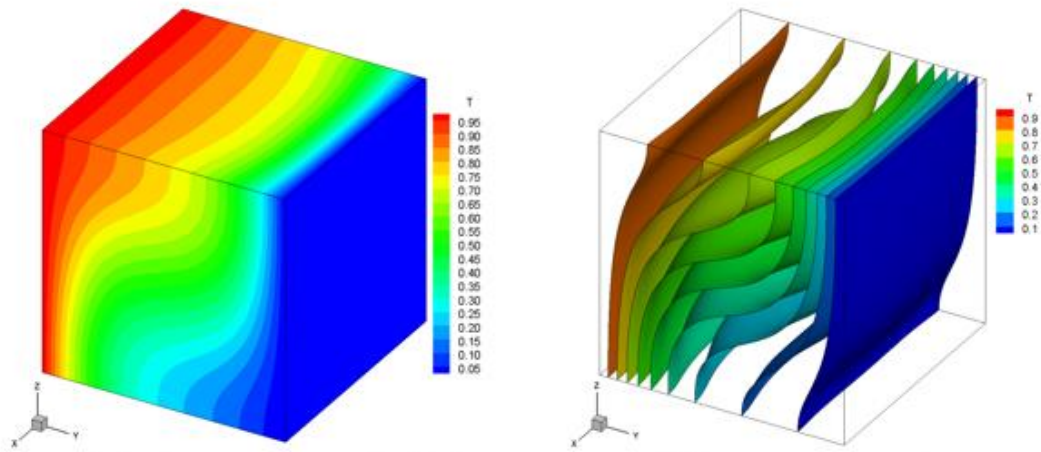
Table 11-3 Type 1, $\overline{Nu_{2D}}$ comparison

	Ref. [130]	50×50×50	60×60×60
$Ra = 1 \times 10^4$	3.72	3.66	3.68
$Ra = 1 \times 10^5$	7.88	7.98	7.98

Table 11-4 Type 1, Velocity comparison, $Ra = 1 \times 10^4$

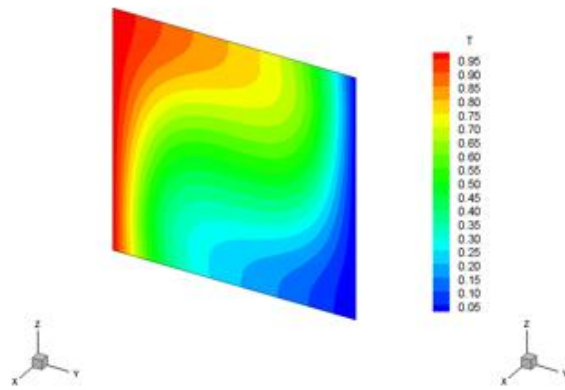
	U	V	W
50×50×50	2.20	16.88	19.23
60×60×60	2.19	16.83	19.20
Ref. [127]	2.16	16.72	18.98

Temperature and velocity fields for the cubic natural convection are very important. But few references include three-dimensional visual results. Figure 10-4 shows the temperature field for Type 1 problem at $Ra = 1 \times 10^4$. Surface temperature distribution and temperature isosurfaces are included in Figs. 11-4 (a) and (b). The temperature turns to be higher with increasing Z in the cubic cavity. Convection has dominated the heat transfer process and temperature isosurfaces does not change a lot in the x -direction. Figure 11-4 (c) to (e) show the temperature distributions on different locations for Type 1 problem. Regarding the boundary settings, it is common to argue the working condition on the mid-plane of the cubic ($X=0.5$) can be viewed as a two-dimensional problem [127]. Temperature field ($X=0.5$) agrees well with the two-dimensional results Chapter 5. In the other two locations ($Y=0.5$ and $Z=0.5$), isothermal lines are almost parallel to the X -axis. It supports the two-dimensional assumption. Figure 11-4 (f) shows the Nusselt number distribution on the hot surface ($Y=0$). Nusselt numbers at the mid-plane of the cubic ($X=0.5$) are higher than that in the other regions due to the side wall effect to these three-dimensional problem. Non-slip condition is applied to all the boundaries and it slows down the convection flow near the boundaries. Consequently, the convection effect to heat transfer is also lowered.

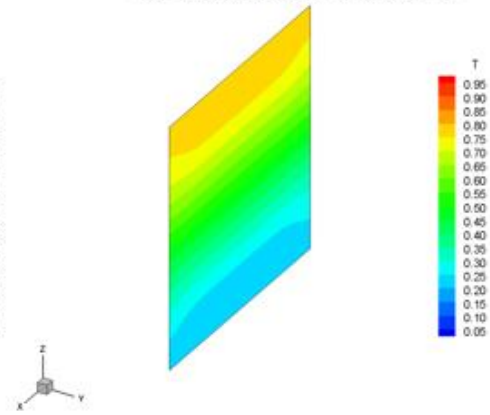


(a) Surface temperature distribution

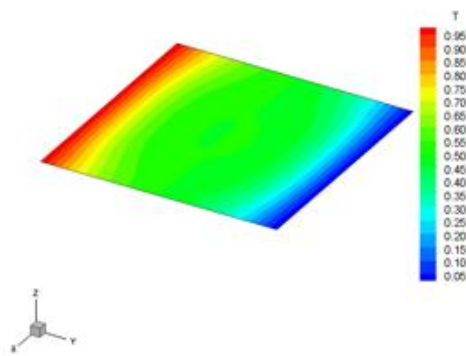
(b) Temperature isosurfaces



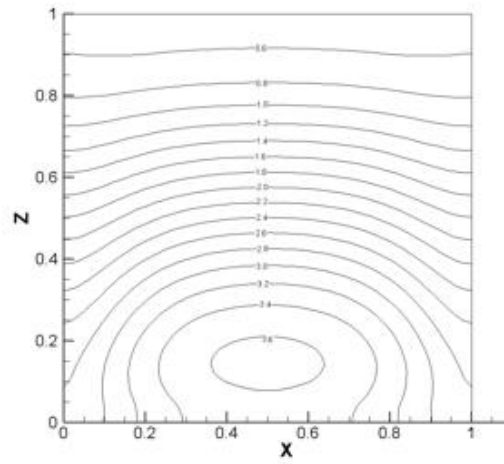
(c) X=0.5



(d) Y=0.5



(e) Z=0.5



(f) Nusselt number distribution

Figure 11-4 Type 1, temperature results, $Ra = 1 \times 10^4$

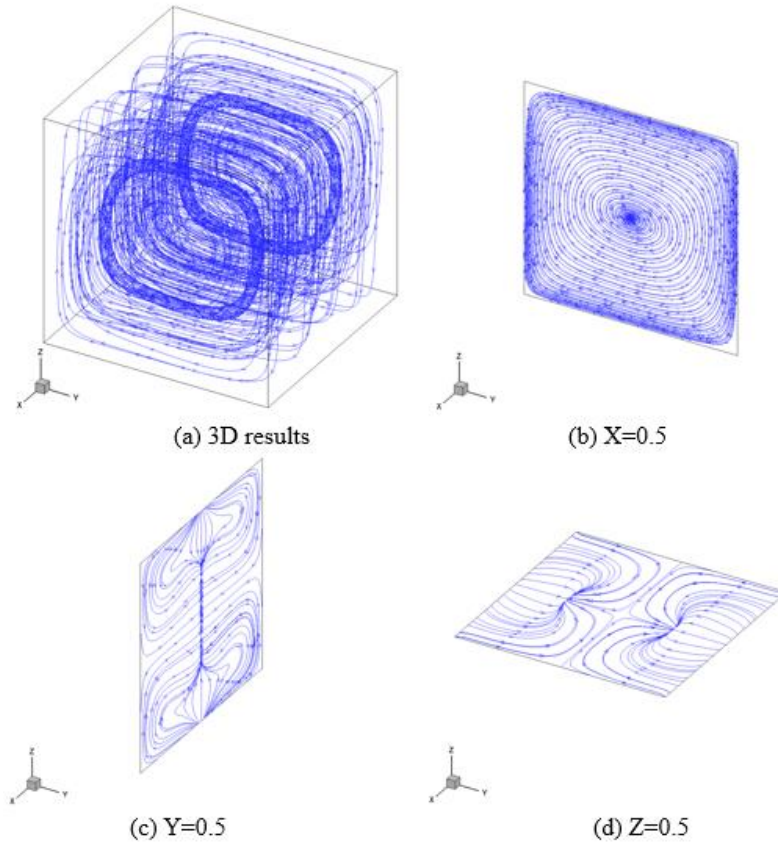


Figure 11-5 Type 1, Streamtrace results, $Ra = 1 \times 10^4$

The velocity field in the cubic cavity is also discussed. Figure 11-5 shows the streamtraces result for $Ra = 1 \times 10^4$. Its main tendency is a two-dimensional flow in the YZ plane. It also has a tendency to flow to the center of the cavity in the X -direction. Figure 11-5 (b)-(d) show the streamtraces on different locations. The results on the mid-plane of the cubic ($X=0.5$) agreed well with two-dimensional ones in Chapter 5. The results on $Y=0.5$ show that the fluid have a tendency to flow to the cavity center in the X -direction. Meanwhile, two intersections exist for the streamtraces on the surface $Z=0.5$. It indicates fluid flowing to the cavity center in the X -direction joins the two-dimensional flow in the Y and Z directions on the mid-plane of the cubic ($X=0.5$).

Type 1 problem is also discussed for $Ra = 1 \times 10^5$. Figure 11-6 shows its temperature results. Convection effect is stronger comparing with the case at lower Rayleigh number. And temperature difference between top and bottom of the cavity turns to be greater. The temperature isosurfaces' changes in the X -direction are limited. Figure 11-6 (c)-(e) are temperature distributions on different locations. Because of the boundary settings and symmetry of this problem, the working condition on mid-plane of the cubic ($X=0.5$) is still close to a two-dimensional one. The temperature field for $X=0.5$ agreed well with the two dimensional result in Chapter 5. Temperature distributions for $Y=0.5$ and $Z=0.5$ also prove that the two-dimensional assumption on the mid-plane of the cubic ($X=0.5$) is reasonable. Nusselt number distribution on the hot surface is shown in Fig. 11-6 (f). It decreases with increasing Z . Its isolines are almost parallel to the X axis except the bottom region. In that region, Nusselt number turns to be higher when closing to the mid-plane of the cubic ($X=0.5$).

Table 11-5 Type 1, Velocity comparison, $Ra = 1 \times 10^5$

	U	V	W
$50 \times 50 \times 50$	10.09	45.00	72.50
$60 \times 60 \times 60$	9.98	44.81	72.72
Ref. [127]	9.70	43.91	71.11

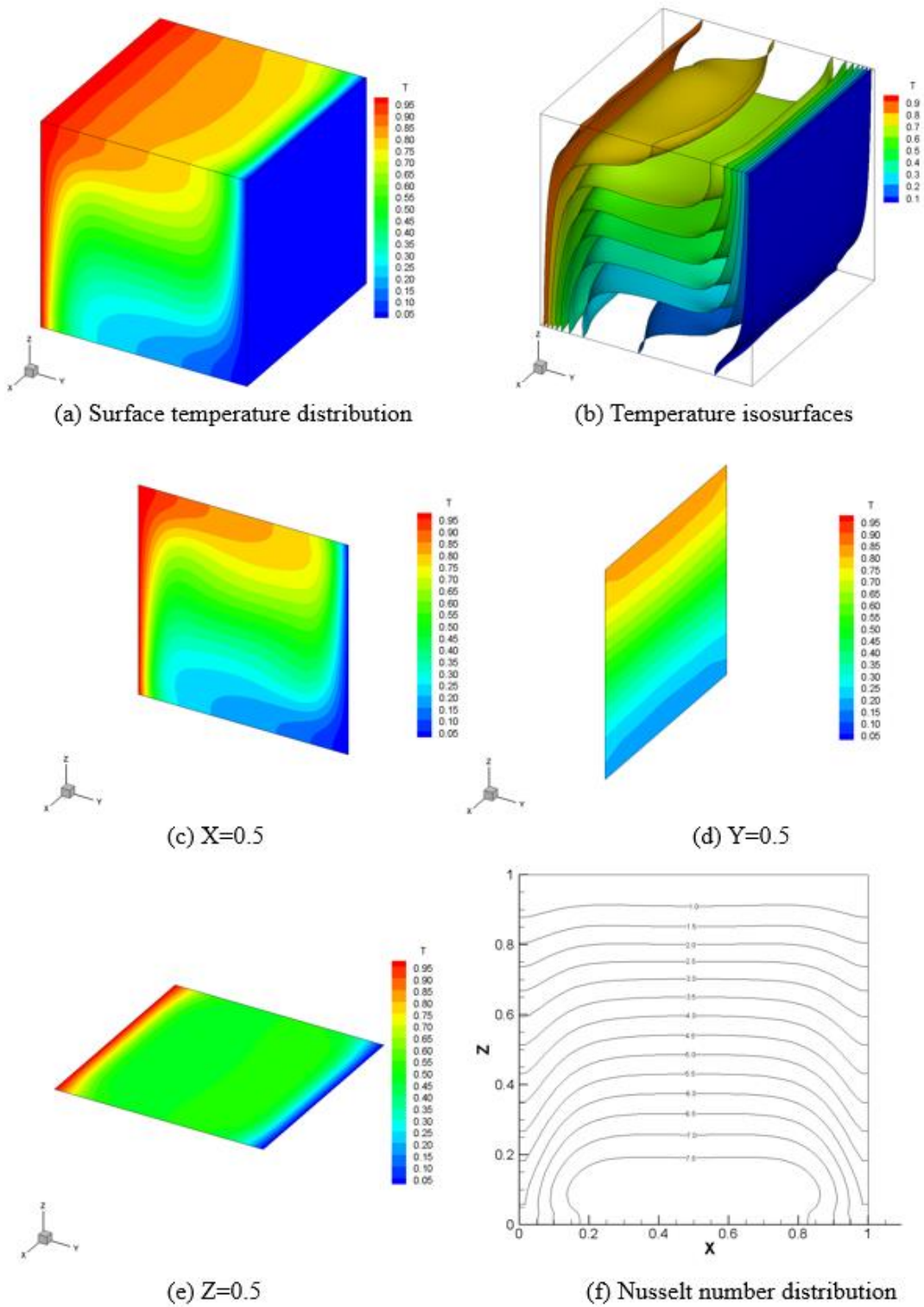


Figure 11-6 Type 1, temperature results, $Ra = 1 \times 10^5$

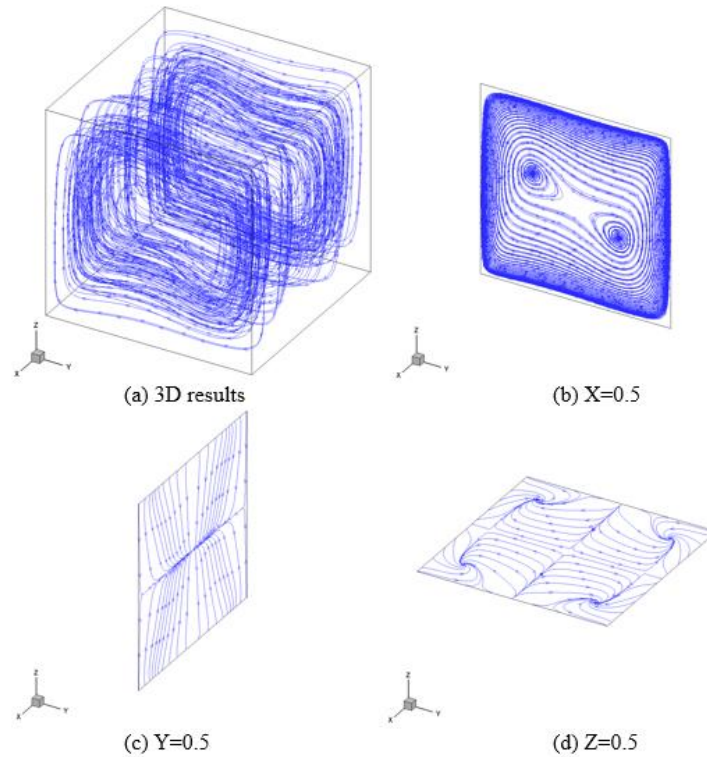


Figure 11-7 Type 1, Streamtrace results, $Ra = 1 \times 10^5$

As shown in Fig. 11-7 (a), the velocity field is more complicated and flow is stronger than that of the case of $Ra = 1 \times 10^4$. The two-dimensional flow in the Y - and Z - directions is still the main tendency. Figure 11-7 (b)-(d) include the surface streamtraces on different locations. Results on the mid-plane of the cubic ($X=0.5$) agree well with the two-dimensional ones in Chapter 5. On the surface of $Y=0.5$, fluid flows to the center in the X -direction. Four streamtrace intersections exist on the surface ($Z=0.5$). It indicates a stronger three-dimensional effect to the fluid flow.

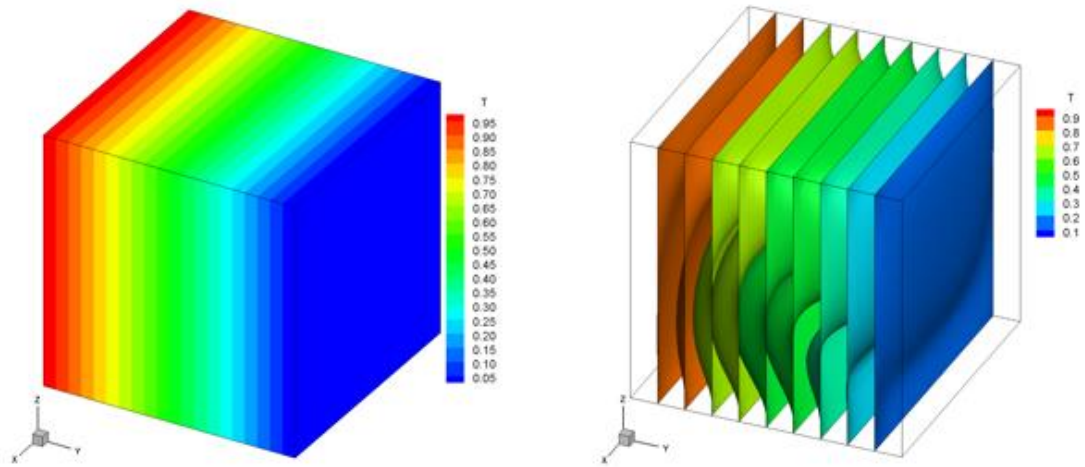
Type 1 cubic natural convection is widely used as a benchmark problem to test numerical methods for three-dimensional fluid flow and heat transfer simulations. The above results show that the proposed double MRT model is reliable for this kind of problem. Meanwhile, few references include three-dimensional visual results. Since type 1 problem

is not physically-realizable [126], we will continue to discuss type 2 cubic natural convection.

11.4.2 Type 2 natural convection

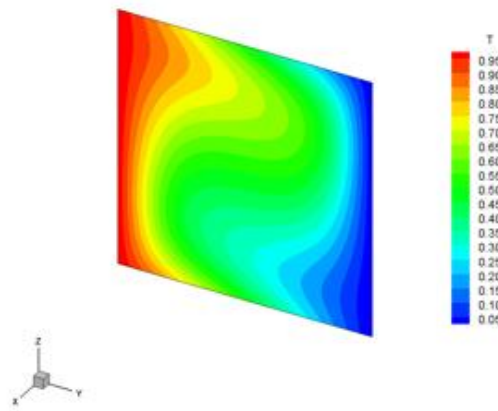
It is physically-realizable regarding its boundary condition settings in Section 2. Leong et al. [126] obtained the experimental results of $\overline{Nu_{3D}}$ for this type of natural convection. For $Ra = 1 \times 10^4$ and $Ra = 1 \times 10^5$, the present $\overline{Nu_{3D}}$ results agree with Ref. [126] ones well shown in Table 6. It also proves that the proposed double MRT model is valid for three-dimensional fluid flow and heat transfer simulation. More detailed results are included for type 2 cubic natural convection as benchmark solutions.

Figure 11-8 shows the temperature results for Type 2 problem at $Ra = 1 \times 10^4$. Hot and cold surfaces ($Y=0$ and $Y=1$) are kept at constant temperatures. The remained four side walls have linear temperature distributions in the Y-direction. The temperature isosurfaces show that convection dominates the heat transfer process. Temperature differences in the X-direction are significant. It indicates that type 2 problem has clear 3-D characteristics. Temperature distributions on different locations are shown in Figs. 11-8 (c)-(e). Results on the mid-plane of the cubic ($X=0.5$) show the convection effect. Results on the surfaces ($Y=0.5$ and $Z=0.5$) indicate that temperature differences at the center of the cavity are not significant. Figure 11-8 (f) shows the Nusselt number distribution on the hot surface for this working condition. The location at which maximum Nusselt number is reached is higher in the cavity than that in Type 1 problem with the same Rayleigh number. Nusselt number at the mid-plane of the cubic ($X=0.5$) can be lower than that in the other locations at the same height.

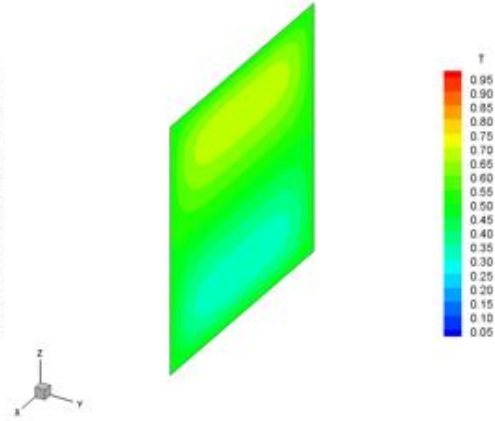


(a) Surface temperature distribution

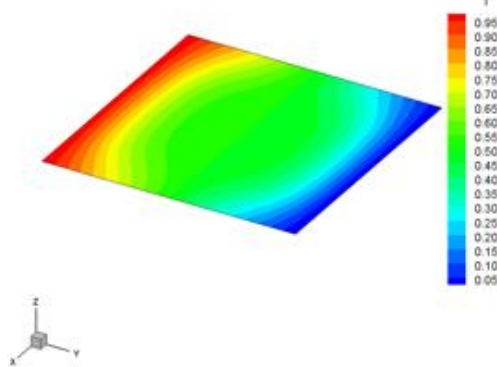
(b) Temperature isosurfaces



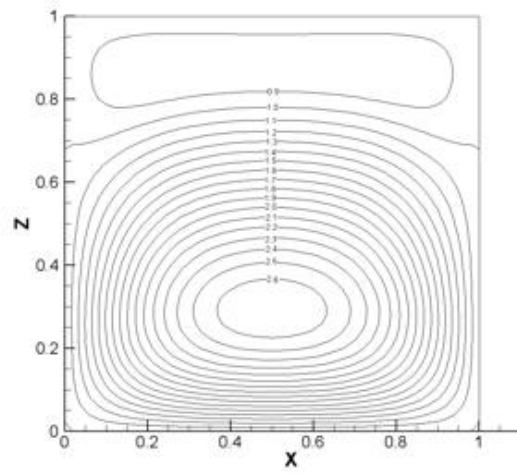
(c) X=0.5



(d) Y=0.5



(e) Z=0.5



(f) Nusselt number distribution

Figure 11-8 Type 2, temperature results, $Ra = 1 \times 10^4$

Table 11-6 Type 2, $\overline{Nu_{3D}}$ comparison

	Ref. [126]	LBM
$Ra = 1 \times 10^4$	1.52	1.49
$Ra = 1 \times 10^5$	3.10	3.06

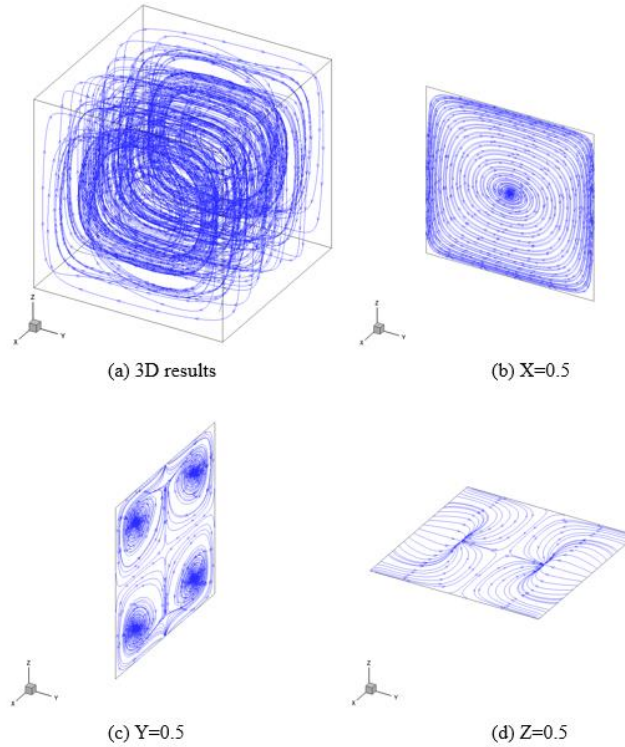


Figure 11-9 Type 2, Streamtrace results, $Ra = 1 \times 10^4$

From Fig.11- 9 (a), we can find two-dimensional flow in the Y - and Z -directions. And the flow in the X -direction is also strong. Streamtraces on different locations are shown in Figs. 11-9 (b)-(d). One vortex locates on the mid-plane of the cubic ($X=0.5$). It is quite similar to that in Type 1 problem for $Ra = 1 \times 10^4$. The surface ($Y=0.5$) has four symmetry vortexes. Streamtraces on the surface ($Z=0.5$) have two intersections. They show the flow tendency in all directions.

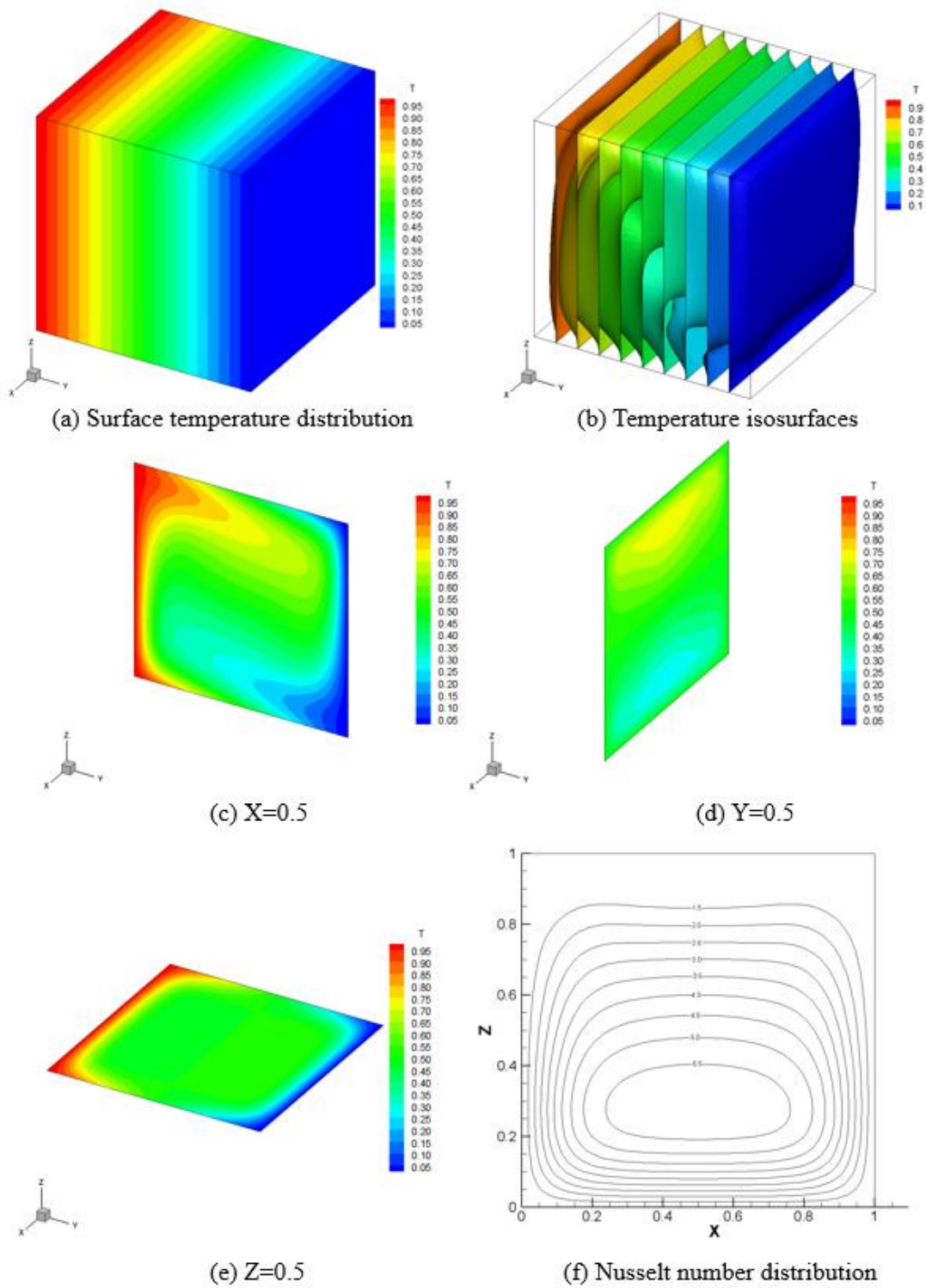


Figure 11-10 Type 2, temperature results, $Ra = 1 \times 10^5$

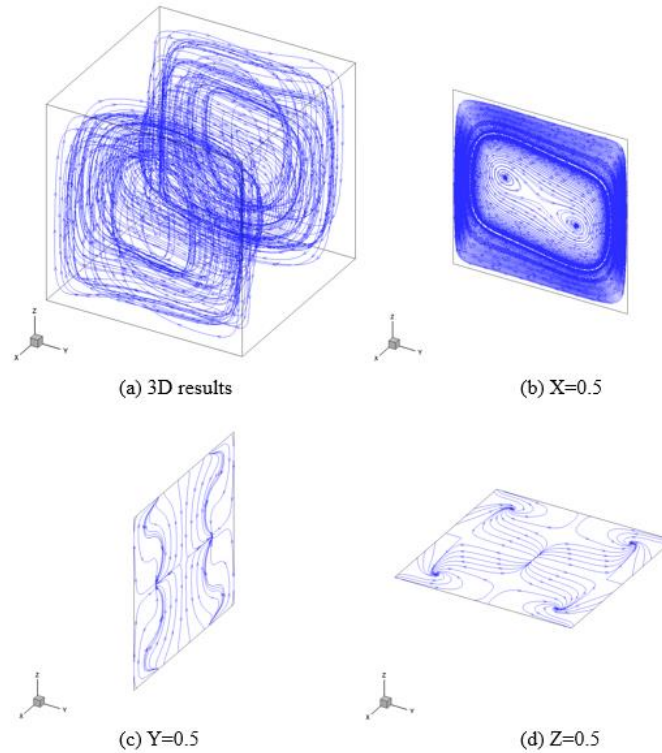


Figure 11-11 Type 2, Streamtrace results, $Ra = 1 \times 10^5$

Convection effect is more valid in Type 2 cubic natural convection when Rayleigh number is 1×10^5 as shown in Fig. 11-10. Nusselt number isolines in Fig. 11-10 (f) have similar tendency as that in Fig. 11-8 (f). The difference is that Nusselt numbers are higher due to the stronger convection effects. All three cases discussed above (Type 1 problem for $Ra = 1 \times 10^4$ and $Ra = 1 \times 10^5$; Type 2 problem for $Ra = 1 \times 10^4$) all have strong two-dimensional flows in the Y- and Z-directions. Cubic cavity streamtraces in Fig. 11-11 shows this two-dimensional flow is not as strong as that in the other cases. Moreover, Figure 11-11 (b)-(d) include streamtraces on different surfaces. Mid-plane of the cubic ($X=0.5$) have two vortices while two and four streamtraces intersections exists on the surfaces ($Y=0.5$ and $Z=0.5$), respectively. Character factors for type 2 problem with different Rayleigh numbers are shown in Table 11-7, which can be used as benchmark solutions.

Table 11-7 Type 2 benchmark solutions

	U_{\max}	V_{\max}	W_{\max}	$\overline{Nu_{2D}}$	$\overline{Nu_{3D}}$	Nu_{\max}
$Ra = 1 \times 10^4$	3.33	21.18	22.42	1.75	1.49	2.68
$Ra = 1 \times 10^5$	30.30	68.97	94.20	3.67	3.05	5.91

Comparing with Type 1 problem, Type 2 cubic natural convection has three advantages to be a benchmark problem to test numerical method for a three-dimensional fluid flow and heat transfer: (1) it is physically-realizable, (2) it has experimental results that agree well with the present numerical ones, and (3) three-dimensional effect is more valid in type 2 problem. On the other hand, type 2 temperature isosurfaces do not change a lot in the X -direction at the region close to the cubic cavity top as can be seen Figs. 11-8 and 11-10. To discuss a real three-dimensional problem, we propose Type 3 cubic natural convections.

11.4.3 Type 3 natural convection

In type 3 cubic natural convection, surfaces ($Y=0$ and $Y=1$) have constant temperatures, and side walls ($X=0$ and $X=1$) have linear temperature distributions in the Y -direction while the top and bottom of the cubic are kept adiabatic.

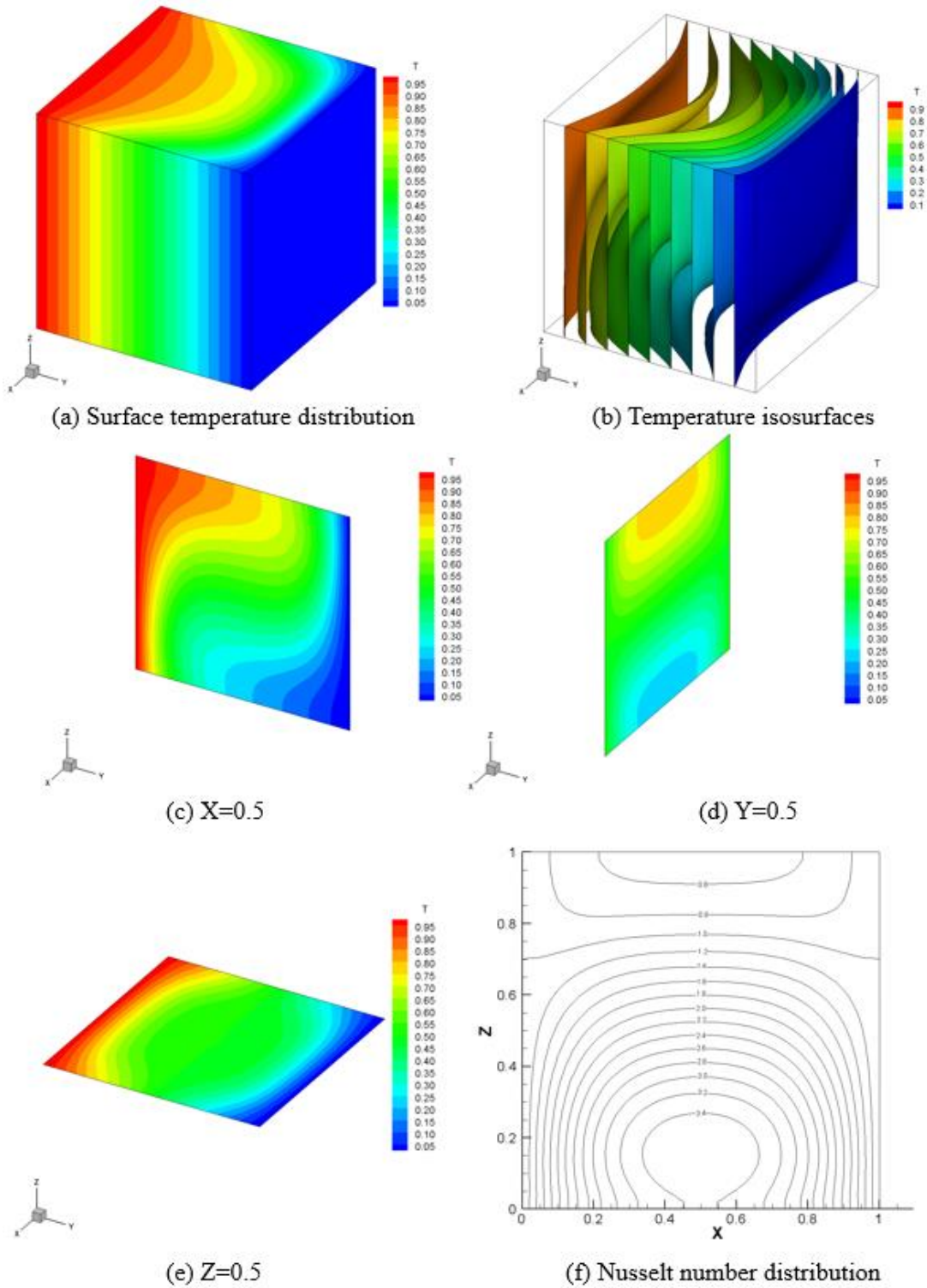


Figure 11-12 Type 3, temperature results, $Ra = 1 \times 10^4$

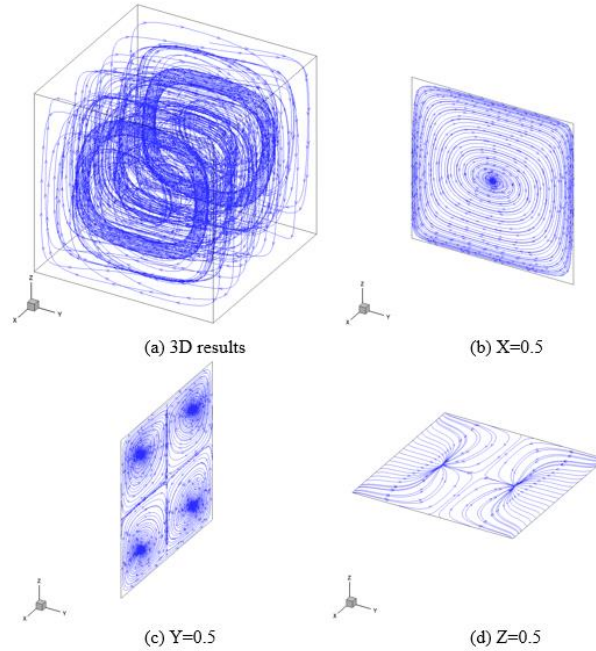


Figure 11-13 Type 3, Streamtrace results, $Ra = 1 \times 10^4$

We discuss the type 3 problem for $Ra = 1 \times 10^4$ first. Figure 11-12 (a)-(e) show the temperature field and temperature distribution on different locations for this case and three-dimensional features are clearly shown. Nusselt number distribution in Fig. 11-12 (f) is similar to that in Type 1 problem shown in Fig. 11-4 (f). For the same Rayleigh number, Nusselt numbers are lower than that in Type 1 problem and higher than that in Type 2 problem. Boundary with linear temperature distribution lowers the convection effect, comparing with the adiabatic condition. Streamtraces shown in Fig. 11-13 indicate the flow in the X -, Y - and Z -directions are all strong. Figure 11-13 (b)-(d) include the streamtraces on different locations. Mid-plane of the cubic ($X=0.5$) has one vortex, four vortices exist on the surface ($Y=0.5$), and streamtraces on the surface ($Z=0.5$) have two intersections. These results are similar to that in Type 2 problem for $Ra = 1 \times 10^4$.

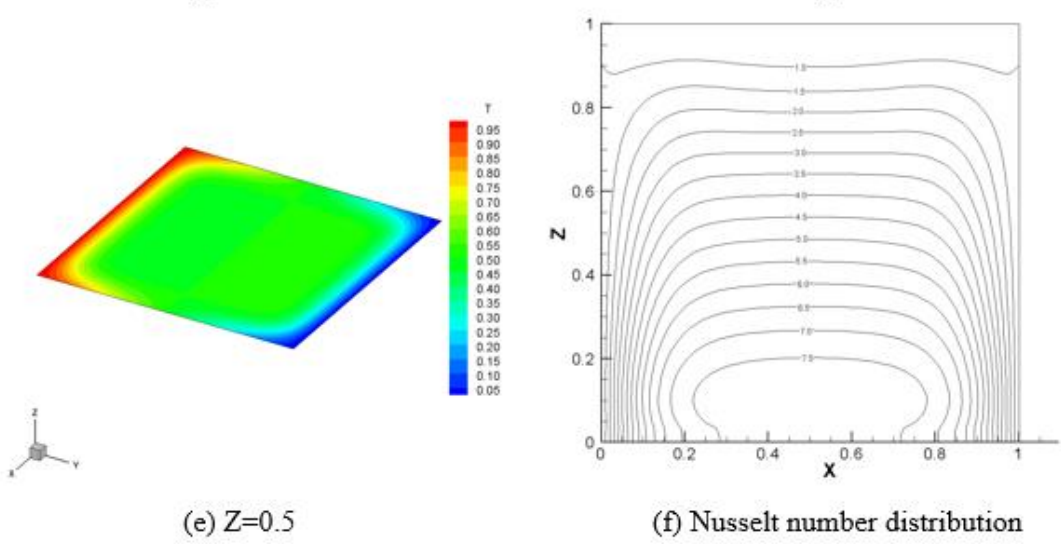
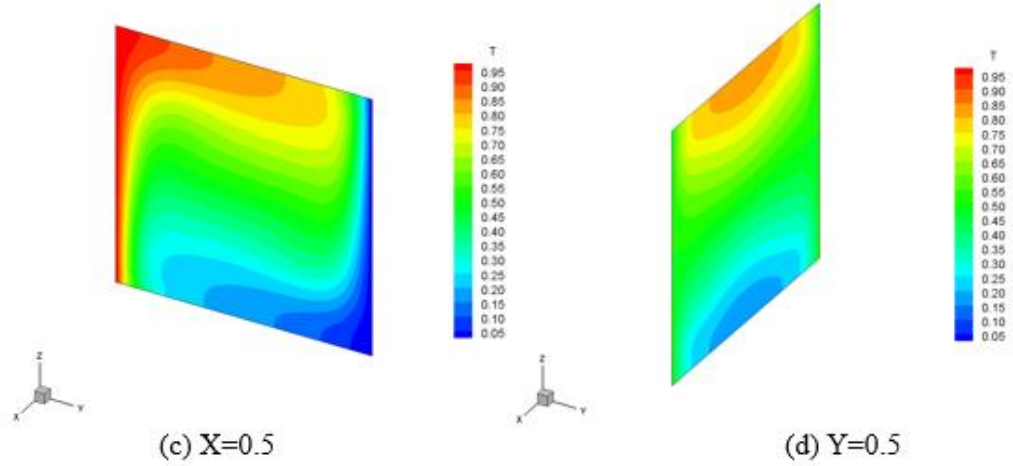
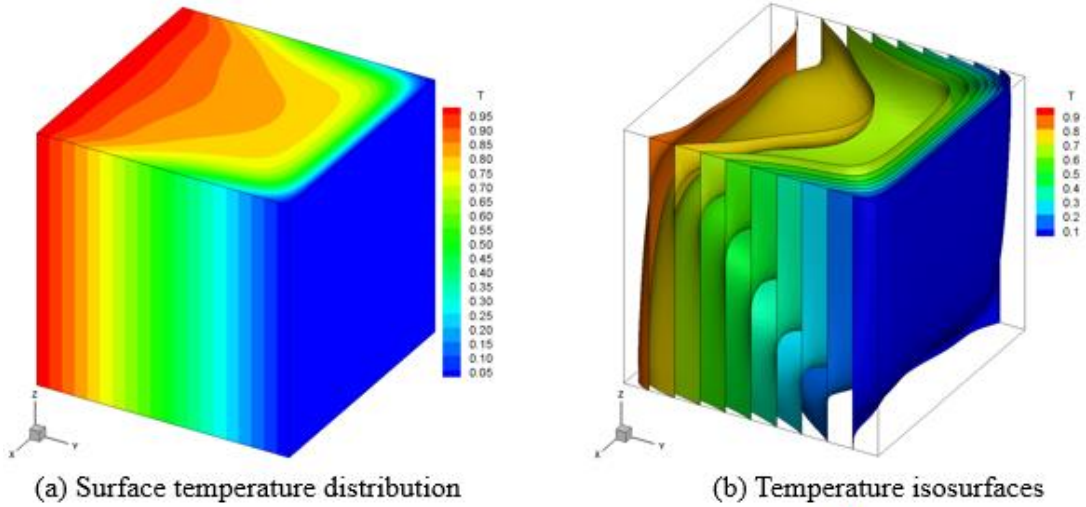


Figure 11-14 Type 3, temperature results, $Ra = 1 \times 10^5$

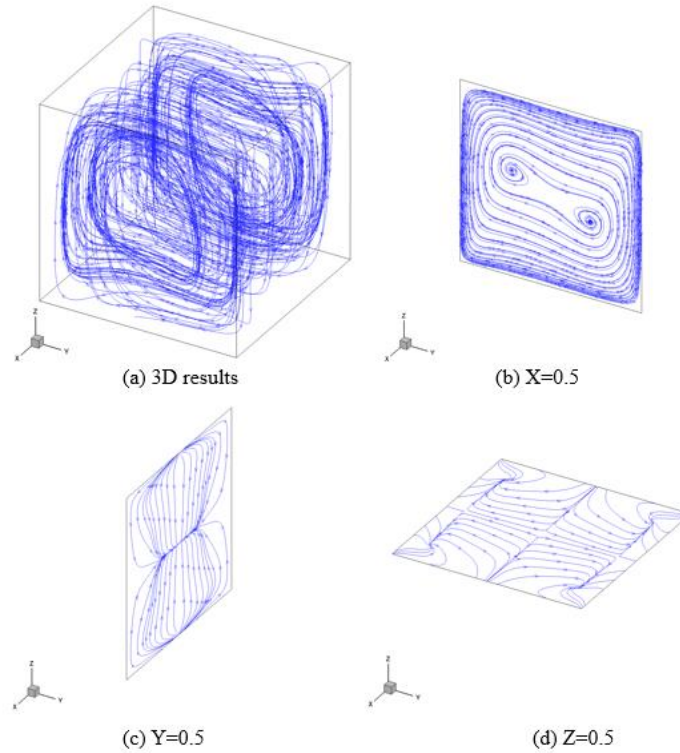


Figure 11-15 Type 3, Streamtrace results, $Ra = 1 \times 10^5$

Table 11-8 Type 3 benchmark solutions

	U_{\max}	V_{\max}	W_{\max}	\overline{Nu}_{2D}	\overline{Nu}_{3D}	Nu_{\max}
$Ra = 1 \times 10^4$	3.80	18.85	20.84	2.21	1.80	3.59
$Ra = 1 \times 10^5$	21.73	59.19	86.26	4.66	3.94	7.96

Type 3 problem is then discussed for $Ra = 1 \times 10^5$ and the results are shown in Figs.11-14 and 11-15. They show more complicated velocity and temperature fields, which have clear three-dimensional features. Temperature isosurfaces changes significantly in the X-, Y- and Z-directions. For the same Rayleigh number, Nusselt numbers for Type 3 problem are still lower than that in Type 1 problem and higher than that in Type 2 problem.

Streamtraces results indicate flow in all directions are strong. It shows clear 3-D characteristics in type 3 problem. Table 11-8 records the characteristic quantities for various Rayleigh numbers. They can be used as benchmark solutions for Type 3 problem.

11.5 Conclusions

Three-dimensional double MRT model is proposed for LBM for fluid flow and heat simulation. Three types of cubic natural convection problems with various Rayleigh numbers are solved with the proposed method. Temperature field, hot surface Nusselt number distribution, velocity field, $\overline{Nu_{2D}}$, $\overline{Nu_{3D}}$, Nu_{\max} and maximum velocities in different directions are discussed. The results of Type 1 problem agreed well with the reference ones, and the results from Type 2 problem fit the reported experimental results well. Therefore, the proposed double MRT is valid for three-dimensional simulation. Type 2 problems are more physically-realizable comparing with the type 1 problems. Their numerical results are reported for the first time. Type 3 problems are also investigated because their results have more general three-dimensional features. All these three types' 3-D natural convection results can be used as benchmark solutions for further researchers.

Chapter 12 Numerical Investigation for 3-D Melting Problems Using Lattice Boltzmann method

12.1 Introduction

In Chapters 3 to 6, various 2-D melting problems have been solved with different numerical methods and their melting fronts are all obtained using interfacial tracking method. In realistic industry applications, 3-D melting problems are more general comparing with 2-D ones. In last chapter, various 3-D natural convections have been solved with LBM. In this chapter a 3-D LBM model to solve melting problems are proposed. The velocity and temperature field in liquid PCM are solved with double MRT model in LBM, and the melting front is reached using interfacial tracking method.

12.2 Problem Statement

Physical model of melting in a cubic cavity is shown in Fig. 12-1.

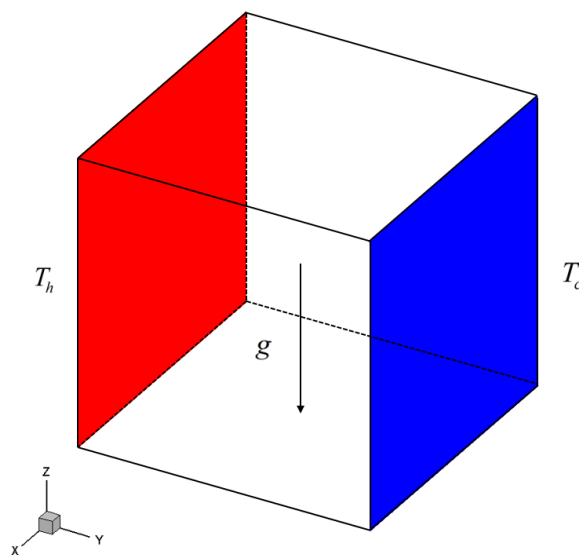


Figure 12-1 Cubic cavity melting model

The cubic cavity with an edge length of H is filled with working fluid of PCM. The left wall ($y=0$) is kept at a constant temperature T_h , which is higher than the melting temperature T_m . The right wall is also kept at a constant T_c that is below or equal to T_m . Meanwhile the top and the bottom of the enclosure are adiabatic. No slip conditions are applied to all the boundaries. The initial temperature of the system is at T_c .

The liquid PCM can be described by the following equations:

$$\frac{\partial u}{\partial x} + \frac{\partial v}{\partial y} + \frac{\partial w}{\partial z} = 0 \quad (12.1)$$

$$\rho \left(\frac{\partial u}{\partial t} + u \frac{\partial u}{\partial x} + v \frac{\partial u}{\partial y} + w \frac{\partial u}{\partial z} \right) = -\frac{\partial p}{\partial x} + \mu \left(\frac{\partial^2 u}{\partial x^2} + \frac{\partial^2 u}{\partial y^2} + \frac{\partial^2 u}{\partial z^2} \right) \quad (12.2)$$

$$\rho \left(\frac{\partial v}{\partial t} + u \frac{\partial v}{\partial x} + v \frac{\partial v}{\partial y} + w \frac{\partial v}{\partial z} \right) = -\frac{\partial p}{\partial y} + \mu \left(\frac{\partial^2 v}{\partial x^2} + \frac{\partial^2 v}{\partial y^2} + \frac{\partial^2 v}{\partial z^2} \right) \quad (12.3)$$

$$\rho \left(\frac{\partial w}{\partial t} + u \frac{\partial w}{\partial x} + v \frac{\partial w}{\partial y} + w \frac{\partial w}{\partial z} \right) = -\frac{\partial p}{\partial z} + \mu \left(\frac{\partial^2 w}{\partial x^2} + \frac{\partial^2 w}{\partial y^2} + \frac{\partial^2 w}{\partial z^2} \right) + \rho g \beta (T - T_c) \quad (12.4)$$

$$\rho \left(\frac{\partial T}{\partial t} + u \frac{\partial T}{\partial x} + v \frac{\partial T}{\partial y} + w \frac{\partial T}{\partial z} \right) = k \left(\frac{\partial^2 T}{\partial x^2} + \frac{\partial^2 T}{\partial y^2} + \frac{\partial^2 T}{\partial z^2} \right) \quad (12.5)$$

Equations (12.1)-(12.5) are subject to the following boundary and initial conditions

$$y = 0, T = T_h \quad (12.6)$$

$$y = H, T = T_c \quad (12.7)$$

$$x = 0, \partial T / \partial x = 0 \quad (12.8)$$

$$x = H, \partial T / \partial x = 0 \quad (12.9)$$

$$z = 0, \partial T / \partial z = 0 \quad (12.10)$$

$$z = H, \partial T / \partial z = 0 \quad (12.11)$$

$$u = v = w = 0 \text{ for all boundaries} \quad (12.12)$$

Melting front:

$$y = s, T = T_m \quad (12.13)$$

$$y = s, \left[1 + \left(\frac{\partial s}{\partial x} \right)^2 + \left(\frac{\partial s}{\partial z} \right)^2 \right] \left[k_s \frac{\partial T_s}{\partial y} - k_l \frac{\partial T_l}{\partial y} \right] = \rho_l h_{sl} \frac{\partial s}{\partial t} \quad (12.14)$$

Initial condition

$$t = 0, T = T_c \quad (12.15)$$

Assuming c_s is the speed of sound and defining the following non-dimensional variables

$$\left\{ \begin{array}{l} X = \frac{x}{H}, Y = \frac{y}{H}, Z = \frac{z}{H}, u_c = \sqrt{g\beta(T_h - T_m)H}, Ma = \frac{u_c}{c_s}, U = \frac{u}{\sqrt{3}c_s}, \\ V = \frac{v}{\sqrt{3}c_s}, W = \frac{w}{\sqrt{3}c_s}, \tau = \frac{t \cdot \sqrt{3}c_s}{H}, \theta = \frac{T - T_m}{T_h - T_m}, P = \frac{p}{3\rho c_s^2}, Pr = \frac{\nu}{\alpha}, \\ Sc = \frac{T_m - T_c}{T_h - T_m}, Ste = \frac{c_{pl}(T_h - T_c)}{h_{sl}}, Ra = \frac{g\beta(T_h - T_m)H^3 Pr}{\nu^2} \end{array} \right. \quad (12.16)$$

Equations (12.1)-(12.15) can be rewritten as:

$$\frac{\partial U}{\partial X} + \frac{\partial V}{\partial Y} + \frac{\partial W}{\partial Z} = 0 \quad (12.17)$$

$$\frac{\partial U}{\partial \tau} + U \frac{\partial U}{\partial X} + V \frac{\partial U}{\partial Y} + W \frac{\partial U}{\partial Z} = -\frac{\partial P}{\partial X} + Ma \sqrt{\frac{Pr}{3Ra}} \left(\frac{\partial^2 U}{\partial X^2} + \frac{\partial^2 U}{\partial Y^2} + \frac{\partial^2 U}{\partial Z^2} \right) \quad (12.18)$$

$$\frac{\partial V}{\partial \tau} + U \frac{\partial V}{\partial X} + V \frac{\partial V}{\partial Y} + W \frac{\partial V}{\partial Z} = -\frac{\partial P}{\partial Y} + Ma \sqrt{\frac{Pr}{3Ra}} \left(\frac{\partial^2 V}{\partial X^2} + \frac{\partial^2 V}{\partial Y^2} + \frac{\partial^2 V}{\partial Z^2} \right) \quad (12.19)$$

$$\frac{\partial W}{\partial \tau} + U \frac{\partial W}{\partial X} + V \frac{\partial W}{\partial Y} + W \frac{\partial W}{\partial Z} = -\frac{\partial P}{\partial Z} + Ma \sqrt{\frac{Pr}{3Ra}} \left(\frac{\partial^2 W}{\partial X^2} + \frac{\partial^2 W}{\partial Y^2} + \frac{\partial^2 W}{\partial Z^2} \right) + \frac{Ma^2 \theta}{3} \quad (12.20)$$

$$\frac{\partial \theta}{\partial \tau} + U \frac{\partial \theta}{\partial X} + V \frac{\partial \theta}{\partial Y} + W \frac{\partial \theta}{\partial Z} = Ma \sqrt{\frac{1}{3Ra \cdot Pr}} \left(\frac{\partial^2 \theta}{\partial X^2} + \frac{\partial^2 \theta}{\partial Y^2} + \frac{\partial^2 \theta}{\partial Z^2} \right) \quad (12.21)$$

$$Y = 0, \theta = 1 \quad (12.22)$$

$$Y = 1, \theta = -Sc \quad (12.23)$$

$$X = 0, \partial \theta / \partial X = 0 \quad (12.24)$$

$$X = 1, \partial \theta / \partial X = 0 \quad (12.25)$$

$$Z = 0, \partial \theta / \partial Z = 0 \quad (12.26)$$

$$Z = 1, \partial \theta / \partial Z = 0 \quad (12.27)$$

$$U = V = W = 0 \quad (12.28)$$

$$Y = S, \theta = 0 \quad (12.29)$$

$$Y = S, \frac{Ma \cdot Ste}{\sqrt{3Ra Pr}} \left[1 + \left(\frac{\partial S}{\partial X} \right)^2 + \left(\frac{\partial S}{\partial Z} \right)^2 \right] \left[\frac{k_s}{k_l} \frac{\partial \theta_s}{\partial Z} - \frac{\partial \theta_l}{\partial Z} \right] = \frac{\partial S}{\partial \tau} \quad (12.30)$$

$$\tau = 0, T = -Sc \quad (12.31)$$

Double LBM-MRT model in Chapter 11 is valid to solve 3-D natural convection problems. In this chapter, it's employed to solve the fluid flow and heat transfer process for liquid PCM. The melting front locations are obtained with interfacial tracking method, which is discussed in Chapters 8-10.

12.3 Results and Discussion

Various conduction and convection melting problems in 3-D are solved using LBM with interfacial tracking method. The conduction melting results are compared with analytical ones to verify the numerical method and convection melting problems in a cubic cavity are solve to discuss the 3-D characters in these processed.

12.3.1 Conduction melting problems

For the case the natural convection is negligible, the melting front moves at a same velocity at any height. Then this problem can be simplified to a 1-D problem governed by conduction. There is an analytical solution for this problem when Sc is equal to 0 [74] and it has been included in Section 8.4.

The cases for Stefan number equals 0.1, 0.5 and 1 are solved for validation. To compare with analytical results, Fo is used to express the non-dimensional time and it relates with τ as:

$$Fo = \tau \cdot Ma / \sqrt{3Ra \cdot Pr} \quad (12.32)$$

Figure 12-2 shows the liquid fraction comparison between numerical and analytical results and they agree with each other very well for various cases. The melting process carries on faster with the Ste increasing.

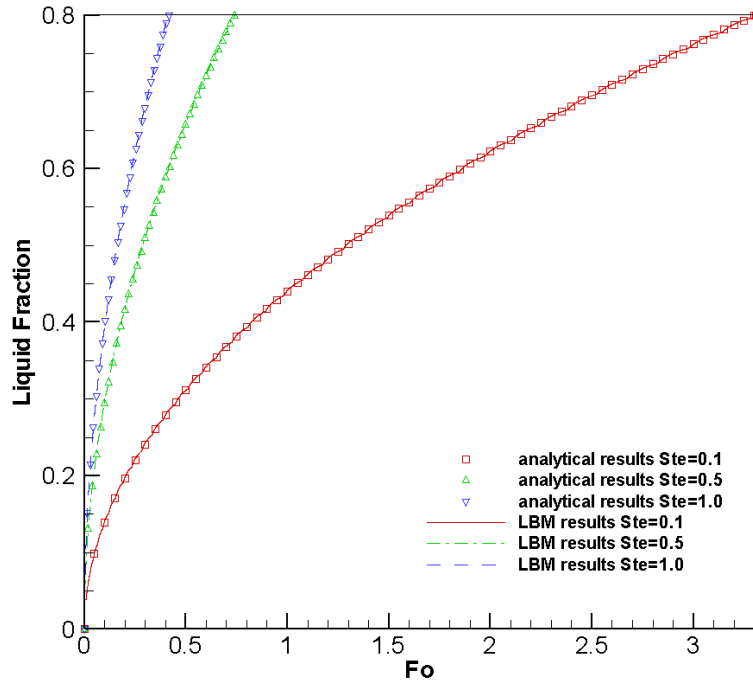


Figure 12-2 Liquid fraction comparison

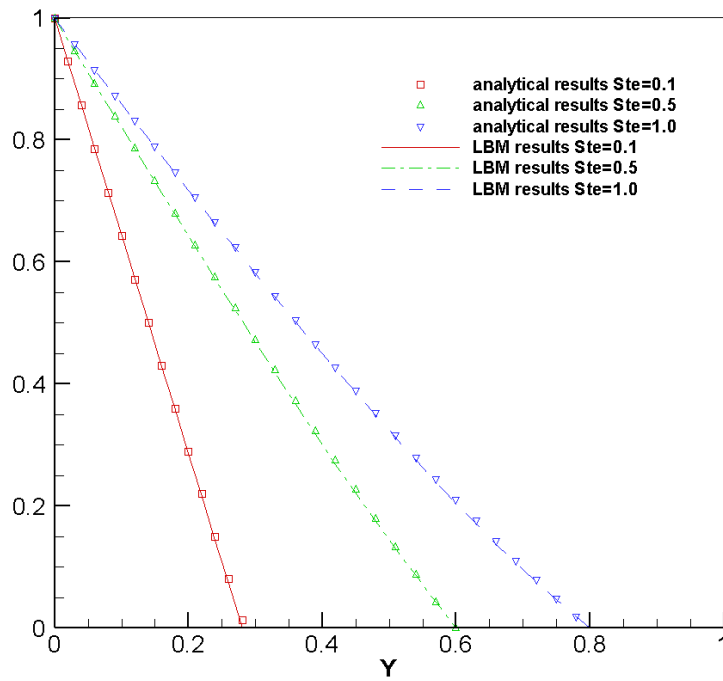


Figure 12-3 Temperature distribution comparison

Figure 12-3 shows the temperature distribution between numerical and analytical results when equals to 0.416. As discussed above, the case with higher Stefan number has shorter time to reach the same interfacial location. The temperature distribution is closer to a straight line with lower Stefan number. And it is difficult to distinguish the LBM results from the analytical result for all three cases.

The numerical results agree with analytical ones well for all three cases. The LBM with interfacial tracking method is reliable for 3-D conduction controlled melting problem. Double LBM-MRT model is valid to solve various 3-D convection problems shown in Chapter 11. It's reasonable to believe double LBM-MRT model with interfacial tracking method is valid to solve 3-D convection controlled melting problems.

12.3.2 Convection melting problems

The convection controlled melting problems in a cubic cavity can be described by the Eqs. (12.16)-(12.31). No subcooling is in consideration and three melting cases are solved using LBM with interfacial tracking method. The non-dimensional parameters in these cases are listed in Table 12-1.

Table 12-1 Two convection melting cases

	Pr	Ra	Ste
Case 1	0.02	25000	0.1
Case 2	0.02	10000	0.1

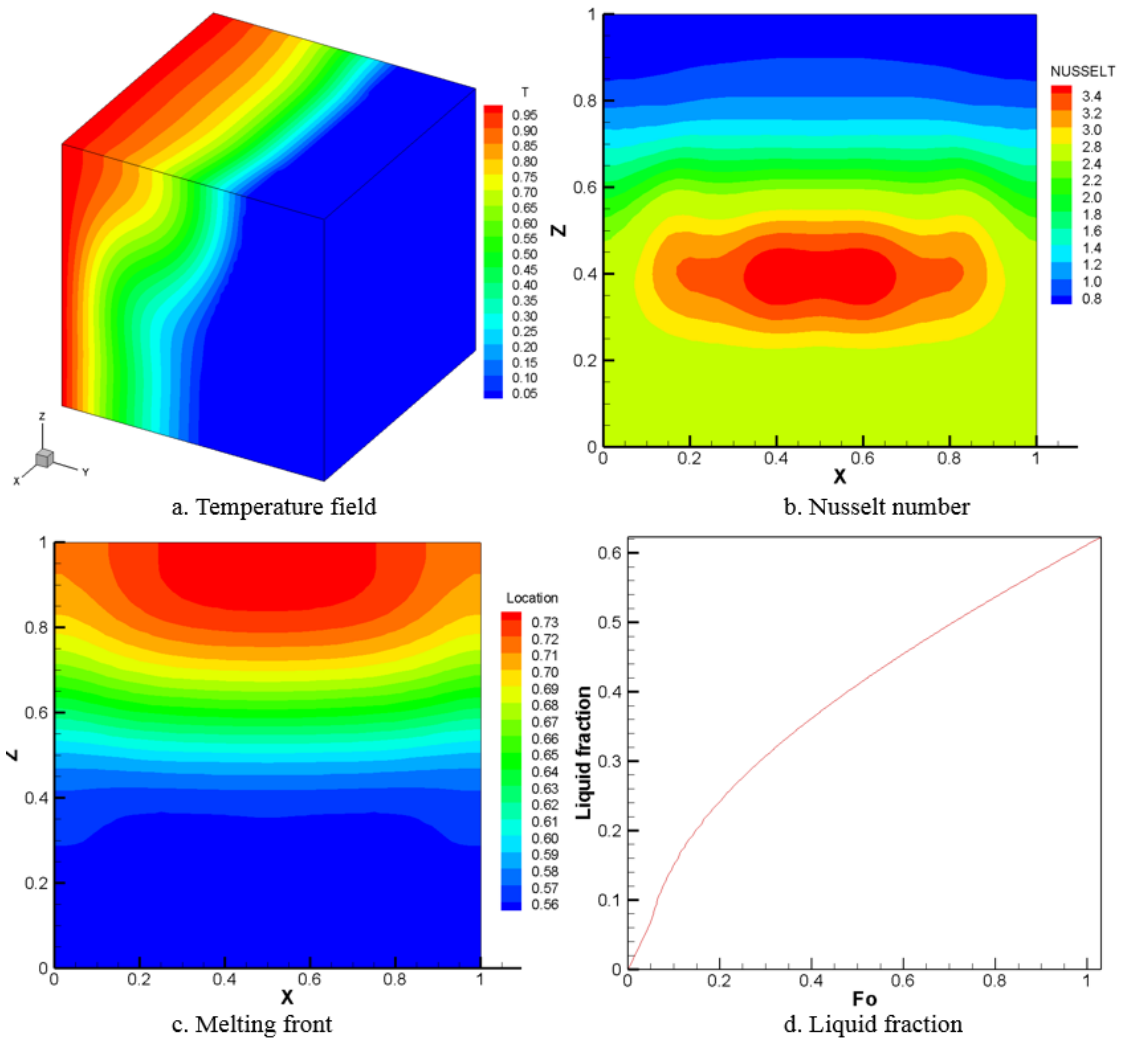


Figure 12-4 Case 1 results $Fo = 1.00$

Figure 12-4 shows case 1 results for $Fo = 1.00$. Temperature in liquid PCM grows with the height Z increasing shown from Fig. 12-4(a). It indicates that convection have controlled the melting process. Nusselt number distribution on the heat surface and melting front location are shown in Figs. 12-4 (b) and (c), which show clear three-dimensional characters. For $X=0.5$, Nusselt numbers are greater and melting fronts also moves faster than the other regions. Non-slip boundary conditions are applied to all the boundaries. The side walls ($X=0$ and $X=1$) slow the fluid flow closed to them. Consequently, the convection

effect is decreased. Liquid fraction tendency is included in Fig. 12-4(d). Comparing with the results in Chapters 8-10, this melting process is governed by conduction at the beginning and convection controlled this process later. Quasi-steady melting process is reached when the liquid fraction is linear to Fo .

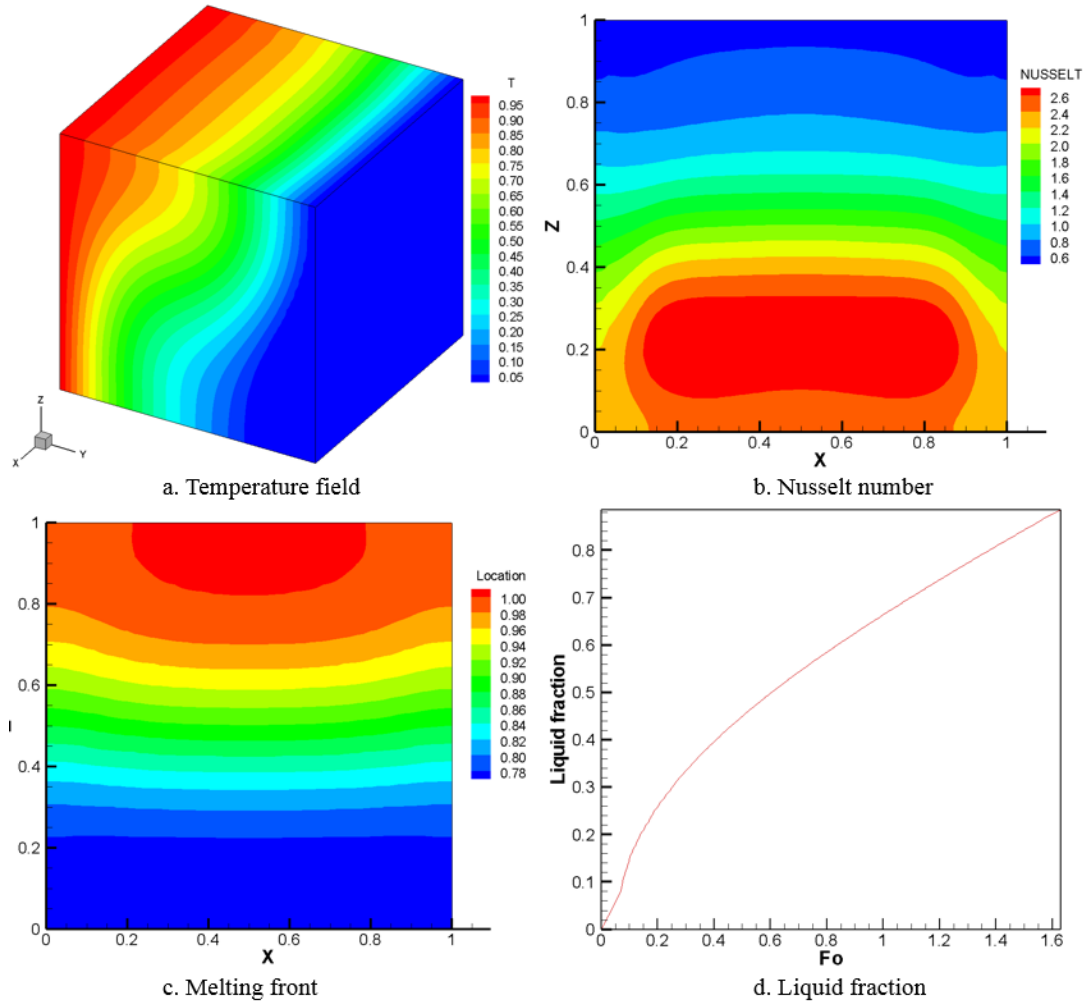


Figure 12-5 Case 2 results $Fo = 1.57$

Figure 12-5 show the case 2 result for $Fo = 1.57$. Regarding Eq. (12.32), these two cases have the same τ . Comparing with the case 1, only Ra is decreased to 10000. Convection also has controlled this melting process and the liquid PCM temperature grows

with the height increasing. From the heat surface Nusselt numbers are smaller than that in case 1, which indicates a weaker convection effect. The melting fronts at the same height don't change as much as that in case 1, which means the side wall effects are not that valid. Liquid fraction tendency is similar to that in case 1 and melting process is slower than last case.

12.4 Conclusions

Various 3-D melting problems are solved using LBM with interfacial tracking method. Numerical results in three conduction melting problems agree with the analytical results well. The double LBM-MRT model with interfacial tracking method is valid to solve 3-D melting problems. Two convection melting problems in a cubic cavity are also solved. With a lower Rayleigh number, the convection effects are weaker; side wall effects are smaller; melting process carries on slower.

Chapter 13 Conclusions

In this dissertation, LBM, FVM and various hybrid methods are employed to discuss different fluid flow and heat transfer problems. Two types of hybrid methods exist: for the first one, the whole domain is divided into multiple subdomains and different domains use various numerical methods. Message passing among subdomains decides the accuracy of this type of multiscale numerical method. For the second one, various parameters are solved with different numerical methods. In Chapter 3, two ways to fulfill first type of LBM-FVM hybrid method are proposed and they are verified by solving lid driven flow. The results indicate that nonequilibrium extrapolation scheme is suitable for the low velocity cases and finite-difference velocity gradient method is valid for the high velocity cases. Based on these results, nonequilibrium extrapolation is employed to combine LBM and FVM for natural convection simulation in Chapter 4 and various geometric settings are used for the first type of hybrid method. The results show that the proposed hybrid method is reliable to solve natural convection problems and geometric settings don't affect the accuracy. In Chapter 5, Second type of LBM-FVM hybrid method is proposed to solve convection problems: velocity field is solved using LBM; temperature field is analyzed with FVM. Second type of LBM-MCM hybrid method is proposed and verified in Chapter 6.

Various hybrid methods have been discussed in Chapters 3 to 6 for natural convection simulation. Another objective of this dissertation is solving various melting problems with different numerical methods. Melting problem can involve various PCMs. Their Prandtl numbers vary from 10^{-3} (liquid metal) to 10^5 (functional oil). Low Prandtl natural

convections are solved with double MRT thermal LBM in Chapter 7. Results can reach steady-state or oscillate depending on different non-dimensional parameters. Based on these results, low Prandtl melting problems are solved with LBM in Chapter 8 and interfacial tracking method is used to calculate the melting front location. The numerical results agreed with the analytical results for conduction controlled melting. For convection controlled melting, the agreement between the results from the present method agreed with that in the reference very well. Therefore the proposed numerical method is valid for the melting problem simulation. Interfacial tracking method is applied to solve high Prandtl melting problems in an enclosure with discrete heating at a constant rate in Chapter 9. The location of melting fronts, melting volume fraction and temperature at the surface of the heat blocks in the numerical results agreed with the experiment results well. With increasing Stefan numbers, the natural convection affects the results more quickly and significantly. When applied to the cooling process, the cooling efficiency is best when the heaters combined together. The effect of the locations of the heater on the maximum temperatures is not significant. Interfacial tracking method is further advanced with porous media assumption in Chapter 10. Various melting problem are solved with LBM-FVM hybrid method: velocity field is solved with LBM; temperature field is reached using FVM. Natural convection governed melting problems with different Stefan numbers are solved for validation. The numerical results agreed with the experimental results very well. Therefore the proposed numerical method is valid for the melting problem simulation.

In Chapters 3 to 10, two-dimensional natural convection and melting problem with various conditions are solved. Double MRT model for more general three-dimensional problems are proposed for fluid flow and heat transfer simulation in Chapter 11. Three

types of cubic natural convection problems with various Rayleigh numbers are solved with the proposed method. First type natural convection is widely used to test three-dimensional numerical method, and numerical results agree well with the reference ones; Second type of natural convection is preferred because it's physically-realizable and the numerical results are reported for the first time, which agree with the experimental ones. The proposed double MRT model is valid for fluid flow and heat transfer simulation. Third type of natural convections are also investigated because their results have more general three-dimensional features. All these three types' three-dimensional natural convection results can be used as benchmark solutions for further researchers. With the proposed double MRT model, three-dimensional melting problem are solve using interfacial tracking method in Chapter 12. Numerical results in three conduction melting problems agree with the analytical results well. The double LBM-MRT model with interfacial tracking method is valid to solve 3-D melting problems. Two convection melting problems in a cubic cavity are also solved. With a lower Rayleigh number, the convection effects are weaker; side wall effects are smaller; melting process carries on slower.

Publication list

Peer Reviewed

1. Z. Li, M. Yang, Z. Wang and Y. Zhang, A corrected method to solve convective-diffusion equation based on SIMPLE, *Journal of Engineering Thermophysics*, Vol. 33, No. 9, pp. 1563-1566, 2012-09-10.
2. Z. Li, M. Yang, Q. Chen and Y. Zhang, Numerical solution of melting in a discretely heated enclosure using an interfacial tracking method, *Numerical Heat Transfer, Part A: Applications*, Vol. 64, No. 11, pp. 841-857, 2013-12-01.
3. Z. Li, M. Yang and Y. Zhang, Hybrid lattice Boltzmann and finite volume method for Natural Convection, *Journal of Thermophysics and Heat Transfer*, Vol. 28, No. 1, pp. 68-77, 2014-01-07.
4. Z. Li, M. Yang and Y. Zhang, A coupled lattice Boltzmann and finite volume method for natural convection simulation, *International Journal of Heat and Mass Transfer*, Vol. 70, pp. 864-874, 2014-03-31.
5. Z. Li, M. Yang and Y. Zhang, Hybrid lattice and finite volume methods for fluid flow problem, *International Journal for Multiscale Computational Engineering*, Vol. 12, No. 3, pp. 177-192, 2014-05-19.
6. Z. Li, M. Yang, and Y. Zhang, A hybrid lattice Boltzmann and finite volume method for melting with natural convection, *Numerical Heat Transfer, Part B: Fundamentals*, Vol. 66, No. 4, pp. 307-325, 2014-08-25.
7. Z. Li, M. Yang and Y. Zhang, Numerical Simulation of Melting Problems Using the Lattice Boltzmann Method with the Interfacial Tracking Method, *Numerical Heat Transfer, Part A: Applications*, Vol. 68, No. 11, pp. 1175-1197, 2015-06-23.

8. Z. Li, M. Yang and Y. Zhang, A hybrid lattice Boltzmann and Monte Carlo method for natural convection simulation, *International Journal for Multiscale Computational Engineering*, Vol. 13, No. 4, pp. 297-309, 2015-08-28.
9. Z. Li, M. Yang and Y. Zhang, Double MRT thermal lattice Boltzmann method for simulating natural convection of low Prandtl number fluids, *International Journal of Numerical Methods for Heat and Fluid Flow*, Vol. 26, No. 5. In press, 2016.
10. Z. Li, M. Yang, Y. Zhang and S. Montgomery-Smith. Effects of initial conditions on oscillatory flow in an oscillating heat pipe. Under review, 2015
11. Z. Li, M. Yang, Y. He and Y. Zhang. Mass balance in velocity Dirichlet boundary conditions for lattice Boltzmann method. Under review, 2015
12. Z. Li, M. Yang and Y. Zhang, Lattice Boltzmann method simulation of 3-D natural convection with double MRT model. *International Journal of Heat and Mass Transfer*. Accepted, 2015.

Not Peer reviewed

1. Z. Li, M. Yang and Y. Zhang, Numerical investigations on three-dimensional melting problem using lattice Boltzmann method. Ready to submit, 2015

Reference

1. Succi S. *Lattice Boltzmann Method for Fluid Dynamics and Beyond*: Oxford University Press; 2001.
2. Zou Q., Hou S., Chen S., Doolen G. “An improved incompressible lattice Boltzmann model for time-independent flows,” *Journal of Statistical Physics*, 1995; 81(35); pp: 35-48.
3. Chen S., Doolen G., “Lattice Boltzmann method for fluid flows,” *Annual Review of Fluid Mechanics*, 1998, 30, pp: 329-364.
4. Chatterjee D., “Lattice Boltzmann simulation of incompressible transport phenomena in macroscopic solidification processes,” *Numerical Heat Transfer, Part B: Fundamentals*, 2010, 58(1), pp: 55-72.
5. Inamuro T., Sturtevant B., “Numerical study of discrete-velocity gases,” *Physics of Fluids*, 1990, 2: pp: 2196–2203.
6. Yu D., Mei R., Luo L., Shyy W., “Viscous flow computations with the method of lattice Boltzmann equation,” *Progr. Aerosp. Sciences*, 2003, 39, pp: 329–367,.
7. Chapman S., Cowling T., *The Mathematical Theory of Non-uniform Gases*. 3rd edition. Cambridge: Cambridge University Press, 1970.
8. Guo Z., Zhao T., “Lattice Boltzmann model for incompressible flow through porous media,” *Physical Review E*, 2002, 66(2), 162-173.
9. Kataoka T., Tsutahara M., “Lattice Boltzmann model for the compressible Navier-Stokes equations with flexible specific-heat ratio,” *Physical Review E*, 2004, 69, 287-316.
10. Luo L., “Theory of the lattice Boltzmann method: Lattice Boltzmann models for

- nonideal gases,” *Physical Review E*, 2000, 62, 49-82.
11. Darbandi M., Vakilipour S., “Developing consistent inlet boundary conditions to study the entrance zone in microchannels,” *Journal of Thermophysics and Heat Transfer*, 2007, 21, p: 3.
 12. Esfahani J., Alinejad A., “Entropy generation of conjugate natural convection in enclosures: the lattice Boltzmann method,” *Journal of Thermophysics and Heat Transfer*, 2013, 27, p: 3.
 13. Gupta N., Gorthi R., Mishra S., “Lattice Boltzmann method applied to variable thermal conductivity conduction and radiation problems,” *Journal of Thermophysics and Heat Transfer*, 2006, 20, p: 4.
 14. He X., Chen S., Doolen G., “A novel thermal model for the lattice Boltzmann method in incompressible limit,” *Journal of Computational Physics*, 1998, 146, pp: 282–300.
 15. Peng Y., Shu C., Chew Y., “Simplified thermal lattice Boltzmann model for incompressible thermal flows,” *Physical Review E*, 2003, 68(2), pp: 125-149.
 16. Guo Z., Shi B., Zheng C., A coupled lattice BGK model for the Boussinesq equations, *Int. J. Numer. Methods Fluids*, 2002, 39, pp: 325–342.
 17. Huber C., Parmigiani A., Chopard B., Manga M., Bachmann O., “Lattice Boltzmann model for melting with natural convection,” *International Journal of Heat and Fluid Flow*, 2008, 29, pp: 1469-1480.
 18. Choi S., Kim S., Lee T., Kim Y. and Hahn D., “Computation of turbulent natural convection in a rectangular cavity with the lattice Boltzmann method,” *Numerical Heat Transfer, Part B: Fundamentals*, 2012, 61(6), pp: 492-504.
 19. Novozhilov V., Byrne C., “Lattice Boltzmann modeling of thermal explosion in natural

- convection conditions,” *Numerical Heat Transfer, Part A: Applications*, 2013, 63(11), pp: 824-839.
20. Kefayati G., “Simulation of ferrofluid heat dissipation effect on natural convection at an inclined cavity filled with kerosene/cobalt utilizing the lattice Boltzmann method,” *Numerical Heat Transfer, Part A: Applications*, 2014, 65(6), pp: 509-530.
 21. Orazio A., Succi S., “Simulating two-dimensional thermal channel flows by means of a lattice Boltzmann method with new boundary conditions,” *Future Generation Comput. Syst.*, 2004, 20, pp: 935-944.
 22. Chen Y., Ohashi H., Akiyama M., “Thermal lattice Bhatnagar–Gross–Krook model without nonlinear deviations in macrodynamic equations,” *Physics Review E*, 1994, 50, pp: 2776 –2783.
 23. Patankar S. V., *Numerical Heat Transfer and Fluid Flow*: McGraw-Hill Book Co., 1980.
 24. Tao W. Q., *Numerical Heat transfer*: Xi’an Jiaotong University Press, 2001.
 25. Abraham F., “Dynamically spanning the length scales from the quantum to the continuum,” *Int. J. Mod. Phys. C*, 2000, 11, pp: 1135-1148.
 26. Grest G., Kremer K., “Molecular dynamics simulation for polymers in the presence of a heat bath,” *Phys. Rev. A*, 1986, 33, pp: 3628–3631.
 27. Pomeau Y., “20 Years of Lattice Dynamics: A Personal view,” *International Journal of Modern Physics C*, 2007, 18(4), pp: 437-446.
 28. Anderson J., *Computational fluid dynamics*: McGraw-Hill Education, 1995.
 29. Versteeg H., Malalasekera W., *An introduction to computational fluid dynamics: the finite volume method approach*: Prentice Hall, 1996.
 30. Kandhai D., Vidal D, Hoekstra A., ”Lattice-Boltzmann and finite element simulations

- of fluid flow in a SMRX static mixer reactor,” *Int. J Numer. Methods Fluids*, 1999, 31, pp: 1019-1033.
31. Nie X., Chen S., “A continuum and molecular dynamics hybrid method for micro- and nano-fluid flow,” *J. Fluid Mech.*, 2004, 500, pp: 55-64.
 32. Flekkoy E., Wagner G., Feder J., “Hybrid model for combined particle and continuum dynamics,” *Europhys. Lett.*, 2000, 52, pp: 271–276,.
 33. O’Connell S., Thompson P., “Molecular dynamics-continuum hybrid computations: A tool for studying complex fluid flows,” *Phys. Rev. E*, 1995, 52, 5792–5795.
 34. Dupuis A., Kotsalis E., Koumoutsakos P., “Coupling lattice Boltzmann and molecular dynamics models for dense fluids,” *Phys. Rev. E*, 2007, 75, 046704.
 35. Werder T., Walther J., Koumout P., “Hybrid atomistic-continuum method for the simulation of dense fluid flows,” *Journal of Computational Physics*, 2005, 205(1), pp: 373-390.
 36. Fedosov D., Karniadakis G., “Interfacing atomistic–mesoscopic–continuum flow regimes,” *Journal of Computational Physics*, 2009, 228(4), pp: 1157–1171.
 37. Christensen A., Graham S., “Multiscale lattice Boltzmann modeling of phonon transport in crystalline semiconductor material,” *Numer. Heat Transfer Part B*, 2010, 57, pp: 89-109,.
 38. Albuquerque P., Alemansi D., Chopard B., Leone P., “Coupling a lattice Boltzmann and finite difference scheme,” *International Conference on Computational Science*, Krakow, Poland, 2004.
 39. Latt J., Hydrodynamic Limit of Lattice Boltzmann Equations, PhD Thesis. University of Geneva 2007.

40. Latt J., Chopard B., Straight velocity boundaries in the lattice Boltzmann method, *Physical Review E*, 2008, 77, 056703.
41. Mondal B., Mishra S., “Lattice Boltzmann method applied to the solution of the energy equations of the transient conduction and radiation problems on non-uniform lattices,” *Int. J. Heat Mass Transfer*, 2008, 51, 68–82.
42. Joshi H., Agarwal A., Puranik B., Shu C., Agrawal A., “A hybrid FVM-LBM method for single and multi-fluid compressible flow problems,” *Int. J. Numer. Methods Fluids*, 2010, 62, 403–427.
43. Mondal B., Mishra S., “The lattice Boltzmann method and the finite volume method applied to conduction–radiation problems with heat flux boundary conditions,” 2009, 78(2), pp: 172-195.
44. Luan H., Xu H., Chen L., “Coupling of finite volume method and thermal lattice Boltzmann method and its application to natural convection,” *Int. J. Numer. Meth. Fluids*, 2012, 70, pp: 200-221.
45. Luan H., Xu H., Chen L., “Evaluation of the coupling scheme of FVM and LBM for fluid flows around complex geometries,” *International Journal of Heat and Mass Transfer*, 2011, 54, pp: 1975-1985.
46. Chen L., He Y., Kang Q., Tao W., “Coupled numerical approach combining finite volume and lattice Boltzmann methods for multi-scale multi-physicochemical,” *Journal of Computational Physics*, 2013, 255(15), pp: 83-105.
47. Mohamad A., Kuzmin A., “A critical evaluation of force term in lattice Boltzmann method, natural convection problem,” *International Journal of Heat and Mass Transfer*, 2010, 53, 990-99.

48. Choi S., Kim S., “Comparative analysis of thermal models in the lattice Boltzmann method for the simulation of natural convection in a square cavity,” *Numerical Heat Transfer, Part B: Fundamentals*, 2011, 60, pp: 2.
49. Chrison M., Gresho P., Sutton S., “Computational predictability of time-dependent natural convection flows in enclosure,” *Int. J. Numer. Meth Fluid*, 2002, 40, 953-980.
50. Zhang K., Yang M., Zhang Y., “A compact finite difference scheme based on projection method for natural convection heat transfer,” *Numerical Heat Transfer, Part B: Fundamentals*, 2012, 61, pp: 259-278.
51. Nie X., Shan X., Chen H., “A lattice-Boltzmann/ finite-difference hybrid simulation of transonic flow,” *47th AIAA Aerospace Sciences Meeting Including the New Horizons Forum and Aerospace Exposition*, 5-8 January 2009, Orlando, Florida.
52. Mezrhab A., Bouzidi M., Lallemand P., “Hybrid lattice-Boltzmann finite-difference simulation of convective flows,” *Computers & Fluids*, 2004, 33, pp: 623–641.
53. Peng G., Xi H., Duncan C., Finite volume scheme for the lattice Boltzmann method on unstructured meshes, *Physical Review E*, 1999, 59, pp: 4675-4682.
54. Mishra S., Roy H., Solving transient conduction and radiation heat transfer problems using the lattice Boltzmann method and the finite volume method, *Journal of Computational Physics*, 2007, 23, pp: 89-107.
55. Howell J., The Monte Carlo method in radiative heat transfer. *Journal of heat transfer*, 1998, 120(3), pp: 547-560.
56. Haji-Sheikh A., Sparrow E., “The solution of heat conduction problems by probability methods,” *Journal of Heat transfer*, 1961, 89(2), pp: 121-131.
57. Chandler R., Panaia J., Stevens R., Zinsmeister G., “The solution of steady state

- convection problems by the fixed random walk method,” *Journal of Heat transfer*, 1968, 90(3), pp: 361-363.
58. Perlmutter M., Howell J., “Radiant transfer through a gray gas between concentric cylinders using Monte Carlo,” *Journal of Heat Transfer*, 1964, 86(2), pp: 169-179.
59. Hannoun N., Alexiades V., Mai T., “Resolving the controversy over tin and gallium melting in a rectangular cavity heated from the side,” *Numerical Heat Transfer, Part B: Fundamentals*, 2003, 44(3), pp: 253-275.
60. Hu H., Argyopoulos S., “Mathematical modelling of solidification and melting: a review,” *Modelling and Simulation in Materials Science and Engineering*, 1996, 4(4), pp: 371-396.
61. Goodman T., Shea J., “The melting of finite slabs,” *Journal of Applied Mechanics*, 1960, 27(1), pp: 16-27.
62. Bell G. E., “A refinement of the heat balance integral method applied to a melting problem,” *Int. J. Heat Mass Transfer*, 1978, 21(11), pp: 1357-1362.
63. Jany P., Bejan A., “Scaling theory of melting with natural convection in an enclosure,” *International Journal of Heat and Mass Transfer*, 1988, 31(6), pp: 1221-1235.
64. Zhang Z., Bejan A., “The problem of time-dependent natural convection melting with conduction in the solid,” *International Journal of Heat and Mass Transfer*. 1989, 32(12), pp: 2447-2457.
65. Zhang Y., Chen Z.. Effect of wall conduction on melting in an enclosure heated by constant rate, *Int. J. Heat Fluid Flow*, 1994, 15, pp: 79-82.
66. Okada M., “Analysis of heat transfer during melting from a vertical wall,” *International Journal of Heat and Mass Transfer*, 1984, 27(11), pp: 2057-2066.

67. Zhang Z., Bejan A., Melting in an enclosure heated at constant rate, *International Journal of Heat Mass Transfer*, 1989, 32(6), pp: 1063-1076.
68. Zhang Y., Chen Z., Wang Q., Wu Q., “Melting in an enclosure with discrete heating at a constant Rate,” *Experimental Thermal and Fluid Science*, 1993, 6(2), pp: 196-201.
69. Ju Y., Chen Z., Zhou Y., “Experimental study of melting heat transfer in an enclosure with three discrete protruding heat source,” *Experimental Heat Transfer*, 1998, 11, pp: 171-186.
70. Benard C., Gobin D., Martinez F., “Melting in rectangular enclosures: experiments and numerical simulations,” *Journal of Heat Transfer*, 1985, 107, pp: 794-803.
71. Dong Z., Chen Z., Wang Q., Ebdian M., “Experimental and analytical study of contact melting in a rectangular cavity,” *Journal of thermophysics and Heat Transfer*, 1991, 5(3), pp: 347-354.
72. Wang Y., Amiri A., Vafai K.. “An experimental investigation of the melting process in a rectangular enclosure,” *International Journal of Heat and Mass Transfer*, 1999, 42(19), 3659-3672.
73. Bertrand O., Binet B., Combeau H., Couturier S., Delannoy Y., Gobin D., Lacroix M., Quere P., Medale M., Mencinger J., Sadat H, Vieira G., “Melting driven by natural convection A comparison exercise: first results,” *International of Journal of Thermal Sciences*, 1999, 38(1), pp: 5-26.
74. Faghri A., Y. Zhang. Transport phenomena in multiphase system. Elsevier, Burlington, MA, 2006.
75. Voller V.. An overview of numerical methods for solving phase change problems. *Advances in Numerical Heat Transfer*, Vol. 1, W. J. Minkowycz and E. M. Sparrow,

- eds., Taylor & Francis, Basingstoke.
76. Ho C., Viskanta R., "Heat Transfer during Melting from an Isothermal Vertical Wall," *J. Heat Transfer*, 1984, 106, 12-19.
 77. Shamsundar N., Sparrow E., "Analysis of multidimensional conduction phase change via the enthalpy model," *Journal of Heat Transfer*, 1975, 97, 333-340.
 78. Voller V., Prakash C., "A fixed grid numerical modeling methodology for convection-diffusion mushy region phase-change problems," *International Journal of Heat and Mass Transfer*, 1987, 30, 1709-1719.
 79. Morgan K., "A numerical analysis of freezing and melting with convection," *Computer Methods in Applied Mechanics and Engineering*, 1981, 28, 275-284.
 80. Hsiao J., "Analyses of heat transfer with melting and solidification," *Numerical Heat Transfer*, 1985, 8, 653-666.
 81. Sasaguchi K., Ishihara A., Zhang H., "Numerical study on utilization of melting of phase change material for cooling of a heated surface at a constant rate," *Numerical Heat Transfer Part A: Applications*, 1996, 29, 19-31.
 82. Binet B., Lacroix M., "Numerical study of natural-convection-dominated melting inside uniformly and discretely heated rectangular cavities," *Numerical Heat Transfer, Part A: Applications*, 1998, 33, 207-224.
 83. Ganaoui M., Semma E., "Lattice Boltzmann coupled to finite volumes method for solving phase change problems," *Thermal Science*, 2009, 13(2), 205-216.
 84. Cao Y., Faghri A., "A numerical analysis of phase-change problem including natural convection," *Journal of Heat Transfer*, 1990, 112(3), 812-816.
 85. Gao D., Chen Z., "Lattice Boltzmann simulation of natural convection dominated

- melting in a rectangular cavity filled with porous media,” *International of Journal of Thermal Sciences*, 2011, 50(4), 493-501.
86. Semma E., Gananoui M., Bennacer R., Mohamad A., “Investigation of flows in solidification by using the lattice Boltzmann method,” *International Journal of Thermal Sciences*, 2008, 47, 201-208.
87. Jourabian M., Faehadi M., Sedighi K., Darzi A., Vazifeshenas Y., “Melting of NEPCM within a cylindrical tube: numerical study using the lattice Boltzmann method,” *Numerical Heat Transfer, Part A: Applications*, 2012, 61, 12, 929-948.
88. Miller W., Succi S., Mansutti D., “Lattice Boltzmann model for anisotropic liquid-solid phase transition,” *Physical Review Letters*, 2001, 86, 3578-3581.
89. Eshraghi M., Felicelli S., “An implicit lattice Boltzmann model for heat conduction with phase change,” *International Journal of Heat and Mass Transfer*, 2012, 55, 2420-2428.
90. Zhang Y., Chen J., “An interfacial tracking method for ultrashort pulse laser melting and resolidification of a thin metal film,” *Journal of Heat Transfer*, 2008, 130, 0624011-06240110.
91. Chen Q., Zhang Y., Yang M., “An Interfacial Tracking Model for Convection-controlled melting problem,” *Numerical Heat Transfer, Part B: Fundamentals*, 2011, 59(3), 209-225.
92. Kosec G., Sarler B., “Solution of a low Prandtl number natural convection benchmark by a local meshless method,” *International Journal of Numerical Methods for Heat & Fluid flow*, 2013, 23(1), 189-204.
93. Hannoun N., Alexiades V., Mai T., “A reference solution for phase change with

- convection. *International Journal for Numerical Methods in Fluids*,” 2005, 48(11), 1283-1308.
94. Li Z., Yang M., He Y., Zhang Y., “Mass balance in velocity Dirichlet boundary conditions for lattice Boltzmann method,” Under review.
95. Ghia U., Ghia K., Shin C., “High-Re solutions for incompressible flow using the Navier–Stokes equations and a multigrid method,” *J. Comput. Phys.*, 1982, 48,387-411.
96. Li Z., Yang M., Wang Z., Zhang Y., “A corrected method to solve convective-diffusion equation based on SIMPLE,” *Journal of Engineering Thermophysics*, 2012, 33(9), pp: 1563-1566.
97. Hortmann M., Peric M., Scheuerer G., “Finite volume multigrid prediction of laminar natural convection: Benchmark solutions,” *International Journal for Numer Methods in Fluids*, 1990, 11, 189-207
98. Minkowycz W., Sparrow E., Murthy J., *Handbook of Numerical Heat Transfer* (Second Edition), John Wiley & Sons, INC, 2006.
99. Faghri A., Zhang Y., Howell J., *Advanced Heat and Mass Transfer*, Global Digital Press, Columbia, MO, 2010.
100. Davis G., “Natural convection of air in a square cavity: A benchmark numerical solution,” *International Journal Numer Methods in Fluids*, 1983, 3, pp: 249-164.
101. Chen S., Chen H., Martinez D., Matthaeus W., “Lattice Boltzmann model for simulation of magnetohydrodynamics,” *Physical Review Letters*, 1991, 67(27), pp: 3776-3779.
102. Qian Y., D'Humières D., Lallemand P., “Lattice BGK model for Navier-Stokes equation,” *Europhysics Letters*, 1992, 17(6), 479-484.

103. Lallemand P., Luo L., “Theory of the lattice Boltzmann method: dispersion, dissipation, isotropy, Galilean invariance, and stability,” *Physical Review E*, 2000, 61(6), pp: 6546-6562.
104. Chikatamarla S., Ansumali S., Karlin I., “Entropic lattice Boltzmann models for hydrodynamics in three dimensions,” *Physical Review Letter*, 2006, 97(1), 010201.
105. Chikatamarla S., Karlin I., “Entropy and Galilean invariance of lattice Boltzmann theories,” *Physical Review Letter*, 2006, 97(19), 190601.
106. Ginzburg I., “Equilibrium-type and link-type lattice Boltzmann models for generic advection and anisotropic-dispersion equation,” *Advance in Water Resources*, 2005, 28(11), pp: 1171-1195.
107. Ginzburg I., d’Humières D., “Lattice Boltzmann and analytical modeling of flow processes in anisotropic and heterogeneous stratified aquifers,” *Advance in Water Resources*, 2007, 30(11), pp: 2202-2234.
108. Lallemand P., Luo L., “Theory of the lattice Boltzmann method: Acoustic and thermal properties in two and three dimensions,” *Physical Review E*, 2003, 68(3), 036706.
109. Luo L., Liao W., Chen X., Peng Y., Zhang W., “Numerics of the lattice Boltzmann method: Effects of collision models on the lattice Boltzmann simulations,” *Physical Review E*, 2011, 83(5), 056710.
110. Wang J., Wang D., Lallemand P., Luo L., “Lattice Boltzmann simulations of thermal convective flows in two dimensions,” *Computers and Mathematics with Applications*, 2013, 65, 262-286.
111. Mezrhab A., Moussaoui M., Jami M., Naji H., Bouzidi M., “Double MRT thermal

- lattice Boltzmann method for simulating convective flows,” *Physical Letters A*, 2010, 374, pp: 3499-3507.
112. Ginzburg I., “Truncation errors, exact and heuristic stability analysis of two-relaxation-times lattice Boltzmann schemes for anisotropic advection-diffusion equation,” *Communications in Computational Physics*, 2012, 11(5), pp: 1090-1143.
 113. Li Z., Yang M., Zhang Y. Stephen Montgomery-Smith, “Effects of initial conditions on oscillatory flow in an oscillating heat pipe,” Under review.
 114. Chakraborty S., Chatterjee D., “An enthalpy-based hybrid lattice-Boltzmann method for modelling solid-liquid phase transition in the presence of convective transport,” *Journal of Fluid Mechanics*, 2007, 592, pp: 155-176.
 115. Sharif M., Mohammad T., “Natural convection in cavities with constant flux heating at the bottom wall and isothermal cooling from the side walls,” *International Journal of Thermal Sciences*, 2005, 44, 865-878.
 116. Ganzarolli M., Milanez L., “Natural convection in rectangular enclosure heated from below and cooled along one side,” *Int. J. Heat Mass Transfer*, 1995, 38, 1063-1073.
 117. Anwarullah M, Rao V., Sharma K., “Experimental investigation for enhancement of heat transfer from cooling of electronic components by circular air jet impingement,” *Heat Mass Transfer*, 2012, 48, 1627-1635.
 118. Siba E., Pillai M., Harris K., “Heat transfer in a high turbulence air jet impinging over a flat circular disk,” *ASME J. Heat Transfer*, 2003, 125, 257-265.
 119. Rodgers P., Eveloy V., Davies M., “An experimental assessment of numerical predictive accuracy for electronic component heat transfer in forced convection,”

- Journal of Electronic Packaging*, 2003, 125, 67-75.
120. Agonafer D., Anderson T., Chrysler G., Convertible cooling module for air or water cooling of electronic circuit components United States Patent, Patent number: 5370178, 1994.
 121. Fok S., Shen W., Tan F., "Cooling of portable hand-held electronic devices using phase change materials in finned heat sinks," *International Journal of Thermal Sciences*, 2010, 49, 109-117.
 122. Lu T., Thermal management of high power electronics with phase change cooling. *International Journal of Heat and Mass Transfer*, 2000, 43, pp: 2245-2256.
 123. Semma E., Gananoui M., Bennacer R., Mohamad A. A., "Investigation of flows in solidification by using the lattice Boltzmann method," *International Journal of Thermal Sciences*, 2008, 47(3), 201-208.
 124. Spaid M., Phelan F., "Lattice Boltzmann methods for modeling microscale flow in fibrous media," *Physics of Fluids*, 1997, 9(9), pp: 2468-2474.
 125. Dardis O., McCloskey J., "Lattice Boltzmann scheme with real numbered solid density for the simulation of flow in porous media," *Physical Review E*, 1998, 57(4), 57-60.
 126. Leong W., Hollands K., Brunger A., "Experimental Nusselt numbers for a cubical-cavity benchmark problems in natural convection," *International Journal of Heat and Mass Transfer*, 1999, 42(11), pp. 1979-1989.
 127. Tric E., Labrosse G., Betrouni M., "A first incursion into the 3D structure of natural convection of air in a differentially heated cubic cavity from accurate numerical solutions," *International Journal of Heat and Mass Transfer*, 2000, 43(21), pp: 4043-

- 4056.
128. Wakashima S., Saitoh T., “Benchmark solutions for natural convection in a cubic cavity using the high-order time-space method,” *International Journal of Heat and Mass transfer*, 2004, 47(4), pp: 853-864.
 129. Salat J., Xin S., Joubert P., Sergent A., Penot F., Quere P., “Experimental and numerical investigation of turbulent natural convection in a large air-filled cavity,” *International Journal of Heat and Fluid Flow*, 2004, 25(5), pp: 824-832,.
 130. Peng Y., Shu C., Chew Y., “A 3D incompressible thermal lattice Boltzmann model and its application to simulate natural convection in a cubic cavity,” *Journal of Computational Physics*, 2003, 193(1), pp: 260-274.
 131. Azwadi C., Syahrullil S., “A three-dimension double-population thermal lattice BGK model for simulation of Natural Convection Heat Transfer in a cubic cavity,” *WSEAS Transactions on Mathematics*, 2009, 8(9), pp: 561-570.
 132. Du H., Chai Z., Shi B., “Lattice Boltzmann study of mixed convection in a cubic cavity,” *Communications in Theoretical Physics*, 2011, 56(1), pp: 144-150.
 133. Seyyedi S., Soleimani S., Ghasemi E., Ganji D., Gorji-Bandpy M., Bararnia H., “Numerical investigation of laminar mixed convection in a cubic cavity by MRT-LBM: effects of the sliding direction,” *Numerical Heat Transfer, Part A*, 2013, 63(4), pp: 285-304.
 134. Leong W., Hollands K., Brunger A., “On a physically-realizable benchmark problem in internal natural convection,” *International Journal of Heat and Mass Transfer*, 1997, 41(23), pp: 3817-3828.
 135. d’Humières D., Ginzburg I., Krafczyk M., Lallemand P., Luo L., “Multiple-

- relaxation-time lattice Boltzmann models in three dimensions,” *Philosophical Transactions*, 2002, 360, pp: 437-451.
136. He X., Luo L., “Lattice Boltzmann model for the incompressible Navier-Stokes Equation,” *Journal of Statistical Physics*, 1997, 88, pp: 927-944.
137. Yoshida H., Nagaoka M., “Multiple- relaxation-time lattice Boltzmann model for the convection and anisotropic diffusion equation,” *Journal of Computational Physics*, 2010, 229(20), pp: 7774-7795.
138. Li L., Mei R., Klausner J., Boundary conditions for thermal lattice Boltzmann equation method, *Journal of Computational Physics*, 2013, 237, pp: 366-395.
139. Wang J., Wang D., Lallemand P., Luo L., “Lattice Boltzmann simulations of thermal convective flows in two dimensions,” *Computers and Mathematics with Applications*, 2013, 65, 262-286.
140. Fusegi T., Hyun J., Kuwahara K., Farouk B., “A numerical study of three-dimensional natural convection in a differentially heated cubical enclosure,” *International Journal of Heat and Mass Transfer*, 1991, 34(6), pp. 1543-1557.

VITA

Zheng Li was born in 1986, and completed his Bachelor degree study in Energy and Power Engineering at University of Shanghai for Science and Technology in Shanghai, mainland of China. He started Ph. D. study in Department of Mechanical and Aerospace Engineering at University of Missouri-Columbia since January 2012.